

UNIVERSITY OF CALIFORNIA

Los Angeles

Performance Based
Implementation of Seismic Protective Devices
for Structures

A dissertation submitted in partial satisfaction of the
requirements for the degree Doctor of Philosophy
in Civil Engineering

by

Wang Xi

2014

UMI Number: 3607964

All rights reserved

INFORMATION TO ALL USERS

The quality of this reproduction is dependent upon the quality of the copy submitted.

In the unlikely event that the author did not send a complete manuscript and there are missing pages, these will be noted. Also, if material had to be removed, a note will indicate the deletion.



UMI 3607964

Published by ProQuest LLC (2014). Copyright in the Dissertation held by the Author.

Microform Edition © ProQuest LLC.

All rights reserved. This work is protected against unauthorized copying under Title 17, United States Code



ProQuest LLC.
789 East Eisenhower Parkway
P.O. Box 1346
Ann Arbor, MI 48106 - 1346

© Copyright by

Wang Xi

2014

ABSTRACT OF THE DISSERTATION

Performance Based Implementation of Seismic Protective Devices for Structures

by

Wang Xi

Doctor of Philosophy in Civil Engineering

University of California, Los Angeles, 2014

Professor Jian Zhang, Chair

In order to improve the seismic performance of structures and to reduce the total cost (both direct and indirect) due to earthquake damages, structural control through seismic protective devices in either passive or semi-active forms is essential to achieve the desired performance goals. This research intends to develop optimal design and placement of seismic protective devices for improving structural performance of buildings and bridges. This is accomplished by deriving (a) optimal nonlinear damping for inelastic structures, (b) hybrid numerical simulation framework to facilitate nonlinear structural control analysis and (c) efficient seismic protective scheme for bridges using base isolation, nonlinear supplemental damping and semi-active MR dampers.

Supplemental energy dissipation in the form of nonlinear viscous dampers is often used to improve the performance of structures. The effect of nonlinear damping is a function of structural properties, ground motion characteristics and performance objectives. In order to quantify the optimal amount of nonlinear damping needed for inelastic structures, a novel

dimensionless nonlinear damping ratio is first proposed through dimensional analysis of inelastic SDOF structures. Subsequently, an equivalent SDOF inelastic system is derived to represent the general MDOF inelastic structures. Based on this equivalency and the help of the nonlinear damping ratio definition, the optimal damping and damper placement for MDOF inelastic structures are developed using genetic algorithms. It's demonstrated that the added nonlinear damping is not always beneficial for inelastic structures, i.e. resulting in the increase of total acceleration response under certain ground motions. A critical structure-to-input frequency ratio exists, upon which an optimal nonlinear damping is needed to balance between the increase of total acceleration and the reduction of structural drift.

Secondly, to facilitate the nonlinear control simulation of complex structures, an existing hybrid testing framework (UI_SimCor) is adopted and modified to enable the dynamic analysis of nonlinear structures equipped with seismic protective devices, including nonlinear viscous dampers, base isolators and MR dampers. Under this framework, inelastic structures can be modeled realistically in general FEM platform (e.g. OpenSees) while the seismic protective devices can be modeled numerically in a different software (e.g. Matlab). Furthermore, control algorithms can also be implemented easily under this hybrid simulation scheme. To validate the hybrid simulation approach, an experimental program is implemented on a scaled 3-story steel frame structure controlled by a semi-active MR damper. Both real-time hybrid simulation and shake table tests were performed and compared. The good agreement between them verifies the accuracy and efficiency of the hybrid simulation scheme. In addition, for application to bridges, special scheme to incorporate multi-support input earthquake motions is also developed so that the significant soil-structure interaction effects on bridges can be simulated.

Finally, the efficient seismic protective scheme for bridges is explored using the hybrid simulation scheme developed. A real highway bridge, the Painter Street Bridge (PSB) is modeled realistically in OpenSees including soil-structure interaction effects while the seismic protective devices and control algorithm are implemented separately in Matlab. Clipped-optimal control algorithm based on LQG regulator and Kalman filter is adopted to derive the optimal structural response of PSB with base isolation and semi-active controlled MR dampers. Eventually, an equivalent passive form of MR dampers is developed, which can mimic the effects of semi-active control to achieve the optimal design of seismic protective devices for highway bridge applications.

The dissertation of Wang Xi is approved.

Scott J. Brandenberg

Ertugrul Taciroglu

Christopher S. Lynch

Jian Zhang, Committee Chair

University of California, Los Angeles

2014

To my father, mother and sister

Fengchang, Yifan & Ning

*for their unconditional
love, encouragement, and support...*

谨以此论文献给我的父亲，母亲和姐姐

奚凤昌, 李懿范 & 奚宁

感谢他们永恒的爱，
热忱的鼓励和不变的期待.....

TABLE OF CONTENTS

ABSTRACT OF THE DISSERTATION	ii
COMMITTEE APPROVAL	v
DEDICATION	vi
TABLE OF CONTENTS	viii
LIST OF FIGURES	xi
LIST OF TABLES	xiv
ACKNOWLEDGMENTS	xv
VITA	xvii
1. INTRODUCTION	1
1.1 Background	1
1.2 Earthquake Damage Mechanism of Highway Bridges	2
1.2.1 Unseating	3
1.2.2 Column Flexural Failure	3
1.2.3 Column Shear Failure	3
1.2.4 Joint Failure	4
1.2.5 Soil Structure Interaction (SSI)	5
1.3 Seismic Protective Devices and Application	5
1.3.1 Passive Seismic Protective Devices	6
1.3.2 Active and Hybrid Seismic Protective Devices	11
1.3.3 Semi-Active Seismic Protective Devices	13
1.3.4 Cons and Pros	15
1.4 Hybrid Testing of Civil Engineering Structures	17
1.5 Performance Based Earthquake Engineering (PBEE)	19
1.5.1 PBEE Methodology	19
1.5.2 Structural Control in PBEE Frame	22
1.6 Scope and Objectives	23
1.7 Organization	25
2. OPTIMAL NONLINEAR DAMPING FOR MDOF INELASTIC STRUCTURES	28
2.1 Dimensional Analysis of SDOF Inelastic Structures Equipped with Nonlinear Viscous Dampers	30
2.2 Effects of Nonlinear Viscous Damping on SDOF Inelastic Structures	34
2.3 Equivalent SDOF Representation of MDOF Inelastic Structures Equipped with Nonlinear Viscous Dampers	40
2.3.1 Methodology	40
2.3.2 Verification of Proposed Equivalent SDOF System	44
2.4 Optimal Nonlinear Damper Design for Shear Type MDOF Structure	48
2.5 Concluding Remarks	54

3.	HYBRID NUMERICAL SIMULATION PLATFORM FOR SEISMIC RESPONSE ANALYSIS OF NONLINEAR STRUCTURES	56
3.1	Hybrid Simulation Platform: UI-SIMCOR	58
3.1.1	Static Condensation and Effective Degree of Freedoms (DOF)	58
3.1.2	Time Integration Method Adopted in UI_SimCor	61
3.1.3	Development of Multiple Support Excitation Scheme in UI_SimCor	63
3.2	Development of Seismic Protective Device Elements	66
3.2.1	Development of Base Isolation Element	66
3.2.2	Development of Nonlinear Viscous Damper Element	67
3.2.3	Development of MR Damper Element	70
3.3	Validation of Hybrid Numerical Simulation Scheme	72
3.3.1	Verification Case I: Linear Viscous Dampers Installed Between Floors	73
3.3.2	Verification Case II: Nonlinear Viscous Damper Installed between First Floor and Outside Fixture	74
3.3.3	Verification Case III: Base Isolators Installed at Base Level of the Structure..	75
3.3.4	Verification Case IV: MR Damper Installed between First Floor and Outside Fixture	75
3.4	Implementation of Structural Control Algorithm with Hybrid Numerical Simulation.....	77
3.4.1	Classical Linear Optimal Control Theory (LQR)	78
3.4.2	Equivalent Optimal Passive Control Approximation	79
3.4.3	Numerical Results	80
3.5	Concluding Remarks	81
4.	EXPERIMENTAL VALIDATION OF NUMERICAL HYBRID SIMULATION SCHEME BASED ON UI_SIMCOR	83
4.1	Basic Information	85
4.1.1	Experimental Structure	85
4.1.2	Earthquake Ground Motion Inputs	87
4.1.3	Three Dimensional Numerical Model in OpenSees	89
4.2	Theory Backgroud	91
4.2.1	Analytical Model and State Space Formulation of the Experimental Structure.	91
4.2.2	Semi-active Control Algorithm of the Experimental Structure Controlled by A MR Damper	93
4.2.3	Eigensystem Realization Algorithm (ERA) for System Identification	94
4.2.4	Analytical Model Updating of Experimental Structure Based on System Identification	97
4.3	Test Setup and Procedure	99
4.3.1	System Identification Test	99
4.3.2	MR Damper Calibration Test	104
4.3.3	Real Time Hybrid Simulation (RTHS) Test	109
4.3.4	Shake Table Test	112
4.4	Numerical Simulation Methodology and Platforms	119
4.4.1	Simulation Platform Based on Simulink of Matlab	119
4.4.2	Simulation Platform Based on Matlab ODE Solver	120
4.4.3	Simulation Platform Based on UI_SimCor	121

4.5	Test Results and Discussion	121
4.5.1	System Identification test	121
4.5.2	MR Damper Calibration Test	125
4.5.3	RTHS and Shake Table Tests	128
4.5.4	Verification of Numerical Simulation Platforms	136
4.6	Concluding Remarks	140
5.	IMPLEMENTATION OF HYBRID SIMULATION FOR SEISMIC PROTECTION DESIGN OF HIGHWAY BRIDGES	142
5.1	Introduction of Painter Street Bridge	144
5.1.1	Geometry and Instrumentation	144
5.1.2	Soil Structure Interaction (SSI) & Kinematic Response of Embankments	146
5.2	Finite Element (FE) Modeling: Platform and Methodology	149
5.2.1	FE model of Original Painter Street Bridge	149
5.2.2	FE model of Painter Street Bridge with Base Isolation	150
5.2.3	FE model of Painter Street Bridge with Base Isolation & MR damper	152
5.3	Validation of the Stick Type FE model of Painter Street Bridge	153
5.3.1	Validation by ABAQUS	153
5.3.2	Validation by Recorded Motion	155
5.4	Design of Base Isolation of Painter Street Bridge	157
5.4.1	Bilinear Model of Base Isolation Devices	157
5.4.2	Eigenvalues and Mode Shapes Of Painter Street Bridge	159
5.4.3	Preliminary Design of Base Isolation Device	159
5.4.4	Numerical Simulation of Base Isolated Painter Street Bridge	162
5.5	MR Damper Design of Base Isolated Painter Street Bridge: Semi-active Control Development and Application	165
5.5.1	Derivation of Optimal Control Force for MR Dampers	166
5.5.2	Semi-active Control Algorithm of MR Damper: Clipped-Optimal Control	168
5.5.3	Evaluation of System Matrices/Vectors Required in Optimal Controller Design	170
5.5.4	Numerical Simulation of Semi-active Control of MR Dampers on Painter Street Bridge	172
5.6	Equivalent Optimal Passive Control Design	178
5.7	Practical Optimal Passive Control Design of MR dampers	185
5.8	Concluding Remarks	201
6.	CONCLUSIONS AND FUTURE WORK	203
6.1	Conclusions	203
6.2	Recommendations for Future Work	206
References		208

LIST OF FIGURES

Fig. 1.1 Highway bridge failure mechanism observed in the historical earthquakes	4
Fig. 1.2 LRB and FPS base isolation systems	7
Fig. 1.3 LRB base isolation system used for buildings	8
Fig. 1.4 LRB base isolation system used for highway bridges	8
Fig. 1.5 FPS base isolation system used for buildings	9
Fig. 1.6 Passive energy dissipation systems	10,11
Fig. 1.7 Example of viscous fluid damper application in highway bridges	11
Fig. 1.8 Composition of AMD system	12
Fig. 1.9 Variable damping devices	14
Fig. 1.10 Semi-active control system application in Highway bridges	15
Fig. 1.11 Architecture of UI_SimCor	19
Fig. 1.12 SEAOC recommended seismic performance objectives for buildings	20
Fig. 1.13 PEER PBEE methodology framework	21
Fig. 1.14 Illustration of PBEE framework with structural control strategy	23
Fig. 2.1 Response similarity with $\Pi_{\xi,n} = 0.10$ and $\Pi_\alpha = 0.35$	34
Fig. 2.2 Dimensionless displacement and total acceleration responses (Type-B)	36
Fig. 2.3 Normalized response spectra under real earthquake	38
Fig. 2.4 Normalized total acceleration spectra under real earthquakes	38
Fig. 2.5 Normalized system responses for different Π_ω and $\Pi_{\xi,n}$	39
Fig. 2.6 Equivalency of nonlinear viscous damper to linear viscous damper	40
Fig. 2.7 Illustration of a general N DOF inelastic structure with nonlinear dampers	41
Fig. 2.8 Comparison of top floor displacement of a 3DOF structure	46
Fig. 2.9 Comparison of top floor displacement of a 8DOF structure	48
Fig. 2.10 Structural response with optimal nonlinear damper design	53
Fig. 3.1 Hybrid numerical simulation scheme	58
Fig. 3.2 Static condensation of multiple DOF structures	59
Fig. 3.3 Formulation of stiffness matrix in UI-SIMCOR	61
Fig. 3.4 Force-displacement loop of base isolator element	67
Fig. 3.5 Modified Bouc-Wen model for MR damper	70
Fig. 3.6 Verification of proposed MR damper element with ODE solver in Matlab	72
Fig. 3.7 Structural control strategies for numerical simulation and verification	73
Fig. 3.8 Comparison of structural response under control by linear viscous dampers	74
Fig. 3.9 Comparison of structural response under control by nonlinear viscous dampers	74
Fig. 3.10 Comparison of structural response under control by base isolation	75
Fig. 3.11 Experimental verification of hybrid numerical simulation for MR dampers (passive-off)	76
Fig. 3.12 Experimental verification of hybrid numerical simulation for MR dampers (passive-on)	77
Fig. 3.13 Numerical example of structural control application with hybrid simulation	78

Fig. 3.14 Response history of 1 st floor with different control designs	81
Fig. 3.15 Response history of top floor with different control designs	81
Fig. 4.1 Experimental structure	86
Fig. 4.2 MR damper installation configuration	87
Fig. 4.3 Ground motions for experimental test and numerical simulation	88,89
Fig. 4.4 Mode shape of the experimental structure by 3D FE model	90
Fig. 4.5 Effect of rotation transformation	97
Fig. 4.6 DAQ system and data processing software	100
Fig. 4.7 Impact hammer used in the test	102
Fig. 4.8 Accelerometer and charge amplifier	102
Fig. 4.9 3D view for sensor placement and hammer hit location	103
Fig. 4.10 MR damper current driver and dSpace 1104	105
Fig. 4.11 Voltage-Current relationship of MR damper	105
Fig. 4.12 2500 KN MTS actuator and 15 KN force transducer	106
Fig. 4.13 MTS Flex GT controller and software	106
Fig. 4.14 Experimental setup for MR damper calibration test	107
Fig. 4.15 Sine wave input of MR damper calibration test	108
Fig. 4.16 Experimental setup for RTHS test	110
Fig. 4.17 Validation of RIAC strategy by theoretical inputs	111
Fig. 4.18 Validation of RIAC strategy by earthquake input	112
Fig. 4.19 Shake table located at HIT	113
Fig. 4.20 Schenck actuator of the shake table	114
Fig. 4.21 DongHua dynamic data acquisition system DH5922	114
Fig. 4.22 Keyence laser displacement sensor and controller	115
Fig. 4.23 Shake table test structure and MR damper	115
Fig. 4.24 Calibration of Keyence laser sensor and LVDT	117
Fig. 4.25 Shake table test setup	118
Fig. 4.26 Numerical modeling of MR damper in Simulink	119
Fig. 4.27 Mutual verification of ODE based and Simulink Based MR damper model ..	120
Fig. 4.28 Transfer function comparison of experimental data and ERA result	122
Fig. 4.29 First 3 modes in y-axis comparison of experimental and analytical solution ..	122,123
Fig. 4.30 Comparison of updated 3D OpenSees model with updated 3DOF model ..	124,125
Fig. 4.31 Force-displacement and force-velocity loops by MR damper calibration test.	125,126
Fig. 4.32 Numerical model VS test data of MR damper	128
Fig. 4.33 Structural response comparison for passive-off control, El-Centro	130
Fig. 4.34 Structural response comparison for semi-active control, El-Centro	131
Fig. 4.35 Structural response comparison for passive-off control, Kobe	132
Fig. 4.36 Structural response comparison for semi-active control, Kobe	133
Fig. 4.37 Structural response comparison for passive-off control, Morgan Hill	134
Fig. 4.38 Structural response comparison for semi-active control, Morgan Hill	135
Fig. 4.39 Comparison of numerical models with shake table test (Passive-off)	137
Fig. 4.40 Comparison of numerical models with shake table test (Passive-on).....	138
Fig. 4.41 Comparison of numerical models with shake table test (Semi-active)	139
Fig. 5.1 Configuration sketch of Painter Street Bridge	145

Fig. 5.2 Plan view of Painter Street Bridge and recording channel setup	146
Fig. 5.3 Free field ground motion of 1992 Petrolia earthquake	146
Fig. 5.4 Amplification effect of kinematic response of embankment	148
Fig. 5.5 Finite element stick model of Painter Street Bridge	150
Fig. 5.6 Base isolator setup for Painter Street Bridge	151
Fig. 5.7 Hybrid model of Painter Street Bridge with base isolators	151
Fig. 5.8 Base isolator and MR damper setup for Painter Street Bridge	152
Fig. 5.9 Hybrid model of Painter Street Bridge with base isolators and MR dampers ...	153
Fig. 5.10 Total displacement and acceleration response comparison	154
Fig. 5.11 Verification of numerical simulation results with recorded motions	155,156,157
Fig. 5.12 Configuration and cyclic loop of commonly used base isolators	158
Fig. 5.13 Bilinear cyclic model for base isolators	158
Fig. 5.14 Modal shape and frequency of Painter Street Overcrossing	160
Fig. 5.15 Pushover analysis of piers in Painter Street Overcrossing	161
Fig. 5.16 Base isolator response of design case II	163
Fig. 5.17 Pier and deck response of design case II	163
Fig. 5.18 Base isolator response comparison of design case I and II	164
Fig. 5.19 Pier and deck response comparison of design case I and II	165
Fig. 5.20 Optimal control force estimation process	169
Fig. 5.21 Modified Bouc-Wen model of MR damper	172
Fig. 5.22 Comparison of structural responses of different control strategies	175
Fig. 5.23 Comparison of base isolator responses of different control strategies	176
Fig. 5.24 MR damper response and control voltage input of clipped optimal control ...	177
Fig. 5.25 Equivalent passive-on voltage based on semi-active control history	180
Fig. 5.26 Comparison of structural response by semi-active and its equivalent passive control	182
Fig. 5.27 Comparison of bearing response by semi-active and its equivalent passive control	183
Fig. 5.28 Comparison of MR damper response by semi-active and its equivalent passive control	184
Fig. 5.29 Shear-wedge model of bridge embankments	186
Fig. 5.30 Normalized soil shear modulus and damping coefficient as function of shear strain	188
Fig. 5.31 Kinematic response of embankments under Pacoima Dam record	189,190
Fig. 5.32 Selection of practical spring and dashpot values of approach embankment ...	192
Fig. 5.33 Maximum structural responses under selected earthquake records ($T_{tgt} = 1s$). Fig. 5.34 Maximum structural responses under selected earthquake records ($T_{tgt} = 2s$). 	195 196

LIST OF TABLES

Table 2.1 Comparison of ξ_d and $\Pi_{\xi,n}$ for nonlinear viscous dampers	34
Table 2.2 Characteristics of chosen pulse represented earthquakes	37
Table 2.3 Equivalent parameters of the SDOF system	45
Table 2.4 Nonlinear damping ratio of 1 st mode of a MDOF structure (%)	47
Table 2.5 Structural properties of a sample 8 degree-of-freedom structure	47
Table 2.6 Optimal design of nonlinear dampers for a 3DOF structure	52
Table 2.7 Structural properties of a sample 8 degree-of-freedom structure	53
Table 2.8 Optimal design of nonlinear dampers for a 8DOF structure	54
Table 4.1 Mechanical properties of experimental structure material	86
Table 4.2 Section shapes and geometry properties of experimental structure	86
Table 4.3 Maximum displacement responses	90
Table 4.4 Maximum absolute acceleration responses	91
Table 4.5 Information of accelerometers	101
Table 4.6 Technical properties of MR damper RD-1005-3	104
Table 4.7 Loading cases of MR damper calibration test	108
Table 4.8 Shake table parameters and capacities	113
Table 4.9 Information of displacement sensors	116
Table 4.10 Modal frequency and damping from system identification	122
Table 4.11 Modified Bouc-Wen model parameters for MR damper	127
Table 5.1 SSI springs and dashpots of Painter Street Bridge	150
Table 5.2 Modeling parameters of base isolators	162
Table 5.3 MR damper installation location	166
Table 5.4 Voltage dependent modeling parameters of MR damper	173
Table 5.5 Constant modeling parameters of MR damper	173
Table 5.6 Equivalent optimal passive design parameters of MR damper ($T_{tgt} = 1s \& 2s$)	181
Table 5.7 Equivalent optimal passive design parameters of MR damper ($T_{tgt} = [1 2]s$)	182
Table 5.8 Earthquake records selected for seismic protective device design	185
Table 5.9 Converged values of the shear modulus, damping coefficient and shear strain under selected strong motion records	191
Table 5.10 Spring and dashpot values that approximate the presence of the approach embankments and pile foundations of Painter Street Bridge	193
Table 5.11 Equivalent optimal passive design of MR dampers for ten ground motions ($T_{tgt} = 1s$)	197,198
Table 5.12 Equivalent optimal passive design of MR dampers for ten ground motions ($T_{tgt} = 2s$)	199,200
Table 5.13 Practical optimal passive design of MR dampers ($T_{tgt} = 1s$)	201
Table 5.14 Practical optimal passive design of MR dampers ($T_{tgt} = 2s$)	201
Table 5.15 Final optimal passive design parameters of MR dampers for $T_{tgt} = [1 2]s$	201

ACKNOWLEDGMENTS

First, I want to express my most gratefulness to my advisor, Professor Jian Zhang, for her continuing support and guidance, as a supervisor in school and as a friend in life. The words from her “Wang, you are capable” is the best encouragement I had, am having and will have ever.

I would like to extend my wholehearted appreciation to the members of my doctoral committee, Prof. Scott J. Brandenberg, Prof. Ertugrul Taciroglu, and Prof. Christopher S. Lynch, for their incomparable lessons and suggestions which not only provided me knowledge, but also delivered to me the attitude of an outstanding researcher.

I also would like to express my most sincere thankfulness to Prof. Shirley Dyke from Purdue University and Prof. Bin Wu from Harbin Institute of Technology, China, for their great and precious support in providing me with experimental facilities and detailed academic guidance that guaranteed the success of the experiments essential for my research work.

It's greatly appreciated of the NSF projects that funded my research work through the Network for Earthquake Engineering Simulation Research Program: Development of Next Generation Adaptive Seismic Protection (NEESR-SG, CMMI-0830391) and Performance-Based Design and Real-time Large-scale Testing to Enable Implementation of Advanced Damping Systems (supplement to NEESR-SG, CMMI-1011534). China Scholarship Council (CSC) also supported my study in UCLA and I deliver my deepest appreciation here as well.

My special thanks go to my friends, Shi-Po Lin and Ali I. Ozdagli. Without their accompany, I couldn't imagine how harder my life would turn to be. The time I spent with them exchanging academic ideas as well as dreams for life, would become the most precious memory of my PhD study.

Now I would like to thank all my research group members, fellow students and professionals, as well as department staff, especially Maida Bassili, who supported me with their constructive comments, pleasant teamwork, and heart-warming help regarding various aspects of my life at UCLA.

My boundless acknowledgement is given to my little friends, Kim Wang, Devon Wang and my cute niece, Jiaxi Liu, for their being angel and cheering me up all the time. Whenever see their smile and hear their voice, I gain the strength and hope to overcome various challenges and difficulties in life.

Last but not least, I want to offer my utmost gratitude to my father Fengchang, my mother Yifan and my sister Ning, for their endless and unconditional love and expectation, which is the origin of all my courage and happiness. I love you, my family, I am so lucky to have you guys by my side.

VITA

EDUCATION

- M.Eng. in Structural Engineering, Tsinghua University, Beijing, China (2004-2007)
- B.Eng. in Civil Engineering, Tsinghua University, Beijing, China (2000-2004)

TEACHING AND RESEARCH ACTIVITIES (SELECTED)

- Graduate Research and Teaching Assistant, Department of Civil and Environmental Engineering, University of California, Los Angeles, U.S.A. (2007-2013)

HONORS AND AWARDS (SELECTED)

- University Fellowship (2007-2008, 2009-2010, 2011-2012 and 2012-2013) and Department Grant for Nonresident Tuition Waiver (2007-2008 and 2008-2009), Department of Civil and Environmental Engineering, University of California, Los Angeles
- EERI Undergraduate Seismic Design Competition, 1st Place for Numerical Prediction, 2013 (Serving as Dynamic Analysis Counselor)
- E-Defense Blind Analysis Contest, 3rd Place for Fixed-Base Configuration, 2011
- Department Travel Grant for Quake Summit 2011 NEES-MCEER Annual Meeting, Department of Civil & Environmental Engineering, University of California, Los Angeles, 2011
- Ph.D. Comprehensive Written Exam, Pass with Distinction, Department of Civil & Environmental Engineering, University of California, Los Angeles, 2008
- Graduate Scholarship of Academic Excellence, 1st Prize, Tsinghua University, 2006
- Graduate Scholarship of Academic Excellence, 3rd Prize, Tsinghua University, 2005
- Undergraduate Scholarship of Academic Excellence, 2nd Prize, Tsinghua University, 2003
- Scholarship of Excellent Social Activities, 3rd Prize, Tsinghua University, 2002

PROFESSIONAL ACTIVITIES (SELECTED)

- President, EERI/UCLA Student Chapter, 2011-2013
- Engineer in Training, California, U.S.A., May 2012

JOURNAL PUBLICATIONS (SELECTED)

- Wang, Y.Q., Xi, W. and Shi, Y.J. (2006). "Experimental Study on Mechanical Properties of Rail Steel at Low Temperature", *Journal of Railway Engineering Society*, (8): 36-48.
- Wang, Y.Q., Xi, W. and Shi, Y.J. (2007). "Experimental Study on Impact Toughness of Rail Steel at Low Temperature", *Journal of Tsinghua University (Science and Technology)*, 47(9): 45-57.
- Wang, Y.Q., Hu, Z.W., Shi, Y.J. and Xi, W. (2009). "Analysis of the Impact Toughness Test and Fracture of Rail Thermit Welding Joints at Low Temperature", *Journal of Lanzhou Jiaotong University*, 28(6): 75-78.

- Wang, Y.Q., Zhou, H., Xi, W. and Shi, Y.J. (2010). "Experimental Study on Mechanical Properties of Thermit Joints of Rail Steels at Low Temperature", *Transactions of the China Welding Institution*, 31(7): 13-16, 21.
- Zhang, J. and Xi, W. (2012). "Optimal Nonlinear Damping for MDOF Inelastic Structures". (To Be Submitted)
- Zhang, J. and Xi, W. (2013). "Numerical Hybrid Simulation for Highway Bridges Equipped with Seismic Protective Devices: Platform Development and Experimental Validation". (Under Preparation)
- Zhang, J. and Xi, W. (2013). "Implementation of Numerical Hybrid Simulation for Seismic Protection Design of Highway Bridges". (Under Preparation)

CONFERENCE PRESENTATIONS (SELECTED)

- Xi, W. (2011). "Performance Based Implementation of Adaptive Stiffness and Damping for Structures", *Quake Summit 2011 NEES-MCEER Annual Meeting*, Buffalo, NY, U.S.A. (Poster Presentation)
- Xi, W. (2011). "Hybrid Simulation for Structural Control of Nonlinear Structures", *Real-time Hybrid Simulation Workshop*, Purdue University, West Lafayette, Indiana, U.S.A.
- Zhang, J. and Xi, W. (2012). "Effect of Nonlinear Damping on Structures under Earthquake Excitation with Dimensional Analysis", *Structures Congress 2012*, Chicago, Illinois, U.S.A.
- Zhang, J., Xi, W., Dyke, D.J., Ozdagli, A.I., Wu, B. (2012). "Seismic Protection of Nonlinear Structures Using Hybrid Simulation", *The 15th World Conference on Earthquake Engineering*, Lisbon, Portugal.
- Ozdagli, A.I., Xi, W., Ding, Y., Zhang, J., Dyke, S.J. and Wu, B. (2012). "Verification of Real-Time Hybrid Simulation with Shake Table Tests: Phase 1 - Modeling of Superstructure", *International Conference on Earthquake Engineering Research Challenges in the 21st Century*, Harbin, China.
- Ozdagli, A.I., Dyke, S.J., Xi, W., Zhang, J., Ding, Y. and Wu, B. (2012). "Verification of Real-Time Hybrid Simulation with Shake Table Tests: Phase 2 - Development of Control Algorithms", *The 15th World Conference on Earthquake Engineering*, Lisbon, Portugal.
- Zhang, J. and Xi, W. (2014). "Optimal Design of Supplemental Damping Devices for Nonlinear MDOF Structures Based on A Novel Nonlinear Damping Index", *Proceedings of the 10th National Conference in Earthquake Engineering*, Earthquake Engineering Research Institute, Anchorage, Alaska, U.S.A. (Accepted)

1. Introduction

1.1 Background

Buildings and bridges are vulnerable to earthquake induced damages. In particular, highway bridges are important components of lifeline system post earthquakes. Their loss of function or failure will result in loss of lives and direct economical loss, delay the post-earthquake recovery efforts and cause indirect economical loss. In past earthquake events, highway bridges have sustained damages to superstructures, foundations and, in some cases, being completely destroyed.

In Great Alaska Earthquake of 1964, nearly every bridge along the partially completed Cooper River Highway was seriously damaged or destroyed. Seven years later, more than 60 highway bridges on the Golden State Freeway in California were damaged in the 1971 San Fernando earthquake. This earthquake cost the state approximately \$100 million in bridge repairs (Meehan 1971). Then in 1989, the Loma Prieta earthquake in California damaged more than 80 highway bridges, with the cost of the earthquake to transportation about \$1.8 billion, of which \$300 million was the damage to highway bridges (United States General Accounting office). The worst disaster of the earthquake was the collapse of the two-level Cypress Street Viaduct of Interstate 880 in West Oakland, which killed 42 people and injured many more (Tarakji 1992). Several years later, the 1994 Northridge earthquake caused 286 highway bridges damaged and 7 of them lost their functionality due to severe damage (Caltrans 1994).

Similar damages were also reported outside USA. The 1995 Kobe earthquake in

Japan resulted in collapses of 9 highway bridges and destructive damages of 16 bridges (Ministry of Construction of Japan 1995). The most extensive damage occurred at a 18-span viaduct of Hanshin Expressway. This bridge collapsed due to failure of RC columns resulted from the premature shear failure. In 1999, the Chi-Chi earthquake of Taiwan, more than 10 bridges, including a cable-stayed bridge, were severely damaged (Chang et al. 2000). Most recently, during the 2008 Wenchuan earthquake in Sichuan of China, more than 328 highway bridges were damaged and 46 bridges of them suffered severe damages as to totally interrupt the traffic due to failed bridge piers or falling beams. The total losses to the transportation system due to the earthquake were over 10 billion dollars, most of which consisted of damage to bridges (Han et al. 2009).

As mentioned above, the historical earthquakes demonstrated the devastating impact they can have on highway bridges that are not adequately protected against seismic forces. After the Northridge (1994) and Loma Prieta (1989) earthquakes, concerns have been raised about the safety of bridges around US. Many states, like California, New Jersey, etc., are designing the new bridges considering seismic specifications and have initiated many retrofit programs. Since then, a lot of research efforts are put in to identify, address and mitigate the response of highway bridges under earthquakes, which is still a leading topic today.

1.2 Earthquake Damage Mechanism of Highway Bridges

One of the most essential reasons of highway bridges failure by earthquakes is seismic shaking, which was well recognized after the 1971 San Fernando earthquake. As a result of seismic shaking, highway bridges suffer severe damages to structural components.

The following summarizes the failure mechanisms of highway bridges, including the observation of span collapse, structure component damages, and other structural component damages.

1.2.1 Unseating

Structure displacement is a major cause of highway bridge span damage and failure during earthquakes. Excessive displacements in the longitudinal direction can fail the bridge via unseating of the superstructure. Unseating failure is particularly possible for simply supported highway bridges if seats or corbels located at the abutments or piers don't possess sufficient length. The entire superstructure span can become unseated, resulting in sudden bridge collapse. An example of unseating failure that happened in the 1999 Chi-Chi earthquake in Taiwan is shown in Fig. 1.1 (a).

1.2.2 Column Flexural Failure

Column flexural failure comes from the deficient reinforcement design for the unexpected seismic shaking, characterized by inadequate strength or inadequate ductility. Flexural failure usually occurs when the longitudinal confinement is not sufficient, which leads to concrete crush as strains exceed the capacity and the column is not tough to sustain the imposed flexural deformations without failure. Fig. 1.1 (b) shows the column flexural failure due to insufficient ductility in the 1995 Kobe earthquake.

1.2.3 Column Shear Failure

The column shear failure is characterized by the failure of the transverse shear reinforcement. Shear failure resulting from seismic shaking is more prominent in old

highway bridges due to insufficient shear reinforcement resulting in brittle and sudden failure.

Such failures can occur at relatively low structural displacements, at which stage the longitudinal reinforcement may have not yet yielded. Examples of shear failure can be found in several of the historical earthquakes. Fig. 1.1 (c) illustrates the shear failure of columns in Hanshin Expressway. Failure of a column can result in loss of vertical load carrying capacity which is often the primary cause of bridge collapse.

1.2.4 *Joint Failure*

Joints may be exposed to critically damaging actions when the joints lie outside of the superstructure. Although joint failures occurred in previous earthquakes, significant attention was not paid to joints until several spectacular failures were observed following the 1989 Loma Prieta earthquake. Fig. 1.1 (d) shows joint damage to the Embarcadero Viaduct in San Francisco during the 1989 Loma Prieta earthquake.



(a) Bridge unseating failure



(b) Bridge column flexural failure



(c) Bridge column shear failure



(d) Bridge joint failure

Fig. 1.1 Highway bridge failure mechanism observed in the historical earthquakes

1.2.5 Soil Structure Interaction (SSI)

When considering the bridge structure alone, the actual behavior of the bridge under seismic load may significantly differ from that from the analysis since the response of a bridge during an earthquake depends not only on the bridge itself, but also on the characteristics of the ground motion and the subsoil conditions. Particularly for soft soils, the foundation input motion during the earthquake differs from the so-called free-field ground motion that may exist in the absence of the bridge. The assumption of fixed support for a bridge upheld on soft soil ignores the interaction effects that result from the scattering of waves when reaching the foundation surface (kinematic interaction) and the flexibility and energy dissipation of foundation-soil system (inertial interaction). These interaction effects lead to dynamic responses that may differ considerably in amplitude and frequency from what is obtained when a fixed support is assumed.

1.3 Seismic Protective Devices and Application

A lot of highway bridge damages result from the particularly strong seismic shaking, which leads to large internal forces in the structural components. Since three decades ago, engineers and researchers have been giving efforts to the structure seismic response mitigation, which turns out to be an advanced field in structural engineering: structural control. A number of civil engineering structures, such as buildings and bridges, have been constructed or retrofitted with seismic protective devices, which has shown significant effectiveness in structural seismic response reduction (Housner et al. 1997). Based on the control mechanism and devices applied, seismic protective devices can be classified into three categories: passive devices, active/hybrid devices and semi-active devices.

1.3.1 Passive Seismic Protective Devices

(1) Base isolation systems

There are two basic types of isolation systems (Buckle and Mayes 1990). The first type is characterized by the use of elastomeric bearings made of rubber. With this approach, the structure is decoupled from the horizontal components of the earthquake ground motion by the rubber layer with low horizontal stiffness which is placed in between the superstructure and the foundation. The rubber layer gives the structure a much lower fundamental frequency than the fixed-base one and also the predominant frequencies of the ground motion. Thus the energy of the high frequency component of the ground motion is isolated and cannot be transmitted to the superstructure (Kunde and Jangid 2003). The mechanism and device of the first type of base isolation system is shown in Fig. 1.2 (a) and (b).

The second type of isolation system is characterized by the sliding system (Kawamura et al. 1988; Zayas et al. 1987). It limits the transfer of shear across the isolation interface. The well-known friction-pendulum system (FPS) is a kind of sliding system which uses a special interfacial material sliding on stainless steel plate. Fig. 1.2 (c) and (d) illustrate the basic configuration of a FPS system and its real construction.

Base isolation technique has been used for several buildings and bridges in the United States, both new and retrofitted construction (Rai et al. 2009). In process of seismic retrofitting, some of the most prominent U.S. monuments like, Pasadena City Hall, San Francisco City Hall, and LA City Hall were retrofitted using base isolation systems. The University of Southern California (USC) hospital (Fig. 1.3), the first isolated hospital building, survived without damage after the 1994 Northridge earthquake (Nagarajaiah and

Sun 2000). The peak ground acceleration outside the building was recorded at 0.49 g while the accelerations inside the building were only around 0.10 to 0.13 g. The records obtained from the USC hospital are particularly encouraging in that they represent the most severe test of an isolated building to date.

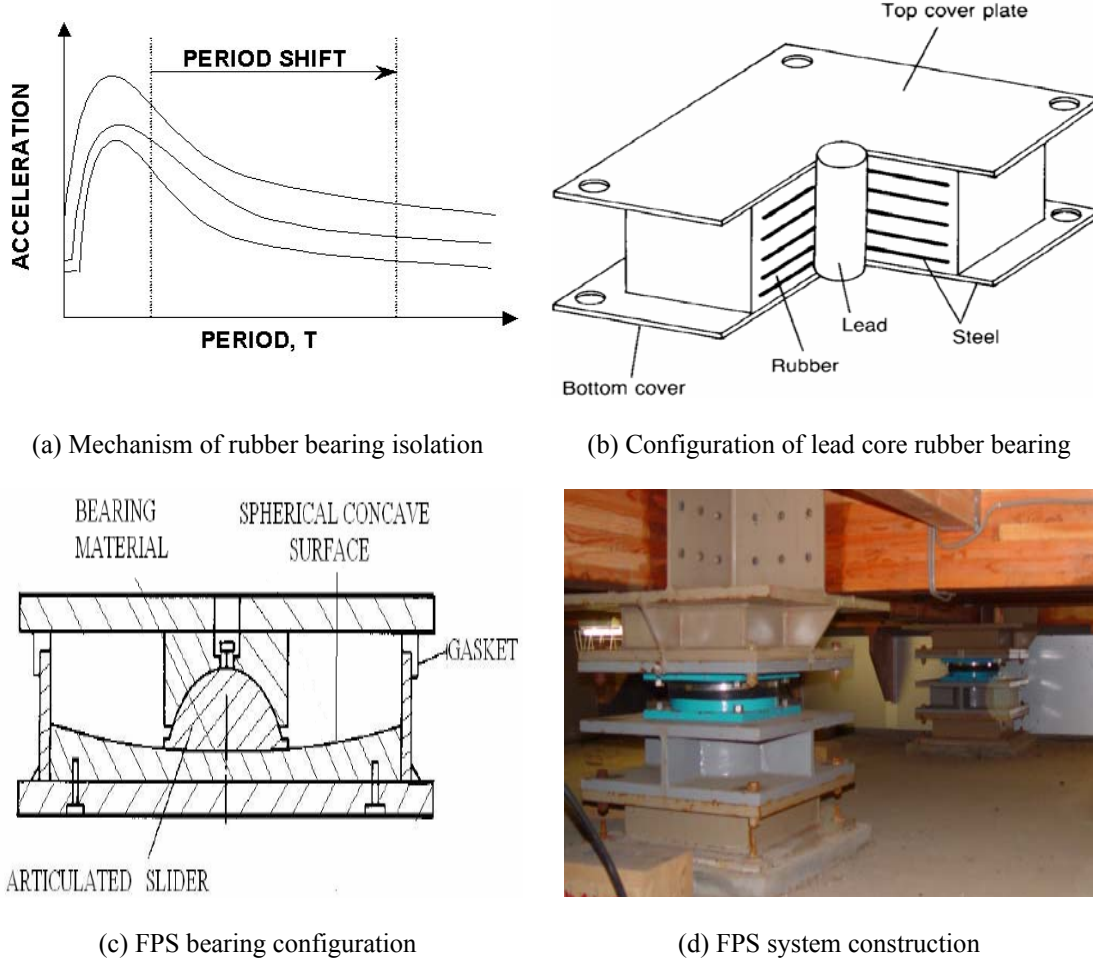


Fig. 1.2 LRB and FPS base isolation systems

(After Kunde and Jangid 2003)



(a) USC hospital building



(b) Lead rubber bearing (LRB)

Fig. 1.3 LRB base isolation system used for buildings

In highway bridges, the base isolation devices can be easily incorporated by replacing the conventional thermal/expansion bearings by the isolation bearings. Base isolation bearings serve the dual purposes of providing damping mechanism dissipating the seismic energy as well as protecting the bridge from dynamic loads by changing the fundamental period. After the 1995 Kobe earthquake in Japan, Fukae Viaduct, Hanshin Expressway was reconstructed by base isolation technique (Kawashima 2004), as shown in Fig. 1.4.



(a) Fukae Viaduct under reconstruction



(b) LRB used in Fukae Viaduct

Fig. 1.4 LRB base isolation system used for highway bridges

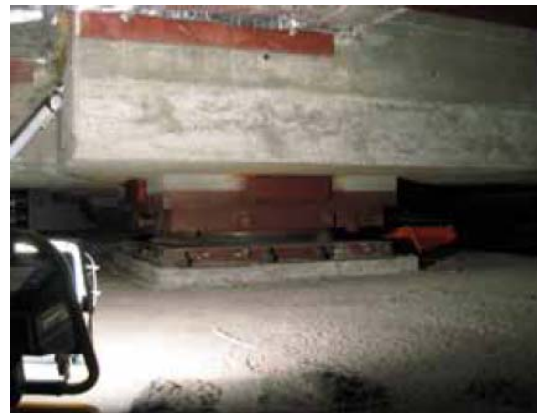
On the other hand, many sliding systems have also been proposed and used in USA.

After the 1989 Loma Prieta earthquake, the 1905 U.S. Court of Appeals and Post Office

Building (Fig. 1.5) in San Francisco was seismically upgraded by FPS system (Amin and Mokha 1995). The project was the federal first and the world's largest seismic or base isolation retrofit project with a construction cost of \$24.4 million. The implemented retrofit will enable the historic 60,000-ton building to ride out an earthquake by gently swaying back and forth like a pendulum.



(a) Building of U.S. Court of Appeals and Post Office



(b) FPS base isolation system used in retrofitting

Fig. 1.5 FPS base isolation system used for buildings

(2) Energy dissipation systems

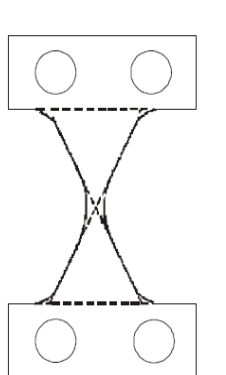
Passive energy dissipation system (Fig. 1.6) uses mechanical devices to dissipate a portion of earthquake input energy, thus reducing structural response and possible damage. Typical passive energy dissipation systems are metallic yield damper, friction damper, visco-elastic damper and viscous fluid damper (Rai et al. 2009; Soong 1997; Aiken et al. 1992; Datta 2003).

(i) Metallic yield damper utilizes added metallic energy dissipaters based on inelastic deformation of the metals. The device uses the mild steel plates with triangular or hourglass shape and yielding is spread almost uniformly throughout the material. Other materials, such as lead and shape-memory alloys can also be used in the metallic yield damper.

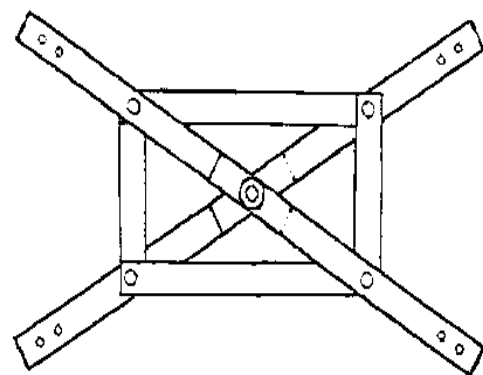
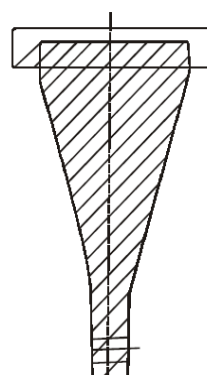
(ii) Friction damper provides an excellent mechanism for energy dissipation. The friction between two solid surfaces with relative sliding dissipates energy before the primary structure yields. The performance of such dampers is not significantly affected by loading amplitude, frequency and number of cycles. Pall x-braced friction dampers have been installed in several newly built and retrofitted buildings.

(iii) The visco-elastic damper consists of layers of visco-elastic material bonded with steel plates. Energy is dissipated through shear deformation of the material sandwiched between steel plates. The visco-elastic damper has been used successfully in a number of buildings, such as World Trade Center in New York, the Columbia Sea First Building in Seattle, etc.

(iv) The viscous fluid damper is widely used in aerospace and civil engineering structures. It typically consists of a piston housed in silicon compound filled cylinder. The piston contains small orifices through which viscous fluid passes. Thus the energy is dissipated via movement of piston in highly viscous fluid.

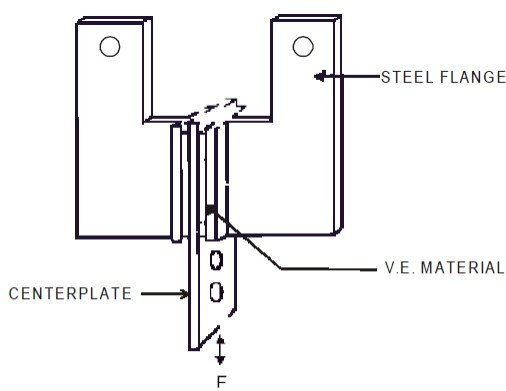


(a) Metallic yield damper

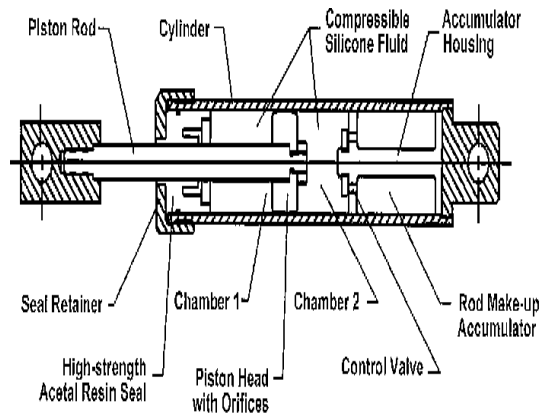


(b) Friction damper

Fig. 1.6 Passive energy dissipation systems (From Rai et al. 2009)



(c) Visco-elastic damper



(d) Viscous fluid damper

Fig. 1.6 (cont.) Passive energy dissipation systems (From Rai et al. 2009)

Viscous fluid dampers have been used on the Terminal Island Suspension Bridge in the Los Angeles harbor and on the San Francisco–Oakland Bay Bridge as shown in Fig. 1.7(a) (Roberts 2005). These dampers are designed to absorb energy and assist in resisting seismic forces. Fig. 1.7 (b) is the viscous fluid damper installed on the 91/5 overcrossing in Orange County, CA (Makris and Zhang 2004).



(a) San Francisco–Oakland Bay Bridge



(b) Viscous fluid damper on 91/5 Overcorssing

Fig. 1.7 Example of viscous fluid damper application in highway bridges

1.3.2 Active and Hybrid Seismic Protective Devices

Because ground motions are stochastic in nature, passive systems have a limited range

of effectiveness. Active control systems are more efficient in reducing the structural response by means of control force generated from external power. Active control system is fully adaptive. A direct combination of passive and active control methods has been referred as hybrid control, which essentially utilizes the idea of active control but requires less external power due to the use of passive devices.

The AMD system was the first active control system developed for the structural control purpose in late 1980s (Ikeda et al. 2001). The AMD device is composed of a large mass whose motion (displacement, velocity and acceleration) in one direction is controlled by an actuator (Fig. 1.8). The mass is suspended in the way allowed to move without having to overcome bearing surface friction. The AMD device can be designed with various mass sizes to obtain various control forces. More than one AMD device can be installed in a structure to allow engineers to control more complex oscillations by the precise interaction of the AMD devices.

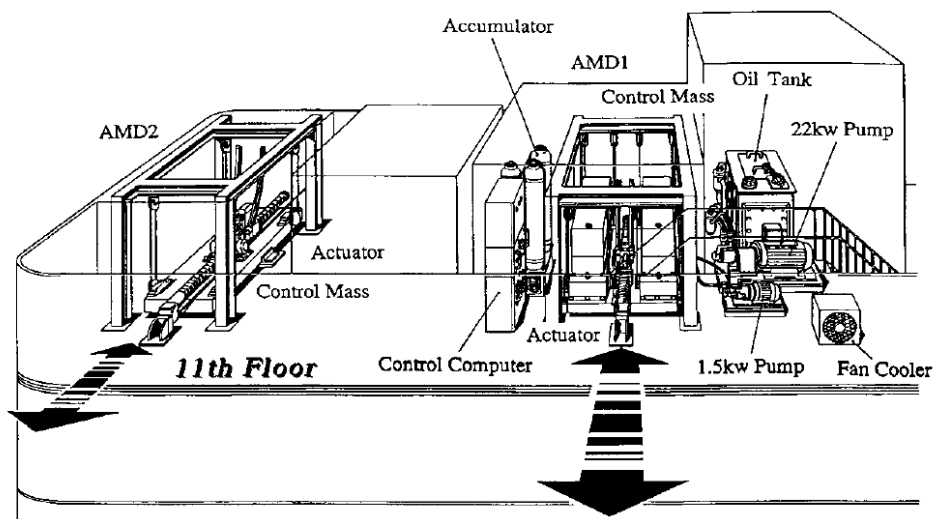


Fig. 1.8 Composition of AMD system (From Ikeda et al. 2001)

1.3.3 Semi-Active Seismic Protective Devices

Semi-active system is a natural evolution of passive system as it incorporates adaptive factors to improve effectiveness of the passive system. It is often referred as controllable or intelligent passive system. Semi-active system requires orders of magnitude smaller external power than a typical active system, in which the control action is produced by the movement of the structure but is regulated by an external source of energy.

A semi-active control system consists of sensors, a control computer, an actuator and a passive device. The sensors measure the excitation and/or structural response which are transmitted to the control computer for processing. The computer generates control signals based on the information from the sensors for the actuator. Then the actuator acts to adjust the behavior of the passive device. The actuator is only used to control the behavior of the passive device instead of applying control force directly onto the structure, thus it only requires a small power supply such as batteries.

(1) Variable damping devices

The variable damping systems that utilize variable orifice fluid dampers for structural systems have been developed. Symans et al. experimentally tested them at both the component level and within multi-story building frames and base-isolated structures (Symans and Constantinou 1997a, 1997b; Madden et al. 2002).

The device consists of a fluid viscous damper combined with a variable orifice on a by-pass pipe containing a valve in order to control the reaction force of the device, as shown in Fig. 1.9(a). The damping characteristics of a variable orifice can be controlled between two damping values (low damping when the valve is completely opened and high damping when

the valve is completely closed) by varying the amount of flow passing through the by-pass pipe from one chamber of the piston into the other. Depending on the type of valve used, either two-stage (on-off) or continuously variable damping could be generated.

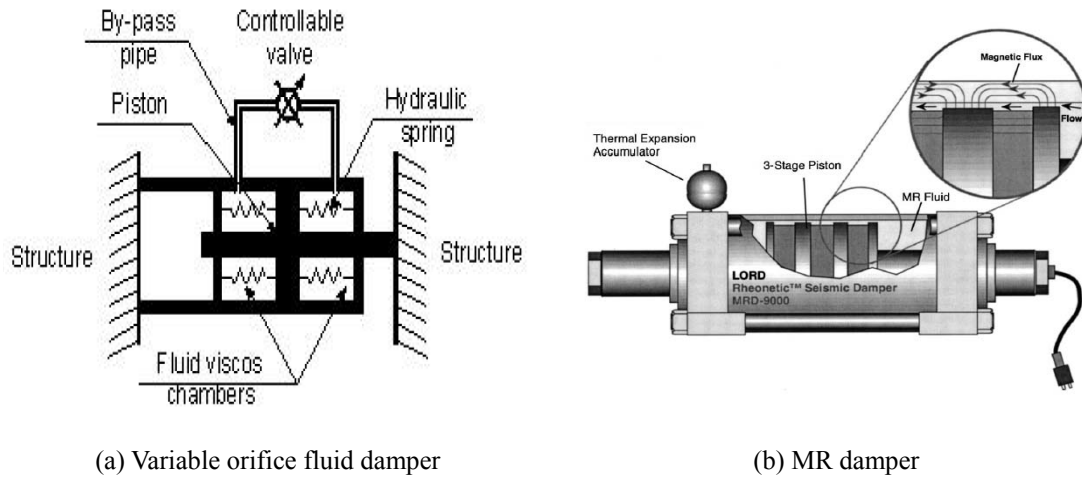


Fig. 1.9 Variable damping devices

Controllable fluid dampers possess fluids with properties which may be influenced by the presence of magnetic fields, which correspond to *magnetorheological* (MR) dampers (Fig. 1.9(b)). When the magnetic field is applied, the behavior of fluid changes from that of a low-viscosity fluid to more of a semi-solid, visco-plastic behavior. Thus, effective viscosity of the damper is actively controlled through applying magnetic field. Recent research in MR fluid dampers has demonstrated their ability in the suppression of vibrations for civil structures due to earthquake excitation (Dyke et al. 1996, 1999; Spencer 1996; Spencer et al. 1997). In addition, a 20-ton MR damper, discussed in (Carlson and Spencer 1996) and (Spencer et al. 1997), demonstrates that these devices can be scaled for civil engineering applications.

The first full-scale application of MR dampers have been implemented in the Tokyo National Museum of Emerging Science and Innovation. Since then MR dampers have been

implemented in several cable stayed bridges and smart base isolated buildings. Full-scale implementation of MR dampers have been accomplished in two bridges in China recently. Ko et al. (2002) implemented 256 MR dampers (made in Lord Corporation, USA) with 2.26kN capacity at the cables of Dongting Lake Cable-stayed Bridge as shown in Fig. 1.10(a) and Ou (2003) implemented 40 MR dampers with 8kN capacity at the cables of Shandong Binzhou Yellow River Highway Bridge as shown in Fig. 1.10(b).



(a) Dongting Lake Bridge and MR dampers installed



(b) Binzhou Yellow River Highway Bridge and MR dampers installed

Fig. 1.10 Semi-active control system application in Highway bridges

1.3.4 Cons and Pros

The passive control system is activated by the structural motion. No external power or

energy is needed to sustain the control effect. Thus it is easy to operate and reliable during large earthquakes even when the main structure loses power supply. But they are not sufficiently adaptive to ever-changing external excitations. For example, TMD is only effective for the structural response with one dominant mode. So under some conditions, passive control may not reach the intended control objectives.

On the other hand, active control system is fully adaptive and can act and adjust simultaneously with the change of structural and external response. It provides the structure ‘variable’ structural properties (damping and stiffness) to efficiently overcome the damaging effect of the earthquake. However, except for protecting small or light weight structures, large active control forces are needed to implement the control purpose, resulting in the demand of significant external power supply and huge force generation equipment. Furthermore, it is vulnerable to power supply outage as a severe earthquake can damage not only the structural members but also the power supply system. As active control process inputs energy into the structure, it will destabilize the structure if unfortunately the actuator control computer has malfunctioned.

As a hybrid between passive and active control, a semi-active control system has an adaptive system incorporated, thus can adjust according to the vibration nature of both structural response and external excitation. At the same time it only requires a small power supply such as batteries, which is a great advantage when the main power source to the structure fail during seismic events. Also, the actuator does not have any harmful potential such as destabilization of the structure as there is no direct force applied to the structure from the actuator. Although semi-active system is a little more complex than passive system, they

are still easy to manufacture, reliable to operate and capable of performing better. The control capacity of semi-active system is still limited as they can only operate within the capacity of the corresponding passive devices on which it is based.

1.4 Hybrid Testing of Civil Engineering Structures

To achieve the reproduction of dynamic behavior of large structural systems, researchers have been developing hybrid testing techniques, with which physical components of a large-scale structures are loaded in the laboratory while the computational simulations of the remaining structure are executed in parallel with necessary information transferred in between. This advanced seismic testing method can be categorized essentially into two major groups: pseudo-dynamic (PSD) hybrid testing and real time hybrid testing (RTHS).

The PSD hybrid test is intended to simulate the dynamic response of a whole structural system, in which critical components are physically tested while the remaining parts of the structure, together with the inertia effects of the physical specimen, are numerically simulated in a computer (Nakashima et al. 1990; Darby 1999). PSD hybrid tests can be conducted in an extended time frame (Mahin and Shing 1985; Shing et al. 1996) when the computed inertia forces are applied statically or quasi-statically to the specimen. Because the dynamic response of the structure is only numerically simulated, the accuracy of PSD hybrid test result relies greatly on the numerical model of the prototype structure and the integration algorithm.

On the other hand, to achieve the realistic inertia and time-dependent effects in the test structure (e.g. viscous dampers) and to overcome the capacity limitation of shake table

test, real time hybrid testing (RTHS) technique is often used to investigate the effect of vibration control devices on the global performance of structures, such as evaluating the performance of rate dependent MR dampers (Christenson et al. 2008) or nonlinear elastomeric dampers (Chen et al. 2009).

Since hybrid testing provides an efficient way to isolate and physically test only the more complex or critical components when test of the full structure is not feasible, it has become one of the main research areas in earthquake engineering in recent years. Numerous studies have verified effectiveness of hybrid testing by comparing hybrid test results to numerical simulations of semi-actively controlled structures equipped with MR damper (Carrion et al. 2009; Castaneda et al. 2012; Christenson et al. 2008).

UI_SimCor (Kwon et al. 2007) is a transparent and fully modular framework that allows for the utilization of analytical platforms alongside experimental facilities for the integrated simulation of a large complex system. The basic concept of the framework is that analytical models associated with various platforms or experimental specimens are considered as super-elements with many DOFs. Each of these elements is solved on a single computer or on different computers connected through the network of UI_SimCor. Fig. 1.11 illustrates the overall architecture of UI-SimCor. The main routine shown in the figure enforces static and dynamic equilibrium and conducts dynamic time integration.

It's noted that UI_SimCor also allows the hybrid simulation composed of numerical modules only, i.e. all the substructures are simulated in computer and just computationally separated.

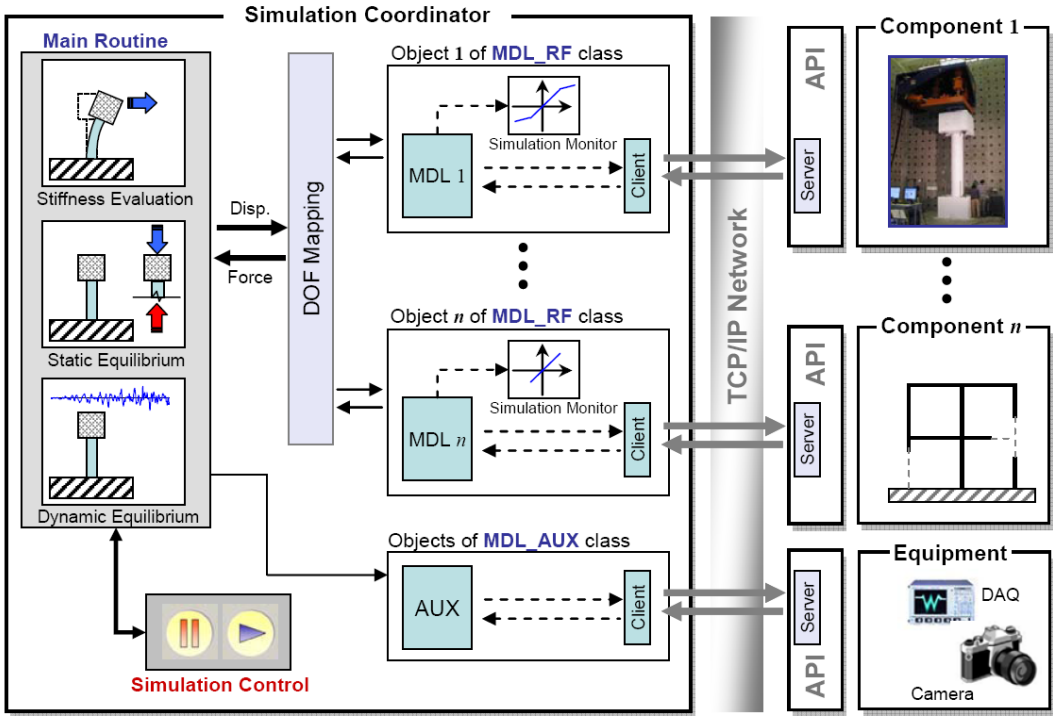


Fig. 1.11 Architecture of UI_SimCor (From Kwon et al. 2007)

1.5 Performance Based Earthquake Engineering (PBEE)

1.5.1 PBEE Methodology

Historically, structural engineers have used allowable-stress design and load-and-resistance-factor design (LRFD), which focus on individual structural elements and connections, and seek to ensure that none will experience loads or deformation greater than it is capable of withstanding. PBEE, a new emerging and promising approach, attempts to address performances primarily at the system level, i.e. a designed highway bridge as a whole will perform in some predictable way, in terms of risk of collapse, fatalities, repair costs, and post-earthquake loss of function.

The Structural Engineers Association of California (SEAOC) created an early sketch of the objectives and methodologies of PBEE, in its Vision 2000 document (Office of

Emergency Services 1995) and Conceptual Framework for Performance-Based Seismic Design (Structural Engineers Association of California 1999). SEAOC's approach addresses performance in terms of a continuum from operability, to life safety, to resistance to collapse, under four discrete levels of seismic excitation (Fig. 1.12). Similarly, the Federal Emergency Management Agency (FEMA) and the American Society of Civil Engineers (ASCE) build their pre-standard, ASCE/FEMA 356 (Federal Emergency Management Agency 2003), which expresses performance in four discrete levels at four slightly different hazard levels.

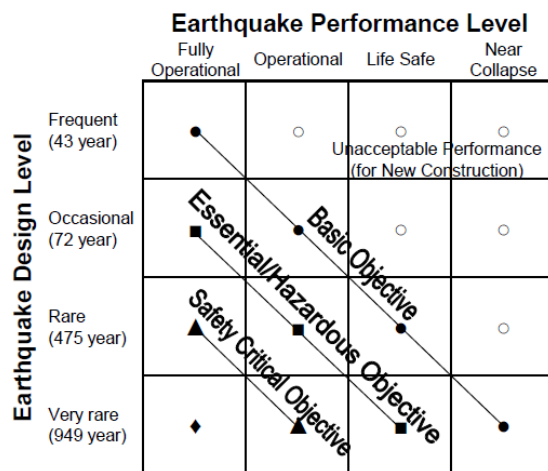


Fig. 1.12 SEAOC recommended seismic performance objectives for buildings

Rather recently, PEER is producing an analysis and design methodology that addresses seismic performance in terms of damage-repair cost and loss-of-use duration, as well as operability, life-safety, and collapse potential. The objective of the methodology is to estimate the frequency with which a particular performance metric will exceed various levels for a given design at a given location. Fig. 1.13 illustrates the PEER methodology. As it shows, PEER's PBEE approach involves four stages: hazard analysis, structural analysis, damage analysis, and loss analysis (Porter 2003).

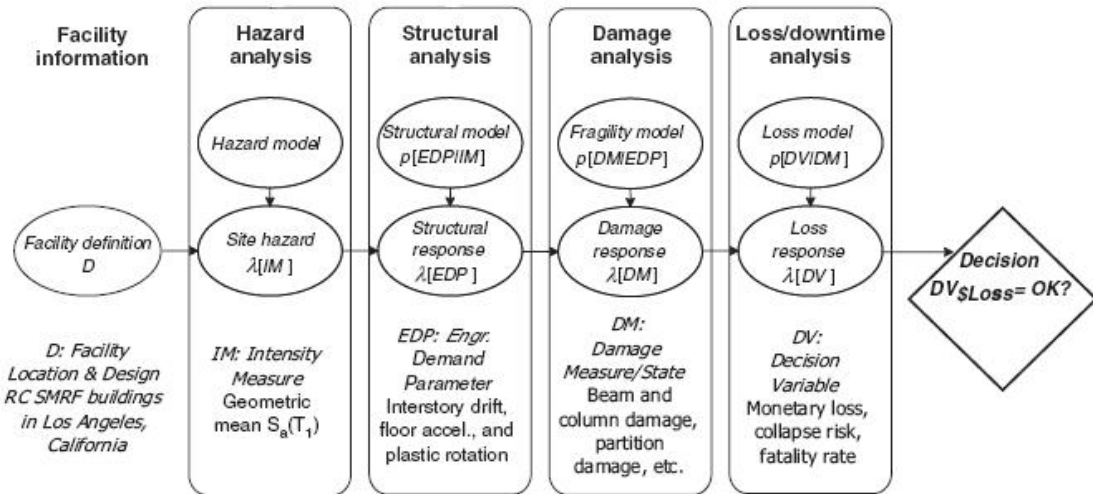


Fig. 1.13 PEER PBEE methodology framework

(i) Hazard analysis. In the hazard analysis, one evaluates the seismic hazard ($\lambda[IM]$) at the highway bridge considering its location, structural, architectural, and other features (jointly denoted by design, D). The seismic hazard describes the annual frequency with which seismic excitation is estimated to exceed various levels. Seismic excitation is parameterized by an intensity measure IM such as $S_a(T_1)$, the damped elastic spectral acceleration at the fundamental period of the structure. The hazard analysis includes the selection of a number of ground-motion time histories whose IM values match different hazard levels of interest, such as 10%, 5%, and 2% exceedance probability in 50 years.

(ii) Structural analysis. In the structural analysis, one creates a structural model of the highway bridge in order to estimate the uncertain structural response, measured in terms of a vector of engineering demand parameters (EDP), conditioned on seismic excitation ($p[EDP|IM]$). $EDPs$ can include internal member forces and local or global deformations, including ground failure. The structural analysis might take the form of a series of nonlinear time-history structural analysis. The structural model need not be deterministic: some PEER analysis have included uncertainty in the mass, damping, and force-deformation

characteristics of the model.

(iii) Damage analysis. EDP is then input to a set of fragility functions that model the probability of various levels of physical damage (expressed by damage measures, or DM), conditioned on structural response, $p[DM | EDP]$. Physical damage is described at a detailed level, defined relative to particular repair efforts required to restore the component to its undamaged state. Fragility functions currently in use give the probability of various levels of damage to individual beams, columns, nonstructural partitions, or pieces of laboratory equipment, as functions of various internal member forces, story drift, etc. They are compiled from laboratory or field experience. For example, PEER has compiled a library of destructive tests of reinforced concrete columns for this purpose (Eberhard et al. 2001).

(iv) Loss analysis. The last stage in the analysis is the probabilistic estimation of performance (parameterized by various decision variables, DV), conditioned on damage $p[DV | DM]$. Decision variables measure the seismic performance of the highway bridge in terms of greatest interest to facility owners, whether in dollars, deaths, downtime, or other metrics. PEER's loss models for repair cost are upon well-established principles of construction cost estimation.

1.5.2 Structural Control in PBEE Framework

The PBEE framework is simply summarized and illustrated in Fig. 1.14 (shaded blocks). Earthquake excitation is defined in terms of an intensity measure, IM . A structural model is used to predict the response, EDP , from the intensity measure. A damage model is then used to predict the physical damage, DM , associated with the response. Finally, a loss model allows prediction of loss, DV , from the physical damage.

Structural control (SC) technologies, including passive, active and semi-active control strategies, can essentially be involved in the PBEE process, by varying the characteristics of

the structural model (structural stiffness and damping) and consequently changing the *EDP*, *DM*, and finally the *DV*. Thus, within the PBEE framework, both the intermediate outputs (*EDP* and *DM*) and the final gain (*DV*) can be adjusted to a specific level for the decision maker through implementation of structural control devices. The introduction of structural control methods has provided structural designers a powerful tool for performance based design.

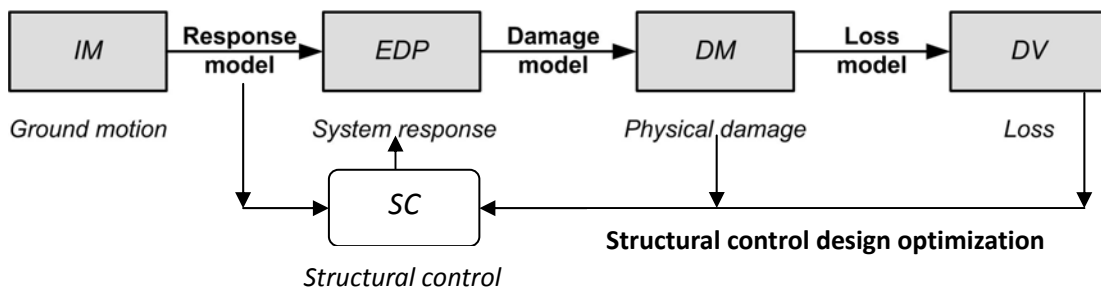


Fig. 1.14 Illustration of PBEE framework with structural control strategy

1.6 Scope and Objectives

Structures (e.g. buildings and bridges) are susceptible to various levels of damages as observed in past major earthquakes. The damages mainly result from insufficient force or displacement design capacity compared to excessive demands due to seismic shaking. This has imposed realistic risks for a large number of existing bridges that were designed and constructed before a seismic provision was adopted.

To minimize the negative impact of damaging earthquakes, seismic protective devices, in either passive or adaptive passive forms, can be used to improve the seismic performances of new bridges in high seismicity regions or provide reliable and economical retrofitting for existing bridges. Careful selection of optimum stiffness and damping properties of these

devices is important to utilize their advantages and achieve multi-performance objectives when subject to earthquakes with various frequency contents and intensities.

Despite the promises of the seismic protective devices, there are a limited number of seismically protected bridges existing in U.S. One major challenge hindering their practical applications is lack of capability of accurate and efficient assessment of seismic response of highway bridges equipped with these highly nonlinear protective devices. Current typical finite element programs (Abuqus, OpenSees, etc) have kinds of elements that can model complex nonlinear structural components, however, there are no well established elements for modelling highly nonlinear seismic protective devices and applying control algorithms simultaneously. Researchers have to write their own finite element code and make huge simplification of the structure model when there is a need for such analysis.

UI_SimCor, which is originally developed for distributed hybrid testing, provides a promising way to overcome this obstacle in numerical modeling and analysis of seismically controlled highway bridges. Utilizing the hybrid simulation idea, the main nonlinear structure can be modeled in general finite element programs such as OpenSees, while the seismic protective devices and the control algorithms can be accurately implemented in Matlab. The individual substructures of the whole structure model can communicate and run simultaneously through platform UI_SimCor.

By this numerical hybrid simulation scheme, the accurate assessment of seismic response of highway bridges equipped with control devices is achieved. The results will further guide the optimal selection of design parameters for these seismic protective devices, also corresponding performance criteria can be developed.

On this basis, the major tasks of this comprehensive research are summarized in the following:

(1) Explore the influence of supplemental damping on structural response

The dimensional analysis is used to quantify the nonlinear damping of structures with nonlinear dampers, resulting in a dimensionless nonlinear damping ratio. Then the optimal nonlinear damping is identified for both SDOF and MDOF structures, which leads to optimal placement of nonlinear dampers.

(2) Development and validation of hybrid simulation scheme for structures

Hybrid simulation scheme is needed to facilitate the nonlinear control analysis of inelastic structures. Numerical models and algorithms are developed for viscous dampers, base isolators and semi-active MR dampers under hybrid simulation framework. The hybrid simulation framework is validated both experimentally and numerically. The soil structure interaction (SSI) effects are also incorporated in this framework.

(3) Implementation of effective seismic protective devices for highway bridges using hybrid simulation scheme

The hybrid simulation framework is applied to bridges with base isolation and MR dampers so as to obtain the realistic structural responses. The structural control theory is implemented to derive the optimal design parameters and the equivalent passive parameters. This will lead to performance based implementation of seismic protective devices for bridges.

1.7 Organization

This dissertation includes a total of 6 chapters in order to address the key issues and

achieve the considered objectives of this research presented in the previous section.

Chapter 1 presents a general description of literatures on highway bridge performance under earthquake, structural control and hybrid simulation methodology, as well as the motivations and objectives of this research.

Chapter 2 includes the investigation of seismic responses of inelastic structures with nonlinear viscous damping subject to pulse-type near fault ground motions using dimensional analysis. A novel definition of nonlinear damping ratio is proposed based on dimensional analysis and equivalent SDOF system analysis for MDOF structures. The genetic algorithm is applied to perform the optimal nonlinear damper design and quantify the optimal damping ratio accordingly.

Chapter 3 proposes the hybrid numerical simulation scheme based on existing hybrid testing software, UI-SIMCOR. Modifications and further development of UI_SimCor is presented. Using a real test structure equipped with various protection devices and control algorithms, it demonstrates the accuracy and versatility of the hybrid numerical simulation scheme proposed.

Chapter 4 focuses on experimental verification of the hybrid numerical simulation methodology based on UI_SimCor. In this chapter, System identification test, MR damper calibration test, RTHS test and Shake table test are presented. These tests are performed for a 3 story steel frame structure controlled by a semi-actively controlled MR damper at Harbin Institute of Technology (HIT) in China.

Chapter 5 presents time history analysis and structural control design of a typical highway bridge, Painter Street Overcrossing, utilizing the hybrid numerical simulation in

UI_SimCor. Base isolators and semi-actively controlled MR dampers are adopted as the protective devices. Clipped optimal control algorithm based on LQG regulator with a Kalman filter is implemented and a systematic strategy is proposed for optimal passive design of seismic protective devices.

Ultimately, Chapter 6 provides the major findings and conclusions of this research along with the recommendations for the future work.

2. Optimal Nonlinear Damping for MDOF Inelastic Structures

In the past twenty years, energy dissipation devices have been implemented to reduce the seismic responses and mitigate the structural damages in buildings and bridges around the world. A significant amount of research has been conducted since early 1990s focusing on the following areas: 1) effects of damping devices on seismic behavior of structures (e.g. Chang et al. 1995; Wanitkorkul and Filiatrault 2008); 2) placement of damping devices in structures (Wu et al. 1997; Shukla and Datta 1999); 3) active and semi-active control of damping devices (Gluck et al. 1996; Cimellaro et al. 2008); and 4) the testing and modeling of various damping devices (Bergman and Hanson 1993; Constantinou and Symans 1993). A detailed state-of-art summary of supplemental energy devices was offered by Soong and Spencer (2002) while a recent paper by Symans et al. (2008) concentrated on the passive energy dissipation devices. Dependent on their different forms, energy dissipation devices exhibit distinctive damping mechanisms such as viscous, rigid-plastic, elasto-plastic, visco-plastic and elasto-viscoplastic etc (Makris and Chang 1998).

Among the common energy dissipation devices, viscous fluid dampers are widely used due to their high energy dissipation capacity and easy installation. They are used alone or in combination of isolation devices. In its linear form, the role of damping in isolated structures has been investigated in detail (Inaudi and Kelly 1993; Kelly 1999). Typically, the additional damping reduces the displacements at the expense of increase of inter-story drift and the floor accelerations (Kelly 1999) and the frequency contents of earthquake motions

determine the effects of damping (Inaudi and Kelly 1993). In order to limit the base shear due to increased damping, nonlinear viscous dampers with a low velocity exponent (say 0.5 or less) can be used to limit the peak damping forces and deliver slightly larger energy dissipation than the linear counterpart. However, for strong earthquakes, most structures employing viscous dampers will experience some level of inelastic response in the structural framing system (Symans et al. 2008). The role of the nonlinear damping is therefore function of the structural properties, the ground motion characteristics and the performance objectives. With the nonlinearity involved, it is difficult to quantify the damping since the equivalent damping ratio has limited meaning (Makris and Chang 1998).

In order to determine the optimal nonlinear damping needed for a structure, the nonlinear damping ratio is necessary to be evaluated first. Several researchers have proposed the energy-based nonlinear damping ratio for linear MDOF structure equipped with nonlinear viscous dampers. However, due to the existence of nonlinear viscous dampers, a nonlinear time history analysis has to be done to obtain the maximum structural response that is needed for calculation of nonlinear damping ratio. In this chapter, the dimensional analysis is utilized to evaluate the seismic responses of inelastic structures with nonlinear viscous damping subject to pulse-type near fault ground motions. A novel definition of nonlinear damping ratio is proposed based on dimensional analysis and equivalent SDOF system analysis for MDOF structures in this study, which doesn't need the structural response information beforehand hence can facilitate the determination of optimal nonlinear damping of MDOF structures and quantify the effects of nonlinear viscous damper. Under this framework, the dimensionless structural responses (e.g. drift and total acceleration) can be expressed explicitly as functions

of dimensionless Π -parameters related to the inelastic structural behavior and ground motion characteristics. The effects of nonlinear damping are therefore quantified, leading to optimal selection of damping properties. Structural nonlinearity is also easily taken into account under this proposed framework.

Many applications of genetic algorithms have been made in structural engineering, such as placement of control actuators in aerospace applications, as well as being applied to the problem of optimal placement of dampers in a building structure, which is adopted in this section. The genetic algorithm is based on that in natural selection the better individuals are likely to survive in a competing environment. It uses the analogy of natural evolution of a population of individuals through generations where the best ones dominate. Genetic algorithm considers simultaneously many designs which does not require any computations of gradients of complex functions to guide their search.

For optimal placement of supplemental damping devices in a structure, a design is considered the best if a performance function associated with this design has the highest/lowest value. The objective is to search for the best design in the search space. In genetic algorithm, the parent generation takes successive evolution into future children generations through the process of genetic operators of crossover and mutations. In this study, the genetic algorithm is applied to perform the optimal nonlinear damper design and indicate the optimal damping ratio accordingly.

2.1 Dimensional Analysis of SDOF Inelastic Structures Equipped with Nonlinear Viscous Dampers

The dimensional analysis has been shown to be an effective way of interpreting the otherwise largely scattered inelastic structural responses from time history analysis using recorded ground motions (Makris and Black 2004a,b). By normalizing the inelastic displacement demand with respect to the energetic length scale of ground motions, the similar response (i.e. independent of the intensity of ground motions) can be obtained. Here the dimensional analysis is conducted at an inelastic SDOF structure equipped with a nonlinear viscous damper. The governing equation of such system can be expressed as:

$$m\ddot{u}(t) + c\dot{u}(t) + f_s(u, \dot{u}) + f_d(\dot{u}) = -m\ddot{u}_g(t) \quad (2.1)$$

where m is the system mass, c is the inherent structural damping (linear) and $\ddot{u}_g(t)$ is the ground acceleration input. The term $f_s(u, \dot{u})$ represents the inelastic structural force and can be represented by the Bouc-Wen model as shown below:

$$f_s(u, \dot{u}) = \varepsilon K_e u(t) + (1 - \varepsilon) K_e D_y Z(t) \quad (2.2)$$

where ε is the post yielding stiffness ratio, K_e is the structural elastic stiffness and D_y is the yielding displacement. The hardening parameter $Z(t)$ is computed by the ordinary differential equation given below:

$$\dot{Z}(t) = -\frac{1}{D_y} (\gamma |\dot{u}(t)| |Z(t)|^{n-1} + \beta \dot{u}(t) |Z(t)|^n - \dot{u}(t)) \quad (2.3)$$

where $\gamma = \beta = 0.5$ and n are model parameters. The nonlinear damping force $f_d(\dot{u})$ in Eq. (2.1) is defined as:

$$f_d(\dot{u}) = c_d |\dot{u}|^\alpha \text{sign}(\dot{u}) \quad (2.4)$$

where c_d is the damping factor of the nonlinear damper (in the units of $N/(ms^{-1})^\alpha$) and α is a constant controlling damper nonlinearity ranging from 0 to 1.

When the near-fault ground motions are considered, simple pulses can be used to

represent the dominant kinematic characteristics of input motions (Makris and Chang 1998).

These simple pulses (e.g. Type-A, Type-B and Type- C_n) contain only two input parameters, the acceleration amplitude, a_p (or velocity amplitude, v_p) and period T_p (or equivalently ω_p).

Eq. (2.1) can also be written in another form:

$$\ddot{u}(t) + 2\xi\omega_0\dot{u}(t) + \varepsilon\omega_0^2u(t) + (1-\varepsilon)\omega_0^2D_yZ + 2\xi_n\omega_0|\dot{u}|^\alpha sign(\dot{u}) = -\ddot{u}_g(a_p, \omega_p) \quad (2.5)$$

where $\omega_0 = \sqrt{k_e/m}$ is the pre-yielding natural frequency of the structure, $\xi = c/(2m\omega_0)$ and $\xi_n = c_d/(2m\omega_0)$ are the damping ratio of linear and nonlinear viscous damping respectively. The structural response $u(t)$ solving from Eq. (2.5) is therefore a function of eight parameters involved:

$$u(t) = f(\omega_0, \xi, \xi_n, D_y, \alpha, \varepsilon, a_p, \omega_p) \quad (2.6)$$

Applying the Buckingham's Π -theorem and choosing a_p and ω_p as the repeating variables, Eq. (2.6) can be reformulated in terms of the dimensionless parameters as:

$$\Pi_u = \phi(\Pi_\omega, \Pi_\xi, \Pi_{\xi,n}, \Pi_{Dy}, \Pi_\alpha, \Pi_\varepsilon) \quad (2.7)$$

where $\Pi_u = u(t)\omega_p^2/a_p$ is the structural displacement normalized by the characteristic length scale of ground motion, $\Pi_\omega = \omega_0/\omega_p$ is the dimensionless frequency ratio, $\Pi_\xi = \xi$ is the linear viscous damping ratio, $\Pi_{uy} = D_y\omega_p^2/a_p$ is normalized yielding displacement, $\Pi_\alpha = \alpha$ is the fractional exponent of nonlinear viscous damper and $\Pi_\varepsilon = \varepsilon$ is the post- to pre-yielding ratio. Most importantly, a dimensionless nonlinear damping ratio is also obtained in this exercise:

$$\Pi_{\xi,n} = \frac{\xi_n}{(a_p/\omega_p)^{1-\alpha}} = \frac{c_d}{2m\omega_0(a_p/\omega_p)^{1-\alpha}} \quad (2.8)$$

Similarly, one can derive the dimensionless acceleration $\Pi_A = a/a_p$ (a is the total

acceleration) in terms of the dimensionless Π parameters defined above. Recall that a damping ratio of a nonlinear damper can also be defined by equating the energy dissipated by the nonlinear viscous damper with that of an equivalent linear viscous damper (Jacobson 1930; Symans and Constantinou 1998):

$$\xi_d = \frac{c_d}{2m\omega_0} \frac{2^{2+\alpha}}{\pi} \omega_e^{\alpha-1} D^{\alpha-1} \frac{\Gamma^2(1+\frac{\alpha}{2})}{\Gamma(2+\alpha)} \quad (2.9)$$

where ω_e is the frequency of the forcing function, D is the absolute maximum displacement of the structure response, and Γ is the gamma function. For pulse-type excitations, the forcing frequency ω_e in Eq. (2.9) is essentially equal to the frequency of the pulse excitation ω_p . It is noted that Eq. (2.9) requires the knowledge of maximum structural response, D , which is not a-priori before an analysis is done.

To investigate the relationship between parameters $\Pi_{\xi,n}$ and ξ_d , time history analysis is performed on bilinear structures with nonlinear viscous dampers using a set of typical values of $\Pi_\omega = 0.25$, $\Pi_\xi = 0.05$, $\Pi_{uy} = 0.8$, and $\Pi_\varepsilon = 0.1$. These were done for varying Π_α values of 0.1 to 0.9, and varying $\Pi_{\xi,n}$ values of 0.2 to 1.0 for each value of Π_α . Type-B pulse excitation is used as input motion. The damping ratios of the nonlinear damper calculated from Eq. (2.9), along with the $\Pi_{\xi,n}$ values, are listed in Table 2.1. It is seen that $\Pi_{\xi,n}$ and ξ_d (computed with the known structural displacement D) are indeed very close to each other in values. This indicates that $\Pi_{\xi,n}$ is a better measurement of the nonlinear damping ratio as it does not require the knowledge of structural response.

The new dimensionless nonlinear damping ratio derived in Eq. (2.8) along with other dimensionless parameters fully defines the structural responses. Fig. 2.1 plots the time history responses (for $\Pi_\omega=0.5$) and spectrum of the dimensionless displacement of a system subject

to a Type-B pulse with different frequencies and amplitudes for case $\Pi_\alpha=0.35$ and $\Pi_{\xi,n}=0.1$. The overlapping curves reveal that the dimensional responses are independent of the input motion amplitude as long as the independent Π -terms, $\Pi_{\xi,n}$ and Π_α (for nonlinear damper) are kept the same along with Π_{uy} , Π_ξ and Π_ϵ (for structure).

Table 2.1 Comparison of ζ_d and $\Pi_{\xi,n}$ for nonlinear viscous dampers

$\Pi_{\xi,n}$	ζ_d				
	$\alpha = 0.1$	$\alpha = 0.3$	$\alpha = 0.5$	$\alpha = 0.7$	$\alpha = 0.9$
0.2	0.18	0.18	0.18	0.19	0.20
0.4	0.36	0.38	0.39	0.39	0.40
0.6	0.54	0.58	0.60	0.61	0.60
0.8	0.79	0.80	0.81	0.82	0.81
1.0	1.21	1.07	1.06	1.05	1.02

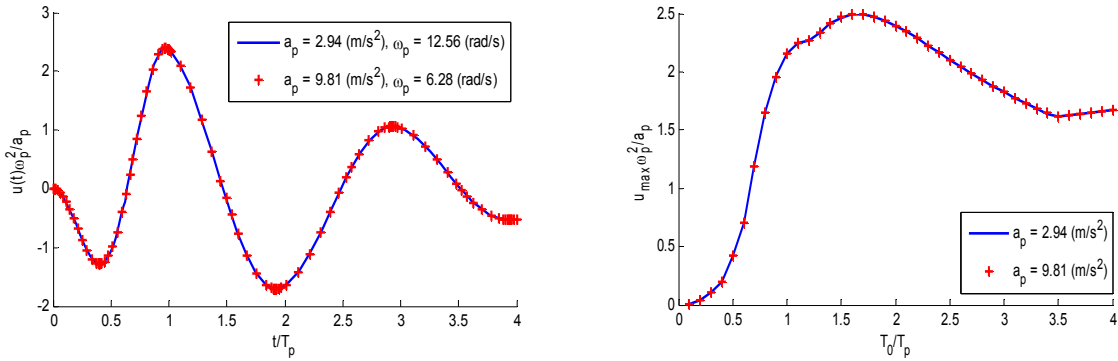


Fig. 2.1 Response similarity with $\Pi_{\xi,n} = 0.10$ and $\Pi_\alpha = 0.35$

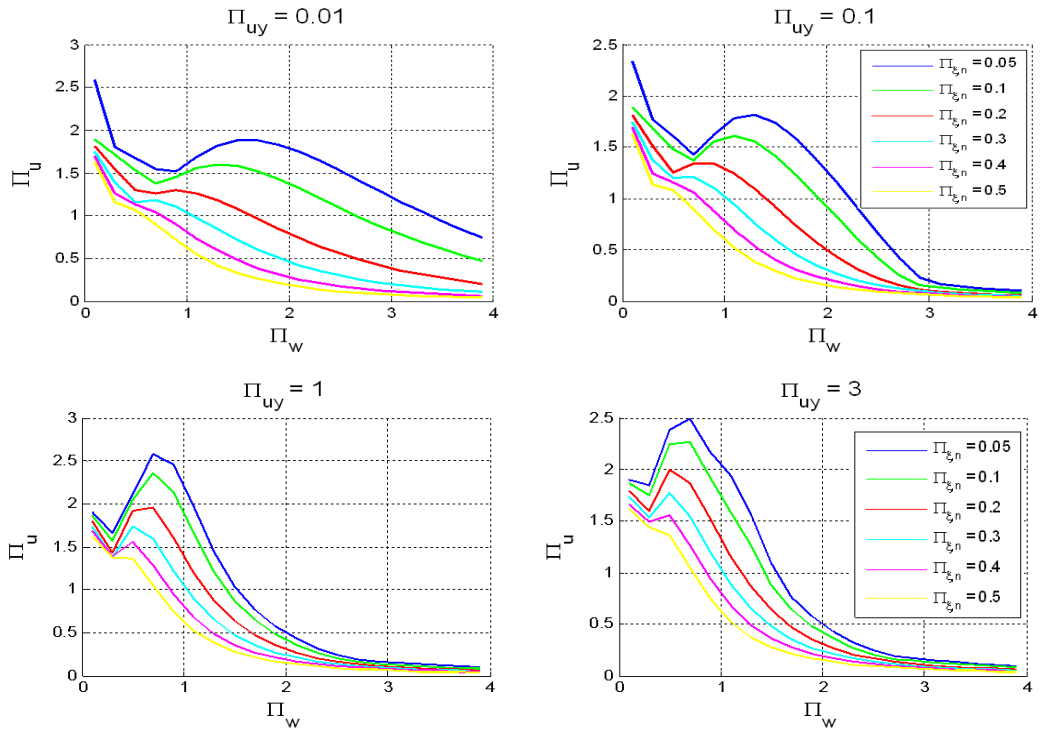
2.2 Effects of Nonlinear Viscous Damping on SDOF Inelastic Structures

A comprehensive parametric study is conducted to evaluate the effects of nonlinear damping for inelastic structures. As indicated by Eq. (2.7), the dimensionless displacement response Π_u and total acceleration $\Pi_A = a/a_p$ are functions of $\Pi_\omega, \Pi_\xi, \Pi_{\xi,n}, \Pi_{uy}, \Pi_\alpha$ and Π_ϵ . To simplify, the parameters Π_ξ, Π_α and Π_ϵ are kept constant at their typical values, i.e. $\Pi_\xi=0.03$, $\Pi_\alpha=0.35$ and $\Pi_\epsilon=0.1$. Numerical time history analyses are performed for different $\Pi_{\xi,n}$ and Π_{uy} values, as well as with the consideration of different types of pulse

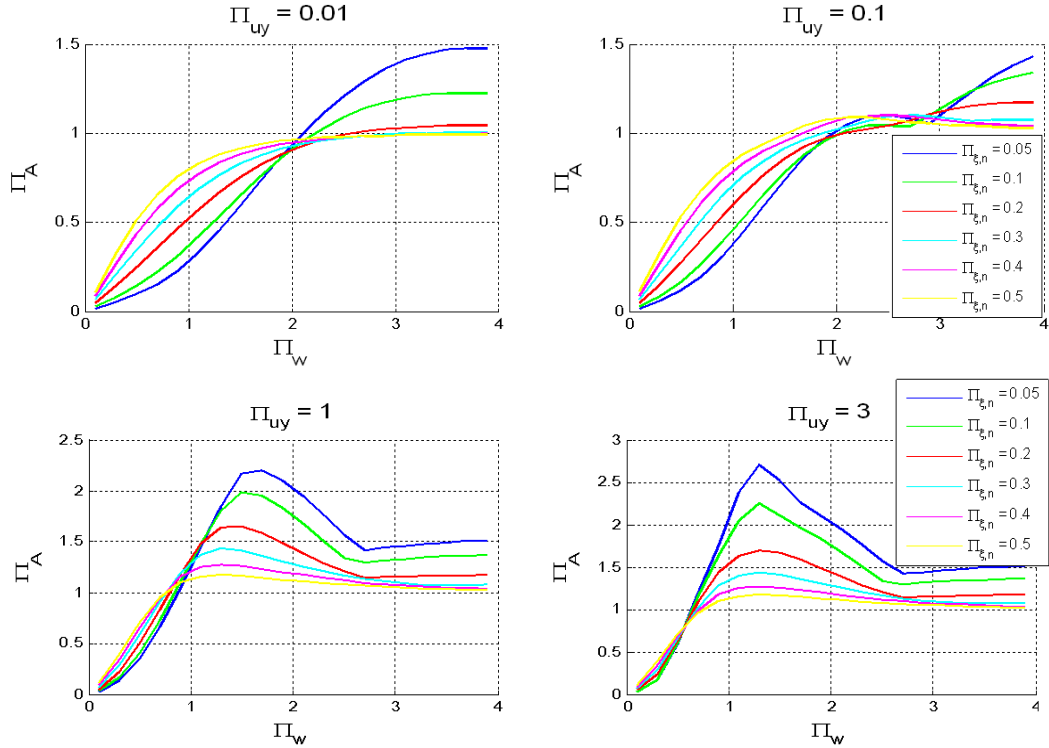
input motions. Fig. 2.2 shows the dimensionless response spectra of Π_u and Π_A as function of Π_o under Type-B pulses for four different values of yielding displacement Π_{uy} .

The case of $\Pi_{uy}=3$ is close to a linear structure case as the yielding displacement D_y is very large. It is seen that the structural displacement and total acceleration responses are both reduced if additional damping is added for linear structure. For inelastic structures, the dimensionless displacement decreases with the augment of nonlinear damping ratio. However, the dimensionless total acceleration is increased due to higher nonlinear damping. Knowing that the total acceleration is related to the total force of springs and dampers and inelastic structures generally have a very small post yielding stiffness, the change of spring force won't be significant when displacement response changes. So reduction of displacement by adding damping will not influence the spring force too much when structure goes into nonlinear range. On the other hand, the damping force will be significantly enhanced if there is more damping involved in. As a result, the total combined force of springs and dampers is increased which is reason why the total acceleration becomes larger in this case. Furthermore, Fig. 2.2 indicates that there is a critical dimensionless frequency, $\Pi_o=2$ under which larger damping will yield larger total acceleration responses. Therefore, it is not good to add more damping if acceleration is of concern.

The effects of nonlinear damping are also evaluated for SDOF inelastic structures subject to real near-fault earthquake motions. Based on the velocity and acceleration characteristics, the near-fault ground motions can be roughly categorized into velocity and acceleration pulse represented (Tang and Zhang 2011). The velocity pulse represented motions usually have a reasonable PGV and intermediate to long pulse period while the acceleration pulse represented ones have reasonable PGA and relatively short period. Table 2.2 lists the information of twenty near-fault motions selected.



(a) Dimensionless displacement



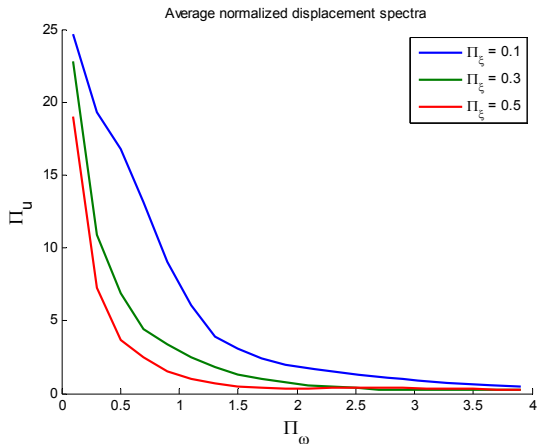
(b) Dimensionless acceleration

Fig. 2.2 Dimensionless displacement and total acceleration responses (Type-B)

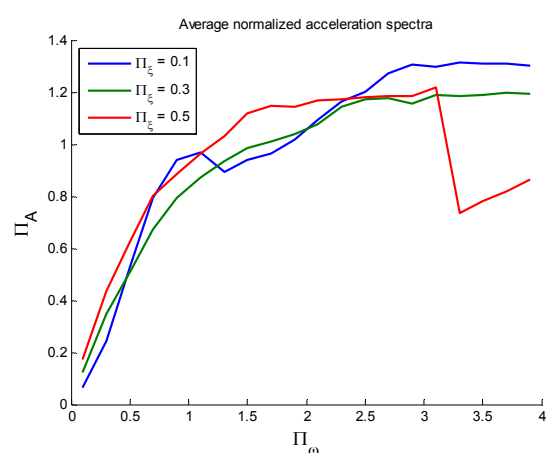
Fig. 2.3 shows the response spectra for different level of nonlinear damping ration under Northridge earthquake. The displacement response is always reduced when damping is increased, yet the acceleration response is overall enlarged with a higher level of damping. Fig. 2.4 plots the averaged dimensionless total acceleration for two nonlinear damping ratios. It is seen that under acceleration pulse represented earthquakes, the critical point for Π_{ω} is shifted towards higher frequency range. At the same time, there is no critical point observed in spectra under velocity pulse represented earthquakes. Therefore, adding more nonlinear damping to structures subject to real earthquake motions is not good for acceleration response in typical range of Π_{ω} .

Table 2.2 Characteristics of chosen pulse represented earthquakes

Earthquake record	a_p (g)	v_p (cm/s)	T_p (s)	PGA (g)	PGV (cm/s)
Velocity pulse represented earthquakes					
SAN FERNANDO, PUL_195	0.475	101.65	1.37	1.435	116.348
IMPERIAL VALLEY, H-E03_233	0.0345	27.40	5.085	0.229	41.054
CAPE MENDOCINO, PET_260	0.118	47.55	2.58	0.615	81.789
PALM SPRINGS, NPS_197	0.275	54.47	1.268	0.67	73.484
NORTHRIDGE, LOS_032	0.112	37.26	2.13	0.466	53.063
KOBE, TAZ_140	0.244	62.89	1.65	0.645	76.452
KOCAELI, GBZ_184	0.053	40.76	4.924	0.238	51.915
CHICHI, TCU136_278	0.0275	39.09	9.1	0.169	51.764
ERZIKAN, ERZ_032	0.212	79.01	2.386	0.486	95.305
CHICHI, TCU103_277	0.0476	57.46	7.729	0.132	62.114
Acceleration pulse represented earthquakes					
CHICHI, TCU080_275	0.46	10.06	0.14	0.501	26.893
COALINGA, A-CPL_045	0.124	2.71	0.14	0.2	8.536
IMPERIAL VALLEY, H-CC4_233	0.13	13.00	0.64	0.13	14.481
MORGAN HILL, G06_058	0.244	7.85	0.206	0.244	35.338
LOMA PRIETA, NAS_038	0.14	13.12	0.6	0.222	32.12
MAMMOTH LAKES, C-XGR_282	0.125	6.05	0.31	0.133	11.723
MT LEWIS, HVR_264	0.128	9.20	0.46	0.155	19.071
NORTHRIDGE, SYL_032	0.611	124.60	0.38	0.733	122.644
SIERRA MAD, 4734A-152	0.241	13.93	0.37	0.327	22.719
TAIWAN SMART1, 05O01_019	0.0914	6.57	0.46	0.115	13.274

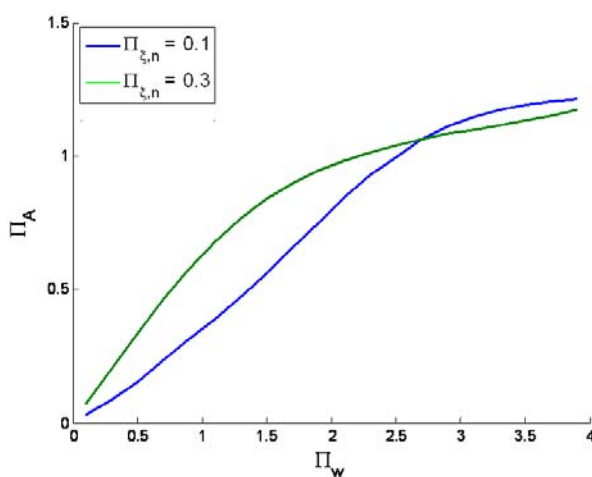


(a) Displacement spectra

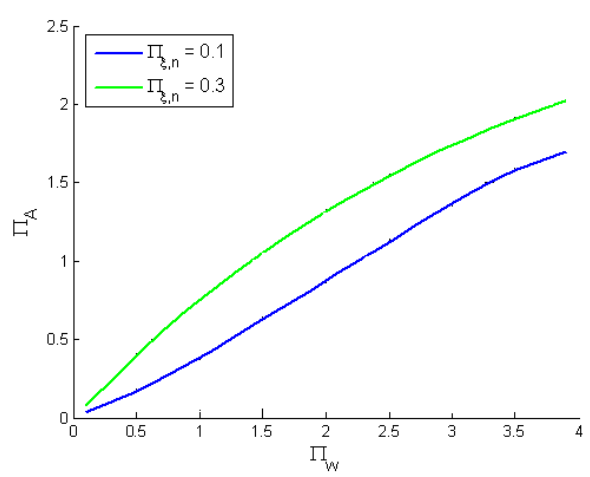


(b) Acceleration spectra

Fig. 2.3 Normalized response spectra under real earthquake



(a) Acceleration pulse represented



(b) Velocity pulse represented

Fig. 2.4 Normalized total acceleration spectra under real earthquakes

In searching for the optimal nonlinear damping of inelastic structures, one has to balance the tradeoff between the reduction in displacement and the increase of acceleration due to increase of damping. This is different from the linear structures where larger damping will generally result in reduced responses. The overall response of the nonlinear structure depends on the relative magnitude of the structural frequency to the dominant frequency of the input motion (Π_{ω}), and the characteristic of the input motion as well (type A, B, or C₂).

pulses). For different types of input motions, there is a critical point of Π_ω , by which the total acceleration response is divided into two parts: when Π_ω is less than the critical point, larger nonlinear damping ratio results in larger acceleration response and when Π_ω is larger than the critical point, larger nonlinear damping ratio yields smaller displacement and acceleration response.

Fig. 2.5 summarizes the normalized system responses under different types of input motions, for the Π_ω range of [1, 2] and $\Pi_{\xi,n}$ range of [0, 0.3]. The Π_ω range is chosen to be on the left side of the critical point. It is again seen that larger nonlinear damping ratio gives smaller relative displacement but larger total acceleration responses. So if the structure is determined to be within this range, designers have to decide a value of nonlinear damping ratio to gain a desired balance between displacement and acceleration responses. And if the structure is ‘located’ on the right side of the critical point, there is no optimal value for the nonlinear damping ratio, that is, adding damping always benefits the system response.

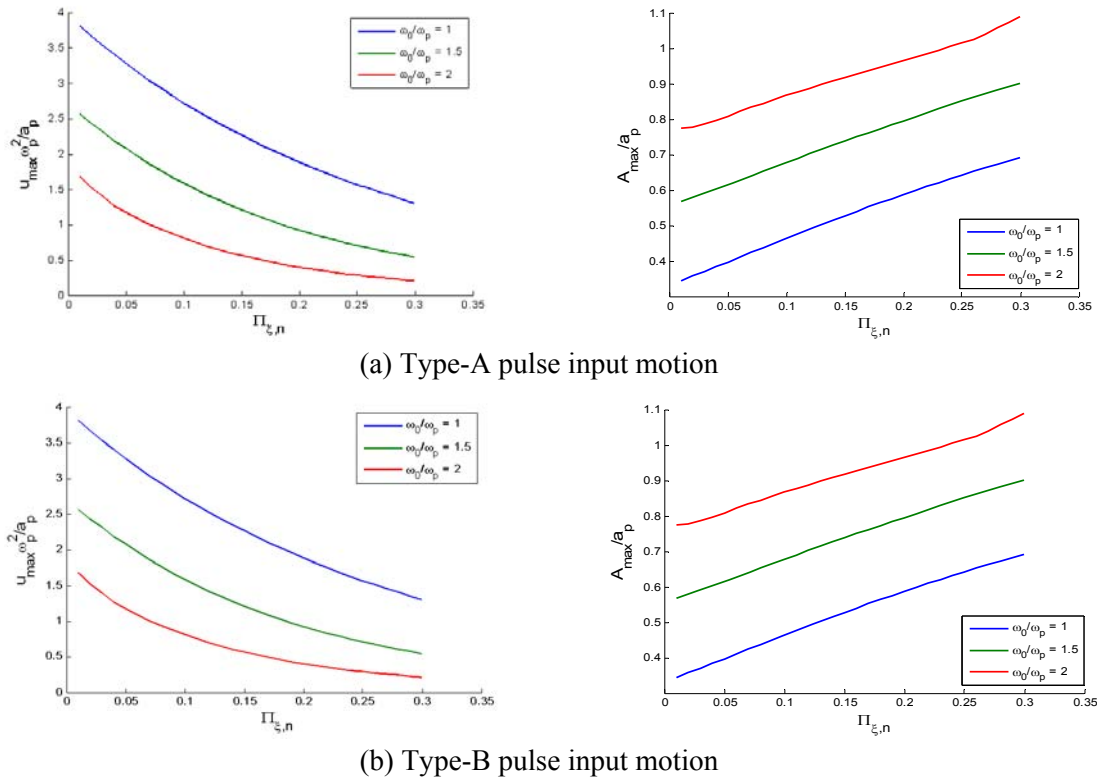
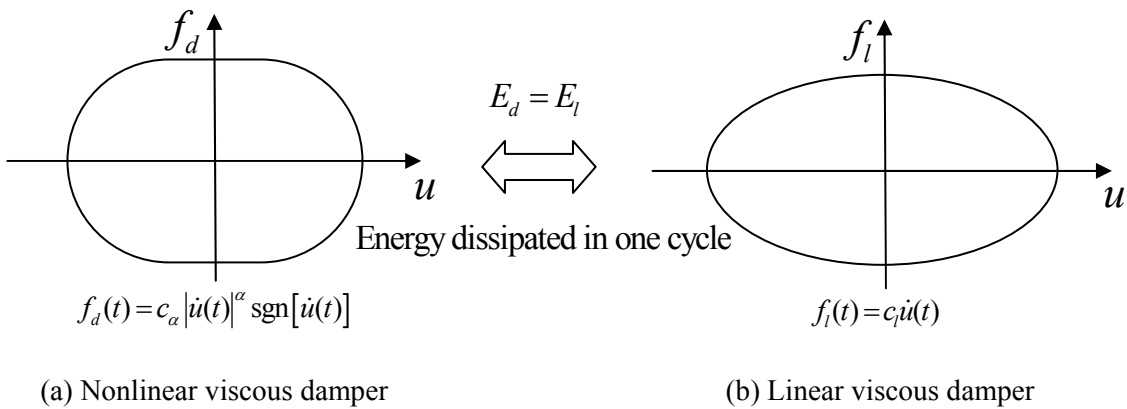


Fig. 2.5 Normalized system responses for different Π_ω and $\Pi_{\xi,n}$

2.3 Equivalent SDOF Representation of MDOF Inelastic Structures Equipped with Nonlinear Viscous Dampers

2.3.1 Methodology

In order to quantify the optimal nonlinear damping for MDOF inelastic structures, one could utilize the optimal nonlinear damping obtained in previous section if an equivalency can be established between the MDOF and SDOF structure. This equivalency is established in several steps. First, the equivalency of nonlinear dampers is established with their linear counterpart for MDOF structures. The typical force displacement loop of nonlinear and linear viscous dampers are as presented as in Fig. 2.6. By making the energy dissipated within one cycle equal to each other, the damping effect of a nonlinear damper could be represented by its corresponding linear equivalency, as shown in Eq. (2.10) (Jacobsen 1930).



(a) Nonlinear viscous damper

(b) Linear viscous damper

Fig. 2.6 Equivalency of nonlinear viscous damper to linear viscous damper

$$c_L = \frac{\lambda}{\pi} \frac{c_\alpha}{(\omega_e u_{\max})^{1-\alpha}} \quad (2.10)$$

where $\lambda = 2^{2+\alpha} \frac{\Gamma^2(1+\frac{\alpha}{2})}{\Gamma(2+\alpha)}$, ω_e is the forcing frequency of the external excitation, and u_{\max}

is the maximum system displacement response. c_L and c_α are the damping coefficient of

the equivalent linear damper and the original nonlinear damper.

With the equivalency between the nonlinear and linear dampers, one can establish a new MDOF inelastic structure with equivalent linear dampers at each floor. Subsequently an equivalent SDOF inelastic structure with linear damping can be derived. Utilizing the equivalency between the nonlinear and linear dampers again, an equivalent SDOF inelastic structure with nonlinear damper can be obtained. The detailed method is described below.

Fig. 2.7 shows a general inelastic structure with N degree of freedoms and is installed with nonlinear viscous dampers at each floor. The $f_{s,n}$ is the restoring force of the nth floor while $f_{d,n}$ and $f_{l,n}$ are the damping force of the original nonlinear damper and equivalent linear damper of nth floor, respectively. Relative displacement $\mathbf{u} = [u_1, u_2, \dots, u_n, \dots, u_N]$ is used to formulate the equation of motion. The variables denoted by superscript of * are the corresponding ones for the equivalent SDOF system.

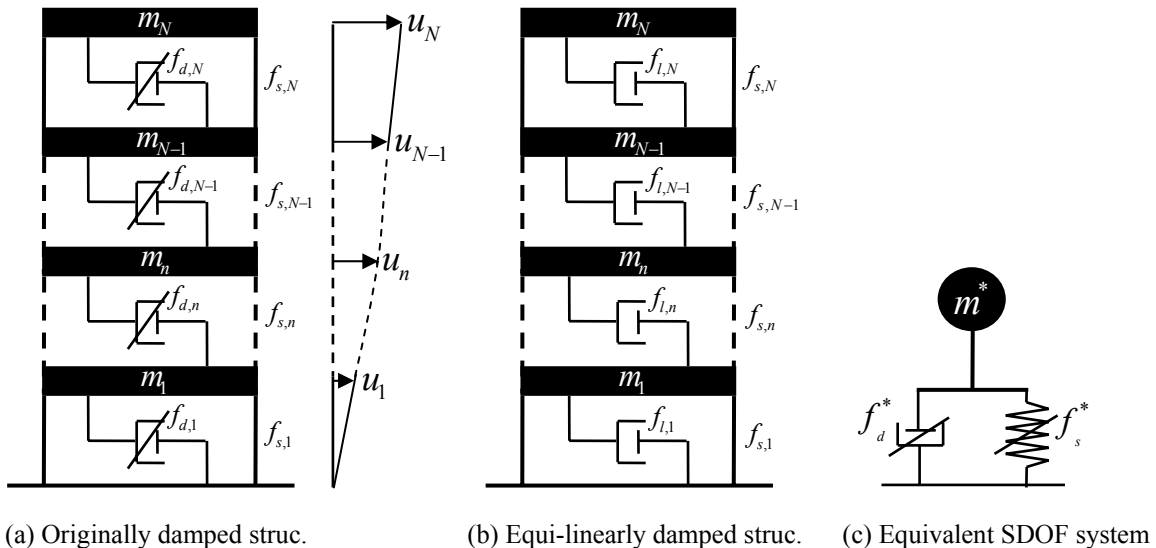


Fig. 2.7 Illustration of a general N DOF inelastic structure with nonlinear dampers

Although the viscous dampers installed are all nonlinear ones, we can apply Jacobson's formula in Eq. (2.10) to convert them into equivalent linear viscous dampers. The nonlinear dampers associated with each DOF could be transformed as:

$$\left\{ \begin{array}{l} c_{L,1} = \frac{\lambda}{\pi} \frac{c_{\alpha,1}}{(\omega_e u_1)^{1-\alpha}} = \frac{\lambda}{\pi} \frac{c_{\alpha,1}}{(\omega_e \phi_{1,1} u_N)^{1-\alpha}} \\ c_{L,2} = \frac{\lambda}{\pi} \frac{c_{\alpha,2}}{\omega_e (\phi_{2,1} - \phi_{1,1}) u_N^{1-\alpha}} \\ \vdots \\ c_{L,n} = \frac{\lambda}{\pi} \frac{c_{\alpha,n}}{\omega_e (\phi_{n,1} - \phi_{n-1,1}) u_N^{1-\alpha}} \\ \vdots \\ c_{L,N} = \frac{\lambda}{\pi} \frac{c_{\alpha,N}}{\omega_e (\phi_{N,1} - \phi_{N-1,1}) u_N^{1-\alpha}} \end{array} \right. \quad (2.11)$$

where $\Phi_1 = [\phi_{1,1}, \phi_{2,1}, \dots, \phi_{n,1}, \dots, \phi_{N,1}]$ is the mode shape of the 1st mode. Subsequently, the equivalent linear damping matrix of MDOF structure becomes:

$$\mathbf{C}_L = \begin{bmatrix} c_{L,1} + c_{L,2} & -c_{L,2} & & & & & \\ -c_{L,2} & c_{L,2} + c_{L,3} & -c_{L,3} & & & & \\ & -c_{L,3} & c_{L,3} + c_{L,4} & & & & \\ & & & \ddots & -c_{L,n} & & \\ & & & & -c_{L,n} & c_{L,n} + c_{L,n+1} & \\ & & & & & -c_{L,n+1} & \\ & & & & & & \ddots & -c_{L,N} \\ & & & & & & & -c_{L,N} & c_{L,N} \end{bmatrix} \quad (2.12)$$

If we assume the MDOF structure is 1st mode dominant, an equivalent SDOF system can be derived (Zhang and Tang 2009). The equivalent damping coefficient for the SDOF structure is:

$$c_L^* = \Phi_1^T \mathbf{C}_L \Phi_1 \quad (2.13)$$

Expend all the terms in Eq. (2.13) with Eq. (2.11) and (2.12), the equivalent linear damping coefficient can be obtained with the explicit form as follows:

$$c_L^* = \phi_{1,1}^2 c_{L,1} + \sum_{n=2}^N (\phi_{n,1} - \phi_{n-1,1})^2 c_{L,n} \quad (2.14)$$

Substituting Eq. (2.11) into Eq. (2.14), the equivalent linear damping coefficient can be related to the original nonlinear damping parameters:

$$c_L^* = \frac{\lambda}{\pi} \frac{1}{(\omega_e u_N)^{1-\alpha}} \left(\phi_{1,1}^{1+\alpha} c_{\alpha,1} + \sum_{n=2}^N \left(\phi_{n,1} - \phi_{n-1,1} \right)^{1+\alpha} c_{\alpha,n} \right) \quad (2.15)$$

Therefore, the original MDOF inelastic structure with nonlinear damper can be obtained by an equivalent SDOF inelastic structure with nonlinear damper, who is governed by the equation of motion as follows:

$$m^* \ddot{D} + f_d^* + f_s^* = -m^* \ddot{u}_g \quad (2.16)$$

where f_d^* and f_s^* are equivalent damping and restoring force of the SDOF system, and

$$f_d^* = c_\alpha^* |\dot{D}|^\alpha \operatorname{sgn}(\dot{D}) \quad (2.17)$$

$$f_s^* = \varepsilon^* k^* D + (1 - \varepsilon^*) k^* D_y^* Z^* \quad (2.18)$$

where ε^* , K_e^* , and Z^* are the post yielding ratio, initial stiffness and Bouc-Wen hysteresis parameter of the equivalent SDOF system. $m^* = \Phi_1^T \mathbf{M} \Phi_1$, $k^* = \Phi_1^T \mathbf{K} \Phi_1$ are the equivalent mass and stiffness. D_y^* is the equivalent yielding displacement which can be calculated according to Chopra (2001):

$$D_y^* = \frac{U_y}{\Gamma_1 \phi_{n,1}} \quad (2.19)$$

U_y is the yielding point of the pushover curve of the original MDOF structure, and

$\Gamma_1 = \frac{\Phi_1^T \mathbf{K} \mathbf{r}}{\Phi_1^T \mathbf{M} \Phi_1}$ is the 1st mode participation factor.

The equivalent displacement D is solved by numerical analysis with Eq. (2.16). The top floor displacement can be computed by:

$$u_N = \Gamma_1 \phi_{N,1} D \quad (2.20)$$

The equivalent nonlinear damping is related to the equivalent linear damping of SDOF system by applying the Jacobson's formula (Eq. 2.10) again, which is shown below:

$$c_\alpha^* = \frac{\pi}{\lambda} (\omega_e D)^{1-\alpha} c_L^* \quad (2.21)$$

Substituting Eq. (2.15) and (2.20) into Eq. (2.21), the equivalent nonlinear damping of SDOF system can be related directly to the nonlinear damper parameters of the original MDOF inelastic structure:

$$c_\alpha^* = \left(\Gamma_1 \phi_{N,1} \right)^{\alpha-1} \left(\phi_{1,1}^{1+\alpha} c_{\alpha,1} + \sum_{n=2}^N \left(\phi_{n,1} - \phi_{n-1,1} \right)^{1+\alpha} c_{\alpha,n} \right) \quad (2.22)$$

It's seen in Eq. (2.22) that the nonlinear damping coefficient of the equivalent SDOF system is only a function of the mechanical properties of the installed dampers and 1st mode shape of the original MDOF structure. All equivalent structural parameters appearing in the SDOF system (i.e. in Eq. (2.16)) are all fully defined.

2.3.2 Verification of Proposed Equivalent SDOF System

A 3DOF shear building structure is adopted for validating the equivalent SDOF method described above. The system mass matrix \mathbf{M} and initial stiffness matrix \mathbf{K} of the structure are given in Eq. (2.23) and (2.24). The yielding displacement of all floors are set to 0.02m.

$$\mathbf{M} = \begin{bmatrix} 200.40 & 0 & 0 \\ 0 & 200.40 & 0 \\ 0 & 0 & 178.00 \end{bmatrix} (kg) \quad (2.23)$$

$$\mathbf{K} = \begin{bmatrix} 238.93 & -119.46 & 0 \\ -119.46 & 238.93 & -119.46 \\ 0 & -119.46 & 119.46 \end{bmatrix} \times 10^3 (N/m) \quad (2.24)$$

There are 3 nonlinear viscous dampers installed in-between the 3 floors of the structure. And two cases of distribution of the nonlinear dampers are considered here: $\mathbf{c}_a = [800 \ 800 \ 800] \ N \cdot (s/m)^\alpha$ (case 1) and $\mathbf{c}_a = [800 \ 400 \ 200] \ N \cdot (s/m)^\alpha$ (case 2).

The nonlinear dampers are first transformed into equivalent linear dampers on the basis of Jacobson's formula shown above, then modal analysis theory is used to get the equation of motion for the 1st mode of the structure. Under the assumption that the structure is first mode dominant (mass participation greater than 90%), the SDOF system represented in the 1st mode equation of motion could be taken as the equivalent SDOF structure of the original 3 DOF structure. Since the original structure is equipped with nonlinear dampers, the linear damping term in the 1st mode equation of motion is transferred back to nonlinear form by Jacobson's formula. The parameters of the equivalent SDOF system is listed in Table 2.3.

Table 2.3 Equivalent parameters of the SDOF system

m^* (kg)	k^* (N/m)	D_y^* (m)	$c_\alpha^* (N \cdot (s/m)^\alpha)$ (case 1)	$c_\alpha^* (N \cdot (s/m)^\alpha)$ (case 2)
351.74	44195.82	0.0365	401.76	292.51

To demonstrate and for simplicity, a pulse-type motion (Type B - cosine pulse) is applied to the equivalent SDOF structure and the original 3DOF structure. The nonlinear responses are obtained and compared in Fig. 2.8. The uniform distribution of nonlinear damping is considered. The mass participation factor of the 1st mode for the selected 3DOF structure is 91.63%. Both linear and nonlinear stiffness distribution are considered. As shown in Fig. 2.8, for both nonlinear damper distribution cases, the top floor displacement has been predicted well by the equivalent SDOF system, which demonstrates that the established equivalency works well.

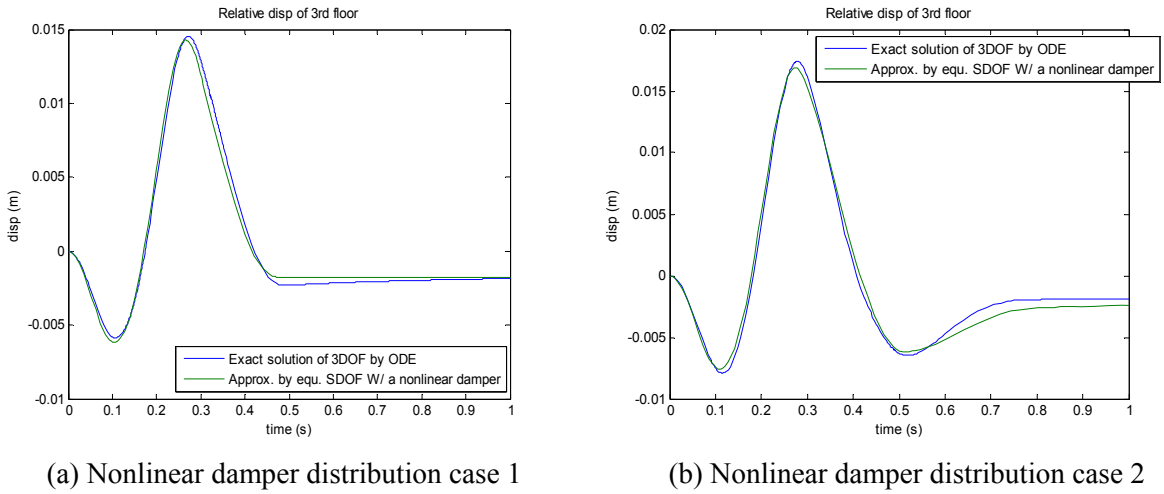


Fig. 2.8 Comparison of top floor displacement of a 3DOF structure

It is noted that there is a nonlinear damping term in the equation of motion of the equivalent SDOF system. This can be used directly to estimate the damping ratio (nonlinear one) of the equivalent SDOF system and can also be referred as the damping ratio of the 1st mode of the original 3DOF structure. Other researchers have proposed a method to define the 1st mode damping ratio of a MDOF structure as following (Diotallevi et al. 2012):

$$\xi_1 = \frac{\sum_{j=1}^N (2\pi)^\alpha T_1^{2-\alpha} \lambda c_{\alpha,j} f_j^{1+\alpha} D_{\text{roof}}^{\alpha-1} \phi_{rj,1}^{1+\alpha}}{8\pi^3 \sum_{j=1}^N m_j \phi_{j,1}^2} \quad (2.25)$$

The formula in Eq. (2.25) is also based on the 1st modal shape and modal period, which is similar to our proposed damping ratio definition. However, to calculate the 1st mode damping ratio using the above formula in Eq. (2.25), the maximum structural response D_{roof} has to be determined beforehand, while the proposed damping ratio in this study doesn't need any structural response information to be computed because it is only a function of structural mechanical properties.

The exact dynamic response of the original 3DOF structure is solved in order to get the damping ratio defined by Eq. (2.25). It is compared with the damping ratios calculated by

the nonlinear damping ratio definition proposed in Eq. (2.8). Table 2.4 shows the comparison for different frictional α values of the nonlinear viscous dampers.

Table 2.4 Nonlinear damping ratio of 1st mode of a MDOF structure (%)

α	0.2	0.4	0.6	0.8	1.0
$\Pi_{\xi,n}^*$	35.04	16.81	8.10	3.92	1.90
ξ_1	42.44	15.65	7.25	3.65	1.90

It's seen that the proposed nonlinear damping ratio definition is quite comparable with the results from the existing formulas. However, the proposed nonlinear damping ratio definition has much simplified expression and doesn't need a-priori knowledge on maximum structural response, i.e. the damping ratio could be calculated only based on the structural properties without any dynamic analysis effort.

In order to evaluate the efficacy of the equivalent systems for system with possible higher mode effects, another 8DOF structure is also used as the second example to show the effectiveness of equivalent SDOF method. The structural properties are summarized in Table 2.5. Both pulse type B motion and El Centro N-S earthquake record is used as the earthquake excitation at the base of the structure.

Table 2.5 Structural properties of a sample 8 degree-of-freedom structure

Story #	1	2	3	4	5	6	7	8
Storey Mass m_i (ton)	345.6	345.6	345.6	345.6	345.6	345.6	345.6	345.6
Storey stiffness k_i (10^5 KN/m)	3.4	3.2	2.85	2.69	2.43	2.07	1.69	1.37
Storey damping $c_{\alpha,i}$	800	800	800	800	800	800	800	800
Storey yield disp. D_{y_i} (cm)	2.0	2.0	2.0	2.0	2.0	2.0	2.0	2.0

Top floor displacement histories are show in Fig. 2.9. It's seen that under both pulse type motion and earthquake input, the response obtained by equivalent SDOF method is quite similar to those of exact numerical solution obtained from the original 8DOF system.

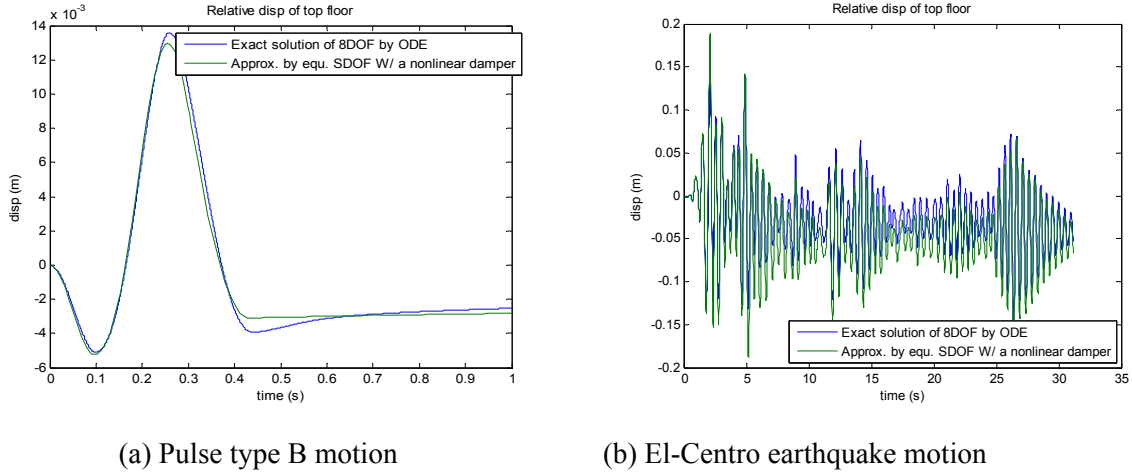


Fig. 2.9 Comparison of top floor displacement of a 8DOF structure

Although the above numerical studies show promising results from the equivalent SDOF method, there are limitations of this method, which come from the following three basic aspects within the aforementioned procedure: (1) The validity of equaling a nonlinear damper to a linear one based on Jacobson's formula, since this formula is energy based but the direct equivalence in the equation of motion should be based on force; (2) The original damping provided by the nonlinear dampers are not classical damping, so the 1st modal shape factor couldn't really diagonalize the damping matrix therefore the 1st mode equation of motion is not indeed decoupled with other modes; (3) The 1st mode dominant is appropriate for most shear buildings but not always the case.

2.4 Optimal Nonlinear Damper Design for Shear Type MDOF Structure

On the promise that a first mode dominated MDOF structure can be approximated by an equivalent SDOF system and the effects of nonlinear damping on SDOF inelastic structure

can be well quantified by the proposed nonlinear damping ratio, in this section, an attempt is carried out to identify the optimal nonlinear damper design for shear type MDOF structure, which includes the damping amount and damper location.

The genetic algorithm is adopted to search for the optimal design of nonlinear viscous dampers for a shear type MDOF structure. The crossover and mutation are the two basic operators of genetic algorithm that create new designs for further evolution. After a new population is created, a performance index is evaluated for each new design to determine its fitness compared to other designs in the same generation, which is repeated for a number of cycles (generations) until no further improvement is obtained in the best individual in the subsequent generations.

To start the genetic algorithm search, first an initial population of a chosen size is randomly generated. In the context of placement of devices, each individual represents a design with a particular scheme of placement of the devices. For example, to place 9 devices in a 3 story building, one possible arrangement of these devices is {2, 1, 2, 3, 2, 2, 3, 1, 1}, which represents an individual of the population. In this placement, the first device is placed in the 2nd story, the second in the 1st story, etc, that is the device locations represent the genes of each individual. There is no set rule to select the size of a population. A larger population may converge to the final solution in less number of iterations but would also require a larger number of performance index calculations for each iteration.

After selecting a population size, the next step is to perform genetic operators of the reproduction process. For this, first performance index of each individual of the population is evaluated. The higher the performance index the better the individual. The individuals are then ranked from the best to the worst. And then they are paired for reproduction according to the roulette-wheel scheme. To avoid a complete domination in the pairing process by the individuals with highest performance indices, the performance indices are mapped into a

fitness function that modulates the relative dominance of the performance index values. In this section, the fitness function of i^{th} design is defined as follow (Goldberg 1989):

$$F(i) = F(i-1) + I(i) \quad (2.26)$$

where $F(0) = 0$ and $I(i)$ is the fitness interval which is given by:

$$I(i) = \frac{2(N+1-i)}{N(N+1)} \quad (2.27)$$

where N is the population size.

Based on the fitness function, the crossover scheme is used to produce offsprings that share the genetic information of the parents. For this, a gene location (i.e. device location) is randomly selected for each pair of individuals, above which the genes are interchanged to create new offsprings. This is one-point crossover.

A small fraction of the parent population is also mutated to introduce new designs. The mutation introduces new genes in the population for further evolutions. This fraction is usually kept low to avoid too many offspring losing the genes of their parents, and thus losing their ability of high performance index. In this section, a one-point mutation rule is carried out where a randomly selected gene in a randomly selected individual is changed to take on a new value from the set of possible values.

After the mutation is finished, the new generation is ranked again according to their performance index values and the same process is repeated until a convergence to the optimal solution is reached. A Matlab program is developed where a genetic algorithm is employed for the optimal damping device design in this section. One can get the design coefficient of the nonlinear damper on each DOF of the structure by this code.

In the context of optimal damper property and location selection for a MDOF structure, we adopt genetic algorithm here for two purposes: (1) how much damping is

needed. This is usually determined roughly by the response reduction objective, for example, 40%. Nonlinear damping ratio could be a good measurement of how much damping is added. (2) where to put the nonlinear dampers. This is determined by iterations through genetic algorithm.

A 3DOF shear type structure used in the previous section is adopted for numerical study. Same mass, stiffness matrices M and K are adopted. There 120 nonlinear viscous dampers available to be used for the response reduction. The design objective is to reduce the undamped response 50% when dampers are installed. The damping coefficient of each nonlinear damper is 100 with a damping exponential index of 0.5. The damping coefficient is chosen to be so small that we can determine the number of dampers set on each floor first then convert them to larger size of dampers but with less counts, which would give us the optimal design of nonlinear dampers (damping coefficients and locations). Both type-B pulse and El Centro earthquake record are used as ground excitations.

The population size is set to be 40, which means 40 damper designs are randomly generated as the initial generation (parent designs) for genetic algorithm. The performance index is chosen as the maximum top floor displacement. Time history analysis is done to calculate the performance indices of all the parent designs and the parent designs are re-ordered from the best to worst according to the performance index values. The ordered parent designs by rank are ready to be used for mating process.

After the fitness function is defined, two random number between $[0, 1]$ are generated to determine which two parent designs are paired to produce two child designs based on where the two random numbers fall on the fitness interval roulette wheel. The child designs are obtained by crossover and mutation. One-point crossover is used where a random gene location is selected above which all the genes of the parent designs are interchanged to attain two new children designs. Crossover is performed on 100% of the population. Then

one-point mutation is carried out where a random gene of a parent design is selected to be replaced by a new gene to obtain a new child design. Mutation is performed on 5% of the whole population.

The 2nd generation (a set of new designs) is obtained when crossover and mutation is finished. The time history analysis is performed again to determine which design in the 2nd generation is the best. This procedure is repeated until not much improvement can be achieved from the evolution. The best design of the last generation is considered as the optimal design.

The optimal design from the genetic algorithm for the 3DOF structure is listed in Table 2.6. The performance index for evenly distributed damping case is also listed for comparison purpose. It shows that putting more damping on the bottom DOFs yields a better design. Nonlinear damping ratio is calculated by the equivalent SDOF method proposed before and presented in Table 2.6 as well. Fig. 2.10 shows the structural response with optimal nonlinear damper design yields a better performance than the evenly distributed dampers case which takes the same level of damping. This comparison concludes the effectiveness of the optimal design with genetic algorithm.

Table 2.6 Optimal design of nonlinear dampers for a 3DOF structure

Design input	Nonlinear damping coeff			Performance Index (m)	Damping ratio (%)
El Centro	Optimal	[5000 4200 2800]		0.0225	59.17
	Evenly	[4000 4000 4000]		0.0263	
B-type pulse	Optimal	[4900 4600 2500]		0.0155	58.89
	Evenly	[4000 4000 4000]		0.0166	

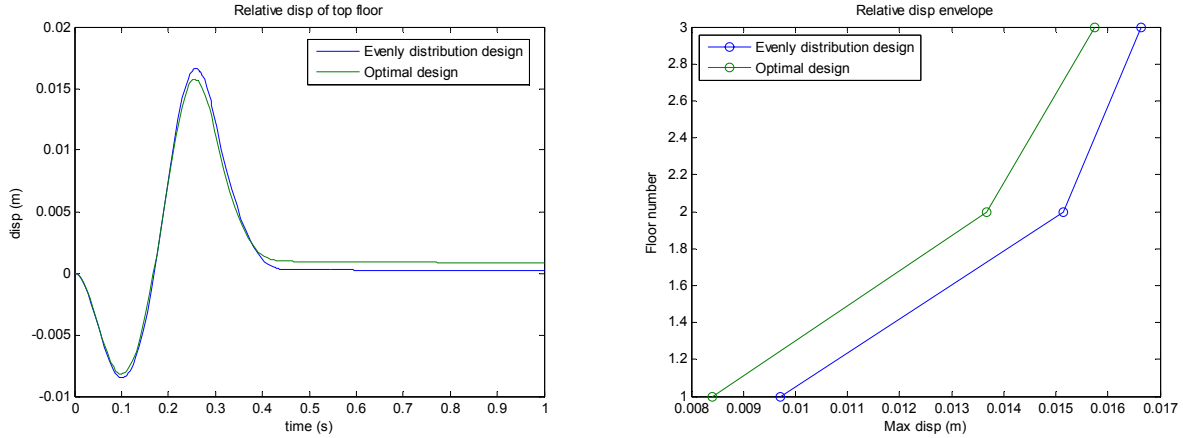


Fig. 2.10 Structural response with optimal nonlinear damper design

To further illustrate the ability of the genetic algorithm in the design for damping devices, a 8DOF nonlinear structure is considered as case study as well. The structural properties are presented in Table 2.7. Meanwhile, three different indices are taken as the performance index: top floor displacement, top floor total acceleration and maximum inter-story drift. The optimal design from the genetic algorithm is listed in Table 2.8. The performance index for evenly distributed damping case is also listed for comparison purpose. Nonlinear damping ratio is calculated by the equivalent SDOF method proposed in section 2 and presented here as well. Type-B pulse input is used as the dynamic excitation for all the cases.

Table 2.7 Structural properties of a sample 8 degree-of-freedom structure

Story #	1	2	3	4	5	6	7	8
Storey Mass m_i (ton)	345.6	345.6	345.6	345.6	345.6	345.6	345.6	345.6
Storey stiffness k_i (10^5 KN/m)	3.4	3.2	2.85	2.69	2.43	2.07	1.69	1.37
Storey yield disp. D_{yi} (cm)	2.0	2.0	2.0	2.0	2.0	2.0	2.0	2.0

Table 2.8 Optimal design of nonlinear dampers for a 8DOF structure

Performance Type	Nonlinear damping coeff ($N \cdot (s/m)^a$) (1e8)					Performance Index	Damping ratio (%)
Top flr. disp. (cm)	Optimal	[2.0239 1.8657 1.6444 1.2965 1.6444 1.2333 1.5179 1.4230]					2.20
	Evenly	[1.5811 1.5811 1.5811 1.5811 1.5811 1.5811 1.5811 1.5811]					2.21
Top flr. accel. (m/s^2)	Optimal	[1.5495 1.5179 1.2965 1.4863 1.6760 1.5495 1.7076 1.8657]					7.50
	Evenly	[1.5811 1.5811 1.5811 1.5811 1.5811 1.5811 1.5811 1.5811]					7.56
Max inter drift (cm)	Optimal	[1.6128 1.2333 1.5495 1.5811 1.4230 1.5179 1.7709 1.9606]					0.31
	Evenly	[1.5811 1.5811 1.5811 1.5811 1.5811 1.5811 1.5811 1.5811]					0.34

2.5 Concluding Remarks

Despite the understanding of the effect of linear damping on structural response, the impact of nonlinear damping on structures is not fully understood. In particular, the nonlinear damping required to achieve the optimal performance of inelastic structures depends on the nonlinear structural responses and the ground motion inputs. This study intends to quantify the effects of nonlinear damping on inelastic structures and determine the optimal amount and locations of nonlinear dampers. Using dimensional analysis of inelastic structures with nonlinear dampers, a dimensionless damping ratio is derived, which can decisively quantify its effects on structural responses (e.g. drift and total acceleration). The effects of nonlinear damping are then studied for idealized SDOF inelastic structures under pulse-type ground motions. Through the parametric study using both simplified pulses and real near-fault ground motions, it is shown that the added nonlinear damping is not always beneficial for structures. Whether the larger nonlinear damping ratio benefits the structural responses depends on the relative frequency between the structure and the input motion (Π_ω), and the

characteristics of the input motion (e.g. pulse type). There exists a critical structure-to-pulse frequency, below which an optimal damping is needed to balance the reduction of structural drift and the increase of the total acceleration.

To extend to the general application to MDOF inelastic structures, an equivalent SDOF inelastic structure is derived with equivalent structural properties and equivalent nonlinear dampers. Based on this equivalency, nonlinear damping ratio for MDOF inelastic structures is subsequently derived. Finally, the optimal damping and damper placement for MDOF inelastic structures are developed utilizing the nonlinear damping ratio and the generic algorithm.

3. Hybrid Numerical Simulation Platform for Seismic Response Analysis of Nonlinear Structures

In light of damages of structures observed in past earthquakes, seismic protection strategies are needed to retrofit existing structures or to improve the design of new structures. In addition to the traditional strengthening/stiffening method, structural control technology can be implemented to improve the performance of structures, e.g. adding damping to structure to reduce drift and deformations during the seismic response. Structural control technologies are typically classified into the passive, active/hybrid and semi-active systems (Housner et al. 1997).

To date, a number of passive systems have been implemented in buildings and other civil engineering structures. Two of the most popular approaches are to use supplemental energy dissipation or base isolation for vibration reduction and energy dissipation. Most passive seismic protective systems are based on the general idea of increasing the damping of structures (Constantinou et al. 1998). Because ground motions are stochastic in nature, passive systems might have a limited range of effectiveness. Active control systems are more efficient in this regard. However, except for protecting small or light weight objects, such as aerospace equipments, the solution on how to deliver large active counter forces is needed before the wide use of this technology in civil structures. Semi-active systems, such as magnet-orheological (MR) dampers, include smart mechanical and material components whose physical parameters can be modified in real-time through switching or on-off operations (Spencer and Nagarajaiah 2003). Due to the variability and use of passive forces, semi-active control is becoming a promising technology of seismic hazard mitigation for civil engineering structures.

In order to optimally select the stiffness and damping values for control devices in design, the structural control of structures with controllable devices needs to be performed

first. However, for structures exhibiting nonlinearity, the structural control cannot be easily conducted within the typical finite element analysis program. Although current FEM programs typically have various elements of modelling complex nonlinear structural components and control devices, there is no well established approach to apply control algorithms in most existing commercial codes. Instead, the structural controls were often conducted on simplified structural models that can be generated in the same simulation platform for control algorithms. For example, efforts have been made to develop the benchmark problems for several structures to allow for a platform to compare various control strategies (Agrawal et al. 2009; Ohtori et al. 2004). Nevertheless, the ability to use advanced and realistic structural models in conjunction with structural control is currently lacking, which also limit the adoption of structural control.

Hybrid simulation is a method for examining the seismic response of structures using a hybrid model comprised of either both physical and numerical sub-structures, or numerical sub-structures only (Saouma and Sivaselvan 2008). This alternative way of physical testing or numerical modelling of an entire system allows for numerical simulations of complex coupled systems performed separately on different computational platforms. In this study, a novel approach utilizing the hybrid simulation is proposed to take advantage of modelling ability of existing finite element software programs and realize the structural control algorithm at the same time. As shown in Fig. 3.1, a complex nonlinear structure can be modelled in any existing finite element software, such as OpenSees, ABAQUS, etc, while the structural control devices of viscous fluid dampers, base isolators or MR dampers are simulated in other software, such as Matlab, where the control algorithms can be easily formulated and implemented using the built-in toolboxes. The main nonlinear structure and the control devices, as two substructure parts, can communicate with each other by transferring force and displacement information through a platform designed for hybrid simulation: UI-SIMCOR. A

nonlinear structure equipped with linear fluid dampers, nonlinear fluid dampers or base isolators is studied using the hybrid simulation hereafter. The structural control is implemented and the equivalent passive parameters are derived. The study verifies the validity of the hybrid numerical simulation scheme in efficiently developing seismic protection strategies for nonlinear structures. Furthermore, the hybrid simulation scheme is also modified to accommodate multi-support excitation input and account for soil-structure interaction effects under earthquake excitations.

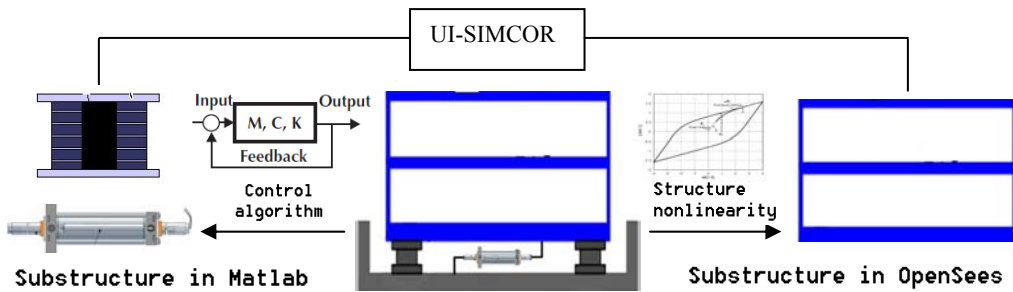


Fig. 3.1 Hybrid numerical simulation scheme

3.1 Hybrid Simulation Platform: UI-SIMCOR

The study builds on an existing hybrid simulation platform and has implemented changes to enable the consideration of various nonlinear seismic protective devices. The UI-SIMCOR was originally developed to facilitate geographically distributed pseudo-dynamic (PSD) hybrid simulation. It has been widely used for PSD hybrid simulation and multi-platform simulation with OpenSees, Matlab, ABAQUS, etc (Kwon et al. 2008). UI-SIMCOR can control distributed PSD test in several sites. The simulation can be either all experiments, combination of experiments and analyses, or all analyses.

3.1.1 *Static Condensation and Effective Degree of Freedoms (DOF)*

The UI-SIMCOR program solves the equation of motion of a dynamic system

generated by static condensation (Kwon et al. 2007). A portal frame with 16 nodes (plus 2 constrained nodes) and 17 beam elements shown in Fig. 3.2 (a) is used for the purpose of illustration. Lumped masses are located at beam column joints and ground acceleration is applied in horizontal direction. There will be mass and stiffness matrices with 48 by 48 elements in the equation of motion of the frame. However, the structure's mass and stiffness matrix can be reduced to 6 by 6 using static condensation if the stiffness and mass matrices are known, as shown in Fig. 3.2 (b).

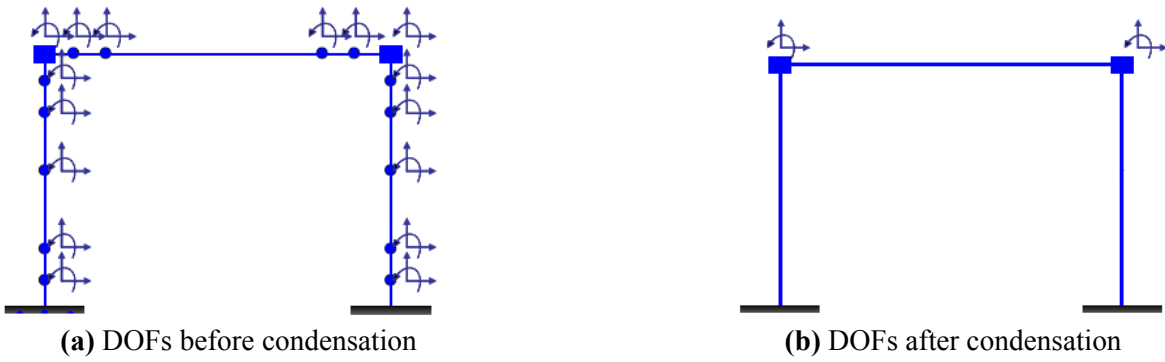


Fig. 3.2 Static condensation of multiple DOF structures

The above procedure is explained mathematically here. It could be seen that certain DOFs can be condensed out from the equation of motion (EOM) through static condensation. Consider a structure subject to ground motion \ddot{u}_g :

$$\begin{bmatrix} \mathbf{M}_i & & \\ & \mathbf{0}_j & \\ & & \mathbf{0}_k \end{bmatrix} \begin{bmatrix} \ddot{\mathbf{u}}_i \\ \ddot{\mathbf{u}}_j \\ \ddot{\mathbf{u}}_k \end{bmatrix} + \begin{bmatrix} \mathbf{K}_{ii} & \mathbf{K}_{ij} & \mathbf{K}_{ik} \\ \mathbf{K}_{ji} & \mathbf{K}_{jj} & \mathbf{K}_{jk} \\ \mathbf{K}_{ki} & \mathbf{K}_{kj} & \mathbf{K}_{kk} \end{bmatrix} \begin{bmatrix} \mathbf{u}_i \\ \mathbf{u}_j \\ \mathbf{u}_k \end{bmatrix} = - \begin{bmatrix} \mathbf{M}_i & & \\ & \mathbf{0}_j & \\ & & \mathbf{0}_k \end{bmatrix} \begin{bmatrix} \mathbf{I}_i \\ \mathbf{I}_j \\ \mathbf{I}_k \end{bmatrix} \ddot{u}_g \quad (3.1)$$

where \mathbf{u} is the structural relative displacement; \mathbf{M} , \mathbf{K} and \mathbf{I} denotes mass, stiffness and ground motion influence matrix respectively. Subscriptions i corresponds to DOFs where mass is defined; j corresponds to interface DOFs which are of our interest and k denotes internal DOFs where neither is mass defined nor of our interest. Eq. (3.1) can be simplified

into:

$$\begin{bmatrix} \mathbf{M}_i \ddot{\mathbf{u}}_i \\ \mathbf{0}_j \\ \mathbf{0}_k \end{bmatrix} + \begin{bmatrix} \mathbf{K}_{ii} & \mathbf{K}_{ij} & \mathbf{K}_{ik} \\ \mathbf{K}_{ji} & \mathbf{K}_{jj} & \mathbf{K}_{jk} \\ \mathbf{K}_{ki} & \mathbf{K}_{ij} & \mathbf{K}_{kk} \end{bmatrix} \begin{bmatrix} \mathbf{u}_i \\ \mathbf{u}_j \\ \mathbf{u}_k \end{bmatrix} = -\begin{bmatrix} \mathbf{M}_i \mathbf{I}_i \ddot{u}_g \\ \mathbf{0}_j \\ \mathbf{0}_k \end{bmatrix} \quad (3.2)$$

Combine the mass terms to right side of the equation, one gets:

$$\begin{bmatrix} \mathbf{K}_{ii} & \mathbf{K}_{ij} & \mathbf{K}_{ik} \\ \mathbf{K}_{ji} & \mathbf{K}_{jj} & \mathbf{K}_{jk} \\ \mathbf{K}_{ki} & \mathbf{K}_{ij} & \mathbf{K}_{kk} \end{bmatrix} \begin{bmatrix} \mathbf{u}_i \\ \mathbf{u}_j \\ \mathbf{u}_k \end{bmatrix} = -\begin{bmatrix} \mathbf{M}_i \mathbf{I}_i \ddot{u}_g + \mathbf{M}_i \ddot{\mathbf{u}}_i \\ \mathbf{0}_j \\ \mathbf{0}_k \end{bmatrix} \quad (3.3)$$

Condense out \mathbf{u}_k in the equation, one gets:

$$\left(\begin{bmatrix} \mathbf{K}_{ii} & \mathbf{K}_{ij} \\ \mathbf{K}_{ji} & \mathbf{K}_{jj} \end{bmatrix} - \begin{bmatrix} \mathbf{K}_{ik} \\ \mathbf{K}_{jk} \end{bmatrix} \mathbf{K}_{kk}^{-1} \begin{bmatrix} \mathbf{K}_{ki} & \mathbf{K}_{ij} \end{bmatrix} \right) \begin{bmatrix} \mathbf{u}_i \\ \mathbf{u}_j \end{bmatrix} = -\begin{bmatrix} \mathbf{M}_i \mathbf{I}_i \ddot{u}_g + \mathbf{M}_i \ddot{\mathbf{u}}_i \\ \mathbf{0}_j \end{bmatrix} \quad (3.4)$$

Denote the stiffness part of left side of the equation by an equivalent form as:

$$\begin{bmatrix} \mathbf{K}_{ii}^* & \mathbf{K}_{ij}^* \\ \mathbf{K}_{ji}^* & \mathbf{K}_{jj}^* \end{bmatrix} \begin{bmatrix} \mathbf{u}_i \\ \mathbf{u}_j \end{bmatrix} = -\begin{bmatrix} \mathbf{M}_i \mathbf{I}_i \ddot{u}_g + \mathbf{M}_i \ddot{\mathbf{u}}_i \\ \mathbf{0}_j \end{bmatrix} \quad (3.5)$$

Now one can rearrange the EOM into:

$$\begin{bmatrix} \mathbf{M}_i & \mathbf{0}_j \\ \mathbf{0}_j & \mathbf{0}_j \end{bmatrix} \begin{bmatrix} \ddot{\mathbf{u}}_i \\ \ddot{\mathbf{u}}_j \end{bmatrix} + \begin{bmatrix} \mathbf{K}_{ii}^* & \mathbf{K}_{ij}^* \\ \mathbf{K}_{ji}^* & \mathbf{K}_{jj}^* \end{bmatrix} \begin{bmatrix} \mathbf{u}_i \\ \mathbf{u}_j \end{bmatrix} = -\begin{bmatrix} \mathbf{M}_i & \mathbf{0}_j \\ \mathbf{0}_j & \mathbf{0}_j \end{bmatrix} \begin{bmatrix} \mathbf{I}_i \\ \mathbf{I}_j \end{bmatrix} \ddot{u}_g \quad (3.6)$$

which can be expressed as:

$$\mathbf{M}^* \ddot{\mathbf{u}}^* + \mathbf{K}^* \mathbf{u}^* = -\mathbf{M}^* \mathbf{I}^* \ddot{u}_g \quad (3.7)$$

Thus the DOFs that have no mass defined and are not of interest are condensed out. UI_SimCor only solves the EOM with these remaining DOFs in analysis, and they are referred as ‘effective DOFs’. For hybrid simulation using UI-SIMCOR, this is very important concept for the preparation of input file where effective DOFs are specified.

After defining the effective DOFs, which are the DOFs with lumped masses or zero

mass, the mass matrix is easily formulated. At the same time, the condensed stiffness matrix can be determined by applying a pre-specified displacement to each effective DOFs and measuring reaction forces as shown in Fig. 3.3 (a). For the hybrid simulation of a frame which is divided into two segments on two sites or two analysis modules, the initial stiffness of a certain DOF can be calculated by applying certain displacement to the segmented structure and take summation of reaction forces from each segment of structure as shown in Fig. 3.3 (b). Then the dynamic analysis can be performed for the structure using reduced DOFs. This concept is very important for the application of hybrid simulation and testing using UI-SIMCOR as well.

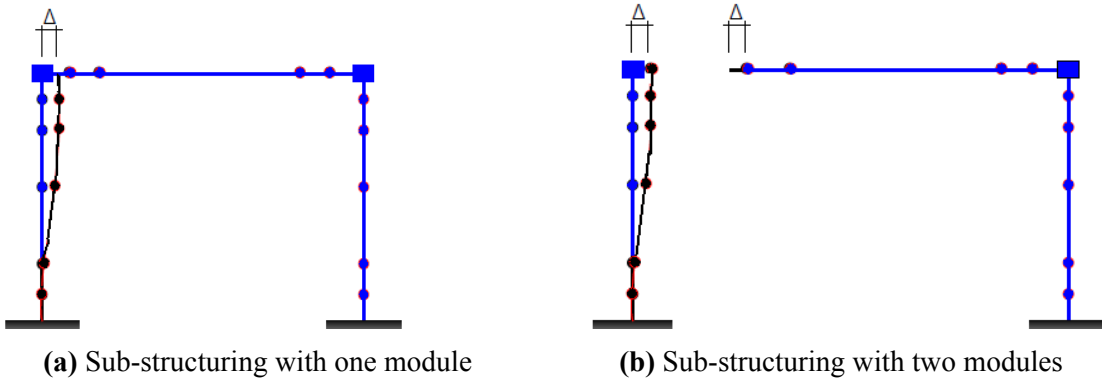


Fig. 3.3 Formulation of stiffness matrix in UI-SIMCOR

3.1.2 Time Integration Method Adopted in UI_SimCor

An explicit integration algorithm of Newmark family, called α operator splitting (α -OS) method (Nakashima et al. 1990), is adopted in UI_SimCor to solve the EOM by a time stepping manner. The EOM of a structure with nonlinear restoring force can be expressed as:

$$\mathbf{M}\mathbf{a}(t) + \mathbf{C}\mathbf{v}(t) + \mathbf{r}(t) = \mathbf{f}(t) \quad (3.8)$$

where $\mathbf{a}(t)$ and $\mathbf{v}(t)$ are acceleration and velocity vector; \mathbf{M} and \mathbf{C} are system mass and

damping matrix; $\mathbf{f}(t)$ is the external excitation and $\mathbf{r}(t)$ is the nonlinear restoring force.

Rewrite Eq. (3.8) in discrete time form and apply the α operator, the EOM becomes:

$$\mathbf{M}\mathbf{a}_{n+1} + (1+\alpha)\mathbf{C}\mathbf{v}_{n+1} - \alpha\mathbf{C}\mathbf{v}_n + (1+\alpha)\mathbf{r}_{n+1} - \alpha\mathbf{r}_n = (1+\alpha)\mathbf{f}_{n+1} - \alpha\mathbf{f}_n \quad (3.9)$$

where n denotes the time step. The equilibrium in Eq. (3.9) is solved according to:

(i) A predictor step

$$\begin{aligned}\tilde{\mathbf{d}}_{n+1} &= \mathbf{d}_n + \Delta t \mathbf{v}_n + \frac{\Delta t^2}{2} (1-2\beta) \mathbf{a}_n \\ \tilde{\mathbf{v}}_{n+1} &= \mathbf{v}_n + \Delta t (1-\gamma) \mathbf{a}_n\end{aligned} \quad (3.10)$$

and (ii) A corrector step

$$\begin{aligned}\mathbf{d}_{n+1} &= \tilde{\mathbf{d}}_{n+1} + \Delta t^2 \beta \mathbf{a}_{n+1} \\ \mathbf{v}_{n+1} &= \tilde{\mathbf{v}}_{n+1} + \Delta t \gamma \mathbf{a}_{n+1}\end{aligned} \quad (3.11)$$

where parameter $\beta = (1-\alpha)^2/4$ and $\gamma = (1-2\alpha)/2$, $\alpha \in \left[-\frac{1}{3}, 0\right]$ allows the tuning of numerical damping of the method. In order to solve the equilibrium in Eq. (3.9) without iteration, the nonlinear unknown term \mathbf{r}_{n+1} is replaced by:

$$\mathbf{r}_{n+1}(\mathbf{d}_{n+1}) \approx \tilde{\mathbf{r}}_{n+1}(\tilde{\mathbf{d}}_{n+1}) + \mathbf{K}^T (\mathbf{d}_{n+1} - \tilde{\mathbf{d}}_{n+1}) \quad (3.12)$$

which is the predicted restoring force $\tilde{\mathbf{r}}_{n+1}(\tilde{\mathbf{d}}_{n+1})$ corrected by a linear force term that is related to system initial stiffness matrix \mathbf{K}^T . Based on this assumption and substituting Eq. (3.10), (3.11) and (3.12) into Eq. (3.9), one can get:

$$\hat{\mathbf{M}}\mathbf{a}_{n+1} = \hat{\mathbf{f}}_{n+1} \quad (3.13)$$

where

$$\begin{aligned}\hat{\mathbf{M}} &= \mathbf{M} + \gamma \Delta t (1+\alpha) \mathbf{C} + \beta \Delta t^2 (1+\alpha) \mathbf{K}^T \\ \hat{\mathbf{f}}_{n+1} &= (1+\alpha)\mathbf{f}_{n+1} - \alpha\mathbf{f}_n + \alpha\tilde{\mathbf{r}}_n - (1+\alpha)\tilde{\mathbf{r}}_{n+1} \\ &\quad + \alpha\mathbf{C}\tilde{\mathbf{v}}_n - (1+\alpha)\mathbf{C}\tilde{\mathbf{v}}_{n+1} + \alpha(\gamma \Delta t \mathbf{C} + \beta \Delta t^2 \mathbf{K}^T) \mathbf{a}_n\end{aligned} \quad (3.14)$$

Finally the acceleration at time t_{n+1} can be solved by:

$$\mathbf{a}_{n+1} = \hat{\mathbf{M}}^{-1} \hat{\mathbf{f}}_{n+1} \quad (3.15)$$

\mathbf{a}_{n+1} is substituted into Eq. (3.11) to update displacement and velocity at time t_{n+1} .

It's noted that the above integration scheme is linearly implicit and doesn't need iteration. This is important to perform physical hybrid test because the repeated or potentially cyclic loading for a single time step may damage the experimental specimen.

3.1.3 Development of Multiple Support Excitation Scheme in UI_SimCor

UI_SimCor is originally developed for dynamic analysis with uniform excitation only as input. This could serve the analysis and simulation needs for most civil engineering structures, such as residential buildings, foundations and soil. However, to accurately simulate the dynamic response of a highway bridge under earthquake excitation, multiple support input has to be applied due to the ground amplification effect of approaching embankments of bridge, which would vary the input motions at different supports significantly. To achieve the goal of analyzing general highway bridge using UI_SimCor and make it a more universal platform, UI_SimCor is further developed by this study such that multiple support excitation could be accommodated in the analysis.

(i) EOM for system under multiple support excitation

The equation of motion (EOM) for structural system under multiple support input has the following form:

$$\mathbf{M}\ddot{\mathbf{X}}(t) + \mathbf{C}\dot{\mathbf{X}}(t) + \mathbf{K}\mathbf{X}(t) = \mathbf{0} \quad (3.16)$$

where \mathbf{M} , \mathbf{C} , \mathbf{K} are the mass, damping and stiffness matrices, and \mathbf{X} is the total displacement vector (relative to the unchangeable global coordinate system). Since there is no direct inertial force coming from uniform excitation, the right side of EOM is set to be $\mathbf{0}$. The \mathbf{M} , \mathbf{C} , \mathbf{K} matrices are composed of the information from all the degree of freedoms (DOF) of the structural system including those at the supports, i.e. all the DOFs are taken as free and not constrained, which would result in free rigid body mode (0 frequency) in the eigenvalue

analysis. Thus \mathbf{K} matrix is not of full rank in Eq. (3.16).

By eliminating the rigid body motion mode in the system described by Eq. (3.16), one can get the equivalent EOM of the original system with that the DOFs at the supports are taken off from the original \mathbf{M} , \mathbf{C} , \mathbf{K} matrices. At the same time, an equivalent external force is formulated based on the acceleration, velocity and displacement inputs at the support DOFs.

$$\mathbf{M}_r \ddot{\mathbf{X}}_r(t) + \mathbf{C}_r \dot{\mathbf{X}}_r(t) + \mathbf{K}_r \mathbf{X}_r(t) = \mathbf{F}_e(t) \quad (3.17)$$

where \mathbf{M}_r , \mathbf{C}_r , and \mathbf{K}_r are the mass, damping and stiffness matrices with support DOFs taken off, which are all of full rank. \mathbf{X}_r is the corresponding total displacement vector containing only the DOFs that are not located at supports. \mathbf{F}_e is the equivalent external force determined by boundary inputs and the components in original \mathbf{M} , \mathbf{C} , \mathbf{K} matrices corresponding to DOFs at the supports.

(ii) Solving the system under multiple support excitation in UI_SimCor

As stated in section 3.1.2, UI_SimCor uses a operator-splitting method to solve the equation of motion. This method still applies for solving the EOM in Eq. (3.17), as long as the \mathbf{M}_r , \mathbf{C}_r , \mathbf{K}_r matrices and \mathbf{F}_e are obtained. By first defining the whole structural model including support DOFs, the original \mathbf{M} , \mathbf{C} , and \mathbf{K} matrices can be obtained automatically from UI_SimCor platform, then \mathbf{M}_r , \mathbf{C}_r , \mathbf{K}_r matrices could be derived through erasing the DOFs at the supports. In our practice, the DOFs at the structure supports are arranged in UI_SimCor in such a way that they all are located at the bottom of the \mathbf{M} , \mathbf{C} , and \mathbf{K} matrices, as shown below:

$$\mathbf{M} = \begin{bmatrix} m_{1,1} & & & \\ & m_{2,2} & & \\ & & \ddots & \\ & & & m_{l,l} \\ \hline & & & \\ & \mathbf{0} & & \\ & & & \\ & & & m_{l+1,l+1} \\ & & & \ddots \\ & & & \\ & & & m_{N,N} \end{bmatrix} = \begin{bmatrix} \mathbf{m}_{\text{I,I}} & \mathbf{0} \\ \mathbf{0} & \mathbf{m}_{\text{II,II}} \end{bmatrix} \quad (3.18)$$

$$\mathbf{C} = \left[\begin{array}{cccc|cccc} c_{1,1} & c_{1,2} & \cdots & c_{1,l} & c_{1,l+1} & \cdots & c_{1,N} \\ c_{2,1} & c_{2,2} & \cdots & c_{2,l} & c_{2,l+1} & \cdots & c_{2,N} \\ \vdots & \vdots & \ddots & \vdots & \vdots & \ddots & \vdots \\ \hline c_{l,1} & c_{l,2} & \cdots & c_{l,l} & c_{l,l+1} & \cdots & c_{l,N} \\ c_{l+1,1} & c_{l+1,2} & \cdots & c_{l+1,l} & c_{l+1,l+1} & \cdots & c_{l+1,N} \\ \vdots & \vdots & \ddots & \vdots & \vdots & \ddots & \vdots \\ \hline c_{N,1} & c_{N,2} & \cdots & c_{N,l} & c_{N,l+1} & \cdots & c_{N,N} \end{array} \right] = \begin{bmatrix} \mathbf{c}_{\text{I,I}} & \mathbf{c}_{\text{I,II}} \\ \mathbf{c}_{\text{II,I}} & \mathbf{c}_{\text{II,II}} \end{bmatrix} \quad (3.19)$$

$$\mathbf{K} = \left[\begin{array}{cccc|cccc} k_{1,1} & k_{1,2} & \cdots & k_{1,l} & k_{1,l+1} & \cdots & k_{1,N} \\ k_{2,1} & k_{2,2} & \cdots & k_{2,l} & k_{2,l+1} & \cdots & k_{2,N} \\ \vdots & \vdots & \ddots & \vdots & \vdots & \ddots & \vdots \\ \hline k_{l,1} & k_{l,2} & \cdots & k_{l,l} & k_{l,l+1} & \cdots & k_{l,N} \\ k_{l+1,1} & k_{l+1,2} & \cdots & k_{l+1,l} & k_{l+1,l+1} & \cdots & k_{l+1,N} \\ \vdots & \vdots & \ddots & \vdots & \vdots & \ddots & \vdots \\ \hline k_{N,1} & k_{N,2} & \cdots & k_{N,l} & k_{N,l+1} & \cdots & k_{N,N} \end{array} \right] = \begin{bmatrix} \mathbf{k}_{\text{I,I}} & \mathbf{k}_{\text{I,II}} \\ \mathbf{k}_{\text{II,I}} & \mathbf{k}_{\text{II,II}} \end{bmatrix} \quad (3.20)$$

where index $l+1 \sim N$ indicate the DOFs corresponding to the supports, or where the excitation is applied. Thus, the \mathbf{M}_r , \mathbf{C}_r , and \mathbf{K}_r defined in Eq. (3.17) are given as:

$$\mathbf{M}_r = \mathbf{m}_{\text{I,I}}, \quad \mathbf{K}_r = \mathbf{k}_{\text{I,I}}, \quad \mathbf{C}_r = \mathbf{C}_{\text{I,I}} \quad (3.21)$$

The equivalent external force \mathbf{F}_e can be obtained utilizing this DOF arrangement as well:

$$\mathbf{F}_e = \mathbf{M}\mathbf{a}^b + \mathbf{C}\mathbf{v}^b + \mathbf{K}\mathbf{d}^b \quad (3.22)$$

where \mathbf{M} , \mathbf{C} and \mathbf{K} are defined through Eq. (3.18) to (3.20). And \mathbf{a}^b , \mathbf{v}^b and \mathbf{d}^b are the applied excitations at the boundary support DOFs $l+1 \sim N$, which have the form:

$$\begin{aligned} \mathbf{a}^b &= [0 \ 0 \ \cdots \ 0 \ a^b_{l+1} \ a^b_{l+2} \ \cdots \ a^b_N]^T \\ \mathbf{v}^b &= [0 \ 0 \ \cdots \ 0 \ v^b_{l+1} \ v^b_{l+2} \ \cdots \ v^b_N]^T \\ \mathbf{d}^b &= [0 \ 0 \ \cdots \ 0 \ d^b_{l+1} \ d^b_{l+2} \ \cdots \ d^b_N]^T \end{aligned} \quad (3.23)$$

With all the information above, the EOM in Eq. 3.17 is solved in UI_SimCor using a operator-splitting method which is originally built in.

3.2 Development of Seismic Protective Device Elements

The ultimate goal of hybrid numerical simulation scheme is to accurately analyze the dynamic response of nonlinear structures equipped with seismic protective devices, such as base isolation bearings, linear/nonlinear viscous dampers and MR dampers. Utilizing the numerical hybrid simulation scheme based on UI_SimCor, one can accurately model the nonlinear structures with well developed finite element softwares, such as OpenSees, ABUQUS, etc. However, the seismic protective devices, which are usually highly nonlinear, need to be modeled separately on another computational program. In this study, Matlab is used to formulate computational elements for seismic protective devices in terms of Matlab function or direct modification of integration scheme of UI_SimCor, as introduced as follows.

3.2.1 Development of Base Isolation Element

Considering a structure with base isolators installed, the EOM in Eq. (3.8) is modified to contain the isolators:

$$\mathbf{M}\mathbf{a}(t) + \mathbf{C}\mathbf{v}(t) + \mathbf{r}(t) + \mathbf{r}_b(t) = \mathbf{f}(t) \quad (3.24)$$

where $\mathbf{r}_b(t)$ is the force vector caused by base isolation device. Rewrite Eq. (3.24) in time discrete form:

$$\mathbf{M}\mathbf{a}_{n+1} + (1+\alpha)\mathbf{C}\mathbf{v}_{n+1} - \alpha\mathbf{C}\mathbf{v}_n + (1+\alpha)\mathbf{r}_{n+1} - \alpha\mathbf{r}_n + (1+\alpha)\mathbf{r}^b_{n+1} - \alpha\mathbf{r}^b_n = (1+\alpha)\mathbf{f}_{n+1} - \alpha\mathbf{f}_n \quad (3.25)$$

where the only new unknown compared to the original equation of α -OS method is \mathbf{r}^b_{n+1} , which is the base isolation force at time t_{n+1} . Similarly, \mathbf{r}^b_{n+1} can be first evaluated by the predictor displacement of base isolation devices $\tilde{\mathbf{d}}_{n+1}^b$:

$$\tilde{\mathbf{r}}_{n+1}^b = \tilde{\mathbf{r}}_{n+1}^b(\tilde{\mathbf{d}}_{n+1}^b) \quad (3.26)$$

Then $\tilde{\mathbf{r}}_{n+1}^b$ is corrected by a linear term that is related to the initial stiffness of base isolation devices \mathbf{K}_b^{-1} to approximate the true base isolation force:

$$\mathbf{r}_{n+1}^b(\mathbf{d}_{n+1}^b) \approx \tilde{\mathbf{r}}_{n+1}^b(\tilde{\mathbf{d}}_{n+1}^b) + \mathbf{K}_b^{-1} (\mathbf{d}_{n+1}^b - \tilde{\mathbf{d}}_{n+1}^b) \quad (3.27)$$

After the only unknown \mathbf{r}_{n+1}^b is formulated, the whole structure with base isolation devices can be solved by the α -OS scheme. Note that within this integration frame, an element that can evaluate the base isolation force in Eq. (3.26) with a predictor displacement input is needed. A Matlab function is written based on classical plasticity theory to model the kinematic hardening behavior of base isolation devices, as shown in Fig. 3.4. This element takes in predictor displacement of base isolator and returns reaction force to UI_SimCor to proceed the time integration for the whole structure by the scheme explained from Eq. (3.24)~(3.27).

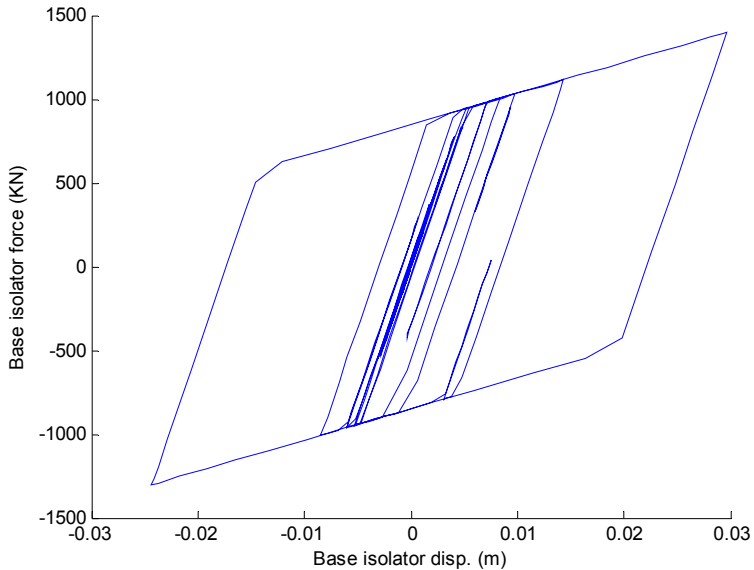


Fig. 3.4 Force-displacement loop of base isolator element

3.2.2 Development of Nonlinear Viscous Damper Element

Due to the open source property, UI-SIMCOR can accommodate different integration schemes that are fit for hybrid simulation. As discussed in section 3.1.2, α -OS method is

written in UI-SIMCOR for solving equation of motion and ready to be modified. The computational element that models a nonlinear viscous damper is incorporated in the time integration section of UI-SIMCOR according to their roles in the equation of motion. The modification of the built-in α -OS method is shown in the following to model nonlinear viscous dampers.

The following derivation is based on a nonlinear N DOF structure equipped with nonlinear dampers on each DOF. By setting damper force to be zero, the locations where dampers are installed can be adjusted accordingly. The equation of motion of this nonlinear system can be expressed as:

$$\mathbf{M}\mathbf{a}(t) + \mathbf{f}_d(t) + \mathbf{r}(t) = \mathbf{f}(t) \quad (3.28)$$

where \mathbf{f}_d is the force vector of nonlinear dampers, $\mathbf{r}(t)$ is the structural restoring force vector and $\mathbf{f}(t)$ is the external force vector. In α -OS method, the numerical solution of Eq. (3.28) is obtained by a two-step scheme: *predictor* step and *corrector* step. Knowing the displacement vector \mathbf{d}_n , velocity vector \mathbf{v}_n and acceleration vector \mathbf{a}_n of previous time step t_n , the predictor displacement and velocity vectors of t_{n+1} are expressed as:

$$\begin{aligned} \tilde{\mathbf{d}}_{n+1} &= \mathbf{d}_n + \Delta t \mathbf{v}_n + \frac{\Delta t^2}{2} (1 - 2\beta) \mathbf{a}_n \\ \tilde{\mathbf{v}}_{n+1} &= \mathbf{v}_n + \Delta t (1 - \gamma) \mathbf{a}_n \end{aligned} \quad (3.29)$$

The *corrector* step yields the true solution of displacement and velocity vectors of t_{n+1} :

$$\begin{aligned} \mathbf{d}_{n+1} &= \tilde{\mathbf{d}}_{n+1} + \Delta t^2 \beta \mathbf{a}_{n+1} \\ \mathbf{v}_{n+1} &= \tilde{\mathbf{v}}_{n+1} + \Delta t \gamma \mathbf{a}_{n+1} \end{aligned} \quad (3.30)$$

where \mathbf{a}_{n+1} is solved from the time discretized form of Eq. (3.28) as following:

$$\mathbf{F}(\mathbf{a}_{n+1}) = \mathbf{M}\mathbf{a}_{n+1} + \mathbf{f}_{d,n+1}(\mathbf{a}_{n+1}) + \mathbf{r}_{n+1}(\mathbf{a}_{n+1}) - \mathbf{f}_{n+1} = 0 \quad (3.31)$$

In general a nonlinear viscous damper can be modeled by:

$$f_d = c_d |v_d|^{\alpha_d} \operatorname{sign}(v_d) \quad (3.32)$$

where c_d is the damping coefficient, v_d is the velocity of the nonlinear damper and α_d is a constant that controls the force-displacement loop of the damper. For a N DOF system including nonlinear viscous dampers, the damper forces are in the vector form:

$$\mathbf{f}_d = [f_{d1} \ f_{d2} \ \dots \ f_{di} \ \dots \ f_{dN}]^T \quad (3.33)$$

Approximating the restoring force term \mathbf{r}_{n+1} as:

$$\mathbf{r}_{n+1}(\mathbf{d}_{n+1}) \approx \tilde{\mathbf{r}}_{n+1}(\tilde{\mathbf{d}}_{n+1}) + \mathbf{K}^I (\mathbf{d}_{n+1} - \tilde{\mathbf{d}}_{n+1}) \quad (3.34)$$

where \mathbf{K}^I is the structural initial stiffness. The derivative of Eq. (3.31) about \mathbf{a}_{n+1} is given by:

$$\mathbf{F}'(\mathbf{a}_{n+1}) = \mathbf{M} + \frac{\partial \mathbf{f}_{d,n+1}}{\partial \mathbf{v}_{n+1}} \frac{\partial \mathbf{v}_{n+1}}{\partial \mathbf{a}_{n+1}} + \frac{\partial \mathbf{r}_{n+1}}{\partial \mathbf{a}_{n+1}} \quad (3.35)$$

where $\frac{\partial \mathbf{f}_{d,n+1}}{\partial \mathbf{v}_{n+1}}$ is a $N \times N$ vector, $\frac{\partial \mathbf{v}_{n+1}}{\partial \mathbf{a}_{n+1}} = \Delta t \gamma \mathbf{I}$, and $\frac{\partial \mathbf{r}_{n+1}}{\partial \mathbf{a}_{n+1}} = \Delta t^2 \beta \mathbf{K}^I$. For the i^{th} nonlinear damper, its derivative is given by:

$$\frac{\partial f_{di}}{\partial v_{di}} = \alpha_i c_{di} |v_{di}|^{\alpha_{di}-1} \quad (3.36)$$

where the velocity across of the i^{th} nonlinear damper v_{di} can be related to global velocity vector \mathbf{v} according to which two DOFs it is installed to. Once $\mathbf{F}'(\mathbf{a}_{n+1})$ is obtained, Newton's iteration is applied to obtain the converged solution for \mathbf{a}_{n+1}

$$\mathbf{a}_{n+1}^{k+1} = \mathbf{a}_{n+1}^k - [\mathbf{F}'(\mathbf{a}_{n+1}^k)]^{-1} \mathbf{F}(\mathbf{a}_{n+1}^k) \quad (3.37)$$

The displacement and velocity vectors can then be obtained by Eq. (3.29) and (3.30) once the acceleration vector \mathbf{a}_{n+1} is solved.

3.2.3 Development of MR Damper Element

Due to the complexity and highly nonlinear mechanical properties, MR damper is very difficult to simulate in the current available finite element softwares. UI_SimCor provides a versatile platform that allows Matlab to be used to model the MR dampers as substructure separately, and connect it to the main structure to perform the analysis. UI_SimCor adopts a time-stepping integration scheme, so any element that models history-dependent behavior should provide the response discretized in time domain.

The first attempt on modeling MR damper is performed by Dyke et al. (1996). The initial model, which combines Bouc-Wen equations proposed with a spring and dashpot in parallel, was sufficient enough to simulate dynamics of the prototype dampers by Lord Corp. As an extension of the simple Bouc-Wen model, Spencer et al. (1997) proposed a modified Bouc-Wen model where additional dashpot and spring elements were introduced with the aim to portray force-velocity characteristics of MR damper more accurately. The modified Bouc-Wen model is graphically illustrated in Fig. 3.5.

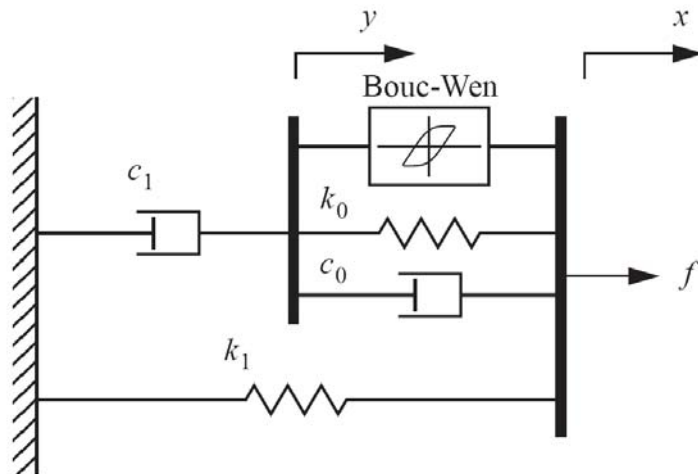


Fig. 3.5 Modified Bouc-Wen model for MR damper

The modified Bouc-Wen model can be expressed mathematically as:

$$f = c_1 \dot{y} + k_1(x - x_0) \quad (3.38)$$

$$\dot{y} = \frac{1}{c_0 + c_1} [\alpha z + c_0 \dot{x} + k_0(x - y)] \quad (3.39)$$

$$\dot{z}(t) = -\gamma |\dot{x} - \dot{y}| z |z|^{n-1} - \beta (\dot{x} - \dot{y}) |z|^n + A(\dot{x} - \dot{y}) \quad (3.40)$$

where f is the MR damper force; α , γ , β , A and n are the parameters for the built-in Bouc-Wen relation; c_0 , c_1 , k_0 and k_1 are coefficients for the linear dashpots and springs in the model. To work compatibly with UI_SimCor integration process, the above equations are converted into the incremental form by Euler's method.

$$f_{N+1} = c_1 \dot{y}_{N+1} + k_1(x_{N+1} - x_0) \quad (3.41)$$

$$y_{N+1} = y_N + dt \left(\frac{1}{c_0 + c_1} (\alpha z_N + c_0 \dot{x}_N + k_0(x_N - y_N)) \right) \quad (3.42)$$

$$z_{N+1} = z_N + dt \left[-\gamma |\dot{x}_N - \dot{y}_N| z_N |z_N|^{n-1} - \beta (\dot{x}_N - \dot{y}_N) |z_N|^n + A(\dot{x}_N - \dot{y}_N) \right] \quad (3.43)$$

$$\dot{y}_{N+1} = \frac{1}{c_0 + c_1} [\alpha z_{N+1} + c_0 \dot{x}_{N+1} + k_0(x_{N+1} - y_{N+1})] \quad (3.44)$$

A Matlab function based on Eq. (3.41)~(3.44) is developed as an element that provides the MR damper behaviour presented in Fig. 3.5. Note that the damper force at time t_{N+1} is essentially a function of x_{N+1} and \dot{x}_{N+1} , the damper displacement and velocity at t_{N+1} , which can be estimated by the predictor quantities of Eq. (3.29). Then the error is compensated with the α -OS integration process in UI_SimCor. This element takes in predictor displacement and velocity of MR damper as input and returns the updated MR damper force.

Before further application of this element, a numerical MR damper model based on ODE solver of Matlab is also developed and used to verify the accuracy of the above presented approach. Fig. 3.6 shows that the MR damper element proposed here yields the same results as ODE solver method, which validates the modelling approach.

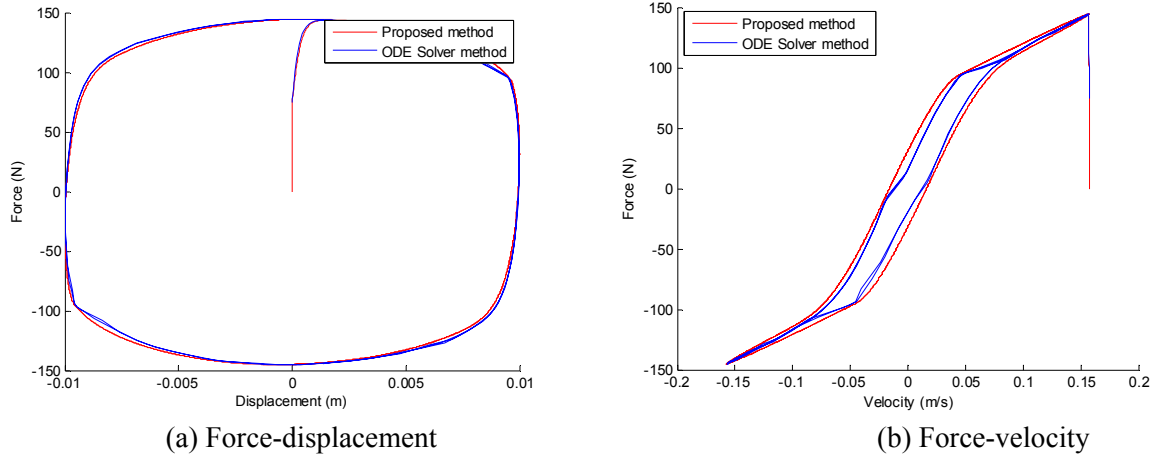


Fig. 3.6 Verification of proposed MR damper element with ODE solver in Matlab

3.3 Validation of Hybrid Numerical Simulation Scheme

To validate the hybrid numerical simulation scheme proposed above, i.e. modelling the main nonlinear structure in a major finite element (FE) software while modelling the seismic protective devices in another computational platform. In this study, OpenSees is chosen as the general FE software to model the nonlinear main structure, and Matlab is used to model the seismic protective devices as stated in section 3.2.

A three story nonlinear frame structure considered for numerical simulation and verification hereafter is shown in Fig. 3.7. This model represents a test structure located in Harbin Institute of Technology, China, which is tested for validating the hybrid numerical simulation scheme experimentally. Detailed description of the structure can be found in Chapter 4 of this study. The beams and columns in the frame are modelled by beam-column elements with bilinear force-displacement material property in OpenSees.

The following structural control strategies are adopted to investigate the structural responses under earthquake excitation: (i) linear viscous dampers are installed between floors; (ii) nonlinear viscous damper is installed between the first floor of the structure and outside fixture; (iii) base isolators are installed on the structure at the base level; and (iv) MR damper is installed between the first floor of the structure and outside fixture. Fig. 3.7 illustrates the

above control strategies for the structure to be analyzed. In implementing the hybrid simulation scheme for this structure, two effective DOFs are selected corresponding to each floor (6 DOFs in total). The equation of motion is solved with the modified integration algorithm in UI-SIMCOR described in section 3.2.

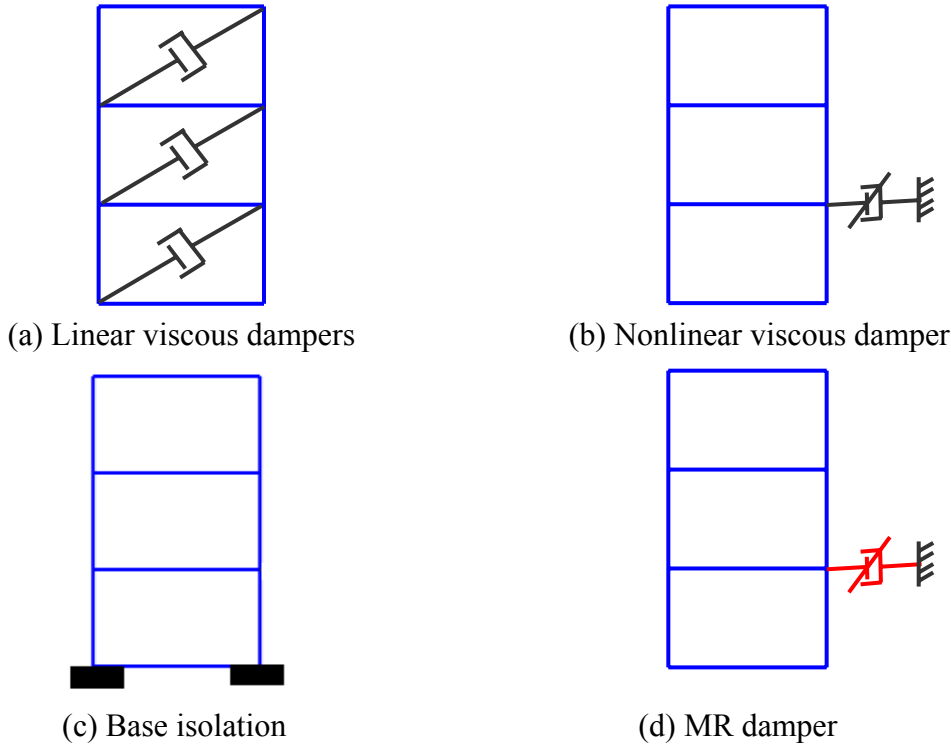


Fig. 3.7 Structural control strategies for numerical simulation and verification

The 1940 El-Centro earthquake record is used as the input ground motion for all the analysis reported here. For control strategies (i)~(iii), the dynamic structural response from the hybrid numerical simulation is compared with that of the whole OpenSees model, where both main structure and control devices are modelled in OpenSees. For control strategy (iv), preliminary experimental test result is used to verify the structural control by MR damper. This will be addressed in more details with a more complex model in Chapter 4.

3.3.1 Verification Case I: Linear Viscous Dampers Installed Between Floors

The structural response under control strategy (i) is shown in Fig. 3.8. It's seen that the

hybrid numerical simulation scheme works well with the linear viscous dampers as the seismic protective devices.

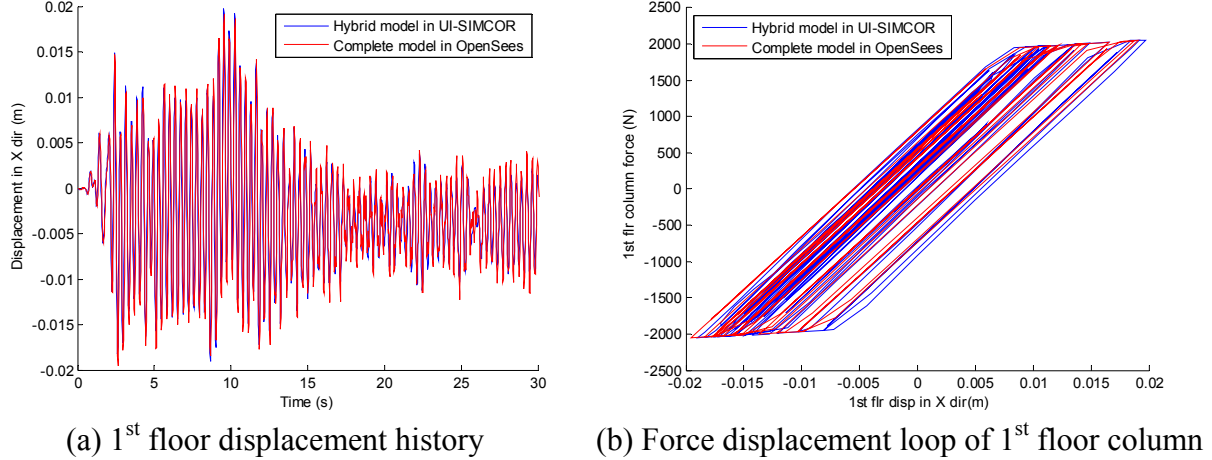


Fig. 3.8 Comparison of structural response under control by linear viscous dampers

3.3.2 Verification Case II: Nonlinear Viscous Damper Installed between First Floor and Outside Fixture

Nonlinear viscous damper is adopted as control device here. One nonlinear damper is installed at the first floor of the same structure. The structural response of the 1st floor and the nonlinear damper is plotted in Fig. 3.9. It shows that the proposed hybrid numerical simulation scheme yields fine results and comparable with the whole model in OpenSees.

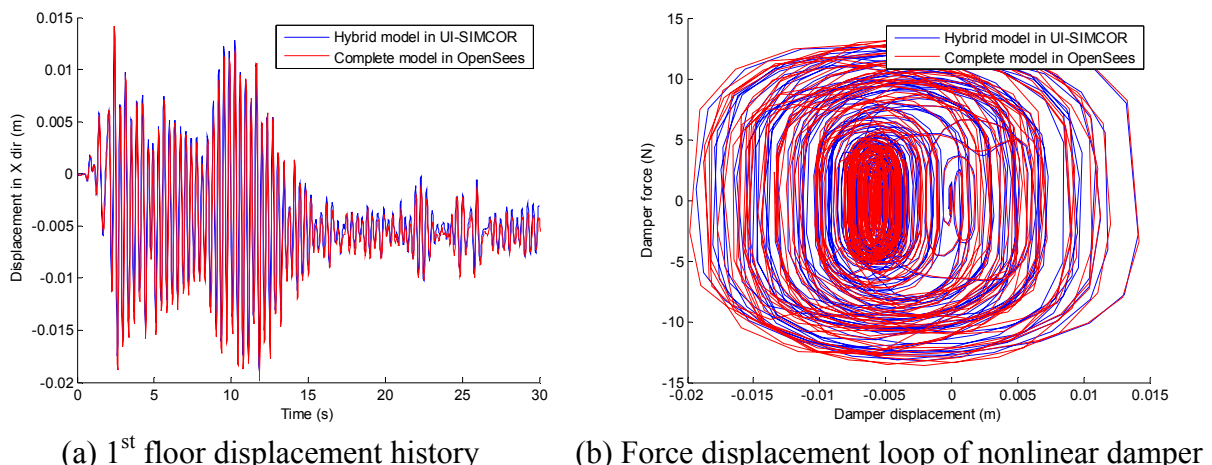


Fig. 3.9 Comparison of structural response under control by nonlinear viscous dampers

3.3.3 Verification Case III: Base Isolators Installed at Base Level of the Structure

The case study here shows the hybrid numerical simulation scheme can also accommodate the effects of base isolators well. Same structure as before is used and base isolators are installed under the 1st floor columns. The structural response shows base isolation effect could also be modeled well with the proposed method.

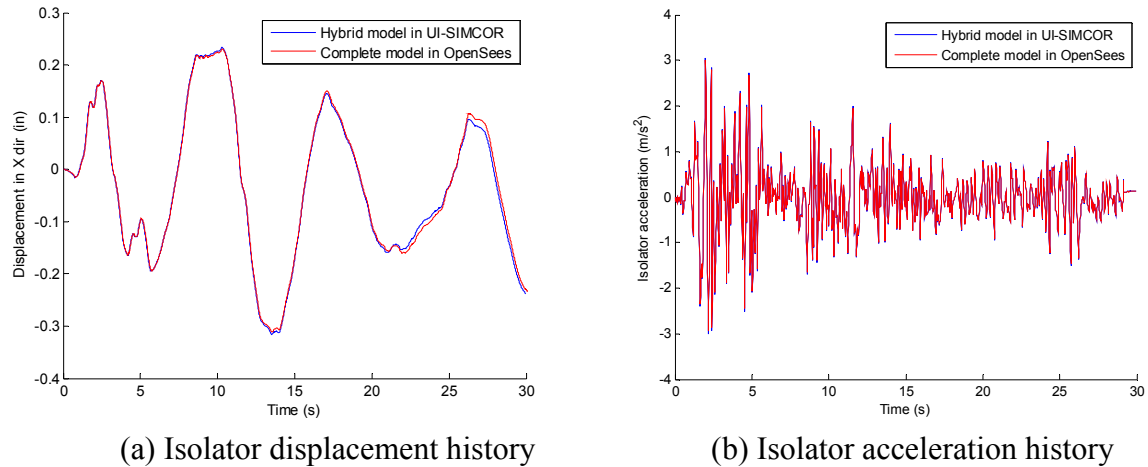
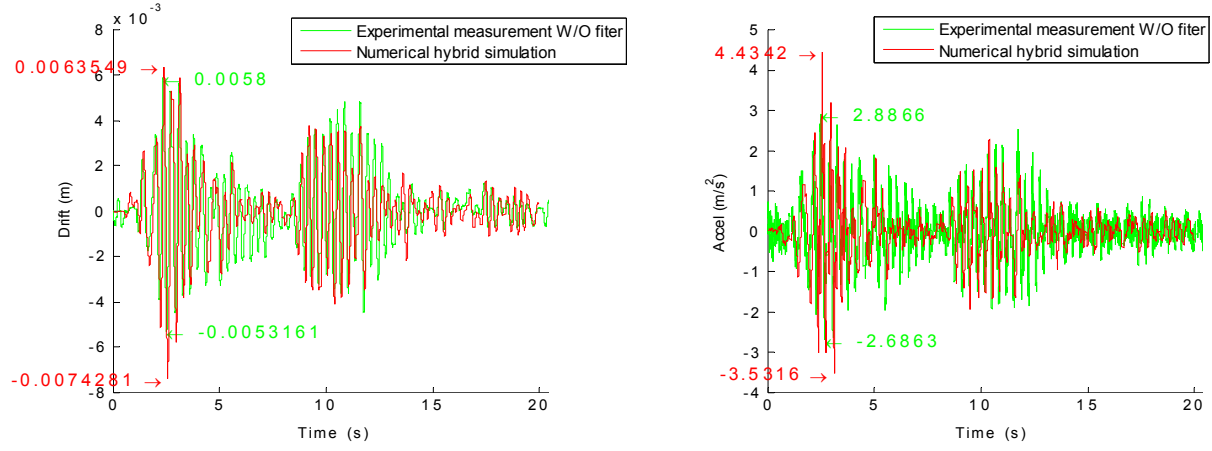


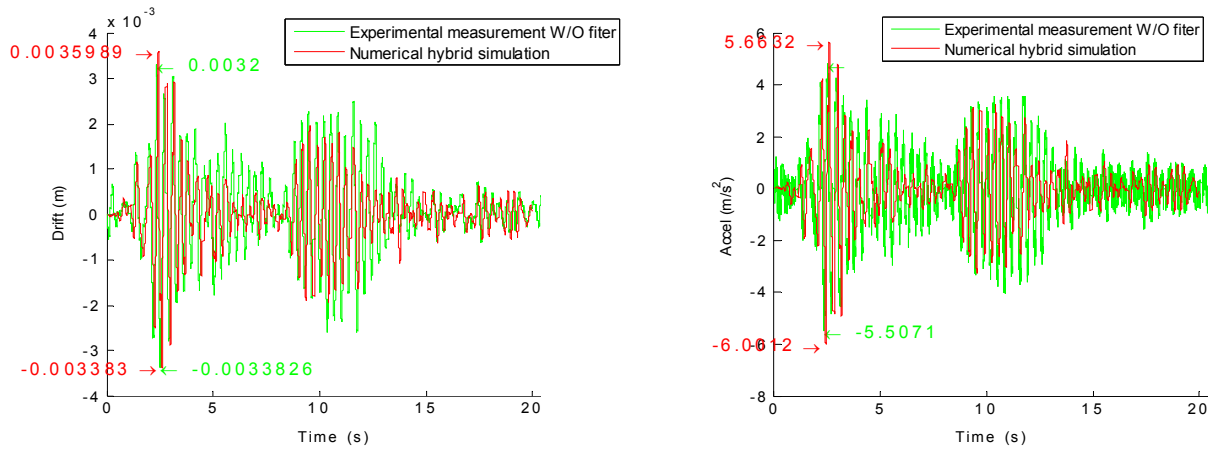
Fig. 3.10 Comparison of structural response under control by base isolation

3.3.4 Verification Case IV: MR Damper Installed between First Floor and Outside Fixture

MR dampers are widely used semi-active control devices in civil engineering structures. Under the hybrid numerical simulation scheme, MR dampers and corresponding control algorithm are easily modelled in Matlab. Passive-off (minimum current applied) and passive-on (maximum allowable current applied) control of the MR damper are implemented here as examples. The structural control responses of the 1st and 3rd floor are shown and compared with experimental results in Fig. 3.11 and 3.12.

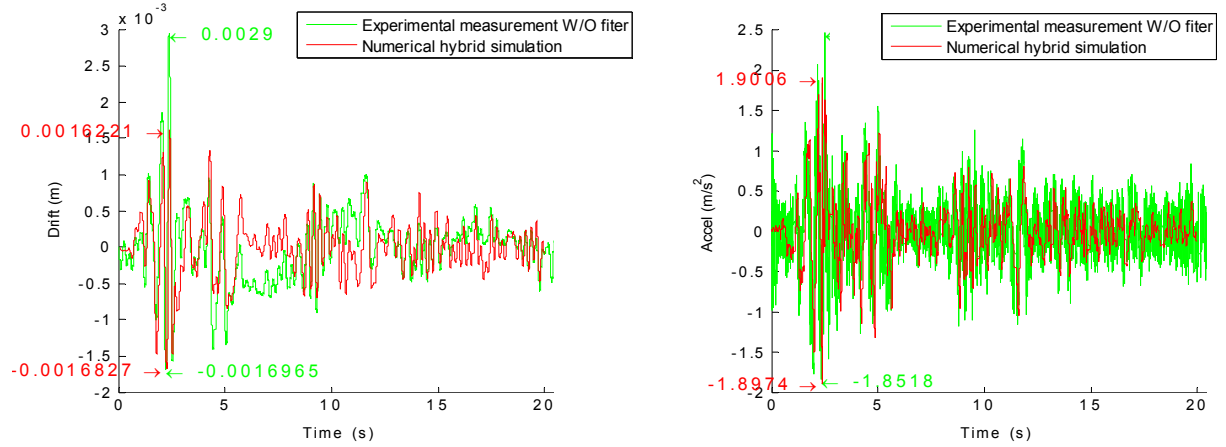


(a) 1st floor drift and absolute acceleration responses

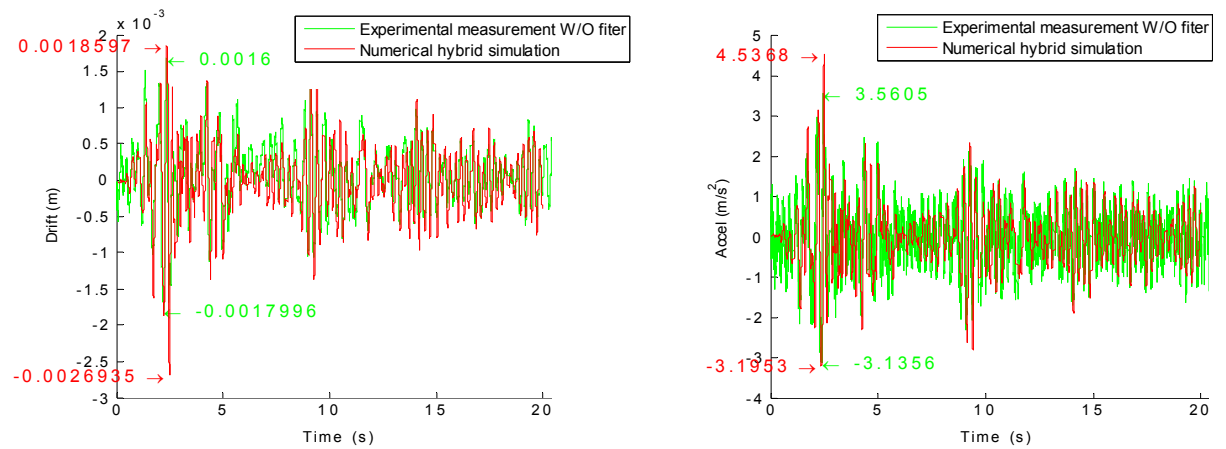


(b) 3rd floor drift and absolute acceleration responses

Fig. 3.11 Experimental verification of hybrid numerical simulation for MR dampers
(passive-off)



(a) 1st floor drift and absolute acceleration responses



(b) 3rd floor drift and absolute acceleration responses

Fig. 3.12 Experimental verification of hybrid numerical simulation for MR dampers
(passive-on)

3.4 Implementation of Structural Control Algorithm with Hybrid Numerical Simulation

In the hybrid simulation scheme stated above, the control devices are modeled separately in Matlab and control algorithms can be applied for the design of their parameters. A three-storey (3DOF) shear building model excited by earthquake motion is numerically analyzed (shown in Figure 3.13) and the active structural control is implemented using LQR theory. The goal is to obtain the stiffness and damping coefficients of the passive devices added to the structure that can provide the response reduction effect most close to that of the

active control method.

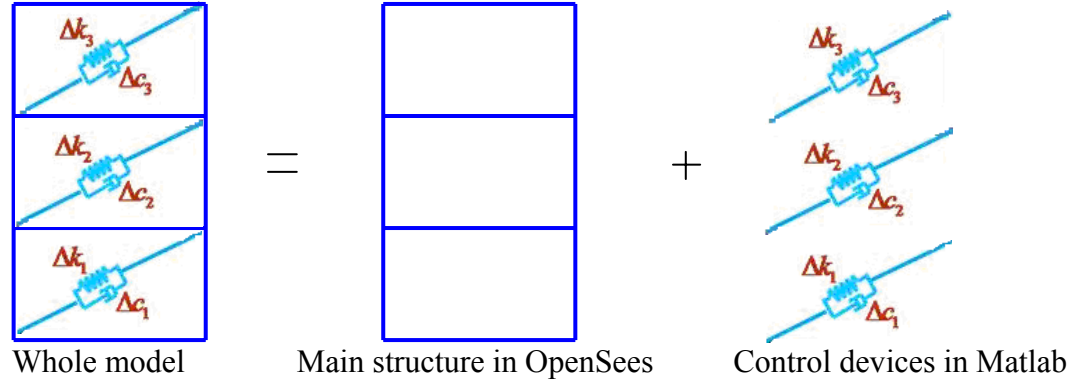


Fig. 3.13 Numerical example of structural control application with hybrid simulation

3.4.1 Classical Linear Optimal Control Theory (LQR)

In classical linear optimal control, the control force $\mathbf{u}(t)$ is chosen in such a way that a performance index J is minimized:

$$J = \int_0^{t_f} [\mathbf{z}^T(t) \mathbf{Q} \mathbf{z}(t) + \mathbf{u}^T(t) \mathbf{R} \mathbf{u}(t)] dt \quad (3.44)$$

where \mathbf{z} vector is the structural response in state space, \mathbf{Q} and \mathbf{R} are referred to as weighting matrices, whose magnitudes are assigned according to the relative importance attached to the state variables and control forces. The equation of motion with control forces applied in state space is:

$$\dot{\mathbf{z}}(t) = \mathbf{A}\mathbf{z}(t) + \mathbf{B}\mathbf{u}(t) + \mathbf{H}\mathbf{f}(t) \quad (3.45)$$

where \mathbf{A} is system matrix. \mathbf{B} and \mathbf{H} are location matrices specifying, respectively, the locations of the control forces and external excitations in the state space. $\mathbf{f}(t)$ is a vector representing external excitation. The optimal control force is given by:

$$\mathbf{u}(t) = \mathbf{G}\mathbf{z}(t) \quad (3.46)$$

The gain matrix \mathbf{G} is given by:

$$\mathbf{G} = -\frac{1}{2} \mathbf{R}^{-1} \mathbf{B}^T \mathbf{P} \quad (3.47)$$

and \mathbf{P} is the solution of Riccati equation:

$$\mathbf{A}^T \mathbf{P} + \mathbf{P} \mathbf{A} - \frac{1}{2} \mathbf{P} \mathbf{B} \mathbf{R}^{-1} \mathbf{B}^T \mathbf{P} + 2\mathbf{Q} = \mathbf{0} \quad (3.48)$$

3.4.2 Equivalent Optimal Passive Control Approximation

Equivalent optimal passive control theory uses LQR method in active control theory to design linear passive stiffness and damping devices (Gluck et al. 1996). The design is aimed at minimizing the difference between the control force from active control theory and those for passive control devices. By considering displacement and velocity feedback, both stiffness and damping devices are designed.

As stated in section 3.4.1, the active control forces are obtained as

$$\mathbf{u}(t) = \mathbf{G}\mathbf{z}(t) = [\mathbf{G}_x : \mathbf{G}_{\dot{x}}]\mathbf{z}(t) = \mathbf{G}_x \mathbf{x}(t) + \mathbf{G}_{\dot{x}} \dot{\mathbf{x}}(t) \quad (3.49)$$

where the gain matrix \mathbf{G} are decomposed to two sub-matrices \mathbf{G}_x and $\mathbf{G}_{\dot{x}}$ which correspond to the stiffness and damping information for the control devices. If the same control forces are supplied by passive devices and they are denoted by

$$\mathbf{u}^*(t) = \mathbf{K}_x \mathbf{x}(t) + \mathbf{C}_{\dot{x}} \dot{\mathbf{x}}(t) \quad (3.50)$$

where \mathbf{K}_x and $\mathbf{C}_{\dot{x}}$ are the matrices containing the stiffness and damping coefficients of the passive devices. Intuitively, the elements in \mathbf{K}_x and $\mathbf{C}_{\dot{x}}$ could be derived by elements in \mathbf{G}_x and $\mathbf{G}_{\dot{x}}$.

Applying the least square approximation to the difference between Equation (3.49) and (3.50), the stiffness and damping parameters of the diagonal control devices, Δk_i and Δc_i , can be determined by the following two approximation approaches.

(1) The response spectrum approach. It includes the influence of all or several modes of vibration relevant. In applications involving structures in earthquakes, sometimes only one mode of vibration is relevant. Then the control device design are governed by

$$\Delta k_i = \frac{\sum_j g_{ij,d} \varphi_{jm}}{\varphi_{im}}, \quad \Delta c_i = \frac{\sum_j g_{ij,d} \varphi_{jm}}{\varphi_{im}} \quad (3.51)$$

where φ is the mass normalized modal shapes. $g_{ij,d}$ and $g_{ij,\dot{d}}$ are elements in the transformation form of gain matrix in terms of interstory drift by multiplying the gain matrix with a transformation matrix \mathbf{T} :

$$\mathbf{G}_d = \mathbf{T}^T \mathbf{G}_x \mathbf{T}, \quad \mathbf{G}_{\dot{d}} = \mathbf{T}^T \mathbf{G}_{\dot{x}} \mathbf{T} \quad (3.52)$$

(2) Truncation approach. This is a much more simplified formulation obtained if only a single gain factor in gain matrix of active control is considered. Design parameters can be obtained directly from truncating all off-diagonal terms in the transformation form of gain matrix in terms of interstory drift. In such case

$$\Delta k_i = g_{ii,d}, \quad \Delta c_i = g_{ii,\dot{d}} \quad (3.52)$$

3.4.3 Numerical Results

A sample earthquake excitation (the 1940 El Centro record) is selected to conduct the time history analysis of structure equipped with the designed supplemental stiffness and damping. The relative displacement and total acceleration time histories are shown for different floors in Fig. 3.14 and 3.15 respectively. It is seen that the optimal passive control designs result in much better structural responses in terms of relative displacement and total acceleration than the uncontrolled case. Single mode design achieves close control effect as that of truncation design.

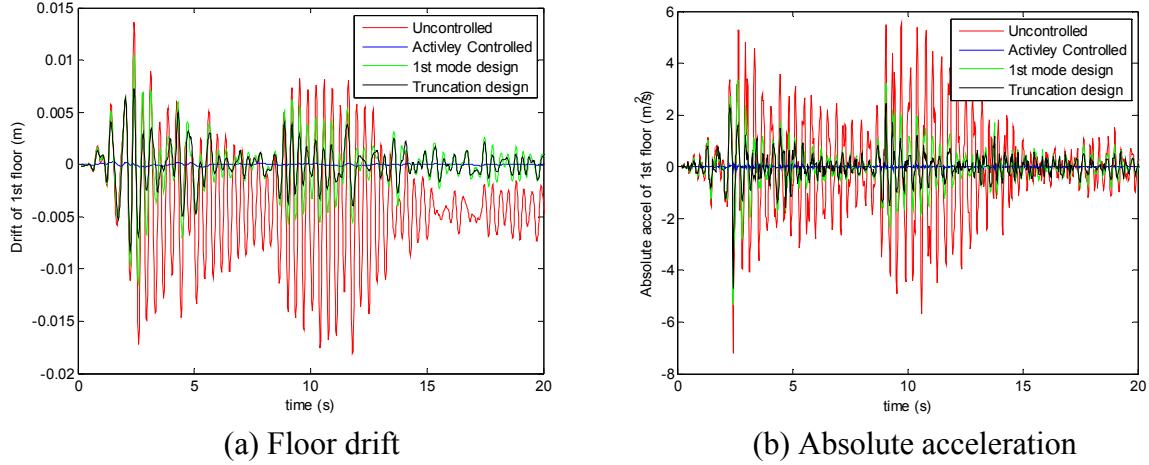


Fig. 3.14 Response history of 1st floor with different control designs

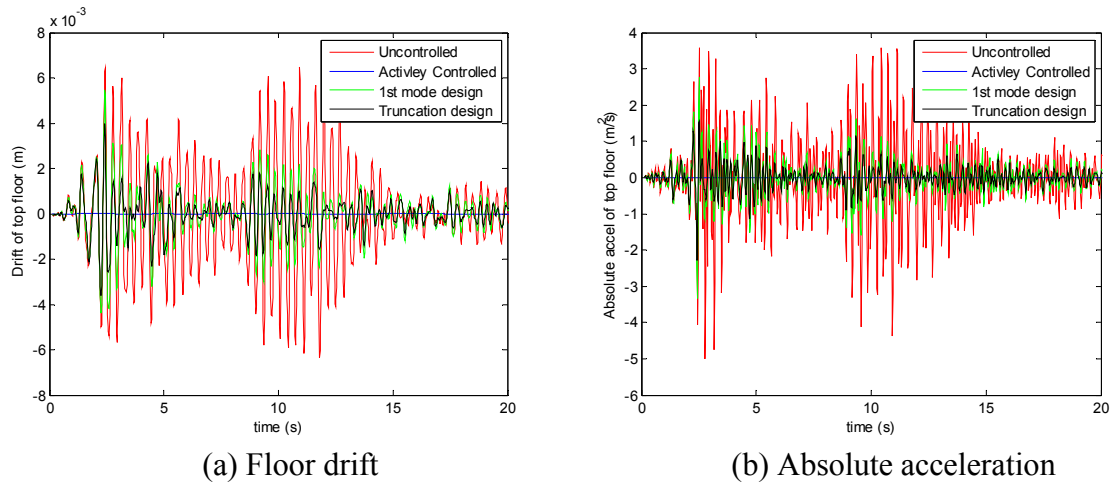


Fig. 3.15 Response history of top floor with different control designs

3.5 Concluding Remarks

This chapter explores using the proposed hybrid numerical simulation scheme to conduct structural control of nonlinear structures so as to derive the optimal passive stiffness and damping values to mimic the actively controlled devices.

In order to achieve this objective, existing hybrid simulation software (UI-SIMCOR) is adopted and modified to enable the integration algorithm to include nonlinear seismic protective devices such as nonlinear dampers, base isolation devices and MR dampers.

While the realistic behavior of nonlinear structures can be modeled separately in

current finite element analysis software package (e.g. OpenSees, ABAQUS etc.), the nonlinear seismic protective devices can be modeled in Matlab and pieced together through hybrid simulation to produce the most realistic overall structural responses. The control algorithms can also be easily implemented under this framework.

Using a real test structure equipped with various protection devices, the study demonstrated the accuracy and versatility of hybrid numerical simulation scheme. Furthermore, this leads to the easy application of different control algorithms that can yield the optimal selection of stiffness and damping values for control devices in design. The successful application of the hybrid numerical simulation scheme promotes its further practice on seismic protective device design for highway bridges.

4. Experimental Validation of Numerical Hybrid Simulation Scheme Based on UI_SimCor

To date, a number of smart structural control systems have been implemented in buildings and other civil engineering structures, either in a semi-active or active way. One of the most popular approaches is to use viscous fluid dampers for vibration reduction and energy dissipation, such as magneto-rheological (MR) dampers, which include smart mechanical and material components whose physical parameters can be modified in real-time through switching or on-off operations. Due to the variability and use of passive forces, semi-active control is becoming a promising technology of seismic hazard mitigation for civil engineering structures.

In order for optimal selection of design parameters of semi-active control devices, time history analysis of structures equipped with controllable devices needs to be performed first. However, the structural control of nonlinear structures cannot be easily conducted. Current typical finite element programs have various kinds of elements of modelling complex nonlinear structural components, but there are no well established elements for modelling control devices and applying control algorithms. Researchers have to write their own finite element code when there is a need to implement structural control technology, such as the work done in structural control benchmark problems (Agrawal et al. 2009; Nagarajaiah et al. 2008; Nagarajaiah et al. 2009).

UI_SimCor, which is originally developed for distributed hybrid testing, provides a promising way to overcome this obstacle in numerical modeling and analysis of semi-actively controlled nonlinear structures. Utilizing the hybrid simulation scheme based on UI_SimCor, the response of a complex nonlinear structure can be obtained by integrating various numerical and physical components as well as using different computational platforms, for example, the main structure is modeled in OpenSees while the seismic protective devices and

the control algorithm are implemented in Matlab. Individual substructures of the whole structure model can communicate and run simultaneously through the ‘data exchange and processing center’: UI_SimCor. By the hybrid simulation scheme proposed, the responses and structural control of complex nonlinear structures can be conducted. The results will further guide the selection of optimal passive parameters of semi-active control devices.

Experimental verification of UI_SimCor and associated numerical hybrid simulation methodology is needed before its further application, especially for analysis of semi-active control devices, because of the fact that there are not well established computational programs that can model a complex nonlinear structure while accurately implementing the semi-active control devices at the same time. In this chapter, real time hybrid simulation (RTHS) test and shake table test are performed to validate the novel approach utilizing the numerical hybrid simulation scheme based on UI_SimCor presented in Chapter 3.

RTHS is recognized as a powerful technique that offers the opportunity for global system evaluation of civil engineering structures to extreme dynamic loading. In this approach a physical portion of the structural system (e.g., a MR damper) is tested, while components of the structure that are well understood may be replaced with a computational model. This approach offers an alternative or enhancement to traditional shake table testing to evaluate global responses for earthquake inputs. Thus, it facilitates testing of larger and more complex structures.

On the other hand, shake table tests have been the “golden standard” by which structural systems are tested for dynamic input. This method provides the most realistic condition for physical structure, input excitation and real time response measurements. Shake table test could serve as mutual validation to RTHS as well.

In this study, both RTHS and shake table tests are performed for a 3 story steel frame structure controlled by a MR damper at Harbin Institute of Technology (HIT) in China. In

RTHS test, the MR damper would be isolated as the only physical component for experimental testing, while the steel frame structure and control algorithm are implemented in Matlab. In the shake table experiment, both the steel frame structure and the control device, i.e. a MR damper, are set up and tested realistically on a shake table. There are four tests introduced in this chapter: (i) System identification test; (ii) MR damper calibration test; (iii) RTHS test and (iv) Shake table test.

4.1 Basic Information

4.1.1 Experimental Structure

The prototype structure used in the test is a three-dimensional 3 story structure located at Harbin Institute of Technology (HIT), China, as shown in Fig. 4.1. The floor plan dimension is 1.84 m by 2.04 m. Each story is 1.2 m in height and the total height is 3.6 m. The columns, beams and girders of the structure are made of structural steel with an elastic modulus of 206 GPa and shear modulus of 78 GPa. The yielding point of the material is assumed to be 235 MPa with a post yielding ration of 0.02. All of the members are connected to each other with solid welds that do not allow free rotation.

The structure is braced in one direction (x-axis) at both sides with v-type braces as shown in Fig. 4.1, which causes the structure to be weak in y-axis and strong along x-axis. The columns are welded to 4 steel plates fixed to ground by 16 bolts, which could be taken as rigid base connection. At each story, a concrete slab weighting about 250 kg is attached as seismic mass. The total mass of the structure including the self-weight of the members is calculated to be 1066 kg. The mechanical and section properties of the columns, beams, girders and braces are all listed in Table 4.1 and 4.2.

For passive-off (minimum constant control voltage is applied to MR damper, usually 0V), passive-on (maximum constant control voltage is applied to MR damper, which is determined by the allowable current that flows through the MR damper) and semi-active

control tests, a MR damper is attached to the structure at first floor. A slight modification is performed at the first floor to connect the MR damper to the frame by adding a horizontal v-brace of the same size of girders in the plan of the floor. Thus, the beam, where the MR damper is attached, will have additional stiffness against deflection due to damper force. Fig. 4.2 shows detail of the v-brace and the whole structure with MR damper installed for passive and semi-active control tests. The additional mass from the v-braces is about 45 kg which makes the total mass of the structure about 1110 kg.

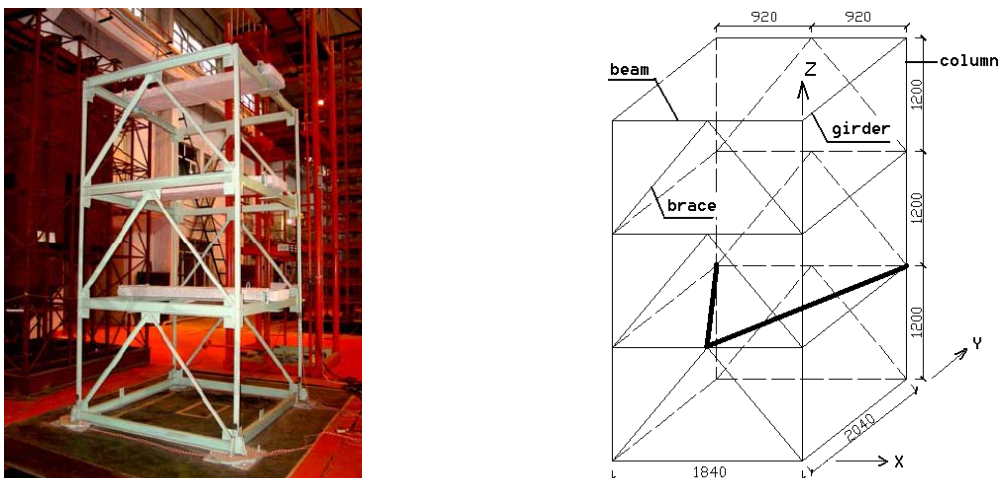


Fig. 4.1 Experimental structure

Table 4.1 Mechanical properties of experimental structure material

E (GPa)	G (GPa)	ν	Post-Yielding Ratio	Yielding Stress (MPa)	Density (g/cm ³)
206	78.63	0.31	0.02	235	7.85

Table 4.2 Section shapes and geometry properties of experimental structure

Beam and Girder					Column					Brace				
A cm ²	I _{X-X} cm ⁴	I _{Y-Y} cm ⁴	J cm ⁴	ρ Kg/m	A cm ²	I _{X-X} cm ⁴	I _{Y-Y} cm ⁴	J cm ⁴	ρ Kg/m	A cm ²	I _{X-X} cm ⁴	I _{Y-Y} cm ⁴	J cm ⁴	ρ Kg/m
12.74	198.3	25.6	223.9	10.0	4.44	10.2	10.2	20.4	3.487	2.31	3.59	3.59	7.20	1.814

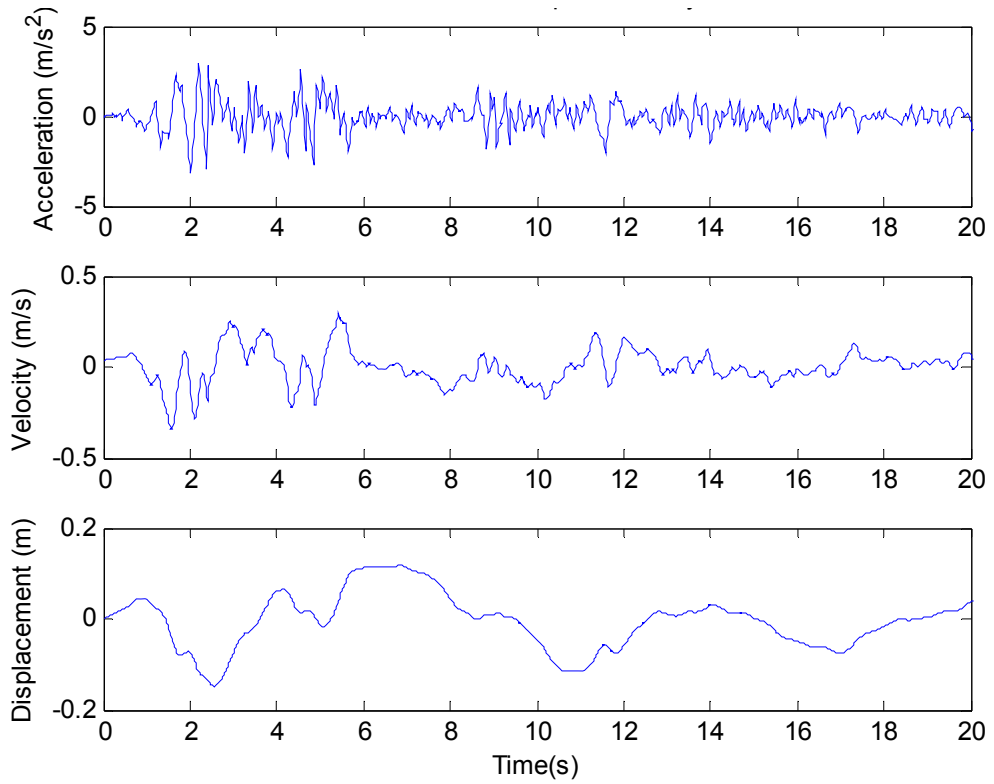


Fig. 4.2 MR damper installation configuration

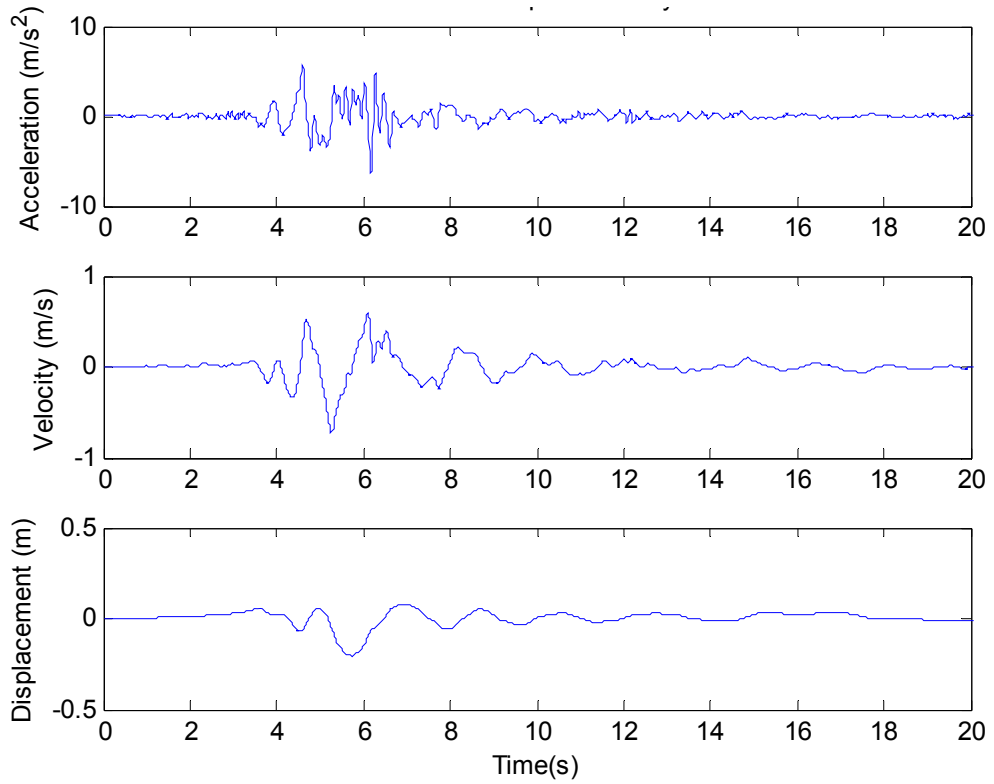
4.1.2 Earthquake Ground Motion Inputs

Three earthquake ground motions are selected for the dynamic testing and numerical analysis in this study, which are: (i) 1940 El-Centro earthquake record (North-South component, Peknold version). The instrument used was attached to the El Centro Terminal Substation Building's concrete floor. (ii) 1984 Gilroy Array #6 record (station 57383, G06) during Apr. 24, 1984 Morgan Hill earthquake. The original record is scaled/converted into fault-normal (FN) component which has an azimuth of 58 degrees. (iii) Takarazuka (TAZ) station record during the Jan. 16, 1995 Kobe earthquake. The original record is scaled/converted into fault-normal (FN) component which has an azimuth of 140 degrees.

El-Centro earthquake is the first major earthquake to be recorded by a strong-motion seismograph located next to a fault rupture. It has been widely used for research, engineering and education purpose. the other two records are also from near-fault shaking and chosen for their kinematic characteristic that can be captured by a pulse in velocity or acceleration. Time histories of the records are illustrated in Fig. 4.3.

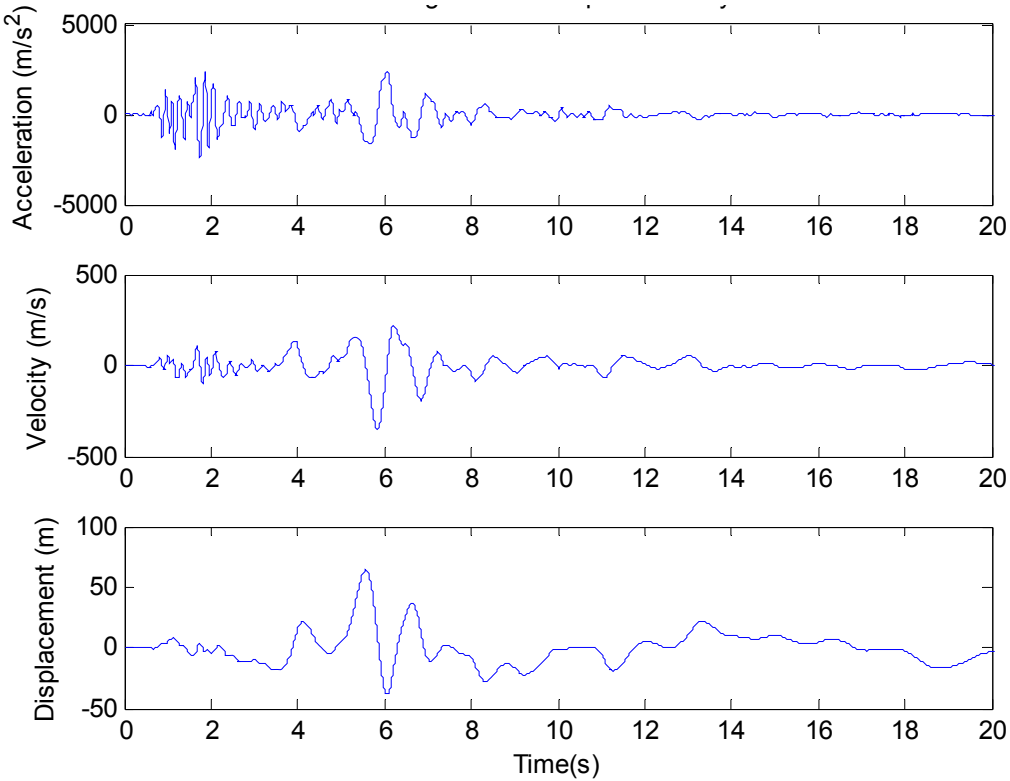


(a) 1940 El-Centro earthquake



(b) Takarazuka station record (1995 Kobe earthquake)

Fig. 4.3 Ground motions for experimental test and numerical simulation



(c) Gilroy Array #6 record (1984 Morgan Hill earthquake)

Fig. 4.3 (cont.) Ground motions for experimental test and numerical simulation

4.1.3 Three Dimensional Numerical Model in OpenSees

Based on the section properties and system identification results, a 3D finite element (FE) model is generated in OpenSees. The base of the structure is fixed in translational and rotational direction. The seismic mass including concrete mass and self-weight of the members is modeled in the software. The damping matrix is determined based on the Rayleigh damping with a modal damping ratio of 1.5%. Displacement based element ‘dispBeamColumn’ is adopted to simulate the structural components and each structural member is comprised of 10 elements. It’s considered as rigid for all the connections between beams, columns and foundation. All 6 DOFs of 1st floor columns are fixed at the base. Distributed mass is assigned along the structural elements, while lumped mass is put on the middle of the two beams which support the concrete slab on each floor. P-Delta effect is also included in the structural analysis. As for the structural nonlinear behaviour, bilinear

kinematic hardening with a post-yielding ratio 0.02 is assumed.

Fig. 4.4 summarizes the first 3 modal frequencies and mode shapes of the structure in the weak direction (y-axis) from the OpenSees 3D model. This finite element model built in OpenSees would be further calibrated and adjusted for use as a substructure of the numerical hybrid simulation method proposed in Chapter 3 to simulate the dynamic response of the experimental steel frame structure controlled by a MR damper. The RTHS and shake table tests of this chapter would be used as a solid validation of this numerical hybrid simulation scheme. Time history analysis of the 3D FE model is performed to predict the structural response beforehand such that reasonable and conservative input motions are determined for the shake table test to avoid any potential and unexpected damage to the structure by excessive shaking. Table 4.3 and 4.4 summarize the predicted maximum structural responses under the input motions that would be adopted in the shake table test.

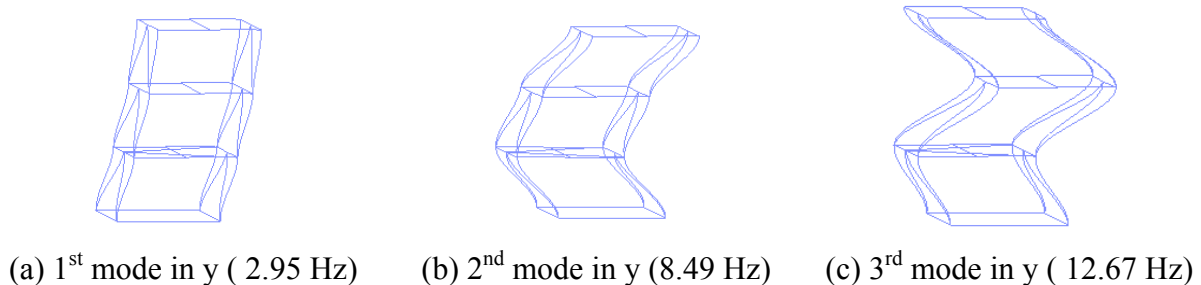


Fig. 4.4 Mode shape of the experimental structure by 3D FE model

Table 4.3 Maximum displacement responses

EQ Name	Scale factor	Max Floor Drift Ratio (%)						Max Top Rel. Disp(m)	
		1 st		2 nd		3rd			
		X	Y	X	Y	X	Y	X	Y
El-Centro	1	0.0017	1.5009	0.0018	1.1666	0.0014	0.7161	0.0001	0.0377
	0.5	0.0009	0.7175	0.0009	0.5921	0.0007	0.3694	0.0000	0.0186
	0.1	0.0002	0.1435	0.0002	0.1184	0.0001	0.0739	0.0000	0.0037
Morgan Hill	1	0.0012	1.0693	0.0012	0.8420	0.0009	0.4943	0.0000	0.0282
	0.5	0.0006	0.5346	0.0006	0.4208	0.0004	0.2468	0.0000	0.0141
	0.1	0.0001	0.1069	0.0001	0.0841	0.0001	0.0493	0.0000	0.0028
Kobe	1	0.0026	3.7604	0.0023	1.3698	0.0015	1.0273	0.0001	0.0652
	0.5	0.0013	1.4836	0.0012	1.2241	0.0008	0.7406	0.0000	0.0410
	0.1	0.0003	0.3185	0.0002	0.2685	0.0002	0.1506	0.0000	0.0087

Table 4.4 Maximum absolute acceleration responses

EQ Name	PGA (g)	Scale factor	Max Floor Absolute Acceleration (m/s^2)					
			1 st		2 nd		3rd	
			X	Y	X	Y	X	Y
El-Centro	0.3188	1	3.17	9.06	3.23	12.40	3.27	14.39
	0.1594	0.5	3.15	5.62	3.18	6.52	3.20	8.01
	0.03188	0.1	3.13	3.42	3.14	3.63	3.14	3.75
Morgan Hill	0.244	1	2.37	5.96	2.35	8.11	2.37	10.33
	0.122	0.5	2.38	3.64	2.37	4.68	2.37	5.52
	0.0244	0.1	2.39	2.41	2.39	2.52	2.38	2.59
Kobe	0.645	1	6.38	17.24	6.39	15.09	6.45	21.30
	0.3225	0.5	6.35	10.73	6.36	13.64	6.38	16.36
	0.0645	0.1	6.33	7.07	6.34	7.26	6.34	7.05

4.2 Theory Backgroud

4.2.1 Analytical Model and State Space Formulation of the Experimental Structure

For the experimental steel frame structure equipped with a MR damper and subjected to external earthquake excitation, the linear equation of motion can be written as:

$$\mathbf{M}\ddot{\mathbf{x}}(t) + \mathbf{C}\dot{\mathbf{x}}(t) + \mathbf{K}\mathbf{x}(t) = \boldsymbol{\Gamma}f(t) - \mathbf{M}\boldsymbol{\Lambda}\ddot{u}_g(t) \quad (4.1)$$

where \mathbf{M} , \mathbf{C} and \mathbf{K} are, respectively, the mass, damping and stiffness matrices; $\mathbf{x}(t) = [x_1, x_2, \dots, x_n]^T$ is the n -dimensional relative displacement vector where n is the number of degree of freedom (DOF) of the structure; $f(t)$ is the control force from MR damper and $\ddot{u}_g(t)$ represents the external earthquake excitation. The $n \times 1$ vector $\boldsymbol{\Gamma}$ is the location matrix which defines the location of MR damper, and $\boldsymbol{\Lambda}$ is the influence vector of the external earthquake excitation which also has the dimension of $n \times 1$. Since the mass of the experimental steel frame is concentrated on each floor of the structure and the frame is relatively weak in one axis (no bracing in y direction), as shown in Fig. 4.1, it's reasonable to simplify the steel frame to be a 3DOF structure. Thus the \mathbf{M} , \mathbf{C} and \mathbf{K} could be expressed in the following form:

$$\mathbf{M} = \begin{bmatrix} m_1 & 0 & 0 \\ 0 & m_2 & 0 \\ 0 & 0 & m_3 \end{bmatrix}, \quad \mathbf{C} = \begin{bmatrix} c_1 + c_2 & -c_2 & 0 \\ -c_2 & c_2 + c_3 & -c_3 \\ 0 & -c_3 & c_3 \end{bmatrix}, \quad \mathbf{K} = \begin{bmatrix} k_1 + k_2 & -k_2 & 0 \\ -k_2 & k_2 + k_3 & -k_3 \\ 0 & -k_3 & k_3 \end{bmatrix} \quad (4.2)$$

where the components in \mathbf{M} and \mathbf{K} matrices are computed based on the material and section properties listed in Table 4.1 and 4.2. The \mathbf{C} matrix can be evaluated by classical mass and stiffness proportional damping, such as Rayleigh damping. $\boldsymbol{\Gamma}$ and $\boldsymbol{\Lambda}$ vector are also simplified in this case:

$$\boldsymbol{\Gamma} = [-1 \ 0 \ 0]^T, \quad \boldsymbol{\Lambda} = [1 \ 1 \ 1]^T \quad (4.3)$$

Rewrite Eq. (4.1) with state-space formulation:

$$\dot{\mathbf{z}}(t) = \mathbf{A}\mathbf{z}(t) + \mathbf{B}f(t) + \mathbf{E}ii_g(t) \quad (4.4)$$

where

$$\mathbf{z}(t) = \begin{bmatrix} \mathbf{x}(t) \\ \dot{\mathbf{x}}(t) \end{bmatrix}, \quad \mathbf{A} = \begin{bmatrix} \mathbf{0} & \mathbf{I} \\ -\mathbf{M}^{-1}\mathbf{K} & -\mathbf{M}^{-1}\mathbf{C} \end{bmatrix}, \quad \mathbf{B} = \begin{bmatrix} \mathbf{0} \\ \mathbf{M}^{-1}\boldsymbol{\Gamma} \end{bmatrix}, \quad \mathbf{E} = -\begin{bmatrix} \mathbf{0} \\ \boldsymbol{\Lambda} \end{bmatrix} \quad (4.5)$$

The structural measurements utilized to compute the optimal control force of MR damper include the absolute accelerations of the three floors of the structure, and the displacement of the MR damper which equals to the 1st floor relative displacement according to the structural configuration in Fig. 4.2, i.e. the measurement vector equals to

$$\mathbf{y} = [\ddot{x}_{a1} \ \ddot{x}_{a2} \ \ddot{x}_{a3} \ x_1] \quad (4.6)$$

where the subscript ‘a’ stands for ‘absolute’. \mathbf{y} can also be written in state space form:

$$\mathbf{y}(t) = \mathbf{C}_m \mathbf{z}(t) + \mathbf{D}f(t) \quad (4.7)$$

where

$$\mathbf{C}_m = \begin{bmatrix} -\mathbf{M}^{-1}\mathbf{K} & -\mathbf{M}^{-1}\mathbf{C} \\ 1 & 0 & 0 & 0 & 0 & 0 \end{bmatrix}, \quad \mathbf{D} = \begin{bmatrix} \mathbf{M}^{-1}\boldsymbol{\Gamma} \\ 0 \end{bmatrix} \quad (4.8)$$

Eq. (4.4) and (4.7) together define a plant for classical control problem:

$$\begin{cases} \dot{\mathbf{z}}(t) = \mathbf{A}\mathbf{z}(t) + \mathbf{B}f(t) + \mathbf{E}\ddot{u}_g(t) \\ \mathbf{y}(t) = \mathbf{C}_m\mathbf{z}(t) + \mathbf{D}f(t) \end{cases} \quad (4.9)$$

4.2.2 Semi-active Control Algorithm of the Experimental Structure Controlled by A MR Damper

The optimal control force from MR damper is derived in such a way that the following performance index is minimized:

$$J = \int_0^{t_f} [\mathbf{y}^T(t)\mathbf{Q}\mathbf{y}(t) + r f^2(t)] dt \quad (4.10)$$

where \mathbf{Q} and r are the weighting quantities for measured structural response and control force given by MR damper, respectively. The time interval $[0, t_f]$ is defined to be longer than that of the external excitation duration. The optimal control force is calculated by:

$$f(t) = -\mathbf{K}_c \mathbf{z}(t) \quad (4.11)$$

where $f(t)$ is the desired optimal force, and \mathbf{K}_c is the control gain matrix which can be computed by the command ‘lqry’ of Matlab control toolbox:

$$\mathbf{K}_c = \text{lqry}(\mathbf{A}, \mathbf{B}, \mathbf{C}_m, \mathbf{D}, \mathbf{Q}, r) \quad (4.12)$$

It's note that the full internal states, $\mathbf{z}(t)$, are need to estimate the optimal control force in Eq. (4.11). But it is hard to measure such states in reality due to instrumentation limitation. Fortunately, unobserved internal states can be restored with the help of observed states $\mathbf{y}(t)$ with a Kalman estimator (Kalman 1960). The estimation of the full internal states is governed by

$$\dot{\hat{\mathbf{z}}}(t) = \hat{\mathbf{A}}\hat{\mathbf{z}}(t) + \hat{\mathbf{B}}\mathbf{Y} \quad (4.13)$$

where

$$\hat{\mathbf{A}} = \mathbf{A} - \mathbf{L}\mathbf{C}_m, \quad \hat{\mathbf{B}} = [\mathbf{L} \quad \mathbf{B} - \mathbf{L}\mathbf{D}], \text{ and } \mathbf{Y} = [\mathbf{y}(t); f(t)] \quad (4.14)$$

where Kalman estimator gain matrix \mathbf{L} can be calculated by the command ‘lqew’ of Matlab control toolbox :

$$\mathbf{L} = \text{lqew}(\mathbf{A}, \mathbf{E}, \mathbf{C}_m, \mathbf{0}, \mathbf{w}, \mathbf{v}) \quad (4.15)$$

where \mathbf{w} and \mathbf{v} are the disturbance covariance matrix and measurement noise covariance matrix, respectively. With the state estimator $\hat{\mathbf{z}}(t)$ obtained, one can calculate the optimal control force by:

$$f_c(t) = -\mathbf{K}_c \hat{\mathbf{z}}(t) \quad (4.16)$$

However, the force generated by the MR damper cannot be controlled directly. A control algorithm needs to be implemented to make MR damper approximately produce the optimal control force. Clipped optimal control proposed by Dyke et al. (1996) is adopted here. Clipped optimal control compares the sign of the desired force and the measured force of MR damper and applies maximum voltage if the signs match, otherwise sets voltage to zero, as expressed in Eq. (4.17):

$$v = V_{\max} H\{(f_c - f) f\} \quad (4.17)$$

where v is command voltage of MR damper, V_{\max} is the maximum allowable voltage and $H\{\bullet\}$ is the Heaviside step function.

4.2.3 Eigensystem Realization Algorithm (ERA) for System Identification

To construct the state space matrices given in Eq. (4.9) and apply semi-active control algorithm, \mathbf{M} , \mathbf{C} and \mathbf{K} matrices need to be first estimated, either from the simplified 3DOF model presented in section 4.2.1 or derived from experimental data of system identification test. Considering the fact that discrepancies between the estimations and experimental data are often evident, implementing a system identification that reveals dynamic properties of the structure is essential.

For this study, a commonly used time-domain approach, Eigensystem Realization Algorithm (ERA) is selected. The success of this algorithm has been verified in multiple studies (Caicedo 2011; Caicedo et al. 2004; Giraldo et al. 2004). Juang and Pappa (1985) proposed ERA to extract modal parameter and create a minimal realization model that

replicates the output response of a linear dynamical system when it is subjected to a unit impulse. The ERA procedure can be summarized in four steps. They are: (i) Hankel matrix assembly, (ii) singular value decomposition, (iii) state-space realization and (iv) eigenvalue extraction.

In general, the impulse response of a linear system can be represented by a discrete-time representation of state space formulation with n -dimensional state vector, \mathbf{z} , m -dimensional control input, \mathbf{u} and p -dimensional measurement vector, \mathbf{y} :

$$\begin{cases} \mathbf{z}(k+1) = \mathbf{A}\mathbf{z}(k) + \mathbf{B}\mathbf{u}(k) \\ \mathbf{y}(k) = \mathbf{C}_m\mathbf{z}(k) \end{cases} \quad (4.19)$$

where \mathbf{A} is $n \times n$ matrix, \mathbf{B} is $n \times m$ matrix and \mathbf{C}_m is $p \times n$ matrix. The matrix impulse response, known as Markov parameter sequence, can be derived from Eq (4.19):

$$Y(k) = \mathbf{C}_m \mathbf{A}^{k-1} \mathbf{B} \quad (4.20)$$

where $Y(k)$ is $p \times m$ matrix and $Y_{ij}(k)$ is i^{th} output to j^{th} input at time step k .

(i) Hankel matrix assembly

As the first step of the ERA algorithm, Hankel matrix for a time step k is formed:

$$H(k-1) = \begin{bmatrix} Y(k) & Y(k+1) & \cdots & Y(k+s) \\ Y(k+1) & Y(k+2) & \cdots & Y(k+s+1) \\ \vdots & \vdots & \ddots & \vdots \\ Y(k+r) & Y(k+r+1) & \cdots & Y(k+s+r) \end{bmatrix} \quad (4.20)$$

For a typical application, r , row of $H(k-1)$ matrix should be at least 10 times the modes to be identified and s , column of $H(k-1)$ should be 2-3 times of r .

(ii) Singular value decomposition

A singular value decomposition is performed using $H(0)$:

$$H(0) = P D Q^T \quad (4.20)$$

where P , Q and D are obtained by singular value decomposition. P is $rp \times n$, Q is $ms \times n$ and D is $n \times n$ diagonal matrix.

(iii) State-space realization

By integrating P , D , Q and $H(k)$, a minimum realization of the identified system in Eq (4.19) can be derived in state space form:

$$\begin{aligned}\mathbf{A} &= D^{-1/2} P^T H(1) Q D^{-1/2} \\ \mathbf{B} &= D^{1/2} Q^T E_m \\ \mathbf{C}_m &= E_p^T P D^{1/2}\end{aligned}\quad (4.21)$$

where $E_p = [I_m \ 0]^T$ and $E_m = [I_m \ 0]^T$.

(iv) Eigenvalue extraction

Natural frequencies, damping ratios and mode shapes can be obtained by applying eigen-decomposition on state matrix, \mathbf{A} , as given in Eq. (4.21). A typical way to obtain the identified parameters is prescribed below:

$$\begin{aligned}[\nu, \lambda] &= \text{eig}(\mathbf{A}) \\ s &= \ln(\lambda) f_s \\ f_{dE} &= \frac{\Im(s)}{2\pi} \\ \xi_E &= \frac{\Re(s)}{|s|} \\ \Phi_E &= E_p^T P D^{1/2} \nu\end{aligned}\quad (4.22)$$

Where ν and λ are eigenvectors and eigenvalues of the system in z-plane (complex plane) since state A is in discrete-time form, f_s is the sampling rate of the system in Hz, s is the Laplace root of the system converted from z-plane, f_{dE} , ξ_E and Φ_E are experimental damped frequency in Hz, damping ratio and complex mode shape, respectively. The experimental natural frequency of the system can be obtained by

$$f_{nE} = \frac{f_{dE}}{\sqrt{1 - \xi_E^2}} \quad (4.20)$$

Most of the above calculations are automated by ‘*damp*’ function in Matlab.

It's note that mode shapes Φ_E here is complex-valued. However the later model

updating process requires real mode shapes (section 4.2.4). A transformation from complex to real mode shape is needed and it should maintain the original information of the identified complex mode shape to conserve dynamic characteristic of the test structure as much as possible (Panichacarn 2006). A rotation transformation is applied to minimize the error between real and complex mode shapes:

$$\Phi_{E,rotate}(:,i) = \frac{\Phi_E(:,i)}{\Phi_E(1,i)} \quad (4.21)$$

$$\Phi_{E,real}(:,i) = sign(\Re(\|\Phi_{E,rotate}(:,i)\|)) \odot \|\Phi_{E,rotate}(:,i)\| \quad (4.22)$$

where $\Phi_{E,rotate}$ is the rotated complex mode shape, and $\Phi_{E,real}$ is the computed real mode shape. Eq. (4.21) is essentially a rotation transformation where $\Phi_E(:,i)$ is normalized with respect to its first element. The procedure here minimizes the imaginary part of the complex mode shape such that Eq. (4.22) is able to produce the real values with a minimal error, i.e. dynamic characteristics of the test structure is conserved. This rotation transformation is intuitively shown in Fig. 4.5

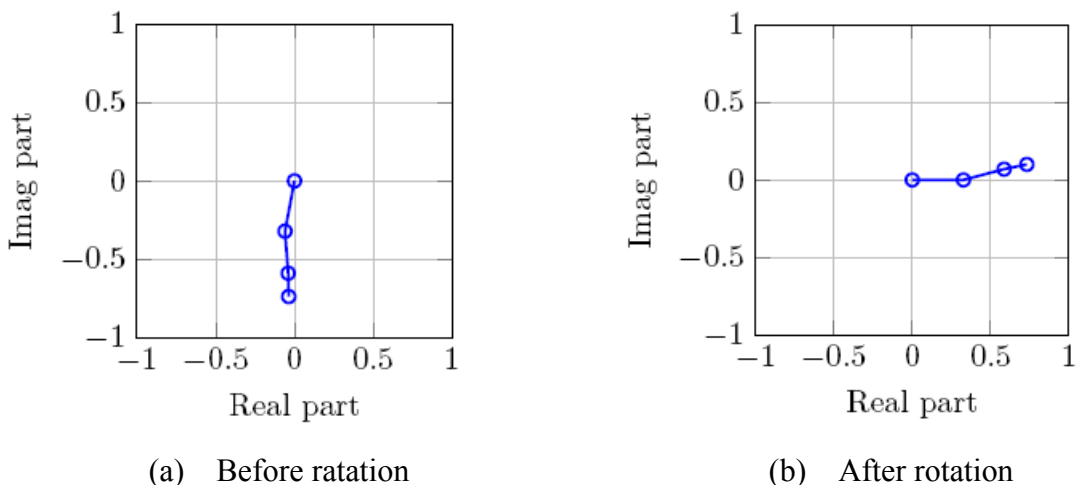


Fig. 4.5 Effect of rotation transformation

4.2.4 Analytical Model Updating of Experimental Structure Based on System Identification

As discussed in the previous section, a state space realization of the structure can be

obtained using ERA procedure based on measured quantities. This state space representation also contains dynamic characteristics of the identified structure, i.e. natural frequencies, damping ratios and mode shapes. However, the ERA-obtained states do not contain any physical information of the structure that is not measured. Consequently, a feedback control algorithm cannot be developed since unmeasured structural responses remain unobservable. To overcome this shortcoming of ERA, Giraldo et al. (2004) proposed a model updating method where experimental results are combined with the analytical model. According to this approach, the stiffness and damping matrices are updated using identified natural frequencies damping ratios and mode shapes as given below:

$$K_E = M_A \Phi_{E,real} [2\pi f_{nE}] \Phi_{E,real}^T \quad (4.23)$$

$$C_E = M_A \Phi_{E,real} [2\xi_E (2\pi f_{nE})] \Phi_{E,real}^T \quad (4.24)$$

where K_E and C_E are updated stiffness and damping matrices based on analytical mass matrix M_A that is proposed in section 4.2.1. In most cases, $\Phi_{E,real}$ is not M_A -orthogonal, i.e. $\Phi_{E,real}^T M_A \Phi_{E,real} \neq \mathbf{I}$, thus resultant K_E and C_E are not symmetric. This asymmetry does not comply with the Maxwell's Reciprocal Theorem. Therefore the analytical mass matrix M_A needs to be modified such that the updated mass matrix can be diagonalized by $\Phi_{E,real}$. M_E can be obtained by minimizing the quadratic error between M_A and M_E as given below:

$$\min \left[\text{vec}(M_E - M_A)^T \mathbf{W} \text{vec}(M_E - M_A) \right] \quad (4.25)$$

subject to

$$\Phi_{E,real}^T M_E \Phi_{E,real} = \mathbf{I} \quad (4.26)$$

where vec is the vectorization operation and \mathbf{W} is the weighting matrix which can be adjusted to give more weight to the elements in $\text{vec}(M_E - M_A)$ that needs to be minimized.

At last, by replacing M_A in Eq. (4.23) and (4.24) with M_E , the complete set of updated mass, stiffness and damping matrices are obtained, i.e. the analytical model of the experimental structure is updated and enhanced by the knowledge from system identification such that it can best represent the real structure for dynamic analysis and simulation.

$$K_E = M_E \Phi_{E,real} [2\pi f_{nE}] \Phi_{E,real}^T \quad (4.27)$$

$$C_E = M_E \Phi_{E,real} [2\xi_E (2\pi f_{nE})] \Phi_{E,real}^T \quad (4.28)$$

4.3 Test Setup and Procedure

4.3.1 System Identification Test

A accurate numerical model is critical for structural control design and RTHS test to obtain the correct prediction of the system performance. A model that could accurately reflect the behavior of the physical experimental structure is needed to minimize the errors between the dynamics of the numerical model and the actual structure for a convincing RTHS test. Typically, models are constructed based on the design specifications and known mechanical properties, however, due to irregularities in material and flaws in construction, a model generated from these quantities may not reflect the real structure in the laboratory. In this sense, system identification could provide an accurate numerical model that could be used for structural control design and RTHS purpose, also as a standard to calibrate numerical models generated from traditional FEM modeling methods.

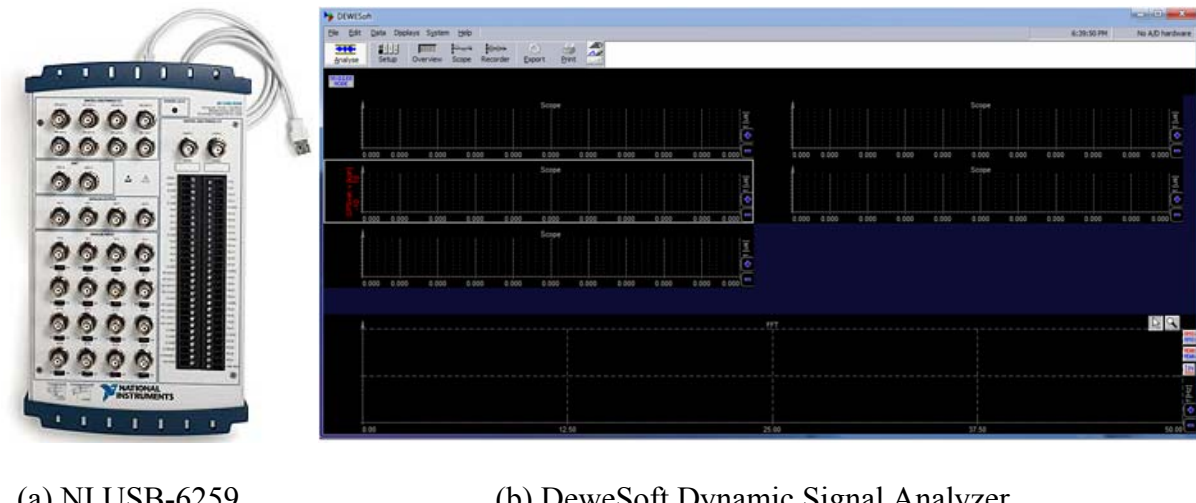
The Eigensystem realization algorithm (ERA) is one of the well established methods to perform system identification, from which a complete mathematical model can be obtained based on the measured data of the hammer test. Using ERA, natural frequencies and mode shapes can be obtained from experimentally produced impulse data.

A system identification test is proposed for the ERA procedure. The test plan consists of the following steps: (i) exciting the test specimen with an impact hammer at predetermined

locations, (ii) obtaining the responses from accelerometers that are placed on the structure at various places, the forces measured by the hammer and revealing transfer function between the output response and input excitation, (iii) developing high quality impulse response functions and (iv) identifying frequencies and mode shapes by applying ERA to impulse functions.

(1) DAQ System

To acquire system identification data of the test structure, NI USB-6259, a multi-functional data acquisition system box made by National Instruments is employed as shown in Fig. 4.6(a). The DAQ system has the capability to sample data up to 1.25MHz rate from 16 differential analog input channels at 16 bit analogto-digital conversion resolution. The data acquired online from DAQ system is transmitted over USB 2.0 to a Dell Inspiron 1720 notebook to be processed by DeweSoft Dynamic Signal Analyzer v6.6 developed by DeweSoft as shown in Fig. 4.6(b).



(a) NI USB-6259

(b) DeweSoft Dynamic Signal Analyzer

Fig. 4.6 DAQ system and data processing software

(2) Instrumentation

The one-hand operatable modally tuned impact hammer used in the tests is made by Jiangsu Lianneng Electronic Technology Limited Corporation with a model #LC-01A from

Sinocera Piezotronics branch as shown in Fig. 4.7. The hammer is equipped with a charge type load cell with model #CL-YD-303 and a rubber tip on it. All together, hammer is rated to generate maximum thrust of 2 KN.

Charge-type accelerometers produced by Brüel & Kjær model #4368 with a flat frequency response between 0.2 Hz and 4800 Hz are used to measure acceleration response (Fig. 4.8(a)). Table 4.5 lists the information of the accelerometers used here.

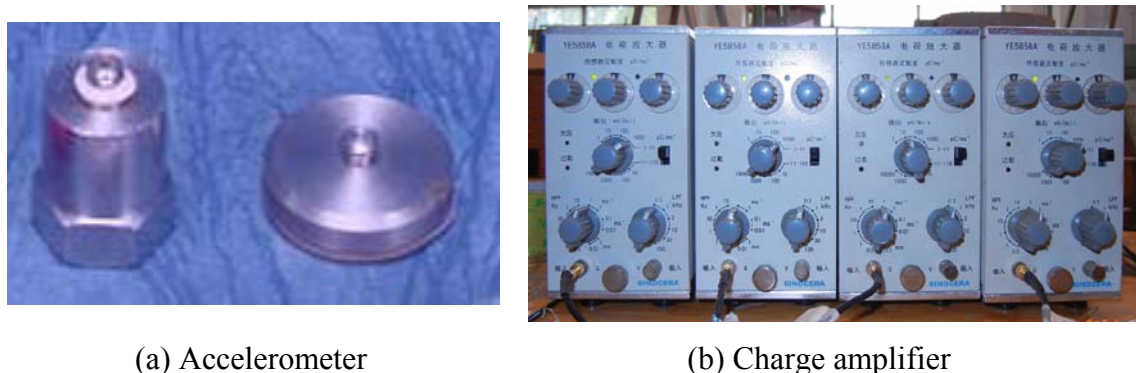
Table 4.5 Information of accelerometers

Sensor # in test	Brand - serial #	Charge Sensitivity	Output Unit
S5	Brüel & Kjær model #4368 - serial #0956116	4.52 pc/m s ⁻²	cm/s ²
S4	Brüel & Kjær model #4368 - serial #0956117	4.46 pc/m s ⁻²	cm/ s ²
S1	Brüel & Kjær model #4368 - serial #0956119	4.44 pc/m s ⁻²	cm/ s ²
S2	Brüel & Kjær model #4368 - serial #0956120	4.46 pc/m s ⁻²	cm/ s ²
S6	Brüel & Kjær model #4368 - serial #0956121	4.36 pc/m s ⁻²	cm/ s ²

The acceleration sensors and impact hammer are powered with signal conditioners capable of producing velocity and displacement by integration, belonging to Sinocera Piezotronics branch with mode #YE5858A (Fig. 4.8(b)), which is based on Brüel & Kjær's model #2635 charge amplifier. The amplifier has selectable dial gains, high-pass filter ranging from 0.3 Hz to 10 Hz for acceleration measurements and a low pass filter from 300 Hz to 100000 Hz (wide-band). All filters attenuate maximum 3 dB at the cutoff frequency during normal operation conditions. The decay rate for low and high pass filters are 12 dB and 6 dB per octave, respectively.



Fig. 4.7 Impact hammer used in the test



(a) Accelerometer

(b) Charge amplifier

Fig. 4.8 Accelerometer and charge amplifier

(3) Setup and Procedure

The sensor placement and hammer hit locations are presented in Fig. 4.9. From the experience of several trials, 3 sensors have been placed to the midpoint of the girder at each floor. This configuration is determined and set up to best reflect the structural response of MR damper controlled structure in the shake table test, where the control force from MR damper would be applied on 1st floor at this hammer hit location and total acceleration feedback from horizontal weak axis (y-axis) of each floor is sent to control core for semi-active control application.

For each trial of hammer test, 25 hits are performed, each having up to 60 second time window in between hits to let the impact energy die out in the system substantially through structural damping. Theoretically, a single hit would suffice for ERA to capture system

dynamics. However, with noise in present, and also small-scale local and global nonlinearities in the structure, some performance degradation during parametric estimations such as erroneous minimum realization or wrong natural frequencies is expected. Performing a large number of impacts will manage the issues stated above to some extent, as it will provide more averaging for frequency domain pre-process and thus result in higher quality data.

For each set of data, including the hammer force, 4 channels are sampled at 3000 Hz. Brüel&Kjær model No. 4368 and impact hammer made by Jiangsu Lianneng Electronic Technology Limited Corporation are used as the sensing unit. 0.1 and 300 Hz are selected as low pass filter and high pass filter respectively for both the sensors and hammer. The test data can be accessed through NEEHub (Ozdagli et al. 2013a,b).

After the data is collected, a post-processing is conducted involving dividing each impact responses into individual time histories associated with corresponding hammer force response. Transfer functions are generated from force to acceleration for all successful hits and averaging is performed in order to increase signal to noise ratio and eliminate structural nonlinearities. Using the averaged transfer functions, impulse response functions are developed for further ERA procedure. 500 columns and 1500 rows with a singular value of 25 are the input parameters to ERA.

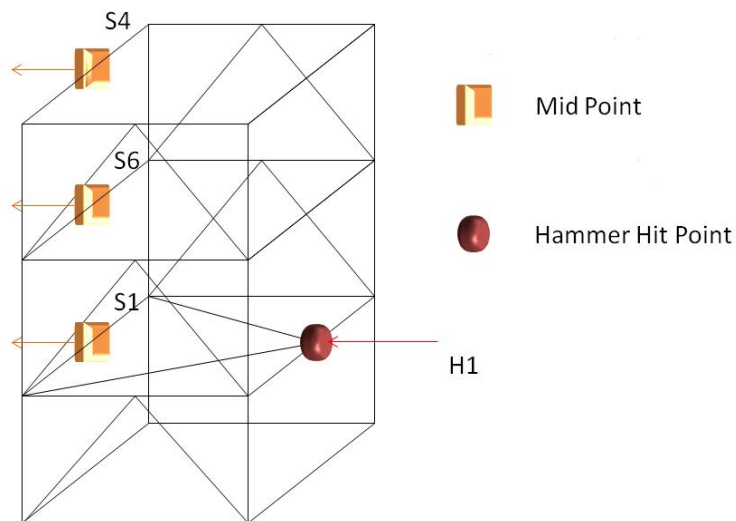


Fig. 4.9 3D view for sensor placement and hammer hit location

4.3.2 MR Damper Calibration Test

In order to ensure a respectable match between shake table results, pure simulations and real-time hybrid simulations, a good understanding of MR damper behavior is necessary. For the MR damper calibration test, the input is the motion applied on the damper movable piston and the current that controls the strength of the magnetic field of the MR fluid; the output is the damping force generated from the device. The ultimate goal of calibrating the MR damper model is to provide a set of damper parameters which can capture the damper's behavior under a variety of displacement inputs and electric current inputs.

(1) Instrumentation

An MR damper (serial# 0409010) made by LORD Corporation with model # RD-1005-3 is adopted for the tests in this study. This product is a compact, magneto-rheological (MR) fluid damper. It's suitable for industrial suspension and small scale structural applications. The continuously variable damping is controlled by the increase in yield strength of the MR fluid in response to magnetic field change. The response time of the MR damper is less than 15 milliseconds, which provides straightforward controls. The technical properties of the MR damper in this test are listed in Table 4.6.

Table 4.6 Technical properties of MR damper RD-1005-3

	Compressed Length (mm)	155	Extended Length (mm)	208
	Body Diameter (mm)	41.4	Shaft Diameter (mm)	10
	Tensile Strength (N)	4448	Operating Temperature (°C)	71
	Damper Force (N) (peak-to-peak)	5cm/sec @1A		>2224
		20cm/sec @0A		<667

Ampere power is driven to the damper with a current driver developed by Harbin Institute of Technology (HIT) as given in Fig. 4.10(a). A series of constant voltages that are given to the current driver is provided by the dSpace 1104 (#127174) given in Fig. 4.10(b). The current driver voltage-current equation is $A = V/1.70$ when including the MR damper as a

closed loop, as shown in Figure 4.11. This provides a way to predict the current within the damper if the applied voltage is known.

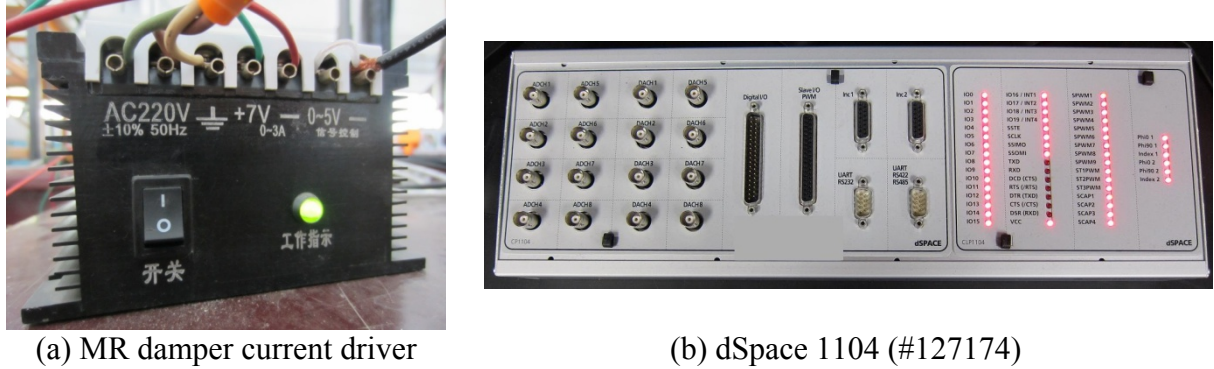


Fig. 4.10 MR damper current driver and dSpace 1104

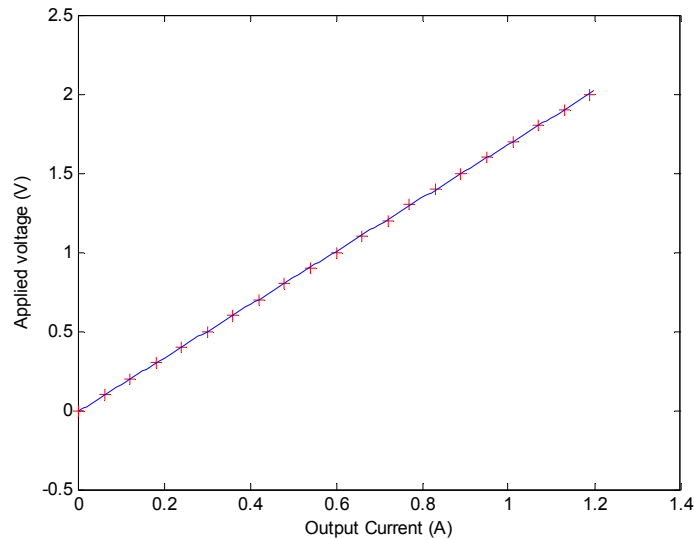


Fig. 4.11 Voltage-Current relationship of MR damper

An MTS actuator with a 2500 KN capacity located at Harbin Institute of Technology is used to drive the MR damper in the test, as shown in Fig. 4.12(a). When all of the pumps of the hydraulic supply unit are turned on, the actuator velocity can reach up to 100 mm/sec. The MTS actuator has a built in force transducer that can measure the reaction force to the machine, however, the maximum output force of the MR damper tested is only 2KN, which is much smaller than the capacity of the actuator. To avoid inaccurate measurement due to sensor noise, a separate load cell is used to measure the MR damper force output. This load

cell (model #661.19F-03, serial #313002, charge sensitivity 0.0066667 V/N) is manufactured by MTS System Corporation and has a capacity of 15KN, which is shown in Fig 4.12(b).



(a) MTS actuator with MR damper



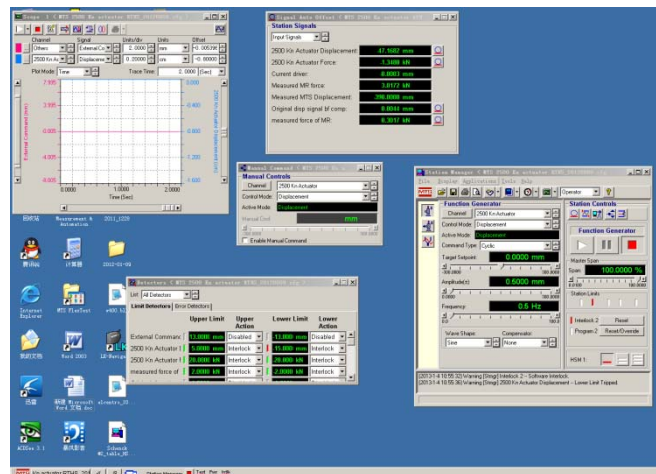
(b) MTS 15 KN force transducer

Fig. 4.12 2500 KN MTS actuator and 15 KN force transducer

The MTS actuator is driven by a MTS Flex GT Controller (MTS Corporation 2001a and b) shown in Fig. 4.13(a). It runs on Model 793.00 system software to operate and control the MTS actuator action. A screenshot of the software is given in Fig. 4.13(b).



(a) MTS Flex GT controller



(b) Model 793.00 system software

Fig. 4.13 MTS Flex GT controller and software

(2) Setup and Procedure

The experimental setup is illustrated in Fig. 4.14. It's seen that the MR damper is attached to the 2500 KN loading system and driven by the actuator, along with the external

passive voltage command is exerted by a Matlab compatible real-time hardware dSpace 1104. MTS Flex GT controller controls the action of the actuator while collecting the MR damper displacement from the internal LVDT and the MR damper force from the 15 KN load cell at a sampling rate of 1000 Hz.

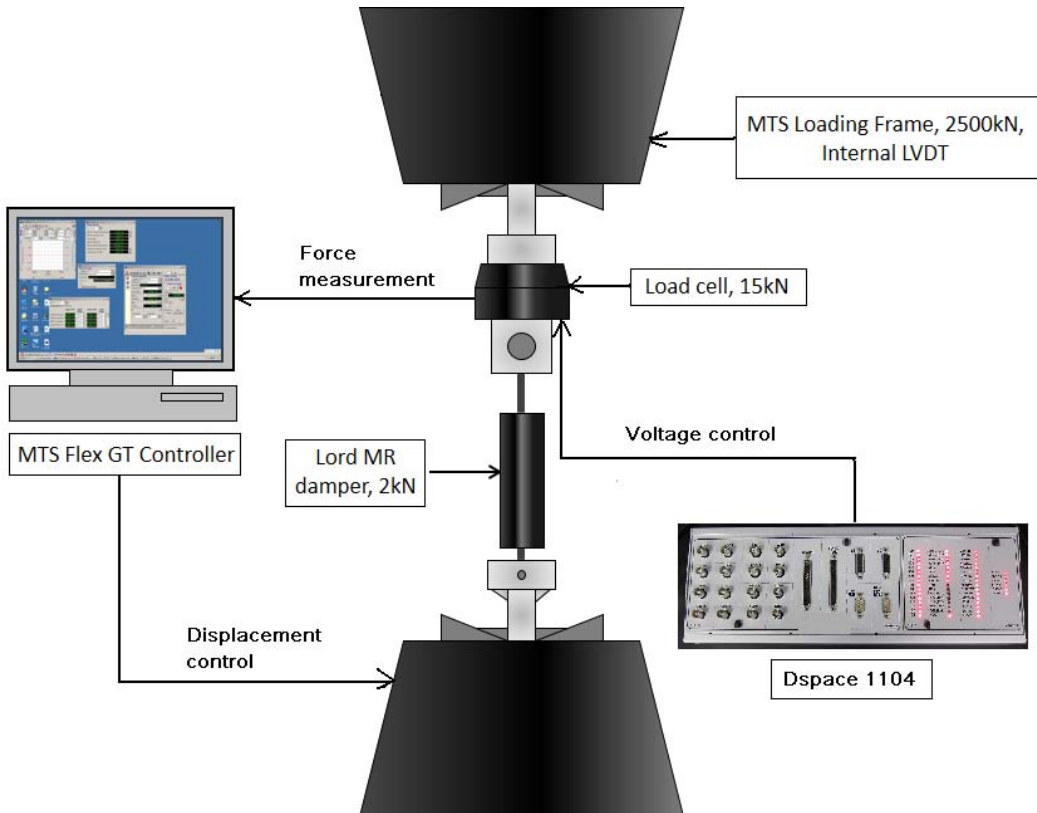


Fig. 4.14 Experimental setup for MR damper calibration test

The damper characterization test involves applying a series of sinusoidal waves at various constant voltage (current) levels. The amplitudes of the controlled sinusoidal displacement inputs here are set to be 5 mm and 10 mm, while the frequencies are chosen to be 2 Hz, 2.9 Hz, 4 Hz which correspond to low, resonant and high frequency response of the test structure according to the numerical prediction. This frequency range of calibration testing is supposed to fully characterize the MR damper behaviour under different conditions. In this test, 6 constant voltage levels are chosen, under which the resulting current in the circuit is in between 0A~1.01A. The input sine waves are shown in Fig. 4.15 and the loading

cases are summarized in Table 4.7.

Table 4.7 Loading cases of MR damper calibration test

Input frequency (Hz)	Input amplitude (mm)	Current in MR damper (A)
2	5	[0 0.20 0.41 0.59 0.83 1.01]
2.9	5	[0 0.20 0.41 0.59 0.83 1.01]
4	10	[0 0.20 0.41 0.59 0.83 1.01]

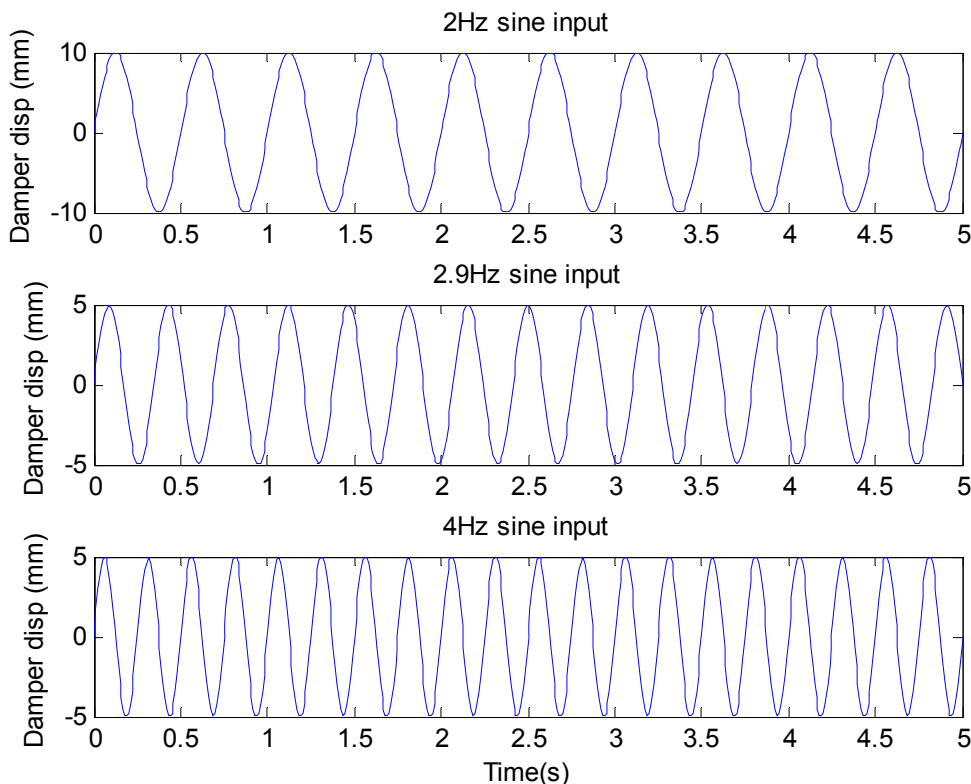


Fig. 4.15 Sine wave input of MR damper calibration test

The minimum current 0A and maximum current 1.01A correspond to so-called ‘passive-off’ and ‘passive-on’ control respectively. These two passive control concepts would be used throughout the later discussions of this study. With 60 sec displacement input, the experimental data is recorded. Based on the force response to the given displacement, a modified Bouc-Wen model as discussed in Chapter 3 can be developed with all the parameters identified by the calibration test. Thus, the behaviour of the MR damper used in our test could be well described numerically.

4.3.3 Real Time Hybrid Simulation (RTHS) Test

RTHS technique is often used to understand the effect of vibration control devices on the global performance of structures, in particular, for evaluating performance of rate dependent devices such as MR dampers. RTHS provides an efficient way to isolate and physically test only the more complex or critical components, where available resources do not allow researchers to test the full-scale structure. To verify RTHS with shake table responses of the three story test structure, an RTHS framework has been developed at Civil Engineering Laboratory at HIT. Particularly, the tests conducted on RTHS setup at HIT investigates performance of a newly developed Robust Integrated Actuator Controller (RIAC) by Purdue University, as well as quality of infrastructure and flexibility of the RTHS configuration for future RTHS.

(1) Instrumentation

The instrumentations used for RTHS test is the same as MR damper calibration test.

(2) Setup and Procedure

The proposed experimental hybrid simulation setup is partitioned into two parts: (i) MR damper attached to the 2500 KN actuator as the experimental substructure and (ii) Analytical 3-story structure model updated by system identification test as the numerical substructure. The diagram of the setup including DAQ system and controllers are shown in Fig. 4.16.

dSpace 1104 is used to realize control over MR damper. This is achieved by the following steps: (i) The updated analytical model of the 3-story structure and control algorithm are edited in Simulink of Matlab and downloaded to dSpace computational unit; (ii) dSpace computes the control displacement based on the equilibrium of the numerical substructure to MTS Flex GT controller to drive the MTS actuator to apply the displacement to MR damper; at the same time, dSpace also determines the control voltage by the control

algorithm and apply it to the current driver of MR damper to activate the magnetic field and enhance its damping. (iii) Displacement and reaction force of the MR damper are sent back from MTS Flex GT controller to dSpace as inputs for control algorithm and equilibrium of the numerical substructure; (iv) dSpace takes both MR damper force feedback and analytical earthquake excitation to compute and send the control displacement, along with the updated control voltage, to MTS Flex GT controller for next time step execution. This process is also illustrated in Fig. 4.16.

RTHS test is repeated for the 3 earthquake excitation inputs mentioned in section 4.1.2: historical 1940 El Centro earthquake, velocity-dominant 1995 Kobe earthquake and acceleration dominant 1984 Morgan Hill earthquake. For each earthquake, passive-off, passive-on and semi-active control tests are performed.

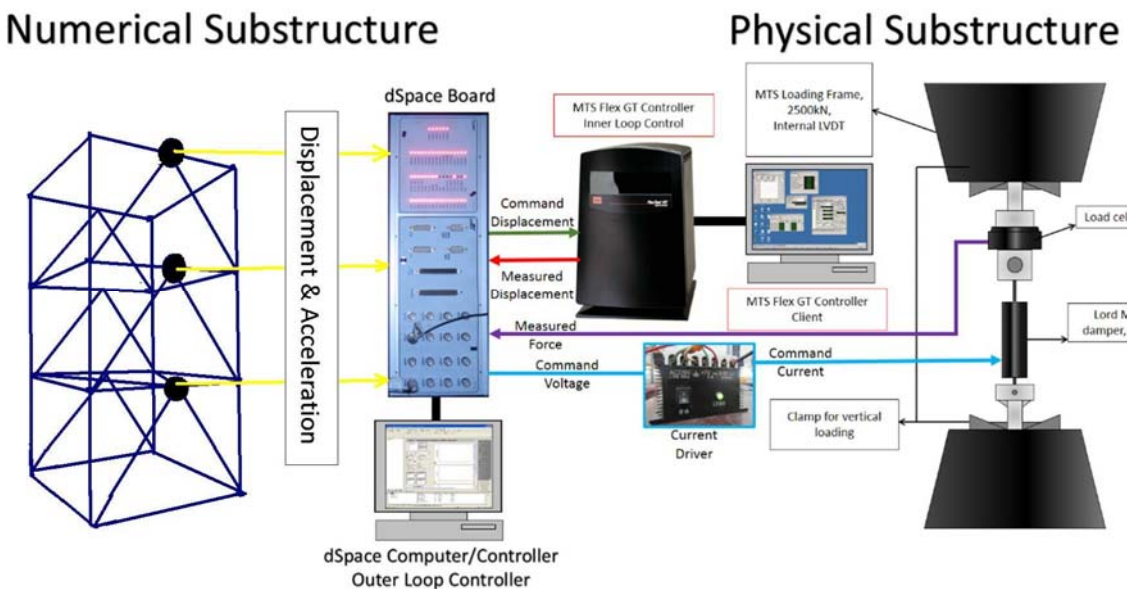


Fig. 4.16 Experimental setup for RTHS test

(3) MTS Actuator Control Compensation

To obtain the most accurate results from RTHS test, a new Robust Integrated Actuator Control (RIAC) strategy is proposed by Purdue University and implemented in this test. The RIAC has three key components; (i) the loop shaping feedback control based on H_∞

optimization; (ii) an additional Kalman filter for feedback estimation and (iii) noise reduction and a pure delay feed-forward block for control performance enhancement. The combination of the aforementioned blocks provides flexible designs according to different evaluation criterion. The efficacy of the proposed strategy is demonstrated through tracking tests of MTS actuator-MR damper system.

Validation of RIAC is first done through two tracking tests with a band-limited white noise with band width of 15Hz and a sinusoid input of 3Hz which is closed to structure first mode, as shown in Fig. 4.17.

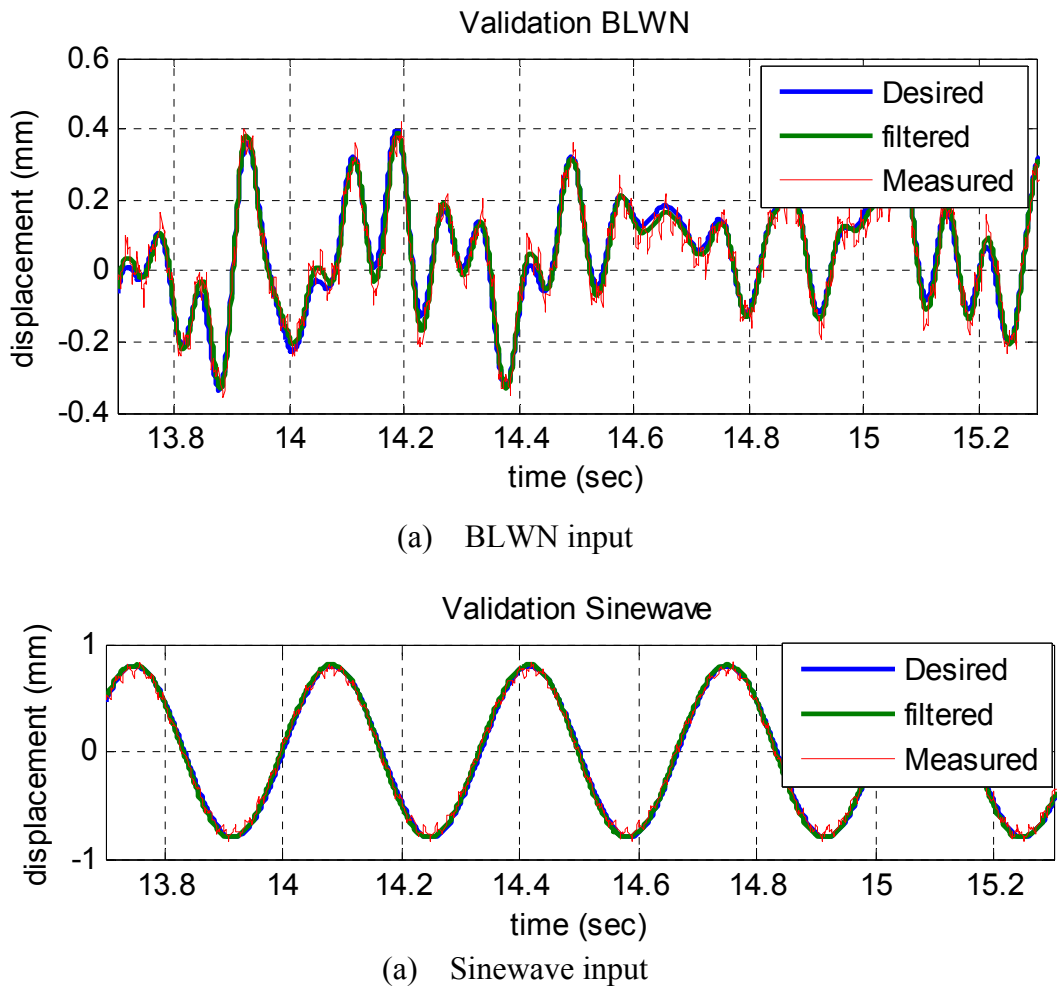


Fig. 4.17 Validation of RIAC strategy by theoretical inputs

Validation of RIAC is also performed through the tracking test of the actuator-damper system with a 35% scale Kobe earthquake. Both MR damper passive-off and passive-on case

are studied, as shown in Fig. 4.18.

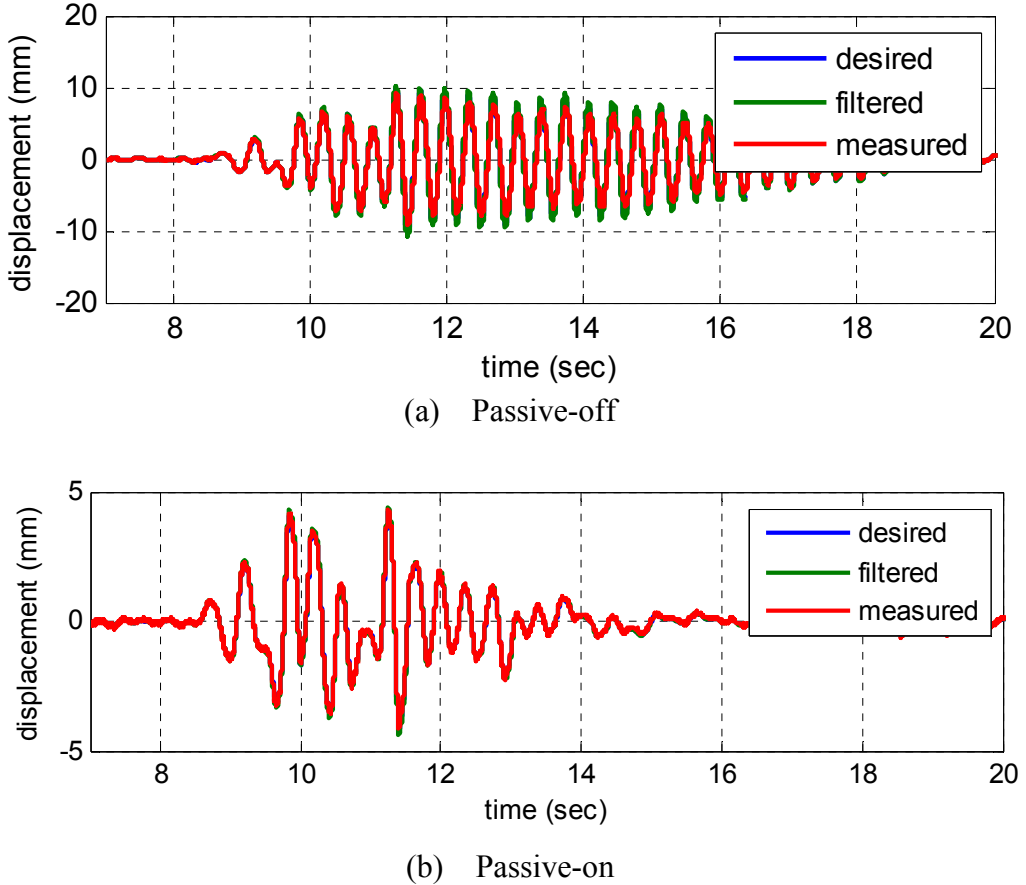


Fig. 4.18 Validation of RIAC strategy by earthquake input

It's seen that for all the cases the RIAC tracking is very accurate except for the passive-off case with Kobe earthquake. This is due to the fact that the hydraulic servo valve reached the velocity limitations. Based on RIAC strategy, both control performance and robustness can be granted even with large noise/signal condition and it compensates uncertain dynamics in terms of small time delay that simulation is failed to capture. The RIAC strategy implementation for RTHS test ensures MTS actuator to exactly follow the displacement control command by dSpace in the test setup.

4.3.4 Shake Table Test

As for model verification, the structure is tested experimentally on the shake table and the results are compared to analytical simulations performed with the updated model.

(1) Instrumentation

The shake table located in Harbin institute of Technology is a unidirectional shake table constructed in 1987. It is 3 meters wide in off-direction and 4 meters long in shaking direction. A picture of shake table is given in Fig. 4.19. The actuator attached to the shake table is made by Schenck. The actuator has a force capacity of 250 KN and it can drive the shake table with a peak acceleration of $\pm 1.33g$, peak velocity of ± 600 mm/s within a stroke of ± 125 mm. The maximum payload and maximum overturning moment of the shake table is limited to 12 t and 30 t-m, respectively. The frequency of the excitation input is bounded between 0-30 Hz. The parameters and capacities of the shaking table are listed in the Table 4.8 and the actuator is shown in Fig.4.20.



Fig. 4.19 Shake table located at HIT

Table 4.8 Shake table parameters and capacities

Size	3m×4m (shaking direction)
Peak acceleration: bare table	$\pm 1.33g$
Peak velocity	± 600 mm/s
Stroke	± 125 mm
Maximum gravity (vertical) payload	12t
Force capacity of actuators	200kN
Maximum overturning moment	30 t-m
Frequency bandwidth	0-30 Hz



Fig. 4.20 Schenck actuator of the shake table

The controller that drives the actuator is MTS Flex GT Controller running on Model 793.00 system software which is the same as that for MR damper calibration test and RTHS test.

All accelerometers used here is the same as system identification test, which is of Brüel&Kjær Model 4368. For data acquisition, a 16-bit, 16 channel China made DongHua dynamic data acquisition system with model # DH5922 is used, as shown in Fig 4.21. The MR damper, current driver, 15KN load cell and dSpace 1104 board that is used to implement control algorithm and apply control voltage, are the same as MR damper calibration test and RTHS test.



Fig. 4.21 DongHua dynamic data acquisition system DH5922

For displacement record, LVDT and Laser sensors are used. The first floor displacement is measured relative to the shake table with a short stroke 50 mm LVDT. Second and third floors are measured as absolute displacement with +/- 100 mm stroke laser sensors (Fig. 4.22(a)). The laser sensors are powered up by LK-G3001V Controller (Fig. 4.22(b)). A filter that cannot be deactivated is setup at 300 Hz at controller level.

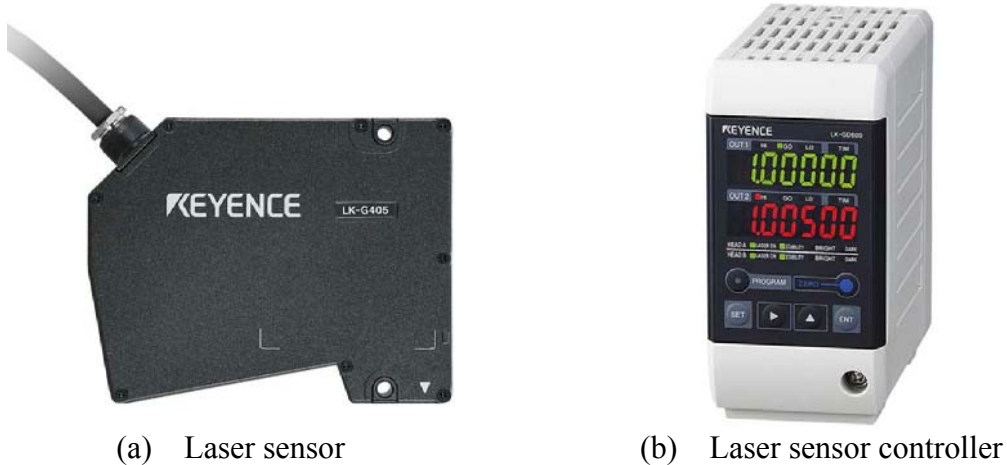


Fig. 4.22 Keyence laser displacement sensor and controller

(2) Setup and Procedure

Shake table test of a 3-story steel frame equipped with a MR damper is performed at HIT. The test structure is shown in Fig. 4.23.

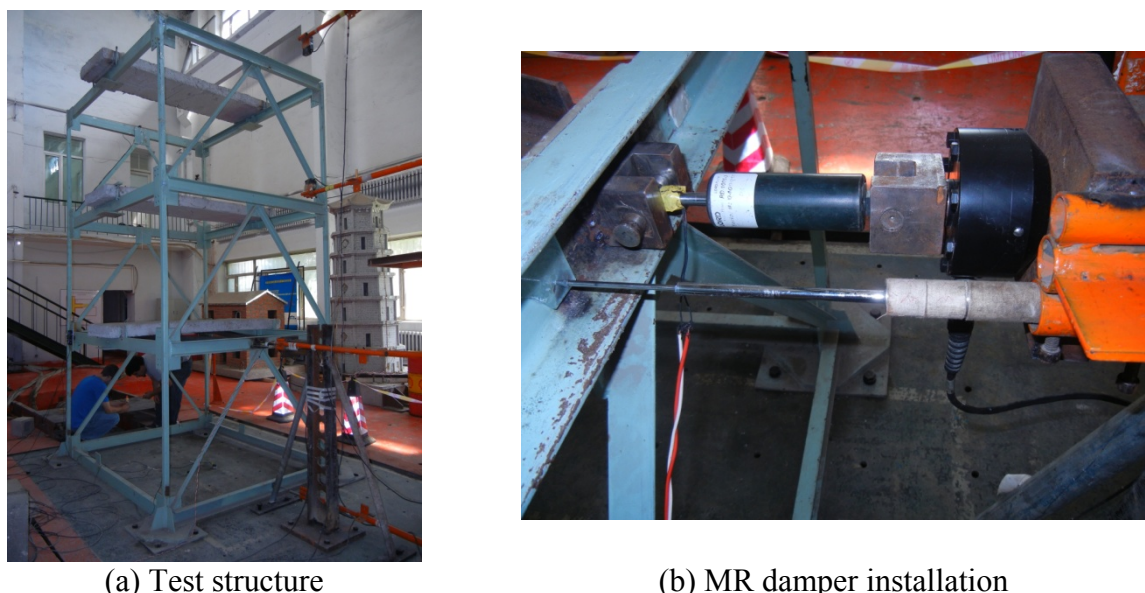


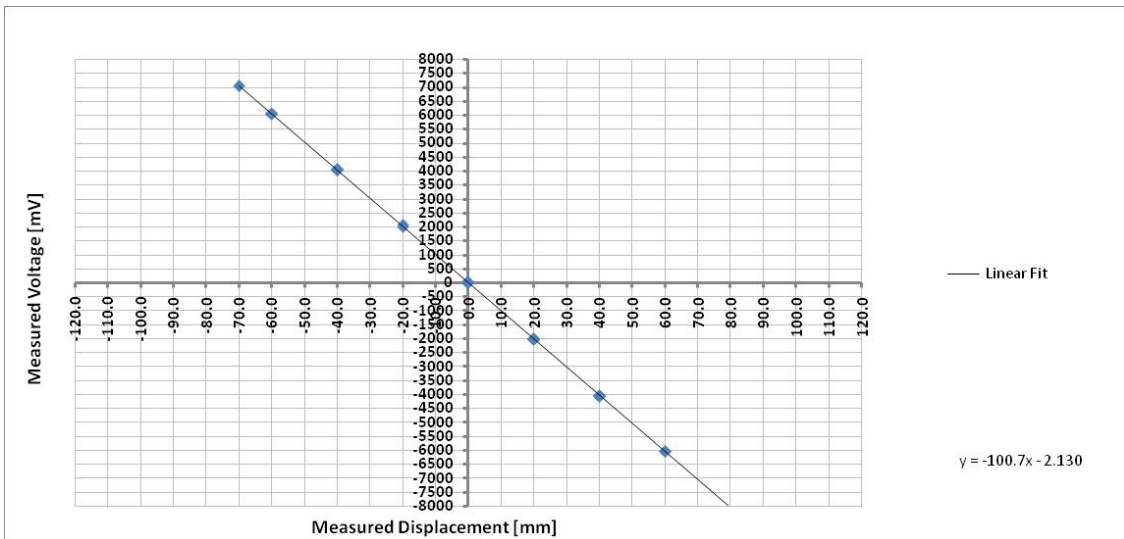
Fig. 4.23 Shake table test structure and MR damper

Before starting the shake table test, Keyence laser displacement sensors and the LVDT on 1st floor are calibrated by measuring the static movement of shake table with an increment displacement of 20mm in the range of [-70 90]mm of shake table coordinate system. The calibration results are shown in Fig. 4.24. The linear relations shown in the figure between measured voltage and displacement would serve as sensitivity numbers for the Keyence laser displacement sensors and the LVDT in the shake table test. Another two accelerometers and one laser displacement sensor are set on shake table and the 1st floor respectively for check purpose. The information of the laser sensors and LVDT is listed in Table 4.9.

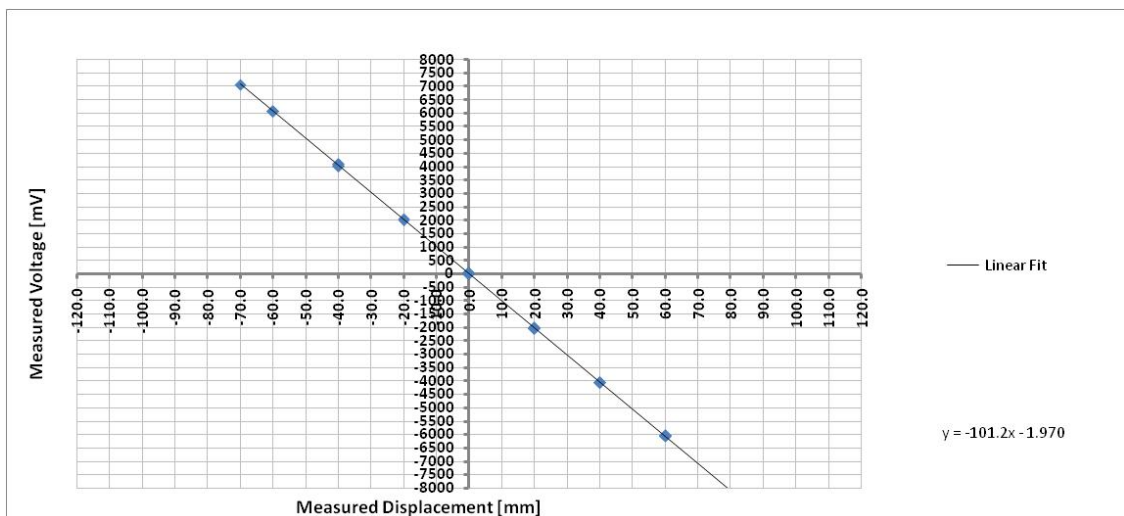
Table 4.9 Information of displacement sensors

Sensor # in test	Make - serial #	Charge sensitivity	Output unit
Actuator LVDT	Schenck	100 mV/mm	mm
LT4	Beijing Haiquan Sensor Technology Co model #DA-50 - serial #K3284	-100.3 mV/mm	mm
LT0	Beijing Haiquan Sensor Technology Co model #DA-150 - serial #K3258	-33.372 mV/mm	mm
LS1	Keyence LK-G405 - serial #1380541	-100.792 mV/mm	mm
LS2	Keyence LK-G400	-101.239 mV/mm	mm

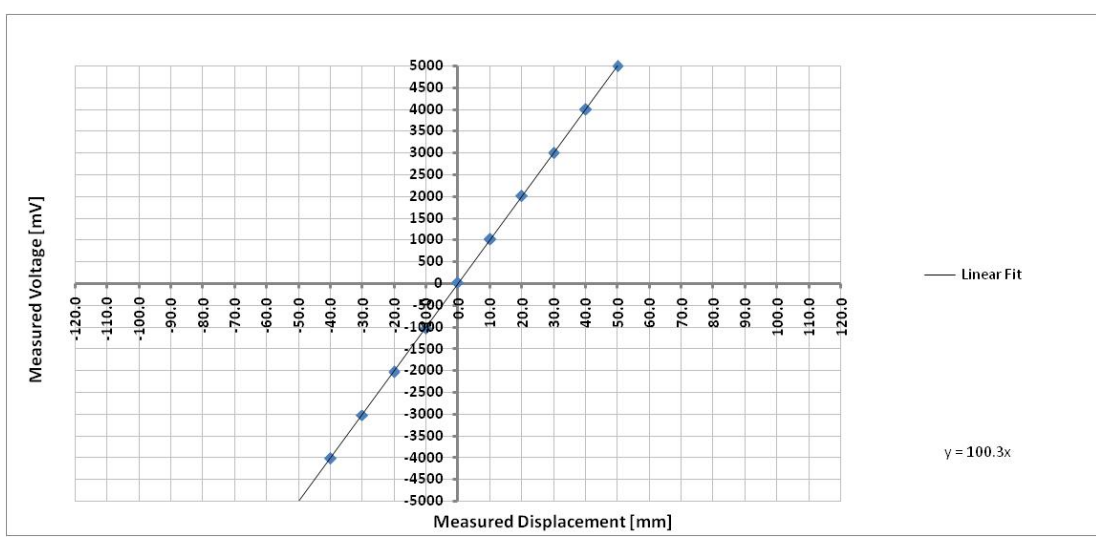
The actuator of the shake table at HIT is controlled on the software level only with PID control. Earthquake excitation inputs are selected as historical 1940 El Centro earthquake, velocity-dominant 1995 Kobe earthquake and acceleration-dominant 1984 Morgan Hill earthquake.



(a) 3rd floor laser sensor



(b) 2nd floor laser sensor



(c) 1st floor LVDT

Fig. 4.24 Calibration of Keyence laser sensor and LVDT

The ultimate aim of these series of shake table tests is comparing the results with numerical hybrid simulation scheme and RTHS test results. Dynamic response of the structure is investigated under uncontrolled (with no MR damper), passive-off, passive-on and semi-active cases. To realize control over MR damper, dspace1104 is used to compute the control voltage of MR damper at each time step with structural response feedback using the control algorithm downloaded. The input voltage to MR damper which is calculated by dSpace is sent to the current driver that activates the magnetic field in MR damper to enhance its damping. The shake table test setup is shown and explained in Fig. 4.25.

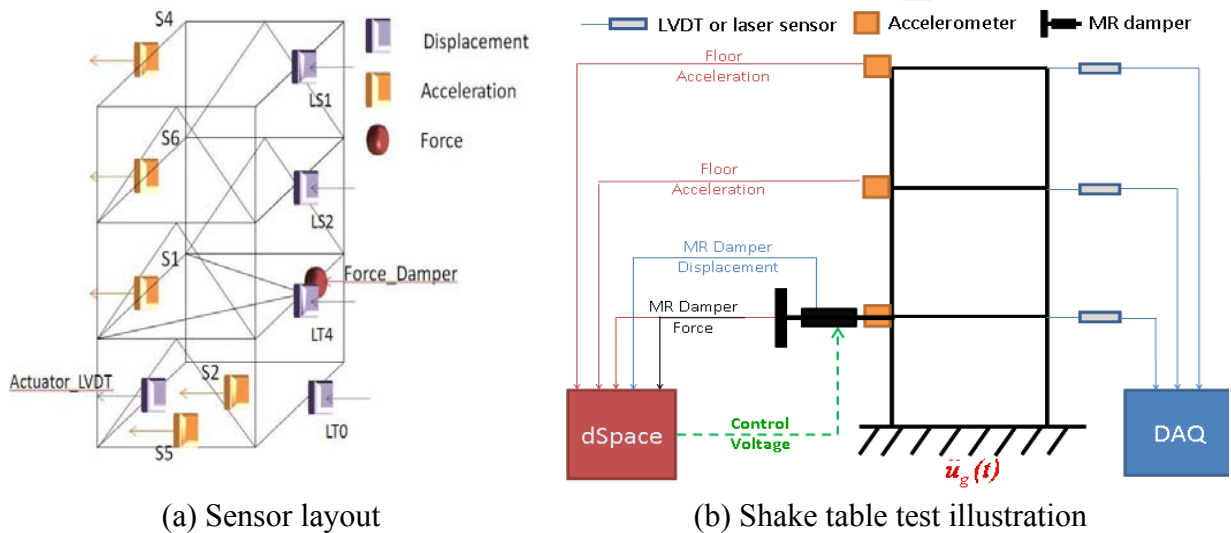


Fig. 4.25 Shake table test setup

(3) Ground motion scaling

Due to repeated use of the frame structure for different test purposes, the ground motion inputs for the shake table test are scaled in such a way that the frame structure would stay in linear region and not have any damage. Based on the dynamic numerical analysis with the 3D OpenSees model as shown in Table 4.4 and 4.5, 50% of the original El-Centro earthquake record, 35% of the original Kobe earthquake record and 105% of the original Morgan Hill earthquake record are used for shake table test.

4.4 Numerical Simulation Methodology and Platforms

In this study, MR damper is adopted to be the passive/semi-active control device and applied to a 3 story steel frame structure to investigate the control effect and algorithm. Full structure plus MR damper shake table test and RTHS test with MR damper as the experimental substructure are carried out as previously introduced.

A numerical model that could mimic the shake table test mathematically is needed for the purpose of simulation on structure with control devices to fix the gap between lack of capability of current general finite element software and the need of numerically simulating structure with control devices and implementing associated control algorithm. There are 3 platforms established for this purpose in the study: (i) Matlab Simulink based (ii) Matlab ODE solver based and (iii) Numerical hybrid scheme based on UI_SimCor. The platform (i) is developed by Purdue University and, platform (ii) and (iii) are developed by this study. A 3D FE model of the steel frame structure in OpenSees as shown in section 4.1.3 is developed for hybrid and general simulation purpose.

4.4.1 Simulation Platform Based on Simulink of Matlab

Purdue University developed a numerical simulation platform based on Simulink of Matlab. The MR damper is modelled by modified Bouc-Wen model and the system dynamic response is solved in Simulink as well with a discrete time manner. Fig. 4.26 shows the modelling scheme in Simulink for the simulation platform by Purdue University.

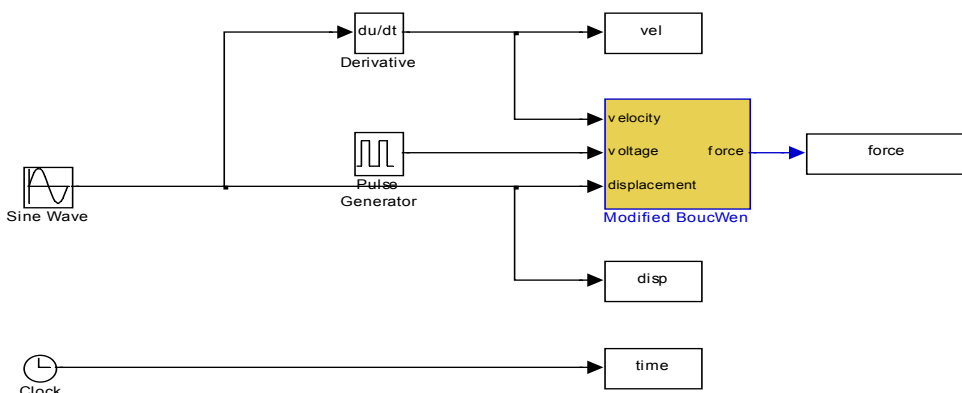


Figure 4.26 Numerical modeling of MR damper in Simulink

4.4.2 Simulation Platform Based on Matlab ODE Solver

After the system identification test is performed, a MCK model is obtained with the complete information of the mass (M), damping (C) and stiffness (K) property of the structure. An MR damper model is established in ODE solver combined with the MCK model from hammer test to simulate the whole structure with the control device. The illustration of modified Bouc-wen model of MR damper is shown in Fig. 3.5. The ODE simulation platform is basically solving the following dynamic system with a MR damper force f .

$$\mathbf{M}\ddot{\mathbf{X}} + \mathbf{C}\dot{\mathbf{X}} + \mathbf{K}\mathbf{X} + f = -\mathbf{M}\ddot{u}_g \quad (4.29)$$

where M, C, K are the mass, damping and stiffness matrices of the structure obtained from system identification test and f is the control force from the MR damper whose model parameters are determined by the damper calibration test. The output force of MR damper is governed by the modified Bouc-Wen model introduced in Chapter 3.

The numerical modeling of MR damper based on ODE solver in Matlab is mutually verified with the numerical model based on Simulink developed by Purdue University. Figure 4.27 demonstrates the ODE MR damper numerical model has the exact same behavior as the Simulink based model. These two simulation platforms are expected to give the same results when used for future simulation.

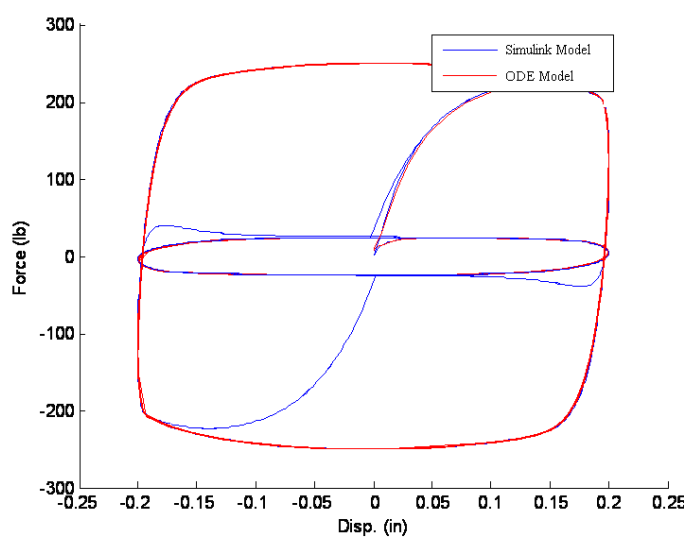


Fig. 4.27 Mutual verification of ODE based and Simulink Based MR damper model

4.4.3 *Simulation Platform Based on UI_SimCor*

Numerical hybrid scheme for simulation based on UI_SimCor is introduced in Chapter 3. This hybrid modeling of an entire system allows for numerical simulations of complex coupled systems performed separately on different computational platforms. In this study, the numerical hybrid simulation scheme introduced in Chapter 3 is proposed to take advantage of modeling ability of existing finite element software and realize the structural control algorithm at the same time. The experimental structure here is modelled with nonlinear elements in OpenSees, while the structural control device MR damper is simulated in Matlab, where the control algorithm can be easily formulated and implemented using the built-in toolboxes. The experimental structure and the MR damper, as two substructure parts, can communicate with each other by transferring force and displacement information through the platform UI-SIMCOR. With shake table test/RTHS test, this study aims at verifying the validity of the proposed numerical hybrid simulation scheme based on UI_SimCor in efficiently developing seismic protection strategies for nonlinear structures.

4.5 Test Results and Discussion

4.5.1 *System Identification test*

(1) *Identified modal properties*

With the ERA procedure stated in section 4.2.3, 11 modes have been identified in the test, however only first three modes along the weak axis are of our interest since the later shake table test is only performed in this direction, and higher modes that are associated with torsion of the structure would not be triggered. The identified modal frequencies and damping ratios are determined as 2.88 Hz, 8.10Hz and 12.34 Hz; 0.57%, 0.21% and 0.15%, respectively, as listed in Table 4.10.

Table 4.10 Modal frequency and damping from system identification

	1 st mode in y-axis	2 nd mode in y-axis	3 rd mode in y-axis
Modal freq. (Hz)	2.88	8.10	12.34
Modal damping (%)	0.57	0.21	0.15

Transfer functions of experimental data are compared to those generated with ERA in Fig. 4.28. The identified mode shapes for first 3 modes in y-axis are compared with analytical solution from OpenSees 3D model is shown in Fig. 4.29. As seen from comparisons of transfer function and identified mode shapes, there is no significant difference between results, i.e. the identified system and the OpenSees 3D model are both fine approximation of the test structure.

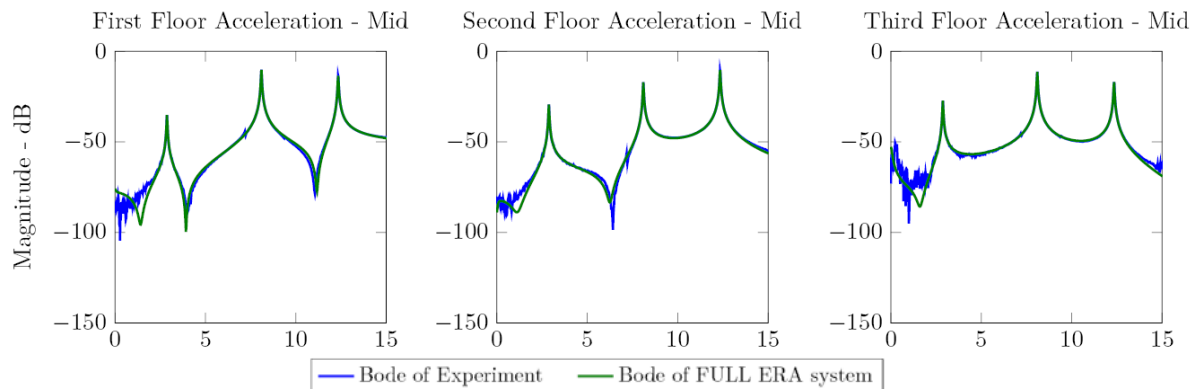


Fig. 4.28 Transfer function comparison of experimental data and ERA result

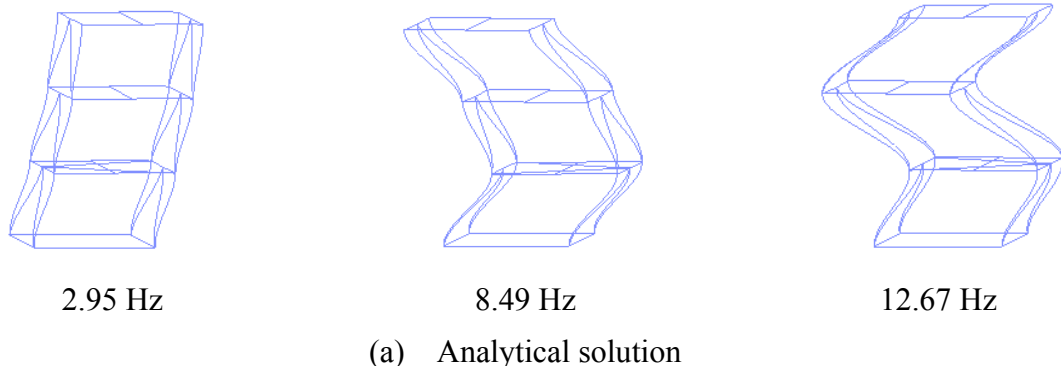
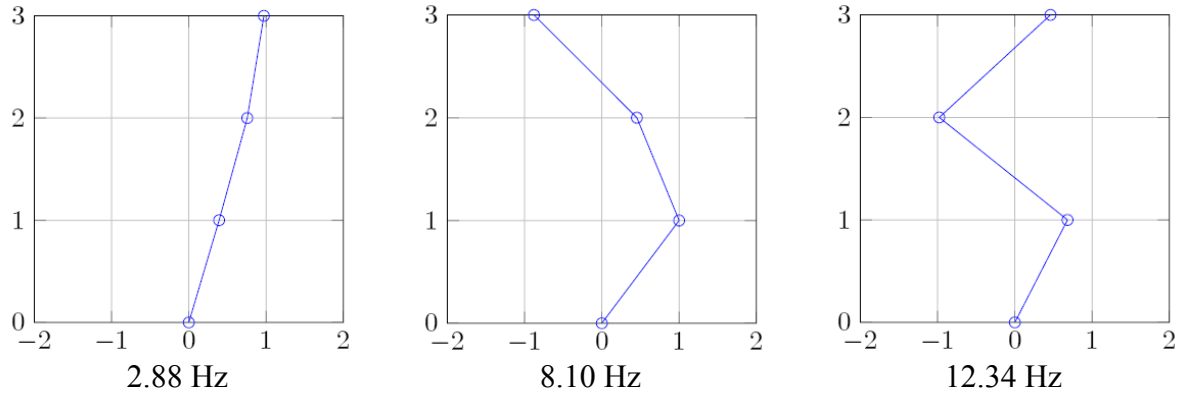


Fig. 4.29 First 3 modes in y-axis comparison of experimental and analytical solution



(b) System identification result

Fig. 4.29 (cont.) First 3 modes in y-axis comparison of experimental and analytical solution

(2) Model updating

Due to the fact that the mass of the experimental steel frame is concentrated on each floor of the structure and the frame is relatively weak in one axis (no bracing in y direction), the test structure can be simplified as a 3DOF lumped mass structure. Knowing the lateral stiffness of a fix-end column is $\frac{12EI}{l^3}$ and the material/section property of the structure, the analytical mass and stiffness matrices of the simplified 3DOF system can be expressed as:

$$\mathbf{M}_A = \begin{bmatrix} 400.1 & 0 & 0 \\ 0 & 355.3 & 0 \\ 0 & 0 & 355.3 \end{bmatrix} \text{kg}, \quad \mathbf{K}_A = \begin{bmatrix} 1222.2 & -611.1 & 0 \\ -611.1 & 1222.2 & -611.1 \\ 0 & -611.1 & 611.1 \end{bmatrix} \text{KN/m} \quad (4.30)$$

The analytical mass and stiffness matrices can be updated by the model updating method stated in section 4.2.4 with Eq. 4.25~4.27. The updated mass and stiffness matrices are computed to be:

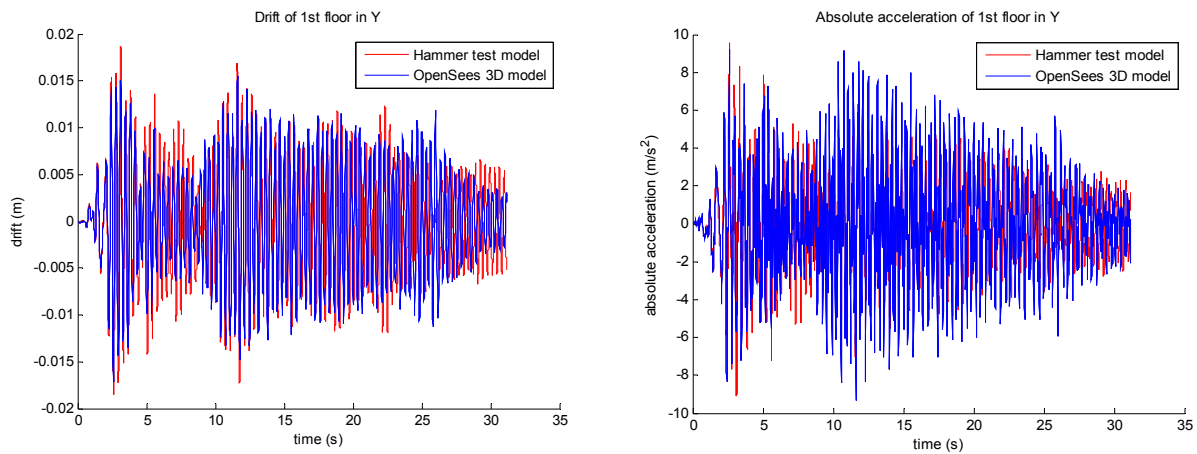
$$\mathbf{M}_E = \begin{bmatrix} 419.5 & 4.4 & 2.2 \\ 4.4 & 364.5 & 10.0 \\ 2.2 & 10.0 & 319.5 \end{bmatrix} \text{kg}, \quad \mathbf{K}_E = \begin{bmatrix} 1432.5 & -721.4 & 37.4 \\ -721.4 & 1306.5 & -607.0 \\ 37.4 & -607.0 & 547.2 \end{bmatrix} \text{KN/m} \quad (4.31)$$

The updated damping matrix can be determined by Eq. 4.28, which is computed to be:

$$\mathbf{C}_E = \begin{bmatrix} 88.1 & -4.1 & -1.8 \\ -4.129 & 74.3 & -4.5 \\ -1.8 & -4.5 & 61.1 \end{bmatrix} \text{ N}\cdot\text{s}/\text{m} \quad (4.32)$$

The matrices \mathbf{M}_E , \mathbf{C}_E and \mathbf{K}_E formulate an updated simplified 3DOF system which can well capture the characteristics of the test structure since they are derived from the system identification results. This updated 3DOF system is referred as ‘3DOF model’ hereafter and would be used to model the test structure in RTHS and shake table tests for control algorithm implementation.

With the updated 3DOF model, the 3D finite element model in OpenSees is also updated by adjusting the mass distribution and column stiffness, such that it can give as close results as the updated 3DOF model. Fig. 4.30(a) shows the comparison of the first floor drift and total acceleration time histories with the updated 3DOF model and updated 3D OpenSees model; Fig. 4.30(b) shows the comparison of the normalized frequency response spectra for first floor drift and total acceleration, which concludes that the updated 3D OpenSees model can capture the main structural response at 1st natural frequency in both time and frequency domain. Thus the updated 3D OpenSees model is an accurate representation of the test steel frame and could be used as the substructure in the numerical hybrid simulation based on UI-SimCor as stated in section 4.4.3.



(a) Time history comparison

Fig. 4.30 Comparison of updated 3D OpenSees model with updated 3DOF model

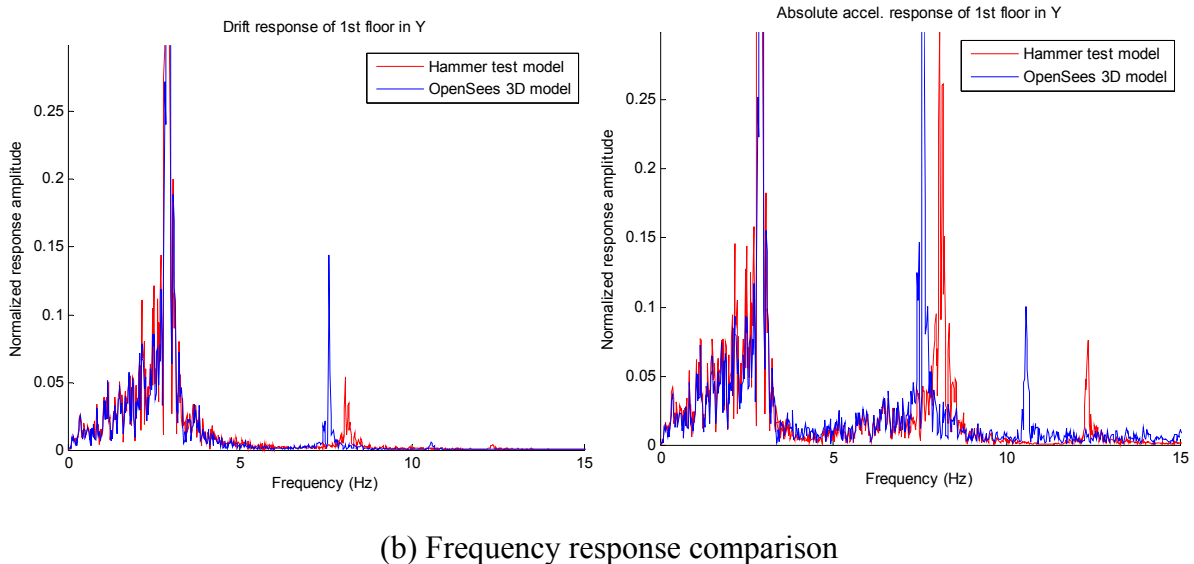
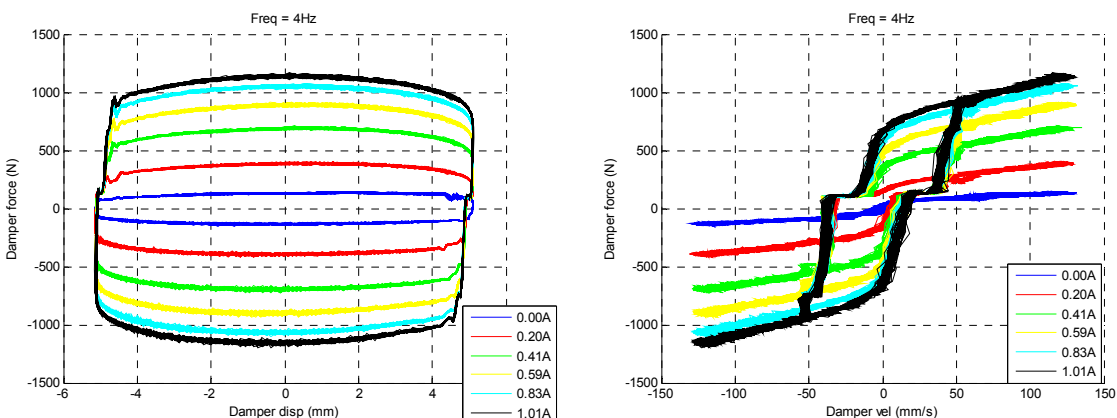


Fig. 4.30(cont.) Comparison of updated 3D OpenSees model with updated 3DOF model

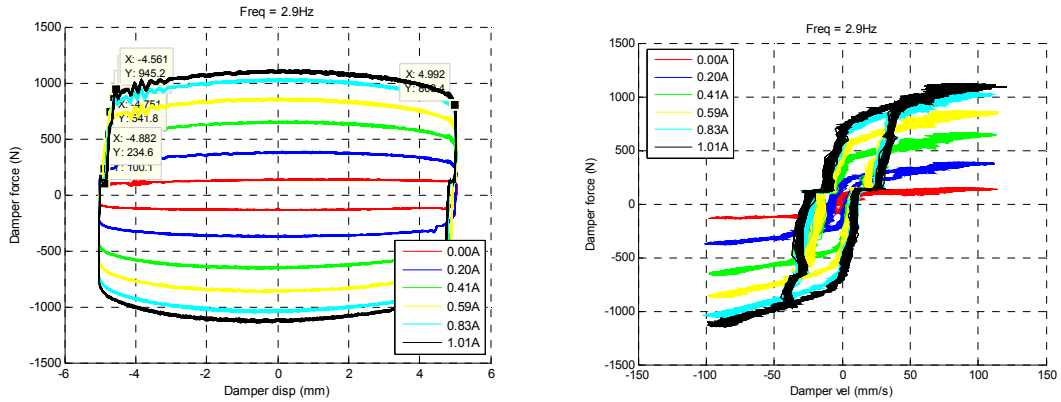
4.5.2 MR Damper Calibration Test

In the MR damper calibration test, 2Hz, 2.9Hz and 4Hz are chosen as the frequency for the input sine wave motions. 2Hz and 4Hz test results represent the MR damper behaviour under low and high frequency inputs respectively, and the 2.9 Hz test results represent the MR damper behaviour when the experimental steel frame structure vibrates around its natural frequency. The input magnitudes for 2 Hz test is 10mm while 5mm magnitude is taken for 2.9 Hz and 4 Hz tests, to make full use of the capacity of MTS actuator. The force-displacement and force-velocity relation curves for different test cases are summarized in Fig. 4.31.

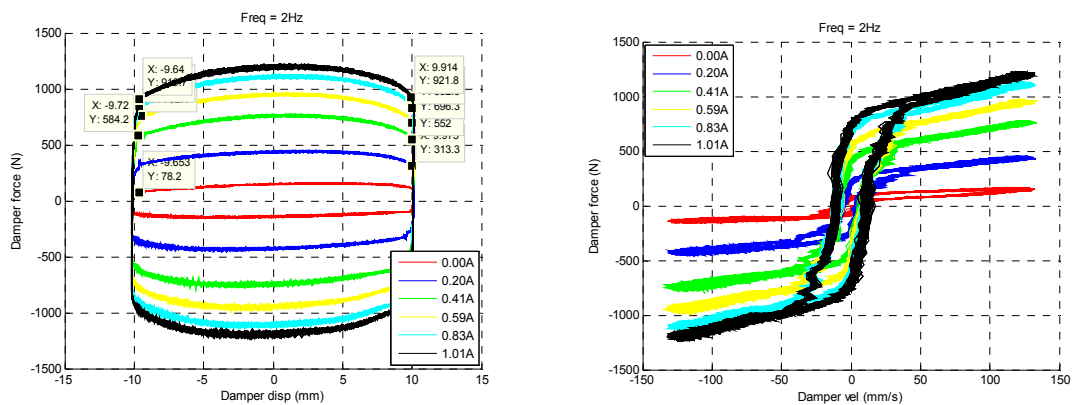


(a) Frequency = 4 Hz and amplitude = 5mm of input motion

Fig. 4.31 Force-displacement and force-velocity loops by MR damper calibration test



(b) Frequency = 2.9 Hz and amplitude = 5mm of input motion



(c) Frequency = 2 Hz and amplitude = 10mm of input motion

Fig. 4.31(cont.) Force-displacement and force-velocity loops by MR damper calibration test

It's seen from the force-displacement and force-velocity loops that the behaviour of MR damper is highly nonlinear. An accurate numerical model of this device is essential to exploit the damping feature of it for future implementation of numerical simulation. Modified Bouc-Wen Model introduced is adopted here to model the MR damper in the test.

Recall that among the parameters of Modified Bouc-Wen model for MR damper, x_0 , k_0 , k_1 , γ , β , A and n are evaluated as constants, while c_0 , c_1 and α are linear function of the voltage v that is applied to the MR damper:

$$c_0 = c_{0a} + c_{0b}v, \quad c_1 = c_{1a} + c_{1b}v, \quad \alpha = \alpha_a + \alpha_bv \quad (4.33)$$

A least square optimization algorithm is written in Matlab and used to generate the MR damper model parameters, x_0 , k_0 , k_1 , γ , β , A , n , c_0 , c_1 and α , by applying the calibration test data to this algorithm. By looking into the force-velocity curve in Fig. 4.31,

one can observe that for different frequencies of movement, the MR damper yields similar level of force output when operated at the same velocity, for example, the MR damper output force is around 1100N and 200N when applied current is 1.01A (passive-on) and 0A (passive-off), which is true for all input frequencies 2Hz, 2.9Hz and 4Hz. Therefore, only the test data with 2.9 Hz input is used to calculate the MR damper parameters, since 2.9 Hz is quite close to the natural frequency of the test structure.

Moreover, the test data of passive-off (minimum control voltage and current) and passive-on (maximum allowable control voltage and current) from 2.9 Hz input case is used to get two sets of MR damper parameters. x_0 , k_0 , k_1 , γ , β , A , n , c_0 and c_1 values of these two sets are almost the same as each other because of the fact that they are independent of control voltage/current of MR damper while c_0 , c_1 and α values are different for passive-off and passive-on cases. The two sets of c_0 , c_1 and α are further used to determine the parameters in Eq. 4.33 by solving corresponding two linear equations with two unknowns. Though derived only based on passive-off and passive-on test data, the parameters obtained here are supposed to have a good fit for other cases with an input voltage/current in between passive-off and passive-on. Table 4.11 lists the resultant parameters and Fig. 4.32 shows the validity of this numerical MR damper model for passive-off and passive-on cases with a sine input of 2.9Hz in frequency and 5mm in magnitude. The good agreement with the test data makes this set of MR damper parameters suitable for future numerical simulation applications.

Table 4.11 Modified Bouc-Wen model parameters for MR damper

x_0 (in)	k_0 (lb/in)	k_1 (lb/in)	γ (in $^{-2}$)	β (in $^{-2}$)	A (1)	n (1)
0.0	11.08	0.009	23.44	23.44	155.32	2
α_a (lb)		α_b (lb/V)	c_{0a} (lb-s/in)	c_{0b} (lb-s/in/V)	c_{1a} (lb-s/in)	c_{1b} (lb-s/in/V)
15.65		57.16	1.00	9.76	19.15	139.96

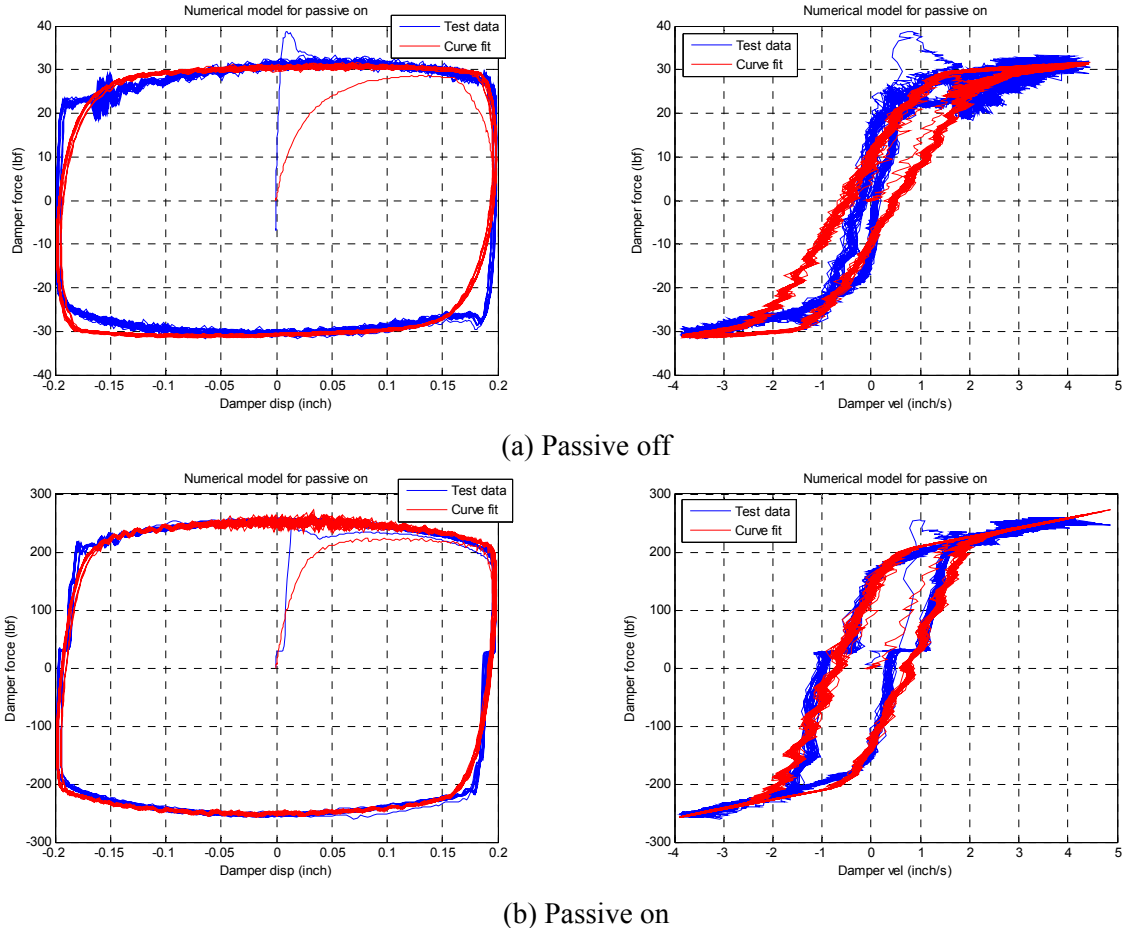


Fig. 4.32 Numerical model VS test data of MR damper

4.5.3 RTHS and Shake Table Tests

Real-time hybrid simulation provides the capability to isolate and physically test critical components of a semi-active controlled structure. The tests are conducted in real-time to fully capture any rate dependencies. RTHS allows for repeatable tests to be conducted to examine various control strategies and a range of seismic inputs in an efficient manner. In this study, the MR damper is isolated as the physical experimental component and all the other parts of the structure are simulated numerically in Matlab with the simplified 3DOF model. Clipped optimal algorithm is implemented for MR damper control design.

Two key points are essential to ensure a successful RTHS test: (i) A realistic numerical model that can best capture the dynamic characteristics of the test structure to provide accurate structural response prediction and effective semi-active control design; (ii) A

fine actuator compensation scheme that ensures the desired control displacement to be implemented on MR damper. These two points are achieved by the updated 3DOF model based on hammer test and the RIAC actuator control compensation strategy. Therefore, the output from RTHS test here is supposed to be in good agreement with that from the shake table test. Fig. 4.33~4.38 certainly certify this expectation. These figures address the comparisons of structural relative displacement to shake table surface and total acceleration between RTHS and shake table tests for passive-off and semi-active control under El-Centro, Kobe and Morgan Hill earthquake records as inputs.

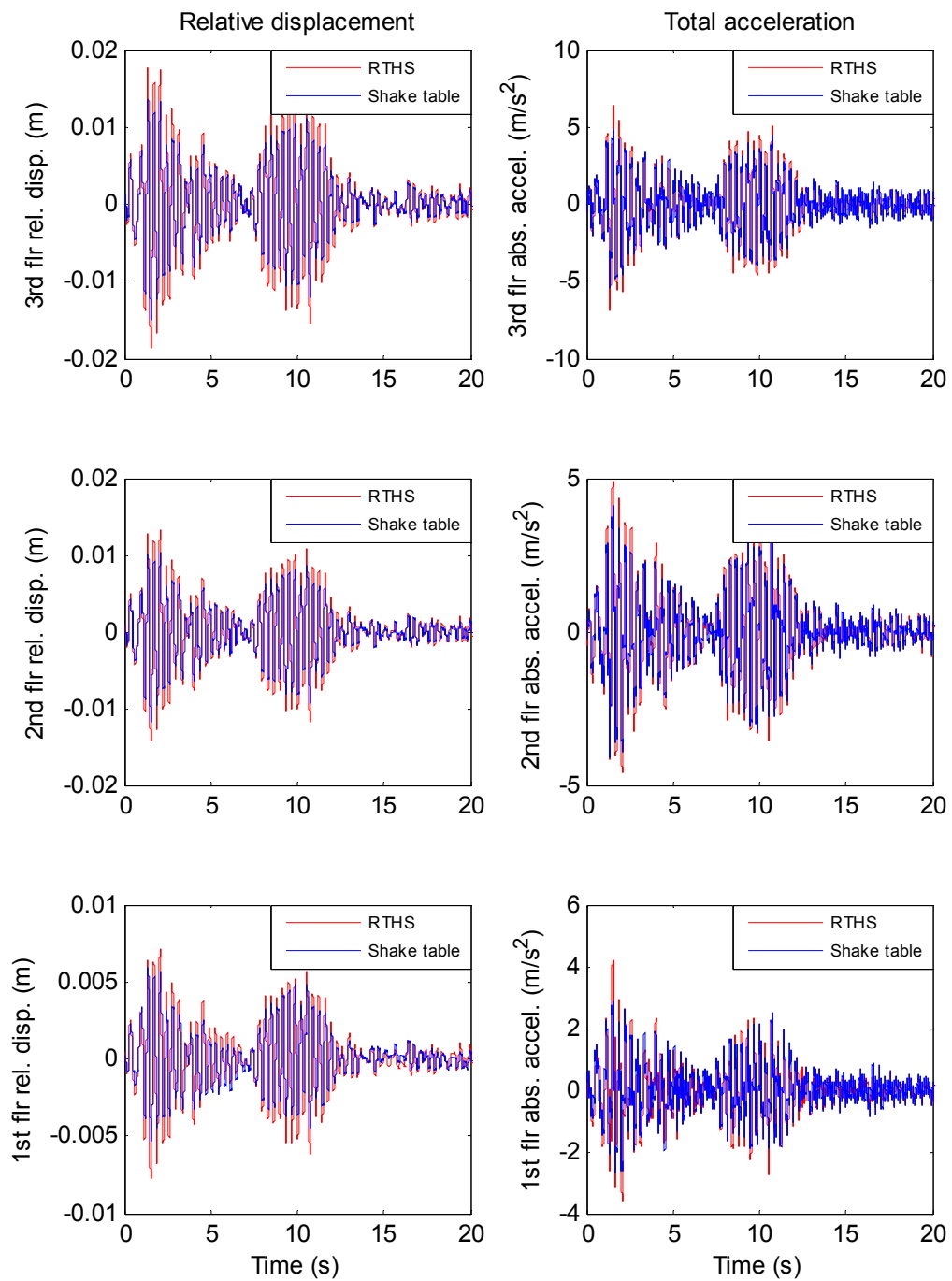


Fig. 4.33 Structural response comparison for passive-off control, El-Centro

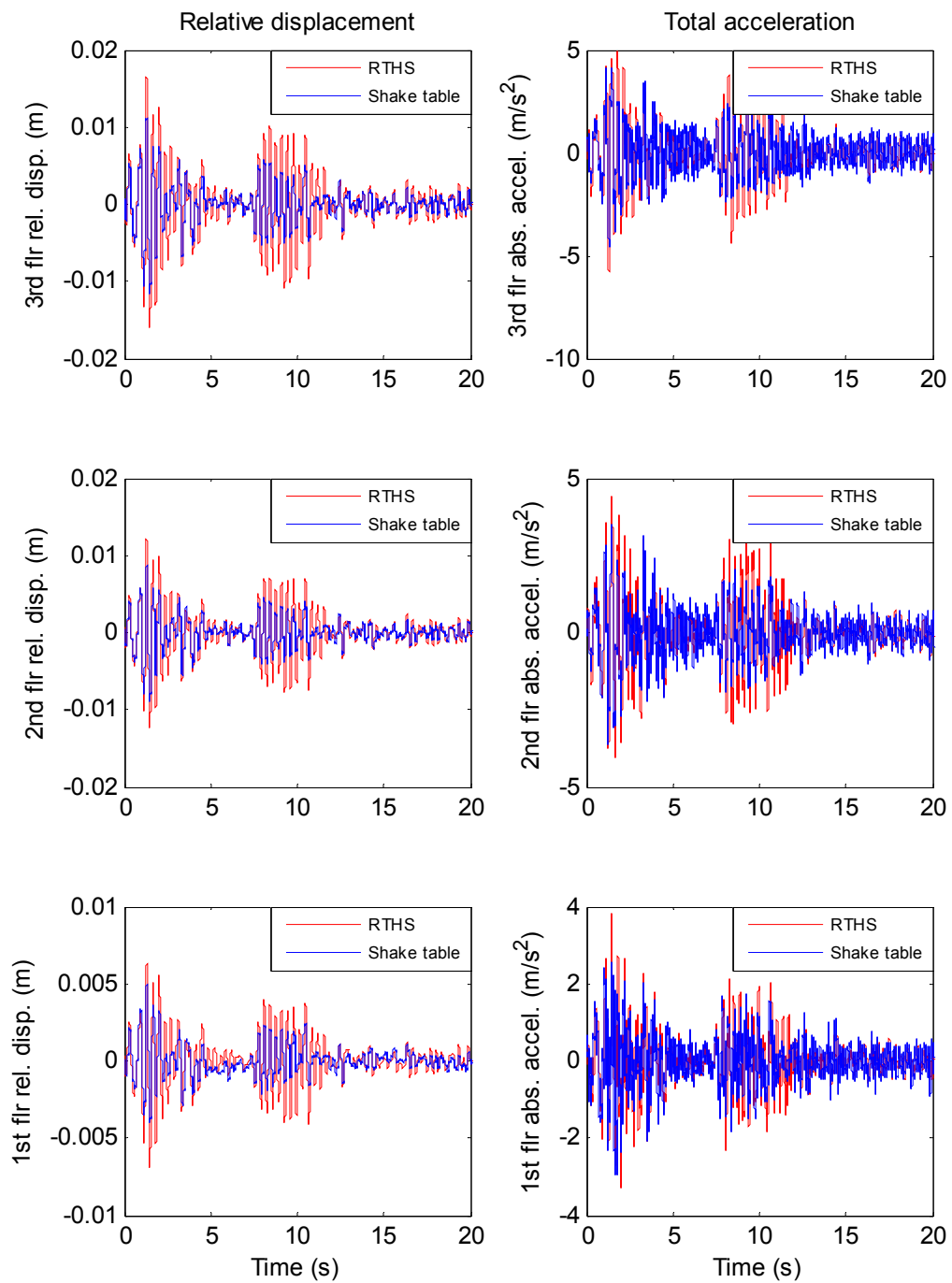


Fig. 4.34 Structural response comparison for semi-active control, El-Centro

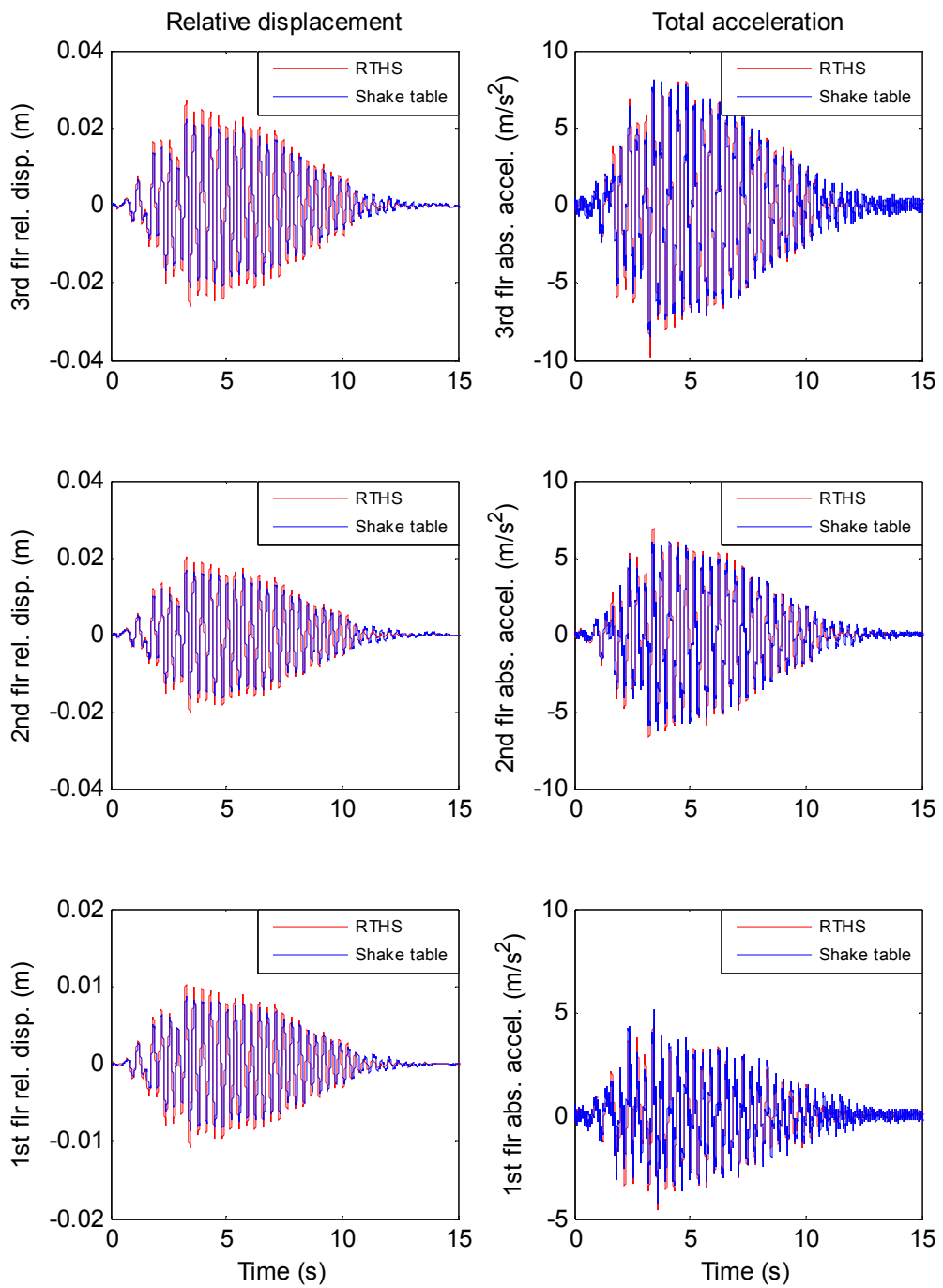


Fig. 4.35 Structural response comparison for passive-off control, Kobe

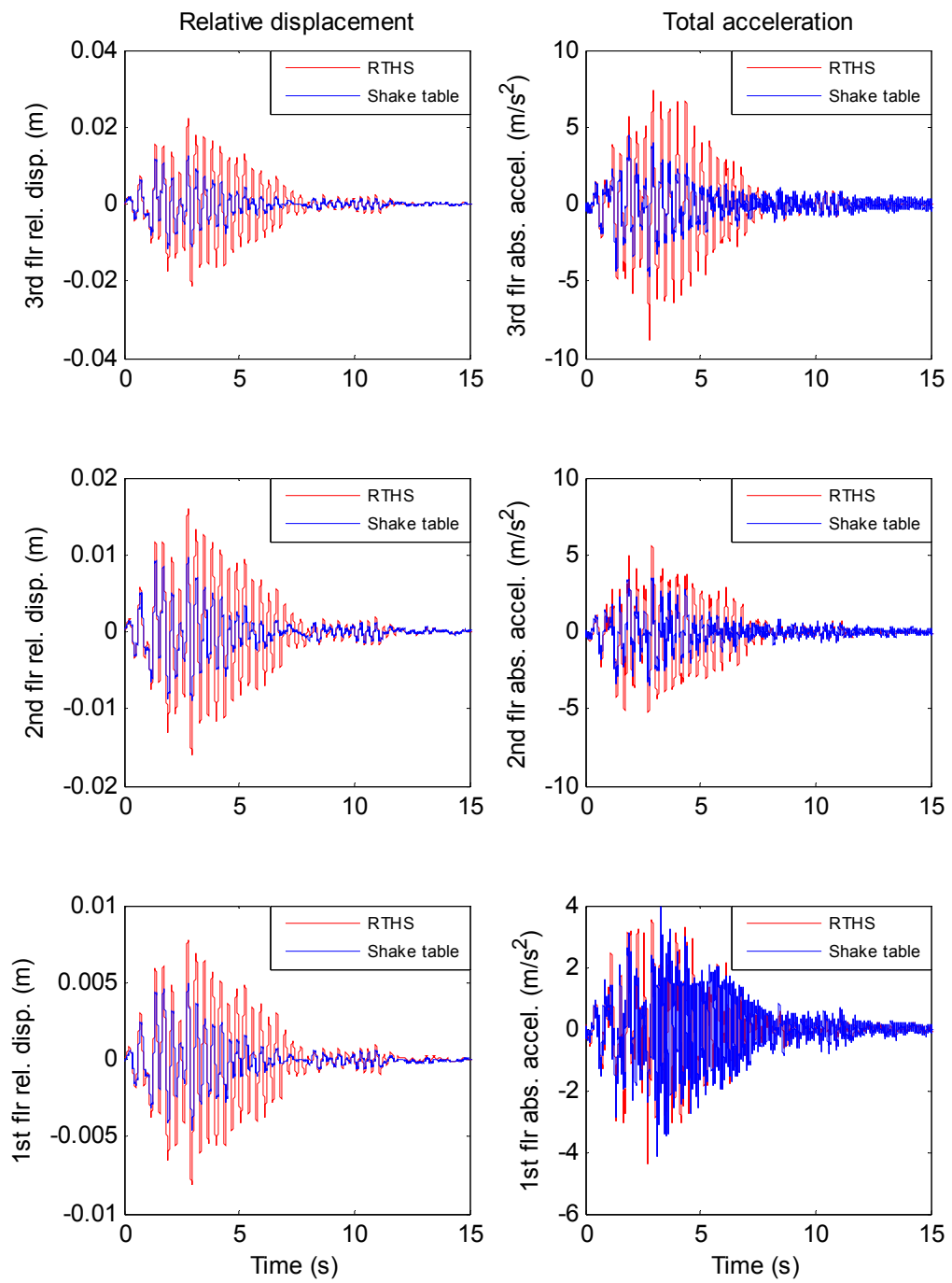


Fig. 4.36 Structural response comparison for semi-active control, Kobe

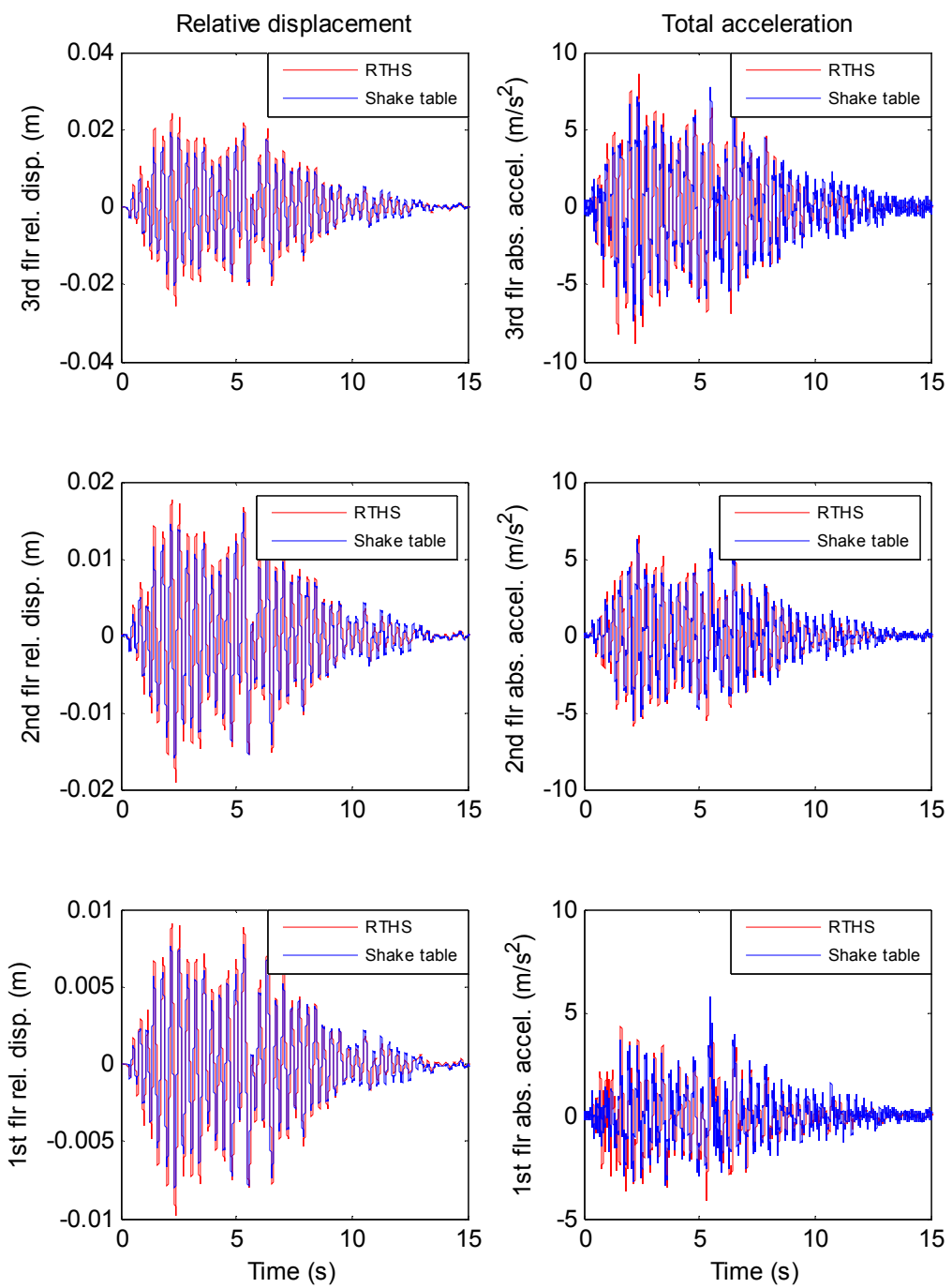


Fig. 4.37 Structural response comparison for passive-off control, Morgan Hill

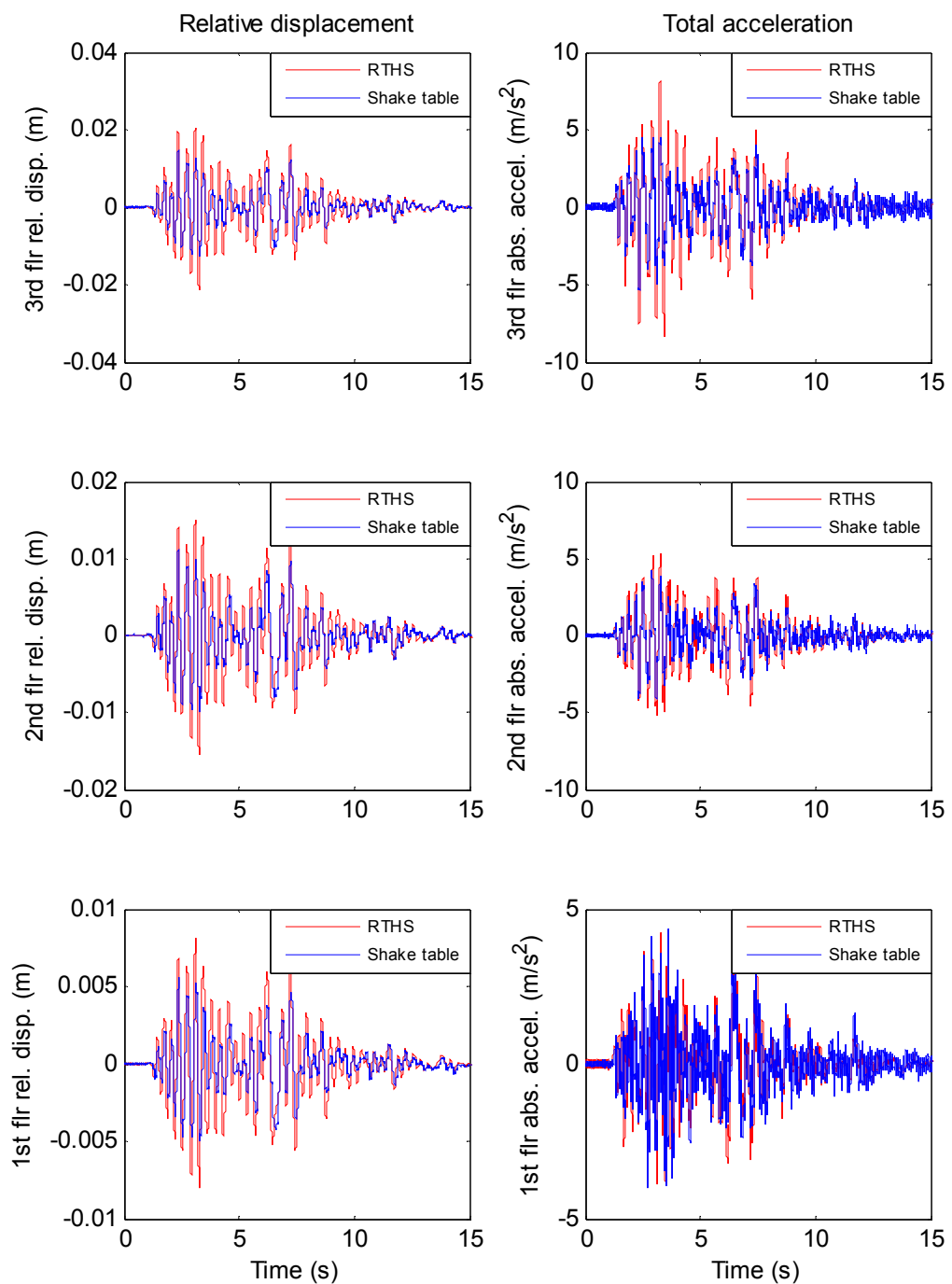


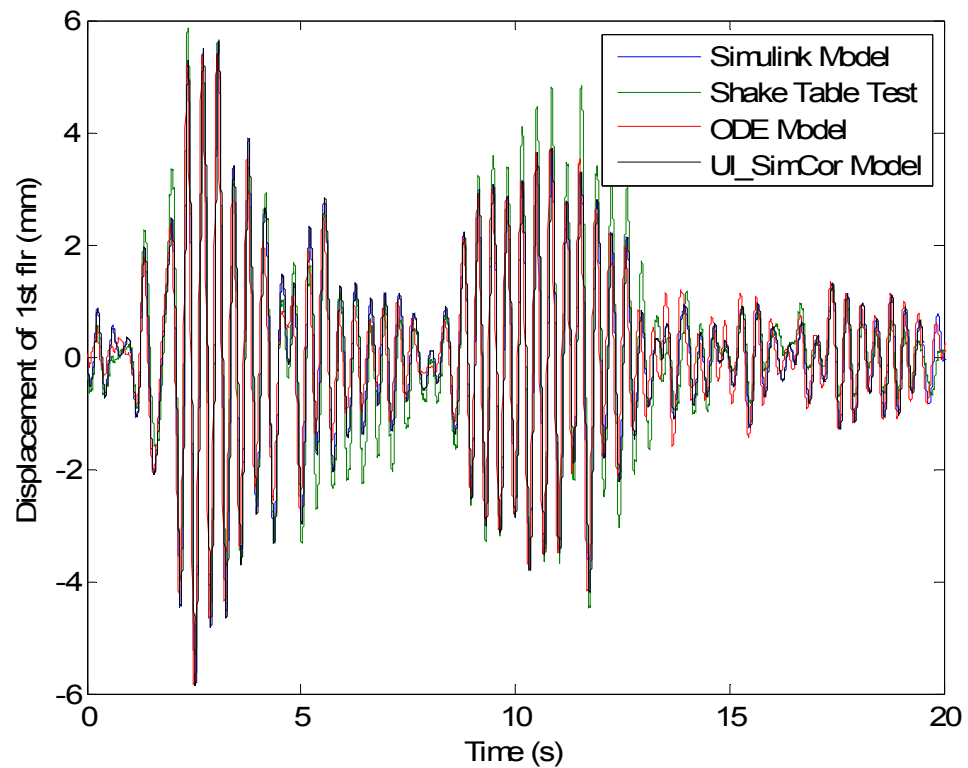
Fig. 4.38 Structural response comparison for semi-active control, Morgan Hill

4.5.4 Verification of Numerical Simulation Platforms

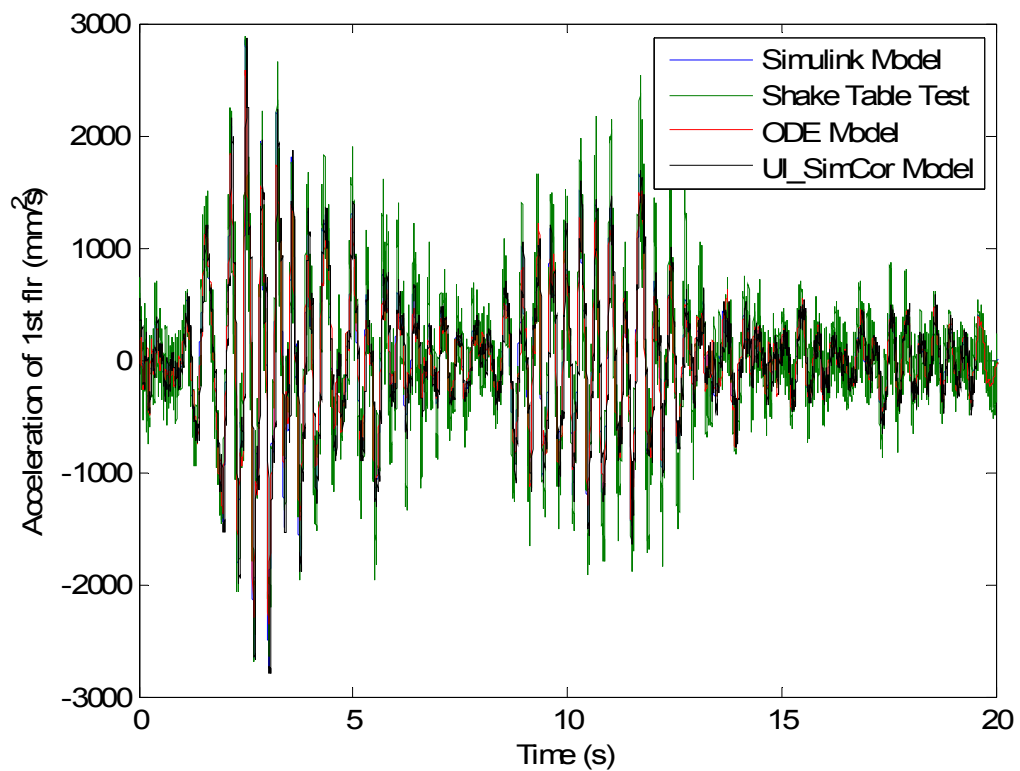
Shake table test could serve as a solid and standard validation for numerical simulations. In section 4.4, three numerical simulation platforms are introduced for the application of simulating the structural response of the test steel frame controlled by a MR damper under earthquake excitation: Matlab Simulink based platform by Purdue University, Matlab ODE solver based platform by this study, and numerical hybrid scheme based on UI_SimCor.

The first two platforms only work with the simplified 3DOF model and have their limitation of not being capable to simulate complex nonlinear structures. The numerical hybrid simulation platform introduced here, on the other hand, is more flexible and universal for the simulation of structures with control devices, since the main structure and the control devices are modeled separately and combined together by UI_SimCor to make full advantage of the modeling capability of different computational programs, such as in this study, the test structure is modeled in OpenSees with general nonlinear elements and the MR damper modeling with control algorithm implementation is fulfilled in Matlab.

The numerical simulation results from the above platforms are compared with shake table test in Fig. 4.39~4.41 for displacement and acceleration response of the structure under different control strategies (passive-off, passive-on and semi-active), which positively verifies the validity of the proposed numerical hybrid simulation scheme in efficiently developing seismic protection strategies for complex nonlinear structures.

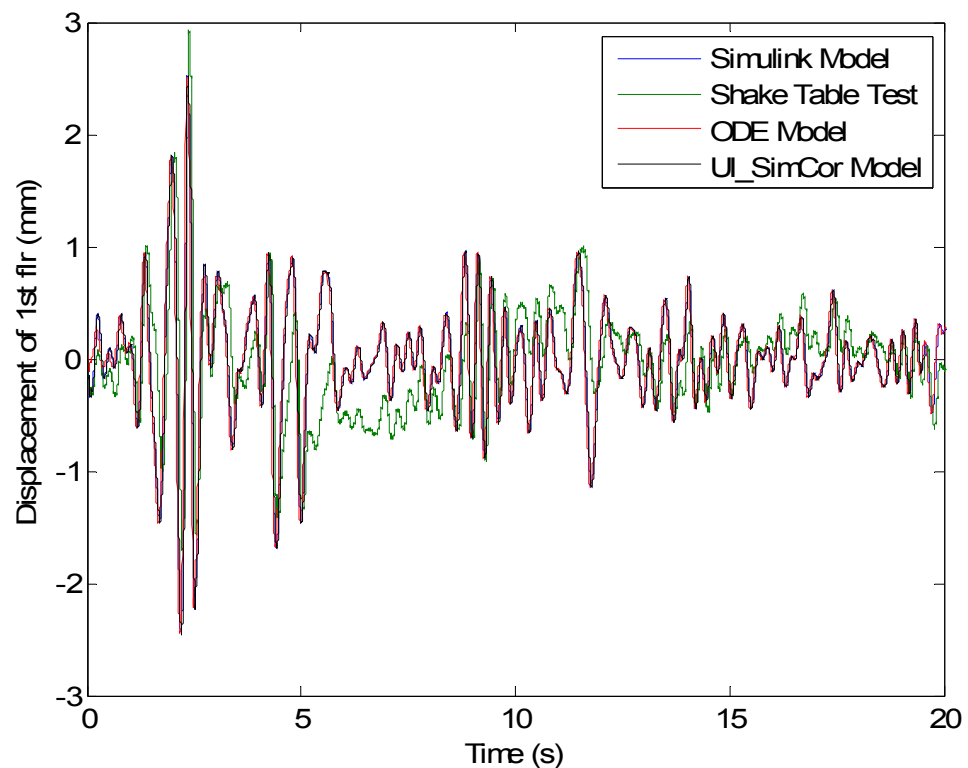


(a) Relative displacement response

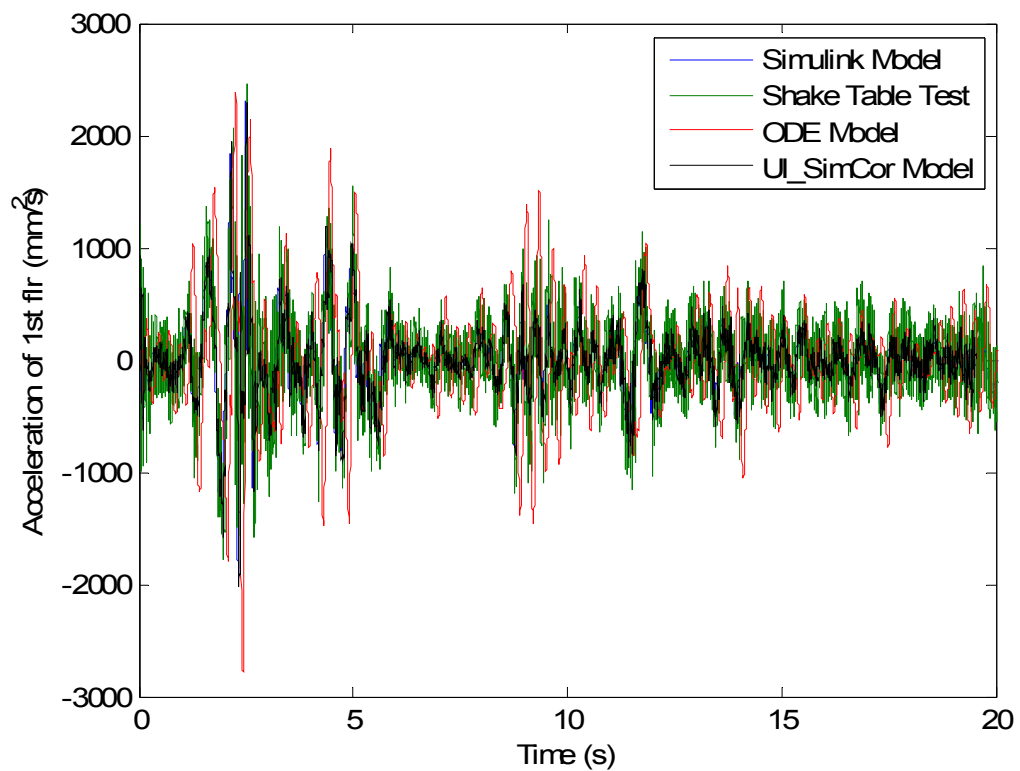


(b) Total acceleration response

Fig. 4.39 Comparison of numerical models with shake table test (Passive-off)

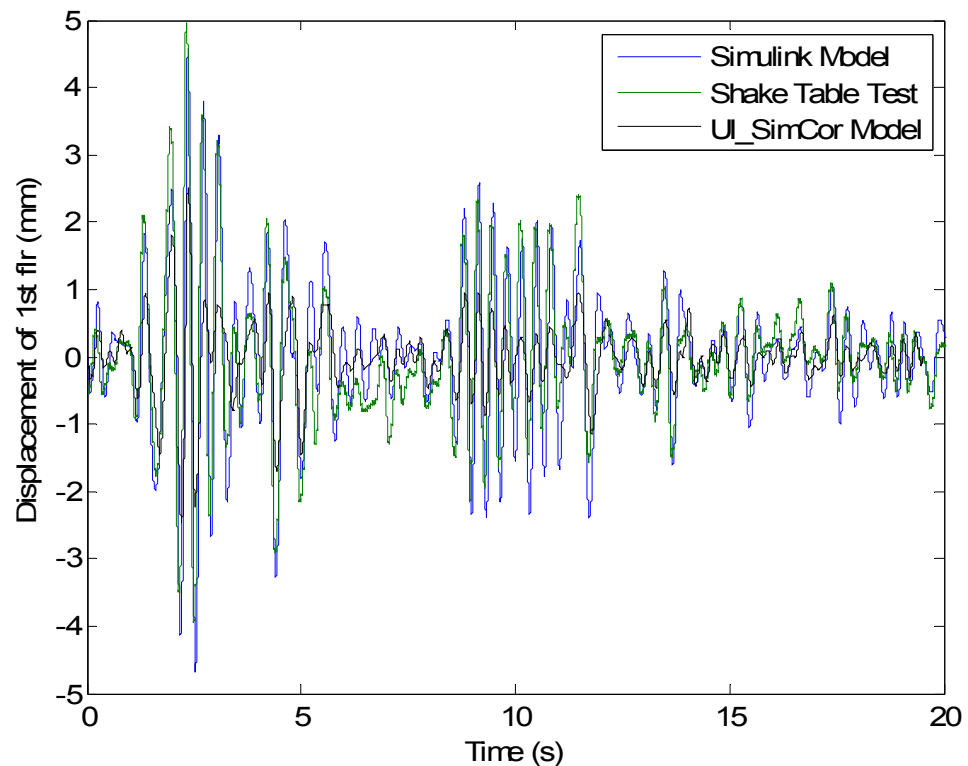


(a) Relative displacement response

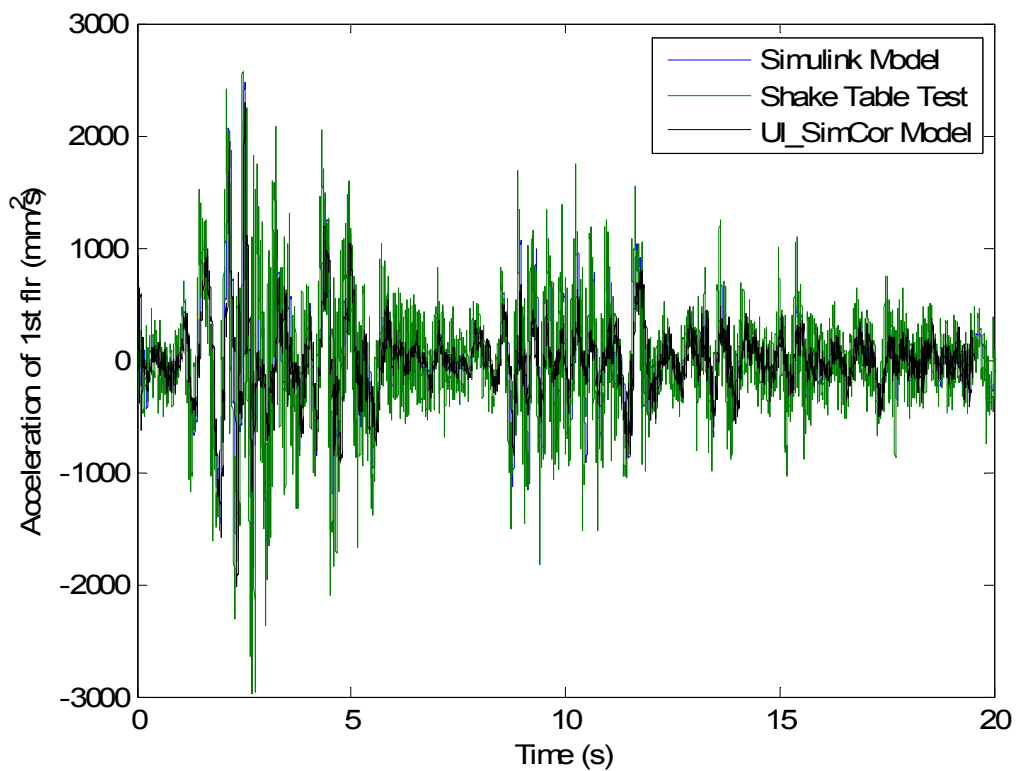


(b) Total acceleration response

Fig. 4.40 Comparison of numerical models with shake table test (Passive-on)



(a) Relative displacement response



(b) Total acceleration response

Fig. 4.41 Comparison of numerical models with shake table test (Semi-active)

4.6 Concluding Remarks

MR damper in structural control shows great potential for hazard mitigation in civil structures. Due to the complexity of MR damper, it is almost not possible to model it accurately in current FE software. The numerical hybrid simulation scheme proposed here provides an approach to isolate the MR damper to be modelled in a software that can fully simulate its behaviour while keeping other parts of a nonlinear structure numerically modelled in general FEM platform. Thus accurate numerical prediction of structural performance of complex nonlinear structures with seismic control devices and corresponding selection of optimal design parameters become possible.

UI_SimCor, which is originally developed for distributed hybrid testing, can provide an efficient way to overcome the obstacle in numerical modeling and analysis of semi-actively controlled nonlinear structures utilizing the methodology of modelling the control devices and main structure separately on different computational platforms and integrating them back together.

Four experiments on a 3-story steel frame structure are carried out in this chapter: (i) System identification test; (ii) MR damper calibration test; (iii) RTHS test and (iv) Shake table test. Numerical models used in simulation are updated according to the results of these tests. Shake table test provides the most realistic condition for physical structure and external excitation and serves as a standard for validation of the proposed numerical hybrid simulation scheme based on UI_SimCor.

It's validated by the shake table test and other numerical simulation platforms that the numerical hybrid simulation scheme proposed has a high level of accuracy and is a powerful tool to predict the dynamic response of nonlinear structure with control devices, such as MR dampers. Thus this methodology can be utilized for further structural application, i.e. numerical analysis and optimal seismic control device design for complex nonlinear

structures.

5. Implementation of Hybrid Simulation for Seismic Protection Design of Highway Bridges

Highway bridges are susceptible to various levels of damages as observed in past major earthquakes. The damages can result from insufficient force or displacement design capacity compared to excessive demands due to seismic shaking. This has imposed realistic risks for a large number of existing bridges that were designed and constructed. To minimize the negative impact of damaging earthquakes, seismic protective devices, in either passive or adaptive passive forms, can be used to improve the seismic performances of new bridges in high seismicity regions or provide reliable retrofitting for existing bridges. Thus, optimal selection of design parameters for these devices is important to utilize their advantages and achieve multi-performance objectives when subject to earthquakes with various frequency contents and intensities.

The major challenge preventing the practical application of seismic protective devices is to systematically evaluate their performance and illustrate fully the relative benefits of various devices with consistent criteria. To realize a reliable design, the properties of the seismic protective devices need to be selected carefully based on the ground motion characteristics, nonlinear dynamic behavior of structural and foundation components, soil-structure interaction, performance objectives and the consideration of inherent uncertainties.

To achieve the optimal responses using seismic protective devices, one could adopt active control theory to guide the selection of mechanical properties of passive devices. The structural control of nonlinear structures can not be easily conducted due to the difficulties in modeling of complex structures and in implementing the control algorithms within the typical finite element programs. Utilizing the hybrid simulation, the response of a complex nonlinear

structure can be obtained by integrating various numerical and physical components as well as using different computational platforms, for example, the structure is modeled in OpenSees while the seismic protective devices and the control algorithm are implemented in Matlab. Through the hybrid simulation scheme proposed in this study, time history analysis and adaptive structural control of the structures can be conducted. The result will guide the selection of passive devices for the structure to roughly mimic the behavior exhibited by adaptive devices. Taking the structural responses resulting from these control algorithms as the design target of the passive and semi-active control devices, mechanical properties of the control devices, such as damping coefficient and force hysteresis loop are determined, which is that the equivalent optimal design of passive devices is achieved.

One efficient strategy for seismic protection of bridges that the California Department of Transportation (Caltrans) is investigating through these years is the implementation of seismic protection devices such as isolation bearings and fluid dampers. The first overcrossing equipped with fluid dampers in United States is the 91/5 HOV Connector/Separator bridge in Orange County, California. There are four fluid dampers installed in addition to the elastomeric bearing pads at each end-abutment.

Concrete box girder bridges are the most common type of bridges in California. They are often used as overcrossings in highway intersections. In most cases, they are two-span overcrossings with their end-abutments supported on approaching earth-embankments and center bents supported by pile foundations. The Painter Street Bridge and Meloland Road Bridge are typical highway overcrossings of this kind.

The strong-motion response data of these two representative bridges which have been instrumented by the Strong Motion Instrumentation Program (SMIP) of the California Division

of Mines and Geology are available to the public: Painter Street Bridge that was subjected to the 1992 Petrolia earthquake and Meloland Road Bridge that was subjected to the 1979 Imperial Valley earthquake.

In this chapter the Painter Street Bridge is adopted along with its recorded data to develop and validate a procedure to analyze the seismic response of freeway overcrossings and optimally select the design parameters of their seismic protection devices. A novel methodology is developed and presented here for this purpose. Such implementation is based on accurate response assessments of bridges using nonlinear time history analysis accounting for soil-structure interaction. By establishing the relationship between the stiffness and damping properties of seismic protective devices with system level performance criteria of bridges, the optimal design is achieved with structural control theory.

The objectives of this chapter are to: 1) conduct accurate and efficient seismic response assessments of bridges; 2) develop the hybrid simulation methodology to effectively conduct the structural control of nonlinear bridge models with seismic protective devices; 3) establish the framework for optimal design of adaptive stiffness and damping properties of seismic protective devices. Through developing new methodology, simulation tools and design procedures, the performance-based implementation of seismic protective devices is achieved

5.1 Introduction of Painter Street Bridge

5.1.1 Geometry and Instrumentation

The Painter Street Overcrossing is located near Rio Dell in northern California. It is a reinforced-concrete bridge, with two spans, monolithic abutments, bent pier columns, and pile foundations for both abutments and pier columns. Its sketch is shown in Fig. 5.1. Each of the two

pier columns is supported with pile foundation consisting of 4×5 pile group and pile cap above the piles. The single pile is with 0.36m diameter and 8.0m depth, spaced with 0.91m center to center distance. The pile cap is 4.6m by 3.7m cross section, 1.1m thick, and embedded in soil with about 1.0m thick soil layer above the top of it. West abutment foundation has 1×16 pile group under the abutment wall which is 3.0m in depth, 20.6m in length and 1.0m thick in the longitudinal direction. East abutment wall has the same size but with 1×14 pile group. These abutment foundation piles are with same diameter 0.36m as those pier foundation piles. The bridge is with a 39° skew alignment for both bent and abutments axis. Accelerometers that were installed on the bridge are denoted in Fig. 5.1 by red characters as well.

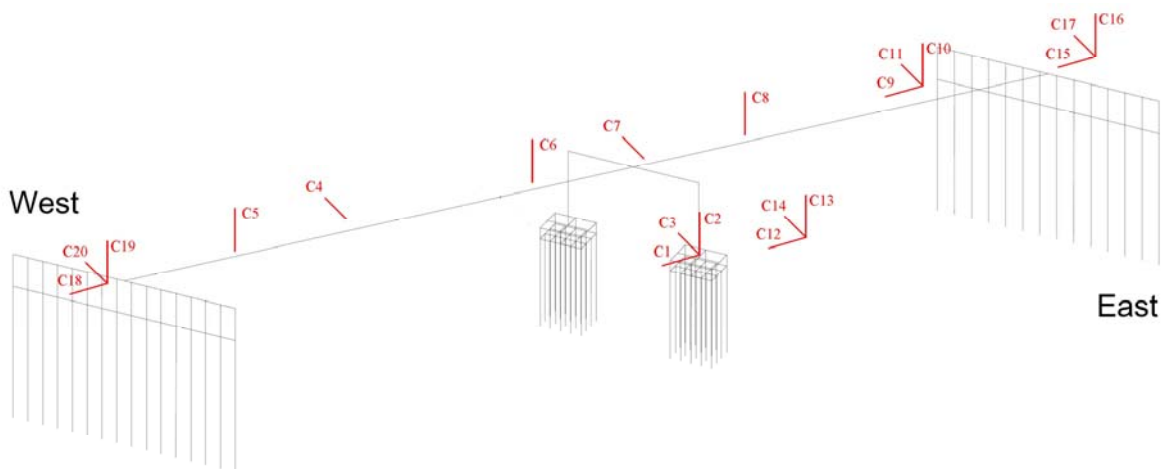


Fig. 5.1 Configuration sketch of Painter Street Bridge

On April 25, 1992, the bridge was severely shaken by the Petrolia earthquake ($M_L = 7.1$, distance to the fault $R = 18\text{km}$) with a peak transverse acceleration of 0.92g recorded on the bridge deck. Fig. 5.2 shows the plan view of the Painter Street Bridge together with the location of accelerometers. Motions were recorded in all accelerometers shown herein. Fig. 5.3 shows the free-field motions recorded with channel 12 (C12 for short) of east-west direction, C14 of north-

south direction and C13 of vertical direction. The Petrolia earthquake would be used as the external excitation for all the numerical analysis in this chapter.

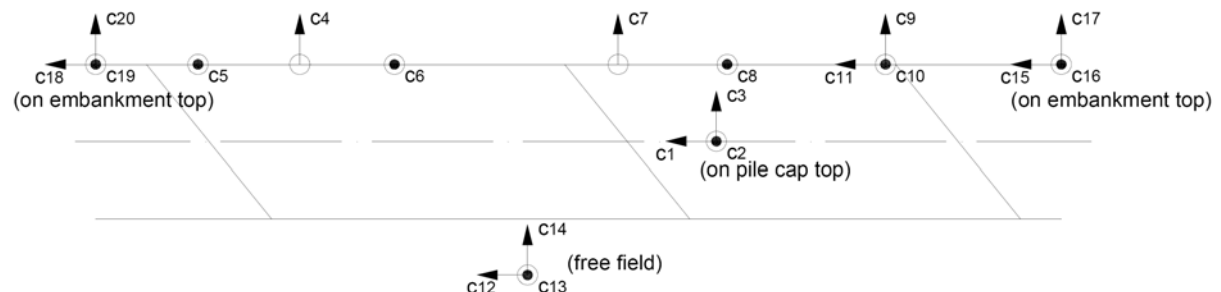


Fig. 5.2 Plan view of Painter Street Bridge and recording channel setup

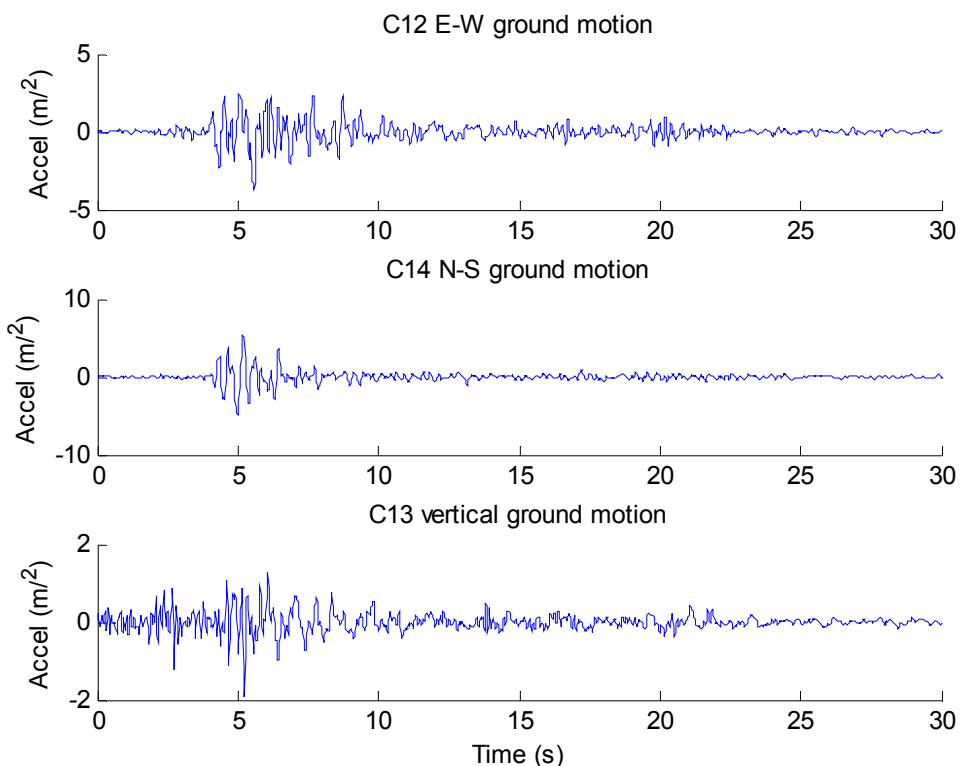


Fig. 5.3 Free field ground motion of 1992 Petrolia earthquake

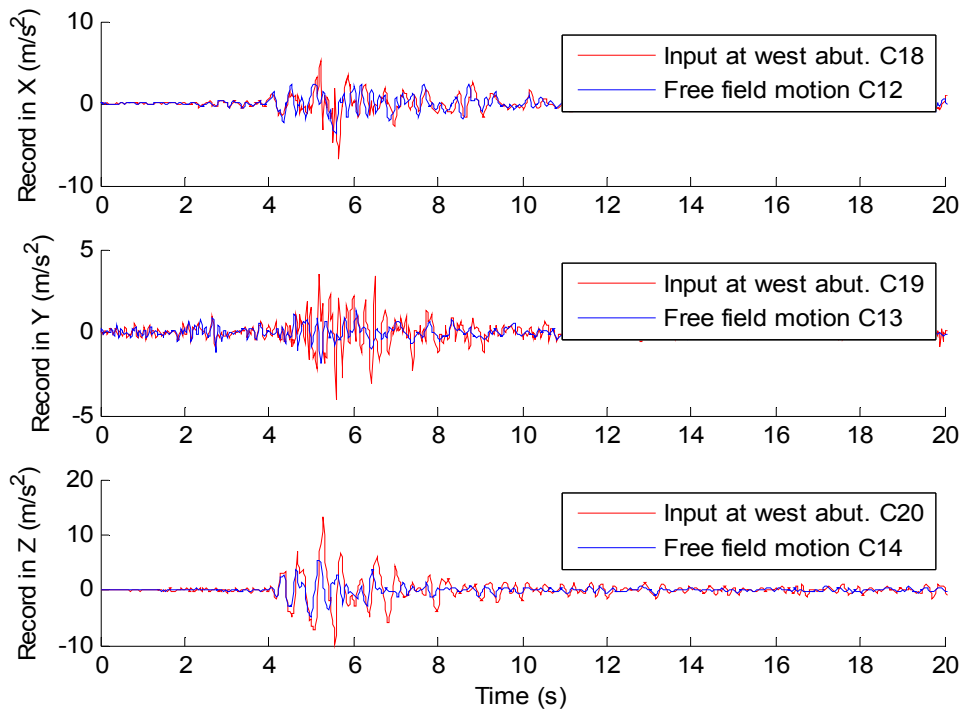
5.1.2 Soil Structure Interaction (SSI) & Kinematic Response of Embankments

Dynamic responses of pile foundation and embankment that supports the end abutment significantly affect the dynamic response of the bridge deck during strong ground shaking due to

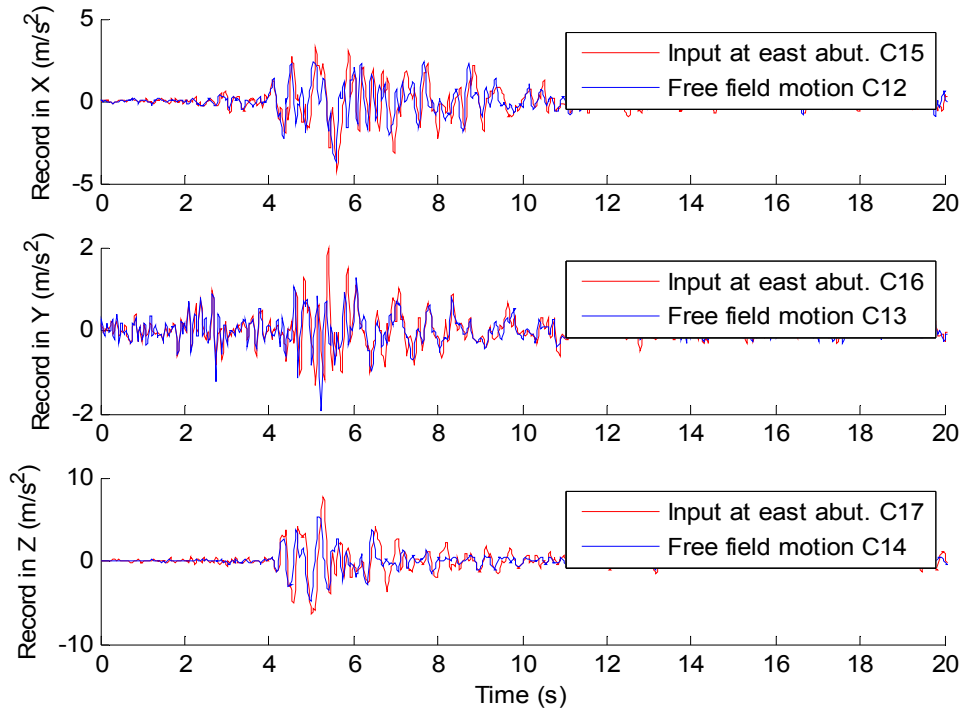
the effect of soil structure interaction. Zhang and Makris (2001, 2002) proposed a systematic approach to derive the stiffness and damping parameters of the pile foundations and embankments of highway bridge to account for the interaction of the bridge superstructure with its foundation and the surrounding soil. In Zhang and Makris' study, the presence of embankment and the pile foundation of the abutment is approximated by springs and dashpots, while the pile foundation at the center bent is approximated by an equivalent flexural-shear beam. This method is also adopted in this study to take into account the effect of soil structure interaction (SSI).

Other than introducing in stiffness and damping, the kinematic response of approaching embankments of highway bridge also amplifies the excitation input onto the structure. Recorded motions at the abutments of Painter Street Bridge reveals that the amplified motions by embankments could be as 2 times as the motions recorded at the pile cap of the center bent and the free field ground motion. Fig. 5.4 shows the comparison of the free field ground motion with the recorded motions at west and east abutments of Painter Street Bridge.

Since the excitation inputs at the abutments are quite different than the input at piles of center bent, multiple-support type of excitations must be used for dynamic analysis of highway bridges to achieve more accurate results than uniform-excitation type of input is adopted. Multiple-support type of inputs are used in this study, i.e. the inputs to west abutment for numerical analysis of Painter Street Bridge are taken as the recorded motions by channel 18, channel 19 and channel 20; inputs to the east abutment are taken as recorded motions by channel 15, channel 16 and channel 17. The inputs to center bent pile foundation could be taken as free field ground motion, since the amplification at this location is not significant.



(a) West abutment



(b) East abutment

Fig. 5.4 Amplification effect of kinematic response of embankment

5.2 Finite Element (FE) Modeling: Platform and Methodology

5.2.1 FE Model of Original Painter Street Bridge

Several researchers have carried out numerical analysis for Painter Street Bridge through finite element simulation. Maragakis and Jennings (1987) introduced a “stick model” enhanced with bilinear “springs” and “dashpots” at its support of skewed overpasses to take into account the effects on bridge dynamic response from soil-structure interaction (SSI). Another comprehensive study by McCallen and Romstad (1994) established the validity of the stick model through computing the natural frequencies, mode shapes and response time histories of the Painter Street Bridge. Other researchers (Zhang and Makris 2001) also practiced with more complex and detailed 3D model by ABAQUS and compared the analysis results with those from the stick model. The comparison revealed the effectiveness and simplicity of the stick model by showing a good agreement with the analysis of detailed 3D models. In this study, general purpose finite element software OpenSees is adopted to construct a similar stick type FE model for all numerical analysis and simulation of Painter Street Bridge herein.

Among the main structure of Painter Street Bridge, including pier columns, bent beams, deck and abutments, pier columns are modeled with ‘dispBeamColumn’ element, while all the others are modeled with ‘elasticBeamColumn’ element in OpenSees. The presence of pile foundations and approach embankments of the abutments is approximated by rate-independent springs and dashpots to take soil structure interaction into account. Particularly, the pile foundations of the pier columns are modeled as equivalent flexural-shear beams (Zhang and Makris 2001). Fig. 5.5 sketches the stick type finite element model of Painter Street Bridge used in this study and the property of SSI springs and dashpots is summarized in Table 5.1.

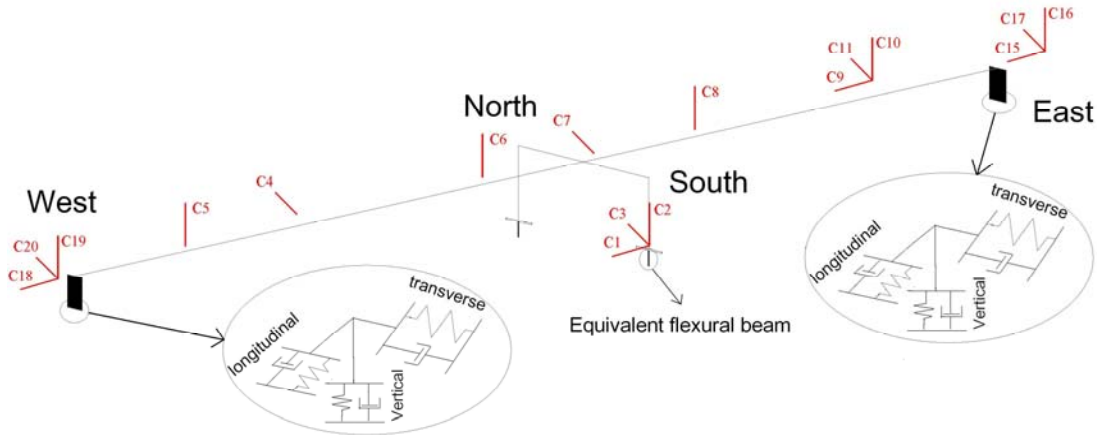


Fig. 5.5 Finite element stick model of Painter Street Bridge

Table 5.1 SSI springs and dashpots of Painter Street Bridge

Location	West abutment		East abutment	
	K (MN/m)	C (MN·s/m)	K (MN/m)	C (MN·s/m)
Translational	317.0	17.5	317.0	17.5
Longitudinal	317.0	18.1	317.0	18.1
Vertical	1360.0	73.2	1360.0	73.2

5.2.2 FE model of Painter Street Bridge with Base Isolation

Based on the knowledge in the previous section, a FE model is developed to simulate the Painter Street Bridge equipped with base isolation devices. The isolation devices are installed at the top of the pier columns and abutments, thus the superstructure (deck + bent beams) is isolated from the underneath supporting elements. As a result, the forces due to strong ground shaking is isolated from the supporting elements as well, which gives significant response benefits for both pier columns and the deck, i.e. relative displacement reduction of pier columns and total acceleration reduction of deck. Fig. 5.6 illustrates the setup of base isolation devices in Painter Street Bridge.

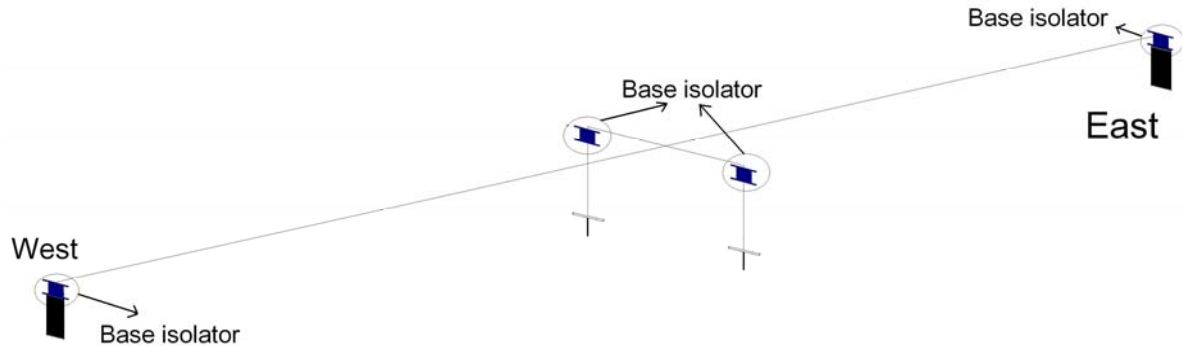


Fig. 5.6 Base isolator setup for Painter Street Bridge

As demonstrated in Chapter 3, hybrid simulation scheme can be implemented to simulate structures with seismic protective devices. This would provide us a more flexible way to model any kind of devices separately utilizing specialized tools for certain purpose, such as control toolbox in Matlab for structural control application. In this study, hybrid simulation scheme based on UI_SimCor platform is used to model Painter Street Bridge equipped with base isolators. The main structure of this hybrid simulation, which is modeled in OpenSees, contains all the elements from the original bridge except that the deck is separated from the piers and abutments due to base isolation. The base isolators are modeled separately in Matlab as the substructure. The main structure and substructure connect and communicate with each other during numerical simulation process through platform UI_SimCor. Fig. 5.7 illustrates this hybrid simulation scheme to model base isolated Painter Street Bridge.

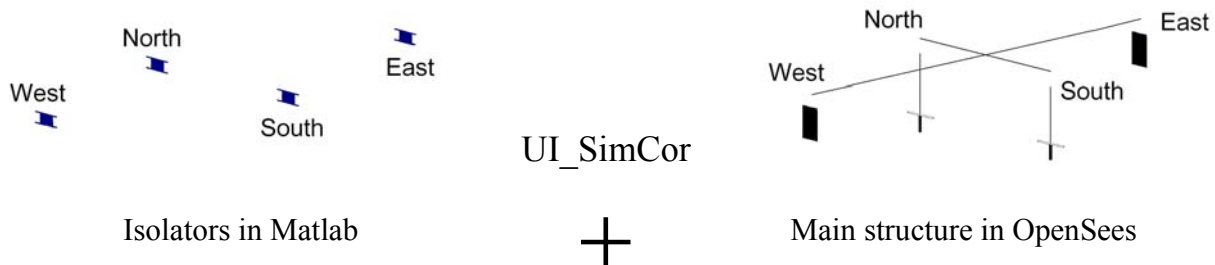


Fig. 5.7 Hybrid model of Painter Street Bridge with base isolators

5.2.3 FE model of Painter Street Bridge with Base Isolation & MR damper

While base isolation has been in structural application for years, supplemental damping devices are being considered as an effective fellow technique together with base isolation to create more robust resistance to strong earthquake for civil engineering structures. Chang et al. (2002) examined the effects of base isolation along with fluid dampers on rigid structures experimentally and analytically. The study found supplemental damping to be effective in reducing both displacement and base shear for structures that have moderately long periods. In this study, MR dampers and semi-active control technique are applied to the base isolated Painter Street Bridge shown in the previous section to further improve the structural response. Fig. 5.8 illustrates the base isolators and MR dampers set on this model. It's seen that each isolator is associated with 2 MR dampers, which are distributed in transverse and longitudinal direction respectively.

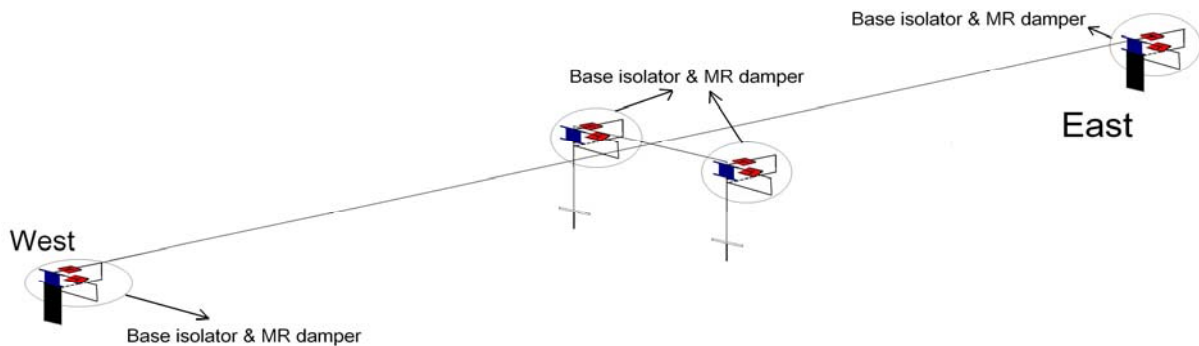


Fig. 5.8 Base isolator and MR damper setup for Painter Street Bridge

Similarly, hybrid simulation scheme is implemented to analyze the seismically protected Painter Street Bridge in Fig. 5.8. Again, the main structure of this hybrid simulation, which is modeled in OpenSees, contains all the elements from the original bridge except that the deck is separated from the piers and abutments. The base isolators and MR dampers are modeled

separately in Matlab as the substructure. The main structure and substructure connect and communicate with each other in simulation through UI_SimCor. Fig. 5.9 illustrates this hybrid simulation scheme to model the bridge equipped with both base isolators and MR dampers.

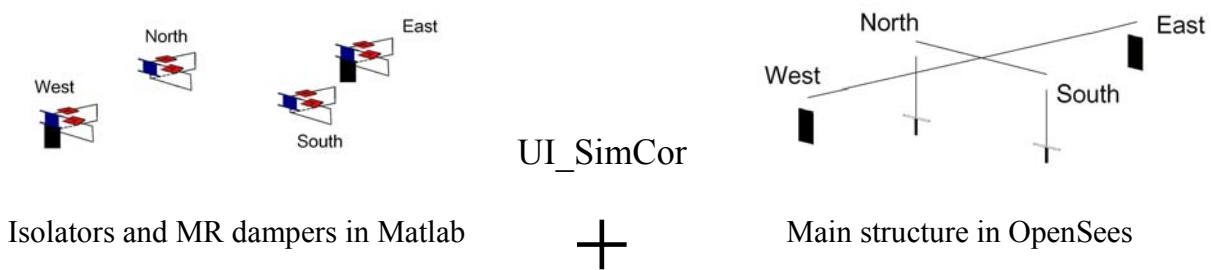


Fig. 5.9 Hybrid model of Painter Street Bridge with base isolators and MR dampers

5.3 Validation of the Stick Type FE model of Painter Street Bridge

A hybrid simulation scheme is introduced in section 5.2 for modeling Painter Street Bridge of different protective device configurations. It's noted that the bridge itself is modeled in OpenSees throughout the numerical analysis of hybrid simulation in this chapter. Therefore, it's necessary to verify the validity and accuracy of the stick type FE model by OpenSees for the bridge.

5.3.1 Validation by ABAQUS

A stick type FE model of Painter Street Bridge is separately established in the general finite element software ABAQUS. This serves as the 1st validation for the model by OpenSees. Fig. 5.10 shows the comparison of the structural responses from these two computational platforms, in terms of total displacement and total acceleration at the deck-center and east deck-end. The good agreement for both transverse (along global X axis) and longitudinal (along global Y axis) direction certifies that the OpenSees model is valid in the sense of FE simulation.

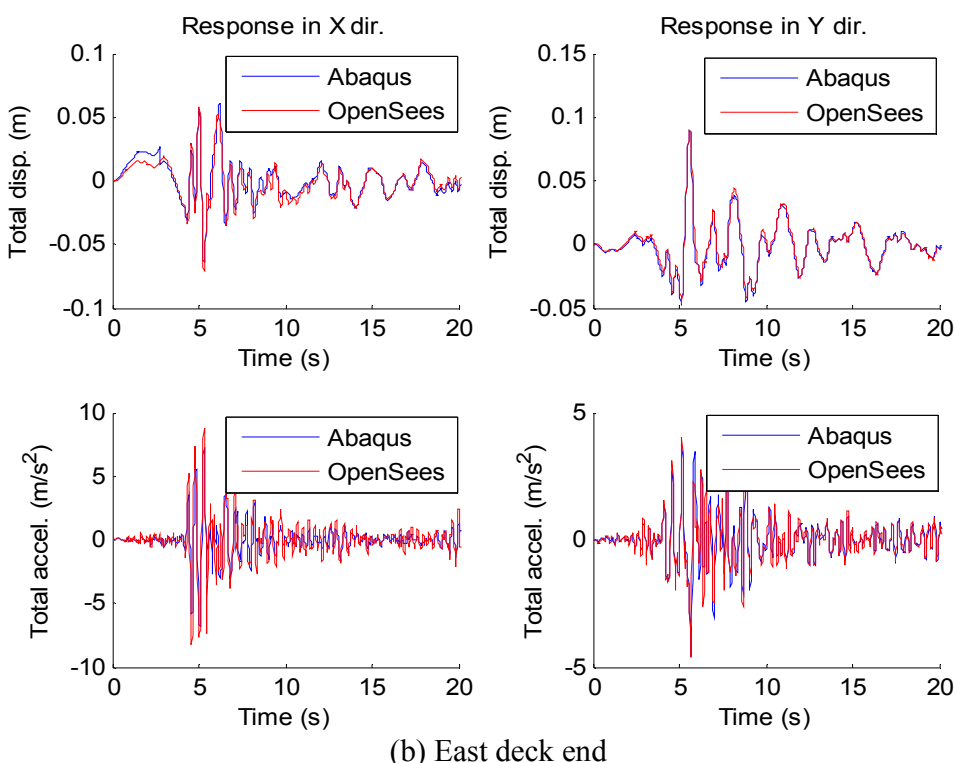
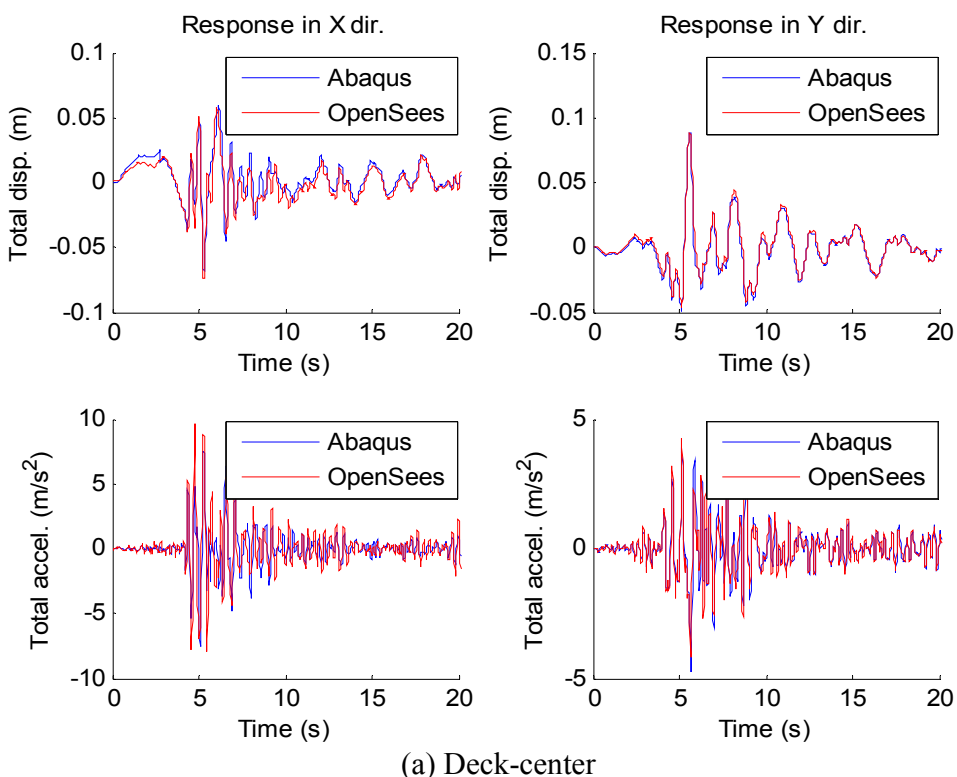
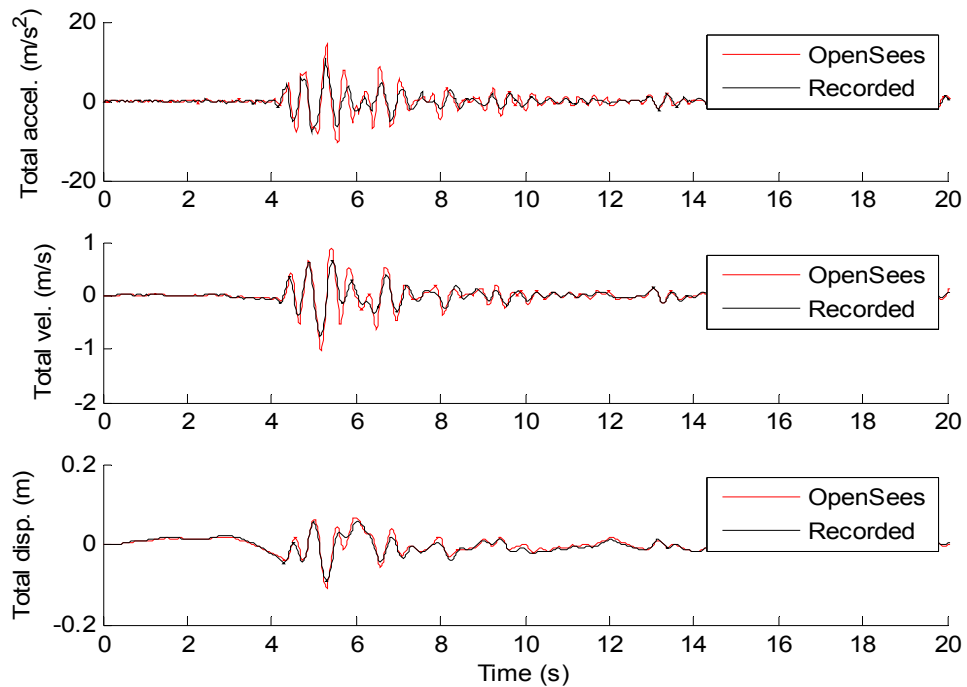


Fig. 5.10 Total displacement and acceleration response comparison

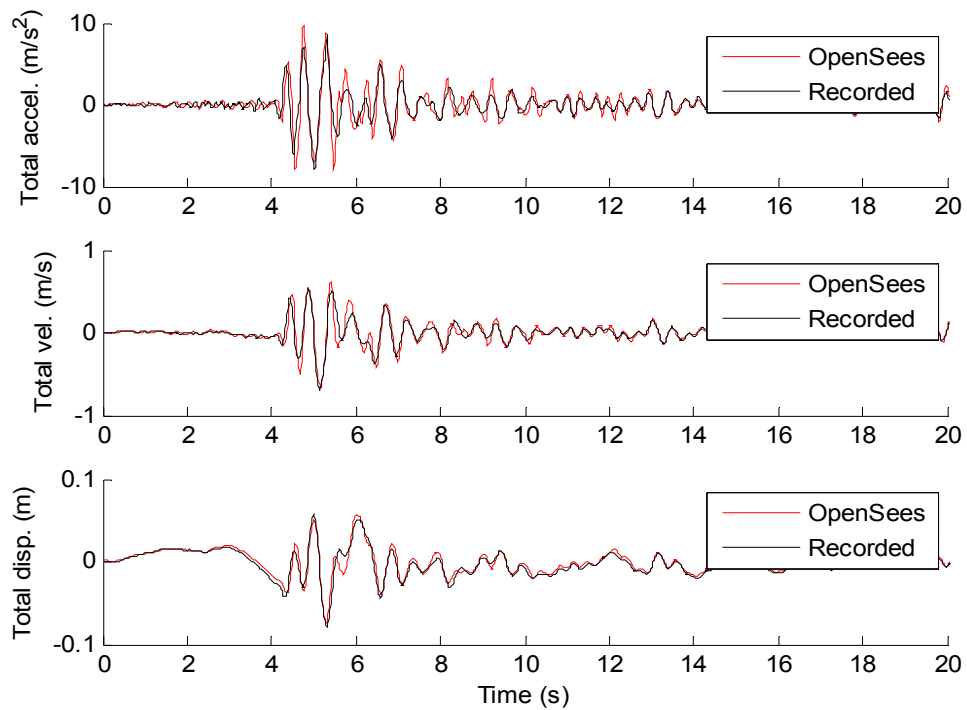
5.3.2 Validation by Recorded Motion

As shown in Fig. 5.2, channel 4 (C4) recorded the transverse (global X axis) acceleration near the west deck end; channel 7 (C7) recorded the transverse (global X axis) acceleration near the deck center; C9 and C11 recorded the transverse and longitudinal (global Y axis) accelerations near the east deck end respectively. The structural response computed by the stick type FE model in OpenSees is compared with these four sets of recorded data in Fig. 5.11. The velocity and displacement with legend ‘Recorded’ in the figure are calculated through numerical integration of corresponding directly measured acceleration data. It’s seen from all the record channels that the recorded motions at different locations all take good agreement with those computed by the stick type FE model adopted in OpenSees. Thus, we can conclude that the stick model by OpenSees is valid and accurate for the future application of hybrid simulation.

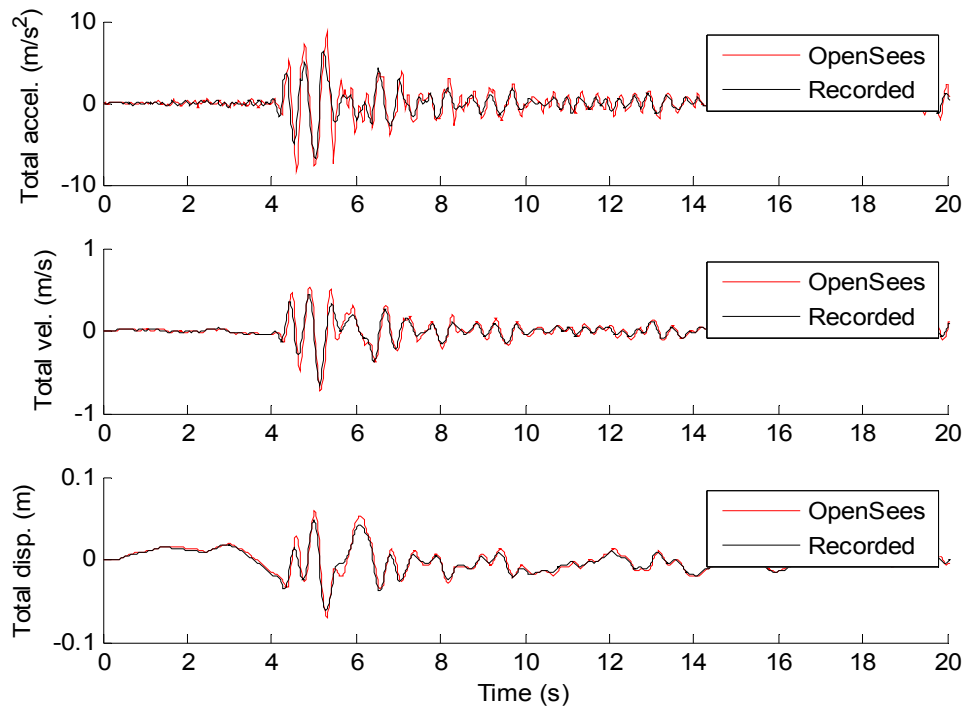


(a) Channel 4

Fig. 5.11 Verification of numerical simulation results with recorded motions

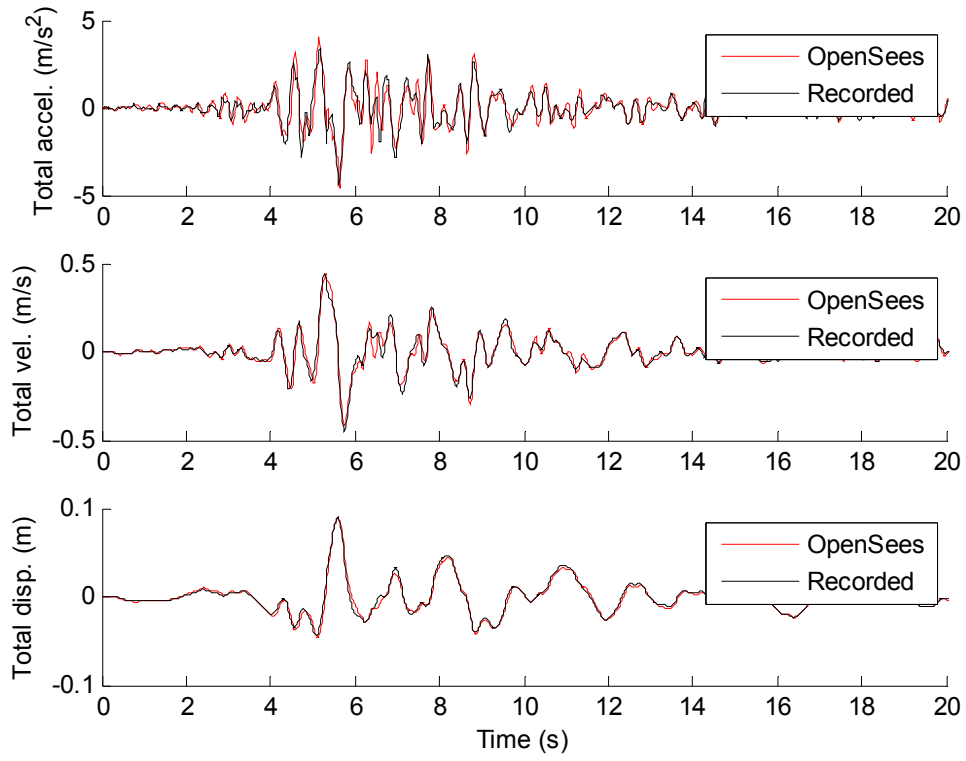


(b) Channel 7



(c) Channel 9

Fig. 5.11(cont.) Verification of numerical simulation results with recorded motions



(d) Channel 11

Fig. 5.11(cont.) Verification of numerical simulation results with recorded motions

5.4 Design of Base Isolation of Painter Street Bridge

5.4.1 Bilinear Model of Base Isolation Devices

Seismic isolation devices show significant effectiveness in improving the seismic response of bridges. Three most common types of isolation device are elastomeric bearing (ERB), lead-rubber bearing (LRB) and friction pendulum bearing (FPS). Fig. 5.12 shows the basic configuration and the corresponding cyclic behavior of these isolation devices. Although their behaviors are different from each other, one can use a bilinear model as shown in Fig. 5.13 to represent their behavior (Naeim and Kelly 1999). The bilinear model can be completely described by the elastic stiffness K_1 , characteristic strength Q and post-yielding stiffness K_2 .

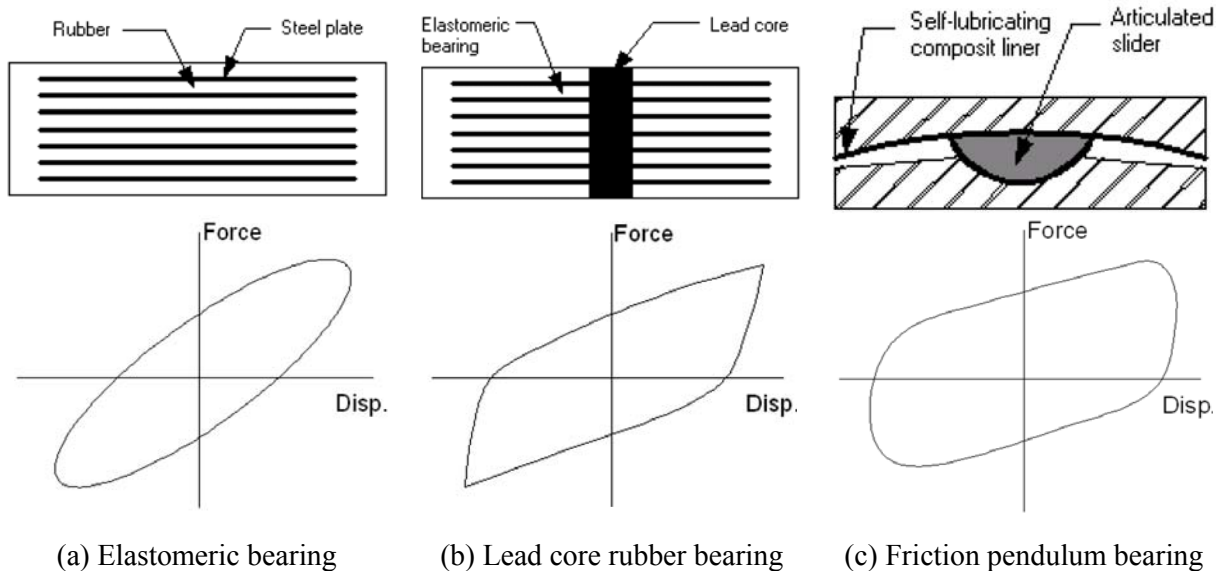


Fig. 5.12 Configuration and cyclic loop of commonly used base isolators

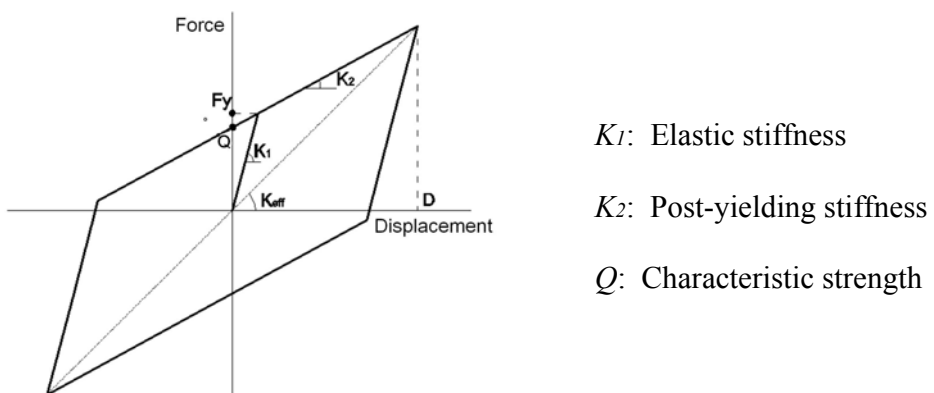


Fig. 5.13 Bilinear cyclic model for base isolators

The approach to determine the parameters of bilinear model for commonly used isolators is summarized hereafter. The ratio between the elastic stiffness K_1 and post-yielding stiffness K_2 is referred as post-yielding ratio denoted by $N = K_1/K_2$. This parameter varies for different kinds of isolation devices.

For ERB, the post-yielding stiffness K_2 is determined by the area (A), total thickness ($\sum t_r$) and shear modulus (G) of rubber slices, i.e. $K_2 = GA / \sum t_r$; the characteristic strength Q

can be obtained by assuming a yielding displacement $u_y = (0.05 \sim 0.1) \sum t_r$; the post yielding ratio is often taken as 1/15~1/5.

For LRB, the Q can be calculated from yielding strength of lead core F_y . The post-yielding stiffness K_2 is similar to that of the elastomeric bearing but multiplied by a factor between (1.15~1.20) to account for the additional stiffness contribution from the lead core; the elastic stiffness K_1 is usually 15~30 times of the post-yielding stiffness K_2 , i.e. $N=1/30 \sim 1/15$.

For FPS, the friction coefficient (μ_s) and sliding surface radius (R) determines the characteristic strength, $Q=\mu_s W$ and post-yielding stiffness $K_2=W/R$, where W is the vertical load or structural weight. The FPS has a very rigid pre-yielding stiffness, which is often taken as 50~100 times the post-yielding stiffness K_2 .

5.4.2 Eigenvalues And mode Shapes of Painter Street Bridge

Zhang and Makris (2001) performed eigenvalue analysis with the stick FE model and the first six modes and modal frequencies of the stick model are summarized in Fig. 5.14. As shown in Fig. 5.14, the 1st mode exhibits transverse and anti-symmetric vertical shape; the 2nd mode exhibits anti-symmetric vertical and torsion about vertical axis; the 3rd mode exhibits torsion about vertical axis and symmetric vertical; the 4th mode exhibits symmetric vertical and longitudinal; the 5th mode exhibits longitudinal; and the 6th mode exhibits second transverse and torsion about longitudinal axis. Since the 1st mode contains the first transverse structural response, the base isolator design in the later section would be based on this mode only.

5.4.3 Preliminary Design of Base Isolation Device

Base isolation of bridge in general aims at two main structural benefits: reduction of total acceleration of bridge deck, and the drift/relative displacement of bridge piers. A preliminary

base isolation design is presented in this section. The base isolators is designed towards the 1st mode of the bridge since it's the first transverse mode informed by the eigenvalue analysis of Painter Street Bridge. Fig. 5.7 shows the base isolation device layout: two base isolators are installed on the top of the piers which isolate the piers from the above bent beams; another two base isolators are installed on top of the abutments which separate the abutments from the above bridge deck.

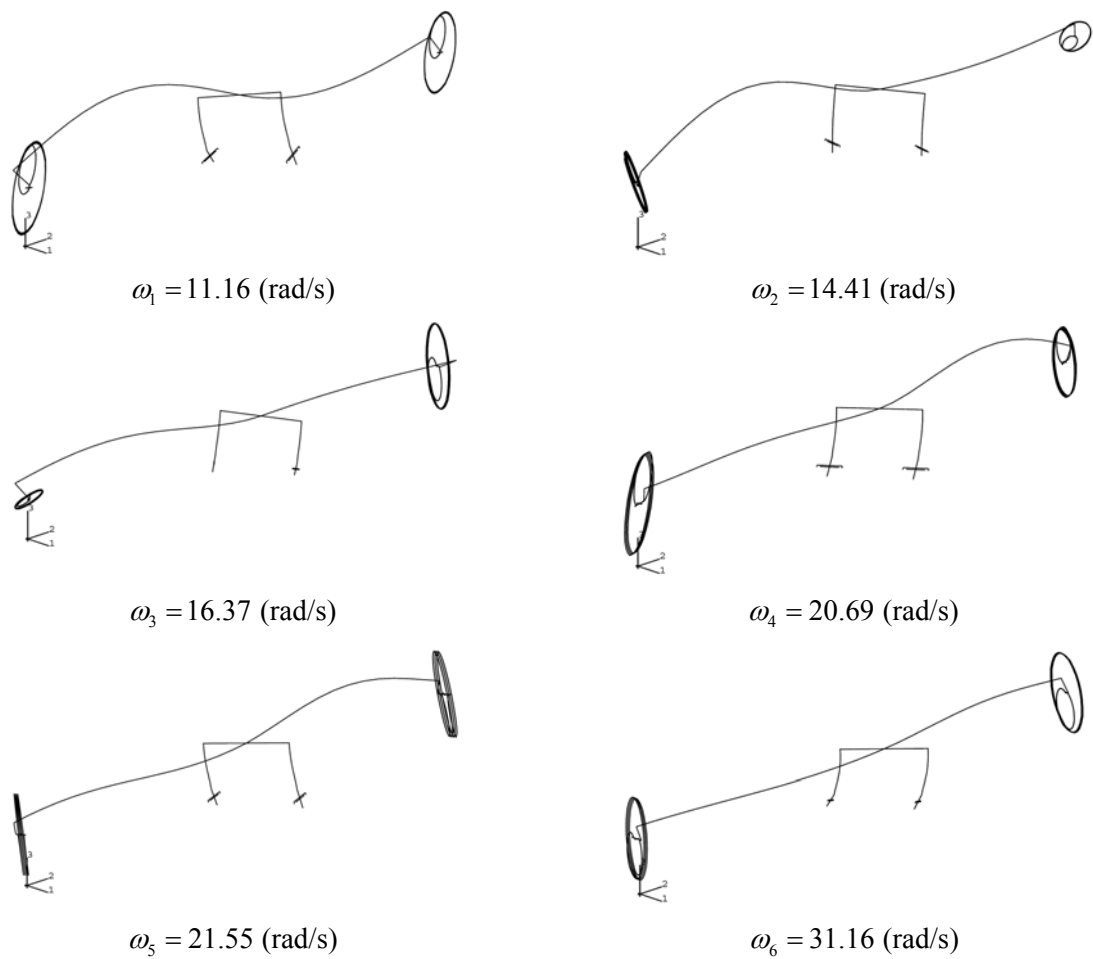


Fig. 5.14 Modal shape and frequency of Painter Street Overcrossing

Since the base isolators are designed based on the 1st transverse mode of Painter Street Bridge, it's reasonable to assume the based isolated bridge to be a single degree of freedom

structure supported by the bridge piers. Thus, one can have the following relation:

$$\frac{K_c}{K_{b2}} = \frac{\omega_l^2}{\omega_{tgt}^2} \quad (5.1)$$

where K_c is the total initial stiffness of the piers, K_{b2} is the total post-yielding stiffness of the 4 isolators, ω_l is the 1st mode frequency of the bridge and ω_{tgt} is the target frequency of the bridge that is base isolated. K_c can be obtained by a pushover analysis of the bridge piers in OpenSees. The pushover response of the piers is illustrated in Fig. 5.15. K_c reads as the initial slope of the pushover curve.

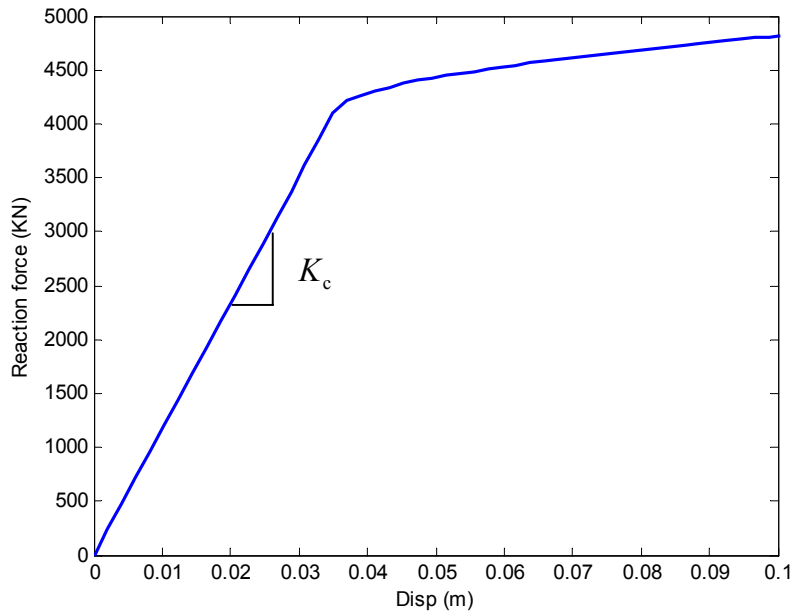


Fig. 5.15 Pushover analysis of piers in Painter Street Overcrossing

In equation (5.1), ω_l and K_c are known from the pushover and eigenvalue analysis, if one selects the target frequency towards which the base isolated bridge is designed, the total post-yielding stiffness of the isolators K_{b2} can be calculated accordingly by equation (5.1). Here the target frequency ω_{tgt} is selected in such a way that the correspondent target period takes the value of 1s and 2s, which yields a stiffer and a softer design for base isolation devices.

The complete definition of the bilinear curve for modeling the base isolators as shown in Fig. 5.13 requires also the evaluation of elastic stiffness K_{b1} and characteristic strength Q . The Q value can be calculated by equation (5.2) which provides a reasonable distribution of seismic forces along the structure with good control of displacements (Ghobarah and Ali 1988)

$$Q = 0.05W \quad (5.2)$$

where $W = 1.70 \times 10^4$ KN is the weight of superstructure (deck + bent beams) above the bearings for Painter Street Bridge. By further assuming the post-yielding ratio of the bearings to be $N = 0.1$, the bilinear cyclic behavior of the bearings is completely defined. Table 5.2 lists the modeling parameters for the bearings used for numerical simulation in this study. In the table, K_{b1} , u_y and F_y are the elastic stiffness, yielding displacement and yielding force of the bearings, respectively.

Table 5.2 Modeling parameters of base isolators

Target period T_{tgt} (s)	K_c (KN/m)	K_{b2} (KN/m)	K_{b1} (KN/m)	Q (KN)	u_y (m)	F_y (KN)
1	117200	37148.77	371487.67	849.04	0.003	943.37
2	117200	9287.19	92871.92	849.04	0.010	943.37

5.4.4 Numerical Simulation of Base Isolated Painter Street Bridge

With the isolator properties obtained in section 5.4.3, numerical analysis is performed for Painter Street Bridge equipped with base isolators as shown in Fig. 5.5. The analysis is completed by two approaches: (1) the whole bridge including base isolators is modeled completely in OpenSees; (2) the analysis is done with the hybrid simulation scheme illustrated in Fig. 5.6. The results from these two methods are expected to echo each other and serve as a validation of the proposed hybrid simulation scheme. Numerical analysis here is based on two design cases defined in the previous section: $T_{tgt} = 1$ s (referred as case I hereafter) and $T_{tgt} = 2$ s (referred as case II hereafter).

Fig. 5.16 presents the base isolator responses, while Fig. 5.17 compares pier drift and deck center total acceleration from the hybrid simulation with that of the complete OpenSees model, for design case II. Excellent agreement is observed of these two methods, which shows the validity of the hybrid simulation scheme proposed here.

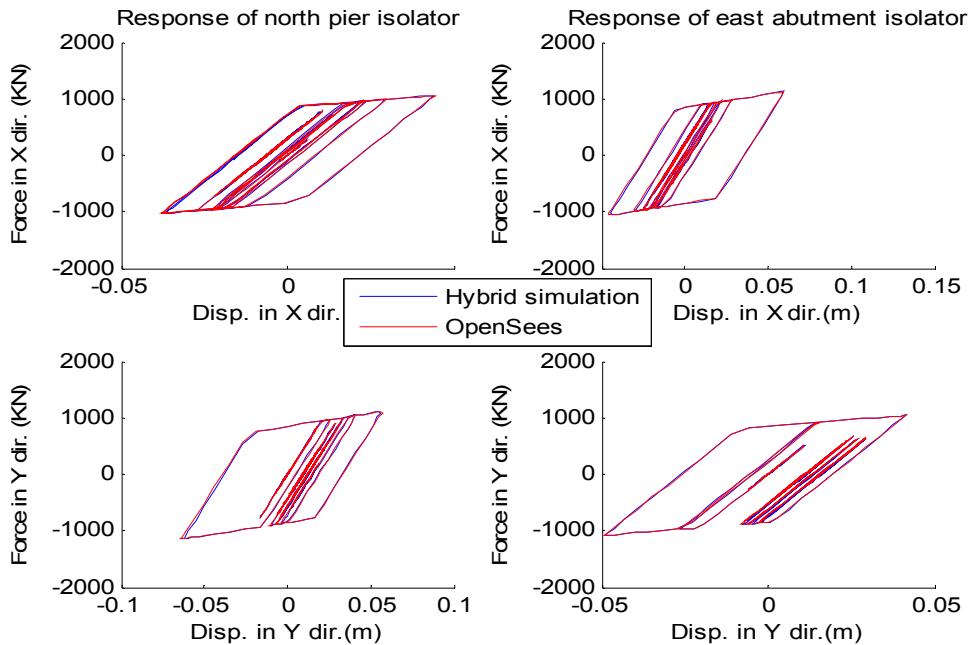


Fig. 5.16 Base isolator response of design case II

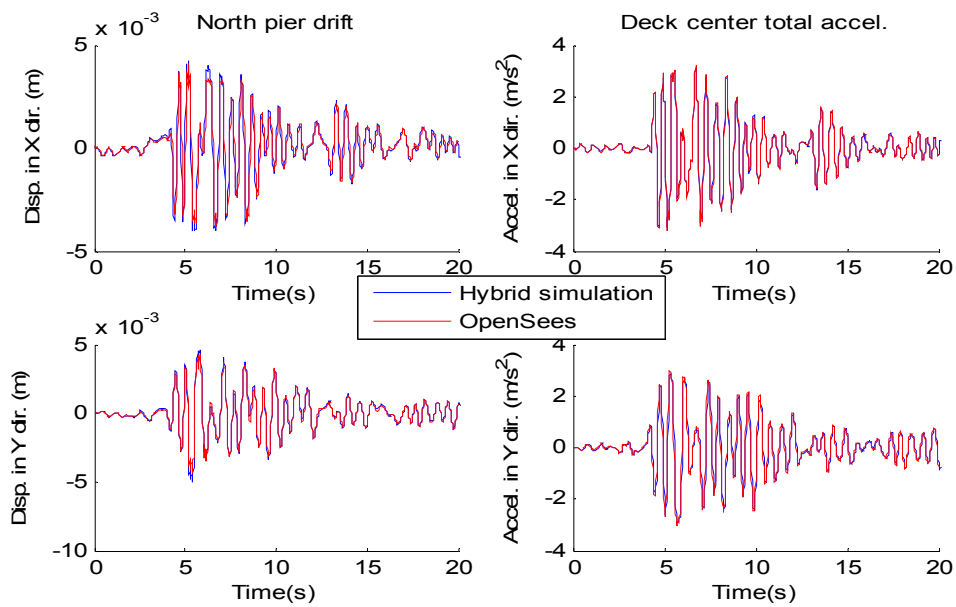


Fig. 5.17 Pier and deck response of design case II

Fig. 5.18 and 5.19 present the same structural responses but with the comparison between base isolation design case I and II. The target period of design case II is 2 seconds which is twice as that of design case I. This leads to a softer isolation design under which the seismic forces transferred to both superstructure and substructure are limited to a low level, resulting in reduction of both pier drift and deck acceleration. Although it best addresses our interest, the cost of higher level of protection for the main structure is that the isolation devices would experience significantly larger deformation which is not practical in certain situations. Therefore, the effectiveness of base isolation on bridges is limited to the allowable deformation of base isolators.

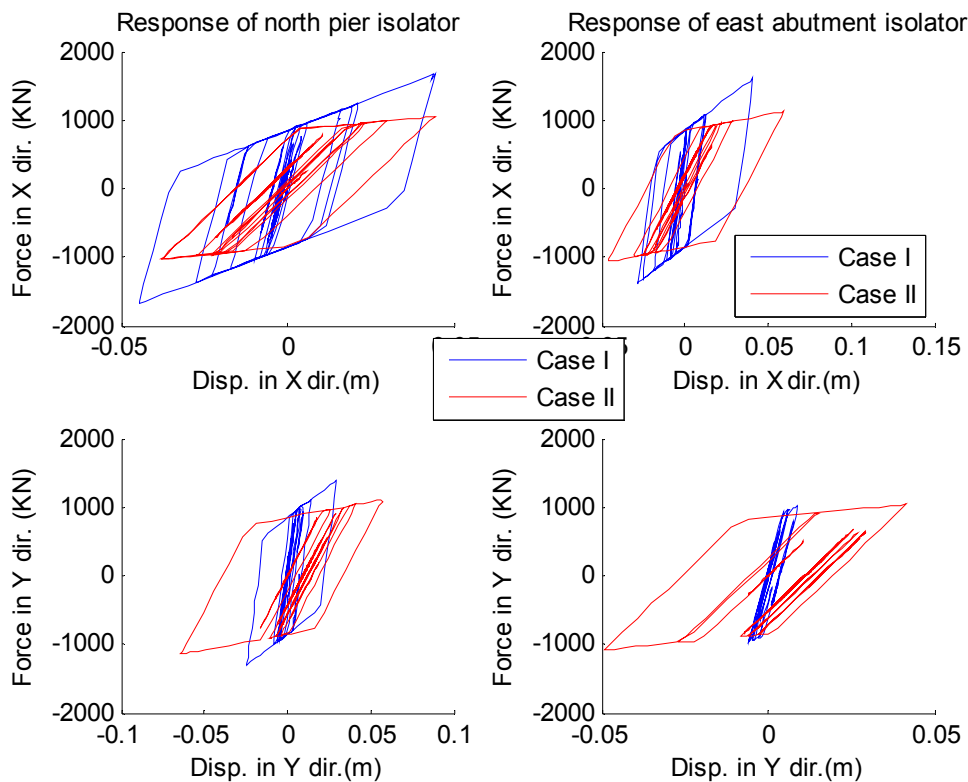


Fig. 5.18 Base isolator response comparison of design case I and II

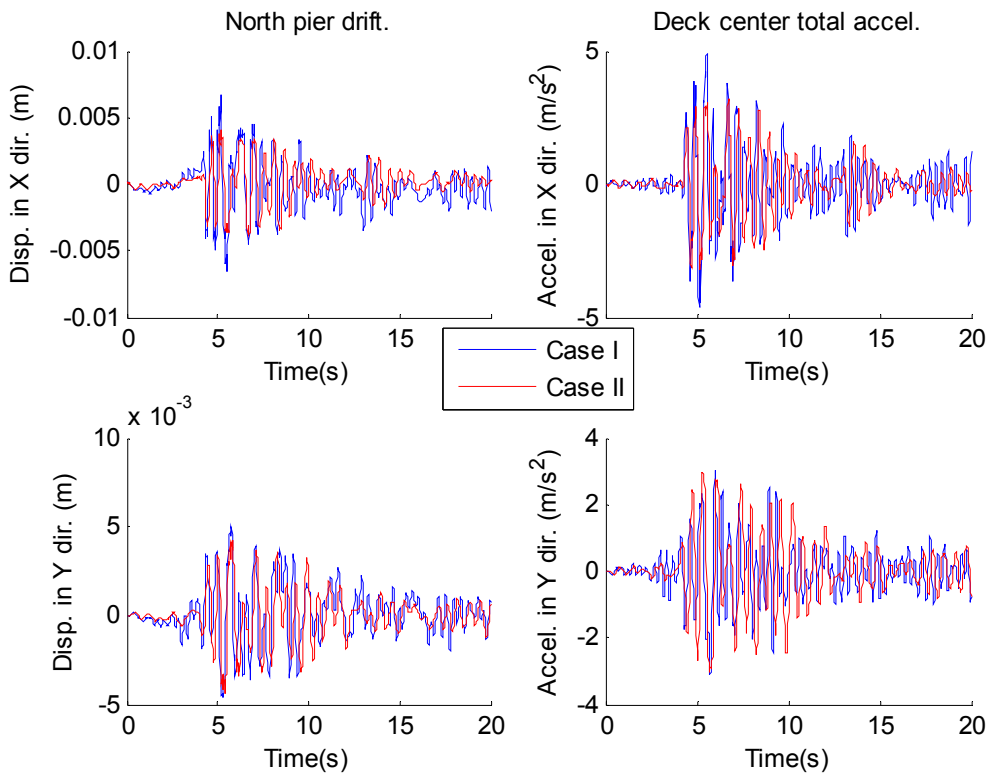


Fig. 5.19 Pier and deck response comparison of design case I and II

5.5 MR Damper Design of Base Isolated Painter Street Bridge: Semi-active Control Development and Application

In this section, seismically protected Painter Street Bridge by base isolation and MR dampers, as illustrated in Fig. 5.8, is modeled and analyzed with hybrid simulation scheme in UI_SimCor. The base isolation devices, MR dampers along with a semi-active control algorithm, are implemented in Matlab, while the main bridge structure is modeled in OpenSees as the previous applications. Total eight MR dampers are installed to four locations of the bridge associated with the base isolators. Each location has two MR dampers built in X and Y direction respectively. The locations on the bridge of MR damper #1~#8 are explained in Table 5.3.

Table 5.3 MR damper installation location

Set in X dir.	#1	#3	#5	#7
	@ north pier	@ south pier	@ west abutment	@ east abutment
Set in Y dir.	#2	#4	#6	#8
	@ north pier	@ south pier	@ west abutment	@ east abutment

5.5.1 Derivation of Optimal Control Force for MR Dampers

Assuming the highway bridge equipped with MR dampers is kept in linear region, the equation of motion (EOM) can be written in a general form as follow:

$$\mathbf{M}\ddot{\mathbf{X}}(t) + \mathbf{C}\dot{\mathbf{X}}(t) + \mathbf{K}\mathbf{X}(t) = \mathbf{Ef}(t) + \boldsymbol{\Gamma}\mathbf{F}_{\text{mr}}(t) \quad (5.3)$$

where \mathbf{M} , \mathbf{C} , \mathbf{K} are the mass, damping and stiffness matrices, and \mathbf{X} is the total displacement vector. This total displacement representation is used when ground excitation takes a multiple-support form. $\mathbf{f}(t)$ is the external force vector computed based on input excitations. \mathbf{E} is the coefficient matrix of $\mathbf{f}(t)$ which equals to identity matrix if \mathbf{X} is total displacement. $\mathbf{F}_{\text{mr}}(t)$ is the MR damper force vector whose each component represents a force of a MR damper in the structure. $\boldsymbol{\Gamma}$ matrix reflects the installation locations of the MR dampers through distributing the MR damper forces to corresponding structural degree of freedoms.

When base isolation devices are installed on the bridge, their effect can be included by adding their initial stiffness to the global stiffness matrix \mathbf{K} . Rewrite Eq. (5.3) into state space formulation with state vector $\mathbf{Z}(t)$, we get:

$$\dot{\mathbf{Z}}(t) = \mathbf{AZ}(t) + \mathbf{BF}_{\text{mr}}(t) + \mathbf{Gf}(t), \quad \mathbf{Z}(t) = \begin{bmatrix} \mathbf{X}(t) \\ \dot{\mathbf{X}}(t) \end{bmatrix} \quad (5.4)$$

where the matrices \mathbf{A} , \mathbf{B} and \mathbf{G} have the following forms:

$$\mathbf{A} = \begin{bmatrix} \mathbf{0} & \mathbf{I} \\ -\mathbf{M}^{-1}\mathbf{K} & -\mathbf{M}^{-1}\mathbf{C} \end{bmatrix}, \quad \mathbf{B} = \begin{bmatrix} \mathbf{0} \\ \mathbf{M}^{-1}\boldsymbol{\Gamma} \end{bmatrix}, \quad \mathbf{G} = \begin{bmatrix} \mathbf{0} \\ \mathbf{M}^{-1}\mathbf{E} \end{bmatrix} \quad (5.5)$$

Structural control design requires acquisition of partial measurement of the structural response in terms of displacement and acceleration. The measurement vector $\mathbf{y}(t)$ could be written as:

$$\mathbf{y}(t) = \mathbf{C}_m \mathbf{Z}(t) + \mathbf{D}\mathbf{F}_{mr}(t) + \mathbf{H}\mathbf{f}(t) \quad (5.6)$$

where the components of matrices \mathbf{C}_m , \mathbf{D} and \mathbf{H} are determined by what measurements of structural response are set in the measurement vector $\mathbf{y}(t)$. Eq. (5.4) and (5.6) constitute the general form of a LQG control design problem, whose system plant is expressed as:

$$\begin{cases} \dot{\mathbf{Z}}(t) = \mathbf{A}\mathbf{Z}(t) + \mathbf{B}\mathbf{F}_{mr}(t) + \mathbf{G}\mathbf{f}(t) \\ \mathbf{y}(t) = \mathbf{C}_m \mathbf{Z}(t) + \mathbf{D}\mathbf{F}_{mr}(t) + \mathbf{H}\mathbf{f}(t) \end{cases} \quad (5.7)$$

where $\mathbf{f}(t)$ serves as the disturbance in the LQG control process, and $\mathbf{F}_{mr}(t)$ serves as the control force for which we want to design and obtain its optimization. The optimal control force from MR damper is derived in such a way that the following performance index is minimized:

$$J = \int_0^{t_f} [\mathbf{y}^T(t)\mathbf{Q}\mathbf{y}(t) + \mathbf{F}_{mr}^T(t)\mathbf{R}\mathbf{F}_{mr}(t)] dt \quad (5.8)$$

where \mathbf{Q} and \mathbf{R} are the weighting matrices for measured structural response and control force given by MR damper, respectively. The time interval $[0, t_f]$ is defined to be longer than that of the external excitation duration. The optimal control force is calculated by:

$$\mathbf{F}_{mr,c}(t) = -\mathbf{K}_c \mathbf{Z}(t) \quad (5.9)$$

where $\mathbf{F}_{mr,c}$ is the desired optimal force vector, and \mathbf{K}_c is the LQG design gain matrix which can be computed by the command ‘lqry’ of Matlab control toolbox:

$$\mathbf{K}_c = \text{lqry}(\mathbf{A}, \mathbf{B}, \mathbf{C}_m, \mathbf{D}, \mathbf{Q}, \mathbf{R}) \quad (5.10)$$

In Eq. (5.9), it's noted that the state vector $\mathbf{Z}(t)$ is required to calculate the optimal control force during the control process. However, the complete knowledge of the structural

response in a control process is most likely not available due to the limitation of measurements. Therefore it's necessary to get an optimal estimation of the state vector using the known information, i.e., available measurements at certain locations of the structure: $\mathbf{y}(t)$. Kalman filter (also known as Kalman estimator) can provide an optimal estimation of the state vector $\mathbf{Z}(t)$ with the input of $[\mathbf{y}(t); \mathbf{F}_{\text{mr}}(t)]$. The state estimation $\hat{\mathbf{Z}}(t)$ is obtained through:

$$\dot{\hat{\mathbf{Z}}}(t) = \hat{\mathbf{A}}\hat{\mathbf{Z}}(t) + \hat{\mathbf{B}}\mathbf{Y} \quad (5.11)$$

where $\hat{\mathbf{A}}$, $\hat{\mathbf{B}}$ and \mathbf{Y} are given by

$$\hat{\mathbf{A}} = \mathbf{A} - \mathbf{L}\mathbf{C}_m, \quad \hat{\mathbf{B}} = [\mathbf{L} \quad \mathbf{B} - \mathbf{L}\mathbf{D}], \quad \text{and} \quad \mathbf{Y} = [\mathbf{y}(t); \mathbf{F}_{\text{mr}}(t)] \quad (5.12)$$

Kalman observation gain matrix \mathbf{L} can be calculated by the command 'lqew' of Matlab control toolbox :

$$\mathbf{L} = \text{lqew}(\mathbf{A}, \mathbf{G}, \mathbf{C}_m, \mathbf{H}, \mathbf{W}, \mathbf{V}) \quad (5.13)$$

where \mathbf{W} and \mathbf{V} are the disturbance covariance matrix and measurement noise covariance matrix, respectively. They can be determined by trials for maximum control effectiveness.

With the state estimator $\hat{\mathbf{Z}}(t)$ obtained, one can now calculate the optimal control force by the estimation of the true state $\hat{\mathbf{Z}}(t)$:

$$\mathbf{F}_{\text{mr,c}}(t) = -\mathbf{K}_c\hat{\mathbf{Z}}(t) \quad (5.14)$$

The above procedure can be explained intuitively by Fig. 5.20.

5.5.2 Semi-active Control Algorithm of MR Damper: Clipped-Optimal Control

Although derived with the background of highway bridge controlled by MR dampers, the optimal control force in section 5.5.1 takes a general form that applies to any linear system

regulated by fully adaptive control forces. However, control force generated by MR damper still holds the passive characteristics which cannot provide the exact desired optimal control force stated in Eq. (5.14). To induce MR damper to generate approximately the demanded optimal force, a type of clipped-optimal controller based on acceleration feedback is adopted herein. This control algorithm has shown its success in many structural control applications of civil engineering (Dyke et al. 1996).

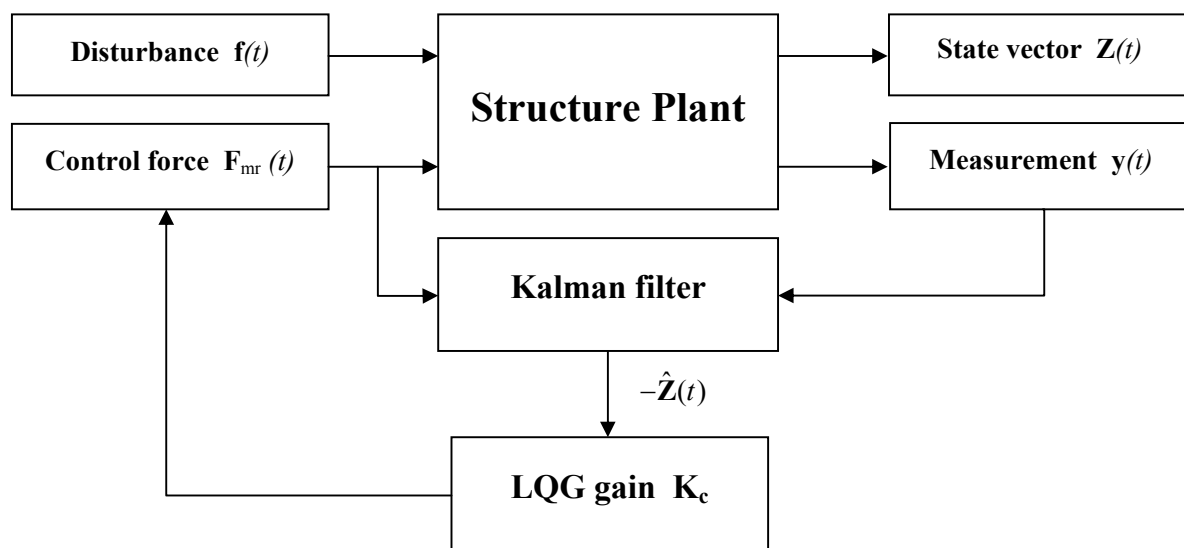


Fig. 5.20 Optimal control force estimation process

Accelerometers can provide reliable and inexpensive measurement of accelerations at arbitrary locations on the structure. In this study, the measurements used for control force determination are the accelerations of selected points on the structure, the displacements of the MR dampers and the measurements of the control forces provided by the MR dampers.

Clipped-Optimal control algorithm is to append a force feedback loop to induce the MR damper to produce approximately a desired control force. It's noted that the force generated by the MR damper cannot be commanded; only the voltage applied to the current driver for the MR

damper can be directly changed. To induce the MR damper to generate approximately the desired optimal control force, the command signal is selected as follows: when the MR damper is providing the desired optimal force, the voltage applied to the damper should remain at the present level; if the magnitude of the force produced by the damper is smaller than the magnitude of the desired optimal force and the two forces have the same sign, the voltage applied to the current driver is increased to the maximum level so as to increase the force produced by the damper to match the desired control force. Otherwise, the commanded voltage is set to zero. This Clipped-Optimal control algorithm can be stated as

$$\mathbf{v} = U_{\max} H \left\{ \left(\mathbf{F}_{mr,c} - \mathbf{F}_{mr} \right) \mathbf{F}_{mr} \right\} \quad (5.15)$$

where \mathbf{v} is command voltage vector, $\mathbf{F}_{mr,c}$ is the desired optimal force vector and \mathbf{F}_{mr} is the corresponding true measurement. U_{\max} is the voltage to the current driver associated with saturation of the magnetic field in the MR dampers and $H\{\bullet\}$ is the Heaviside step function.

5.5.3 Evaluation of System Matrices/Vectors Required in Optimal Controller Design

As stated previously, Matlab is used to design the optimal controller for the bridge with MR dampers as control devices. Several system matrices or vectors need to be evaluated or determined before one can perform the controller design. They are:

$$\mathbf{A}, \mathbf{B}, \mathbf{Y}, \mathbf{C}_m, \mathbf{D}, \mathbf{G}, \mathbf{H}, \mathbf{Q}, \mathbf{R}, \mathbf{W} \text{ and } \mathbf{V} \quad (5.16)$$

The meanings of the above matrices/vectors have been explained in the correspondent sections of this chapter. Among all these matrices/vectors:

A and **B** are calculated by Eq. (5.5) with system matrices **M**, **C** and **K** which can be generated in the simulation platform UI_SimCor.

$$\mathbf{G} = \begin{bmatrix} \mathbf{0} \\ \mathbf{M}^{-1}\mathbf{E} \end{bmatrix} \text{ where } \mathbf{E} \text{ equals to identity matrix } \mathbf{I} \text{ when system EOM is expressed in the}$$

way of total displacement.

$$\mathbf{Y} = \begin{bmatrix} \mathbf{y}(t) \\ \mathbf{F}_{\text{mr}}(t) \end{bmatrix} \text{ where } \mathbf{y}(t) \text{ and } \mathbf{F}_{\text{mr}}(t) \text{ are evaluated as follows:}$$

$$\mathbf{y}(t) = \begin{bmatrix} \text{Deck center total acceleration in X direction} \\ \text{Deck center total acceleration in Y direction} \\ \text{West abutment total acceleration in X direction} \\ \text{West abutment total acceleration in Y direction} \\ \text{East abutment total acceleration in X direction} \\ \text{East abutment total acceleration in Y direction} \\ \text{Displacement of MR damper located at north pier in X direction} \\ \text{Displacement of MR damper located at north pier in Y direction} \\ \text{Displacement of MR damper located at south pier in X direction} \\ \text{Displacement of MR damper located at south pier in Y direction} \\ \text{Displacement of MR damper located at west abutment in X direction} \\ \text{Displacement of MR damper located at west abutment in Y direction} \\ \text{Displacement of MR damper located at east abutment in X direction} \\ \text{Displacement of MR damper located at east abutment in Y direction} \\ \text{North pier drift in X direction} \\ \text{North pier drift in Y direction} \\ \text{South pier drift in X direction} \\ \text{South pier drift in Y direction} \end{bmatrix}_{18 \times 1} \quad (5.17)$$

$$\mathbf{F}_{\text{mr}}(t) = \begin{bmatrix} \text{Force of MR damper located at north pier in X direction} \\ \text{Force of MR damper located at north pier in Y direction} \\ \text{Force of MR damper located at south pier in X direction} \\ \text{Force of MR damper located at south pier in Y direction} \\ \text{Force of MR damper located at west abutment in X direction} \\ \text{Force of MR damper located at west abutment in Y direction} \\ \text{Force of MR damper located at east abutment in X direction} \\ \text{Force of MR damper located at east abutment in Y direction} \end{bmatrix}_{8 \times 1} \quad (5.18)$$

$\mathbf{F}_{\text{mr}}(t)$ and $\mathbf{y}(t)$ are measured in real time and feedback to the Kalman filter to estimate the state vector which is further used to evaluate the optimal control force in Eq. (5.14). The

components of $\mathbf{y}(t)$ are chosen based on two criteria: (1) Easy to measure and available in the physical real world, such as the total acceleration and MR damper displacement components; (2) Aim to minimize, such as the deck center accelerations and pier drifts. Since $\mathbf{y}(t)$ is used to estimate the whole state vector $\mathbf{Z}(t)$, it should include as many measurements as possible in the real world application. $\mathbf{F}_{\text{mr}}(t)$ has the dimension of 8×1 because there are total 8 MR dampers are set on the bridge model.

\mathbf{C}_m , \mathbf{D} , and \mathbf{H} are dependent of the components in $\mathbf{y}(t)$ and derived reversely by making the equilibrium $\mathbf{y}(t) = \mathbf{C}_m \mathbf{Z}(t) + \mathbf{D} \mathbf{F}_{\text{mr}}(t) + \mathbf{H} \mathbf{f}(t)$ satisfied.

Weighting/covariance matrices \mathbf{Q} , \mathbf{R} , \mathbf{W} and \mathbf{V} can be determined by trials and evaluated with values that result in the best structural response.

5.5.4 Numerical Simulation of Semi-active Control of MR Dampers on Painter Street Bridge

Recall those discussed in Chapter 3 and illustrated in Fig. 5.21 again, modified Bouc-Wen model gives good approximation of MR damper behavior and can be used to model MR dampers numerically.

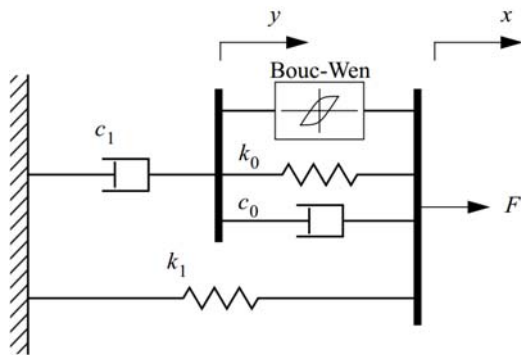


Fig. 5.21 Modified Bouc-Wen model of MR damper

$$F = c_1 \dot{y} + k_1(x - x_0) \quad (5.19)$$

$$\dot{y} = \frac{1}{c_0 + c_1} [\alpha z + c_0 \dot{x} + k_0(x - y)] \quad (5.20)$$

$$\dot{z}(t) = -\gamma |\dot{x} - \dot{y}| z |z|^{n-1} - \beta (\dot{x} - \dot{y}) |z|^n + A(\dot{x} - \dot{y}) \quad (5.21)$$

Among the parameters contained in Eq. (5.19)~(5.21), x_0 , k_0 , k_1 , γ , β , A and n are evaluated as constants, while c_0 , c_1 and α are linear function of the voltage $v(t)$ that is applied to the current driver of MR damper.

$$c_0(t) = c_{0a} + c_{0b}v(t), \quad c_1(t) = c_{1a} + c_{1b}v(t), \quad \alpha(t) = \alpha_a + \alpha_bv(t) \quad (5.22)$$

where all the parameters with subscript a or b are constants and directly related to their mother variables that have no subscript of a or b .

For simplicity, all the MR dampers set on Painter Street Overcrossing share the same parameters in the simulation of this section. The voltage dependent MR damper parameters are listed in Table 5.4 and the constant ones are listed in Table 5.5. The maximum and minimum applied voltage to MR damper here is assumed to be $U_{\max} = 1.5V$ and $U_{\min} = 0V$ respectively.

Table 5.4 Voltage dependent modeling parameters of MR damper

c_0 (KN-s/m)		c_1 (KN-s/m)		α (KN)	
c_{0a}	c_{0b}	c_{1a}	c_{1b}	α_a	α_b
175.1	1709.2	3502.4	24516.5	2731.8	9999.2

Table 5.5 Constant modeling parameters of MR damper

x_0 (m)	k_0 (KN/m)	k_1 (KN/m)	γ (m^{-2})	β (m^{-2})	A (1)	n (1)
0.0	1926.3	1.8	35650.1	35650.1	155.0	2.0

In section 5.4.3, two base isolation designs are developed aiming at target period $T_{tgt} = 1s$ and $T_{tgt} = 2s$. Table 5.2 lists the base isolator properties corresponding to these two cases. To investigate the structural response of semi-actively controlled Painter Street Overcrossing with base isolation, MR dampers are added to the bridge and work together with the base isolators as illustrated in Fig. 5.8.

Fig. 5.22(a) and (b) plot the structural response of deck center accelerations and pier drifts for $T_{tgt} = 1s$ and $T_{tgt} = 2s$ respectively. The correspondent results from analysis of the original bridge and base isolated bridge are also plotted on the same figure for comparison. B.I. in the legend is the short for ‘base isolation.’ It’s seen that semi-active control of the bridge yields the same level of performance as that of base isolation only, i.e. significant reduction of pier drifts and deck center accelerations. The promising advantage of semi-active control is that while keeping the level of overall structural performance, it also reduces the bearing displacements remarkably due to the participation of MR dampers, which is clearly observed in Fig. 5.23 of base isolator responses. The bearings are even drawn into linear region for the softer bearing design case ($T_{tgt} = 2s$). Therefore, the semi-active structural response can be considered as the optimal standard or criteria for passive design of MR dampers. The combination of MR damper plus base isolator designed towards $T_{tgt} = 2s$ turns out to be the better one out of the two designs.

Fig. 5.24 (a) and (b) plot the MR damper responses of the devices set on north pier and east abutment for $T_{tgt} = 1s$ and $T_{tgt} = 2s$ respectively. The time history of the associated control voltage input to corresponding MR damper is also plotted in the figure. One can see the ‘on-off-on’ nature of the control voltage input, which results from the successful application of clipped

optimal control algorithm. The control voltage is an essential factor that would be used for equivalent optimal passive design of MR damper in the following section.

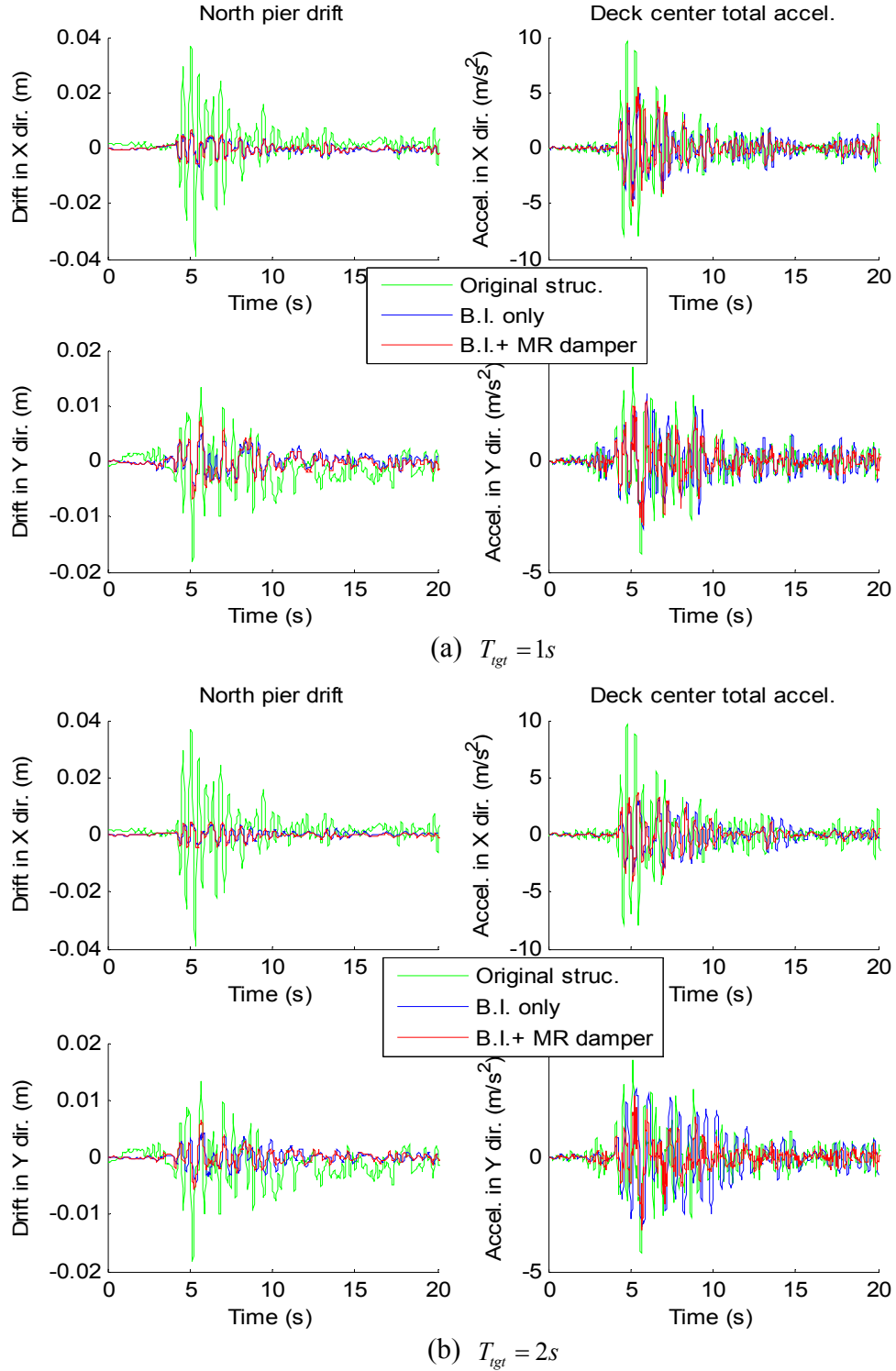
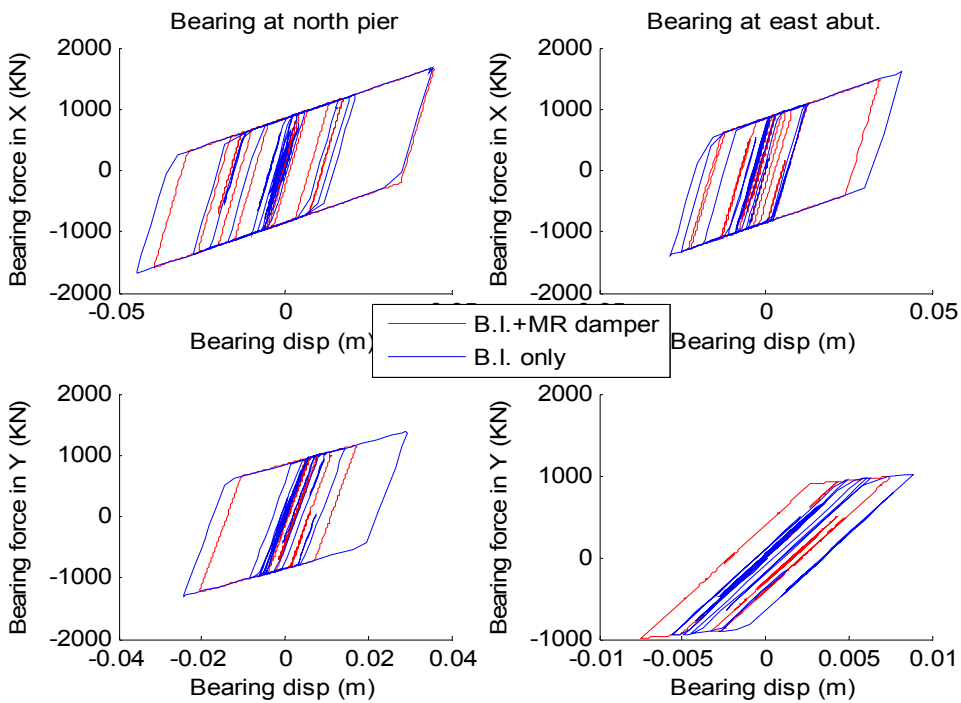
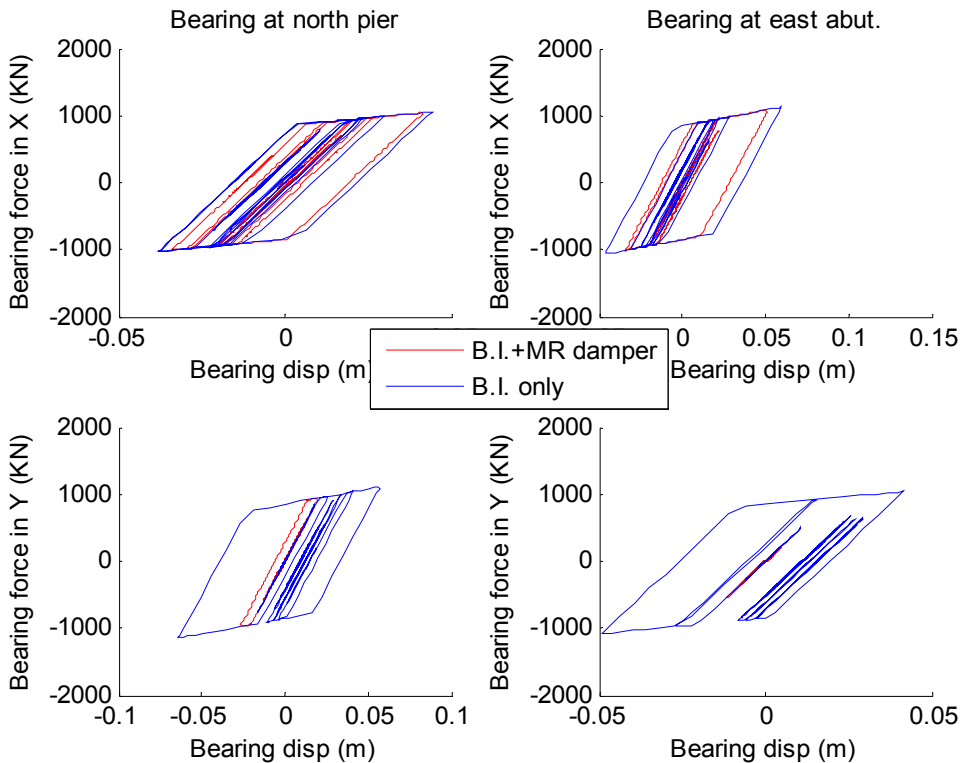


Fig. 5.22 Comparison of structural responses of different control strategies

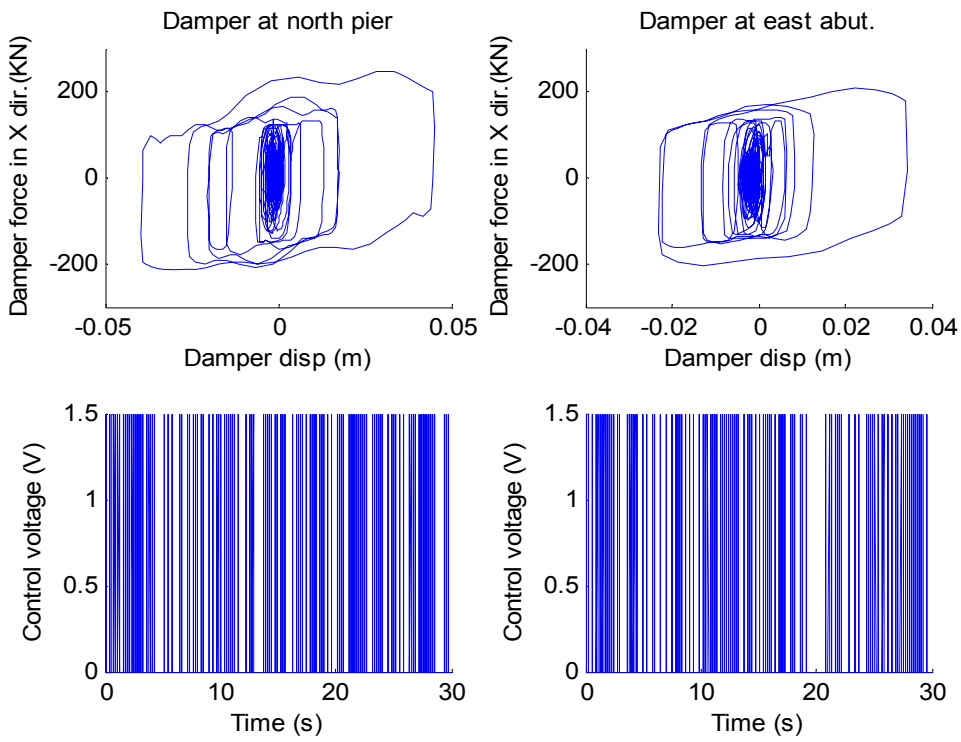


(a) $T_{tgt} = 1s$

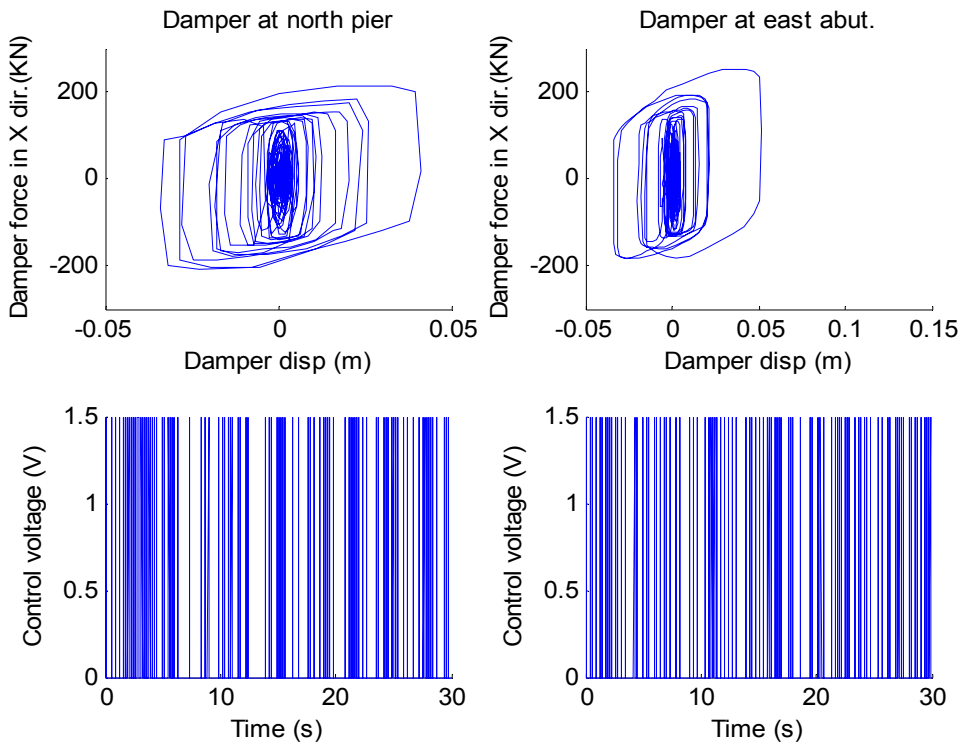


(b) $T_{tgt} = 2s$

Fig. 5.23 Comparison of base isolator responses of different control strategies



(a) $T_{tgt} = 1s$



(b) $T_{tgt} = 2s$

Fig. 5.24 MR damper response and control voltage input of clipped optimal control

5.6 Equivalent Optimal Passive Control Design

Although semi-active control of MR damper could provide structure the optimal response by actively adjusting damping property, it still has the risk of failure under strong ground motion because of the fact that any active or semi-active control involves the participation of a computational core that processes the structural measurements and sends out the control command. Therefore a passive design of MR damper that can mimic the behavior of semi-active control would be the first choice in practice.

Recall that c_0 , c_1 and α parameters vary the property of MR damper, i.e. change and determine its damping behavior, thus define the design of a MR damper. In this section, a novel equivalent optimal passive control is proposed and the corresponding optimal passive design of MR damper is expressed in terms of c_0 , c_1 and α values.

Note that c_0 , c_1 and α are linear function of control voltage v input to MR damper, they are expressed by:

$$c_0(t) = c_{0a} + c_{0b}v(t), \quad c_1(t) = c_{1a} + c_{1b}v(t), \quad \alpha(t) = \alpha_a + \alpha_bv(t) \quad (5.23)$$

Integrate Eq. (5.23) over the control time duration $[0, t_f]$ and divided by the time interval t_f , one can get the average of $c_0(t)$, $c_1(t)$ and $\alpha(t)$ over the control time duration, respectively:

$$\begin{aligned} c_{0,ep} &= \frac{\int_0^{t_f} c_0(t)dt}{t_f} = \frac{\int_0^{t_f} [c_{0a} + c_{0b}v(t)]dt}{t_f} = c_{0a} + c_{0b} \frac{\int_0^{t_f} v(t)dt}{t_f} \\ c_{1,ep} &= \frac{\int_0^{t_f} c_1(t)dt}{t_f} = \frac{\int_0^{t_f} [c_{1a} + c_{1b}v(t)]dt}{t_f} = c_{1a} + c_{1b} \frac{\int_0^{t_f} v(t)dt}{t_f} \\ \alpha_{ep} &= \frac{\int_0^{t_f} \alpha(t)dt}{t_f} = \frac{\int_0^{t_f} [\alpha_a + \alpha_bv(t)]dt}{t_f} = \alpha_a + \alpha_b \frac{\int_0^{t_f} v(t)dt}{t_f} \end{aligned} \quad (5.24)$$

Since $c_{0,ep}$, $c_{1,ep}$ and α_{ep} are averaged over control time duration of $c_0(t)$, $c_1(t)$ and $\alpha(t)$, it's reasonable to take them as the equivalent constant parameters for the passive design of MR damper. Subscription 'ep' here stands for 'equivalent passive.' Thus, if the time history analysis of a semi-active control process with MR damper can be performed and consequently the histories of $c_0(t)$, $c_1(t)$ and $\alpha(t)$ are obtained, the above stated equivalent passive design parameters $c_{0,ep}$, $c_{1,ep}$ and α_{ep} can be evaluated.

Eq. (5.24) shows that all the equivalent passive parameters are function of $\frac{\int_0^{t_f} v(t)dt}{t_f}$,

which is related to time history of control voltage input to MR damper $v(t)$ directly. So the average over control time duration of $v(t)$ should be evaluated first in order to compute $c_{0,ep}$, $c_{1,ep}$ and α_{ep} for equivalent passive design of MR damper.

The procedure for the proposed equivalent optimal passive design of MR damper is summarized as follows:

Step 1. Perform time history analysis of the structure with semi-actively controlled MR dampers;

Step 2. Get the time history of control voltage $v(t)$ of each MR damper;

Step 3. Calculate the average voltage over control time duration of $v(t)$ for each MR damper by

$$v_{ep} = \frac{\int_0^{t_f} v(t)dt}{t_f}, \text{ as illustrated in Fig. 5.25;}$$

Step 4. Take the average voltage over time v_{ep} obtained from Step 3 of each MR damper as the equivalent passive constant voltage and apply it to corresponding MR damper as a 'passive-on' control command;

Step 5. Calculate the equivalent passive parameters $c_{0,ep}$, $c_{1,ep}$ and α_{ep} for each MR damper by

$$c_{0,ep} = c_{0a} + c_{0b}v_{ep}, \quad c_{1,ep} = c_{1a} + c_{1b}v_{ep}, \quad \alpha_{ep} = \alpha_a + \alpha_bv_{ep} \quad (5.25)$$

which concludes the equivalent optimal passive design of a MR damper;

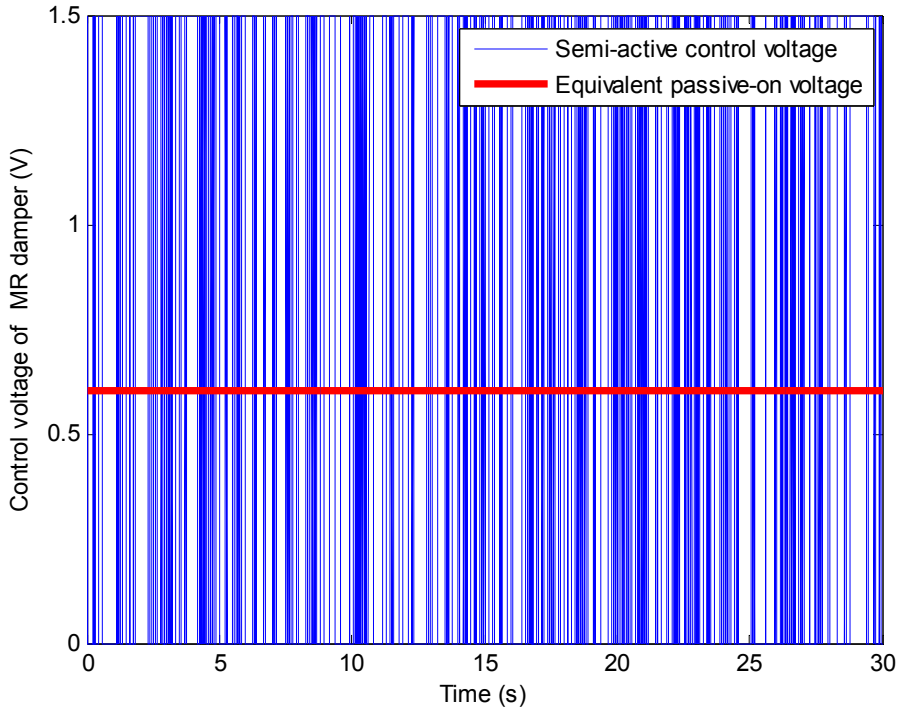


Fig. 5.25 Equivalent passive-on voltage based on semi-active control history

Step 6. (as needed) Re-perform the time history analysis with each MR damper controlled passively by the equivalent constant control voltage v_{ep} to obtain the structural response under equivalent optimal passive control.

Following the above procedure, numerical analysis is performed for $T_{tgt} = 1s$ and $T_{tgt} = 2s$ of the base isolated Painter Street Bridge by hybrid simulation scheme using UI_SimCor. The equivalent optimal passive parameters of each MR damper are listed in Table 5.6. Locations on the bridge of MR damper #1~#8 are explained in Table 5.3.

Table 5.6 (a) Equivalent optimal passive design parameters of MR damper ($T_{tgt} = 1s$)

MR damper #	1	2	3	4	5	6	7	8
$c_{0,ep}$ (KN-s/m)	283.0	1333.4	283.3	1333.1	215.3	1236.0	222.8	1206.6
$c_{1,ep}$ (KN-s/m)	5049.4	20117.2	5054.3	20112.3	4078.5	18719.8	4186.4	18298.1
α_{ep} (KN)	3362.8	9508.3	3364.8	9506.3	2966.8	8938.4	3010.8	8766.4

Table 5.6 (b) Equivalent optimal passive design parameters of MR damper ($T_{tgt} = 2s$)

MR damper #	1	2	3	4	5	6	7	8
$c_{0,ep}$ (KN-s/m)	245.9	1178.6	245.9	1178.4	223.3	1085.1	227.8	1079.3
$c_{1,ep}$ (KN-s/m)	4517.3	17896.0	4517.3	17893.6	4193.7	16555.0	4257.5	16471.6
α_{ep} (KN)	3145.8	8602.4	3145.8	8601.4	3013.8	8055.4	3039.8	8021.4

Fig. 5.26~5.28 compare the structural responses of the bridge and seismic protective devices (base isolators plus MR dampers) of semi-active control with those of the equivalent passive control design of MR damper. It's shown that the proposed equivalent optimal passive control produces almost the same response of that from the semi-active control scheme, which verifies and validates that the proposed optimal passive design method is applicable and could serve as a direction for optimal passive design of MR dampers.

Table 5.7 presents the average of the figures in Table 5.6(a) and 5.6(b). Since the two optimal passive designs in Table 5.6(a) and 5.6(b) are towards the base isolation target period $T_{tgt} = 1s$ and $T_{tgt} = 2s$ respectively, it's reasonable to assume that the passive design represented by the parameters in Table 5.7 is an approximately optimal for all the base isolation designs whose target period falls in between 1s and 2s. Therefore, if the design parameters of MR dampers in Table 5.7 are adopted, one can further optimize the property of base isolation devices within $T_{tgt} = [1 \ 2]s$ by well established methods, such as the approach proposed by Zhang and Huo (2009), such that both optimal designs of base isolation and MR dampers are achieved at the same time.

Table 5.7 Equivalent optimal passive design parameters of MR damper (for $T_{tgt} = [1 \ 2]$ s)

MR damper #	1	2	3	4	5	6	7	8
$c_{0,ep}$ (KN-s/m)	264.4	1256.0	264.6	1255.7	219.3	1160.5	225.3	1142.9
$c_{1,ep}$ (KN-s/m)	4783.4	19006.6	4785.8	19002.9	4136.1	17637.4	4221.9	17384.9
α_{ep} (KN)	3254.3	9055.4	3255.3	9053.9	2990.3	8496.9	3025.3	8393.9

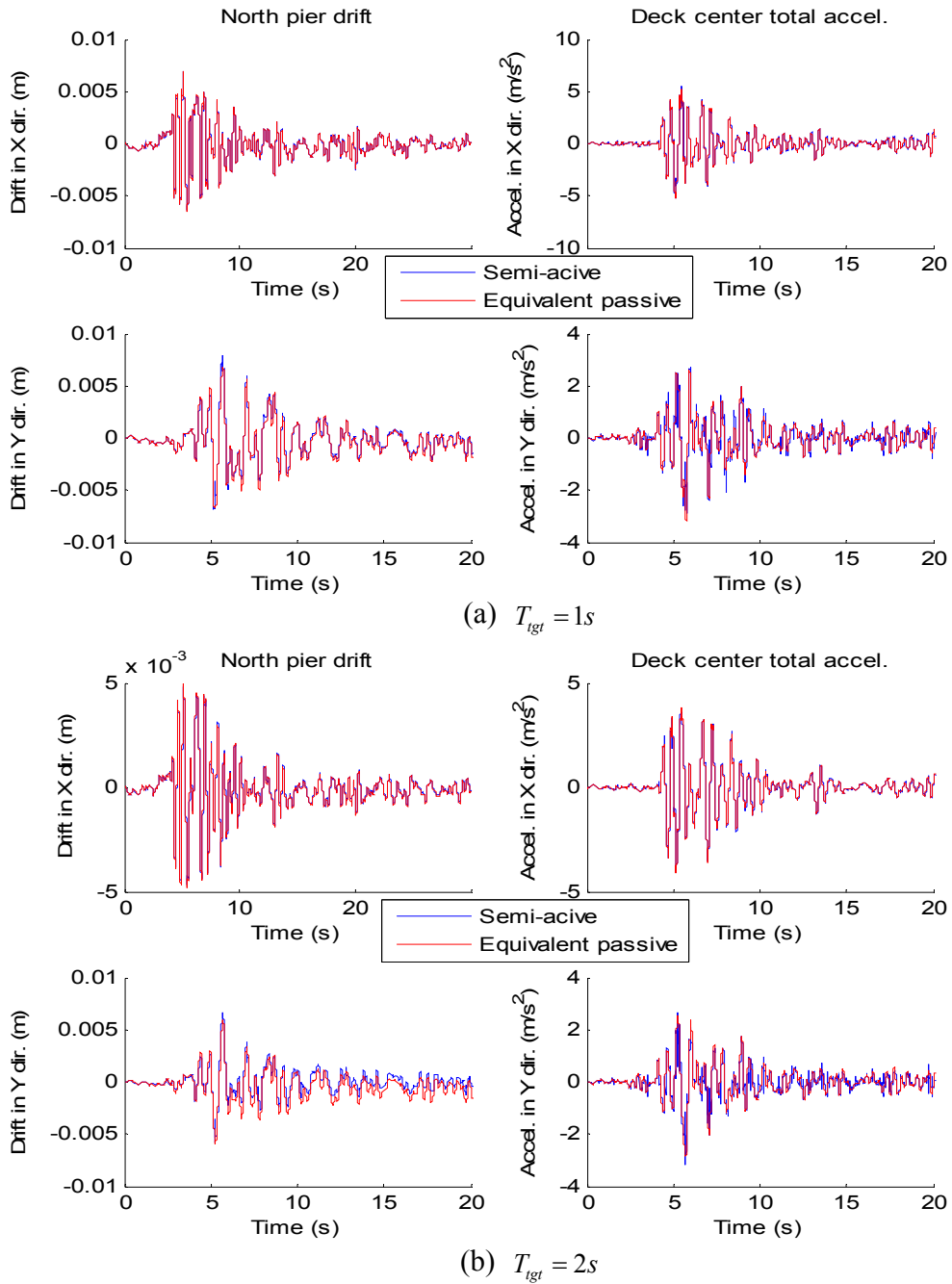
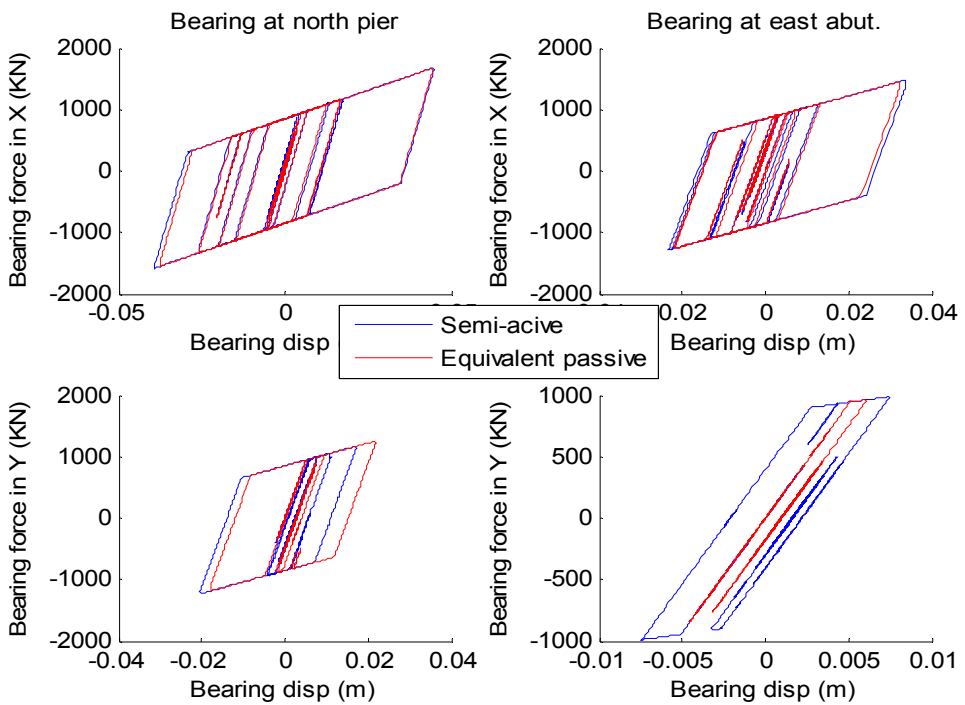
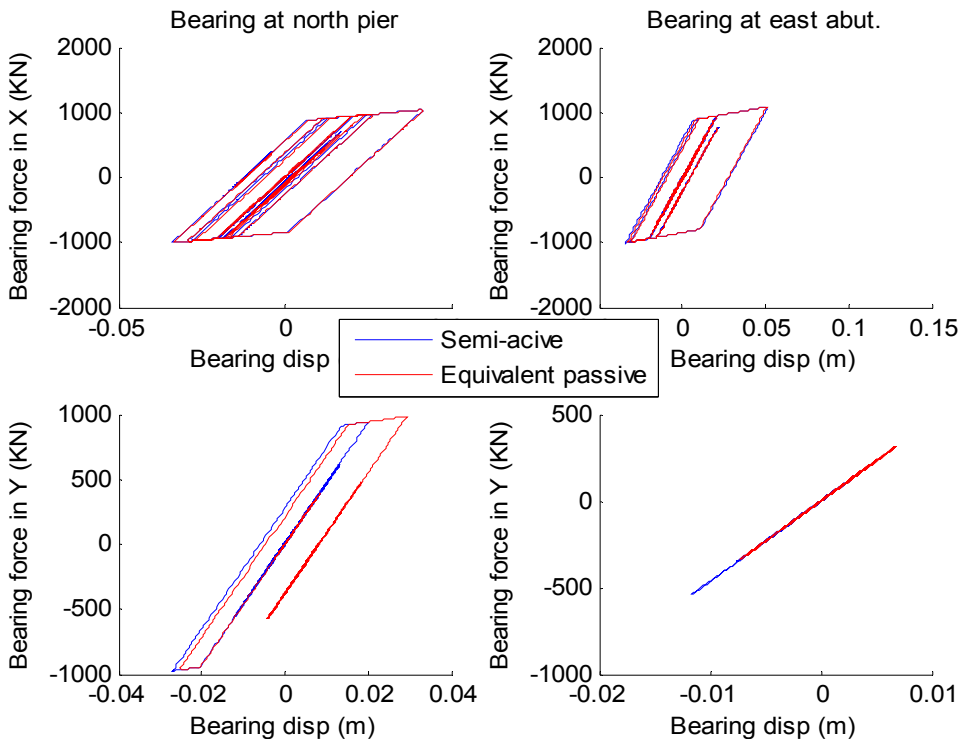


Fig. 5.26 Comparison of structural response by semi-active and its equivalent passive control

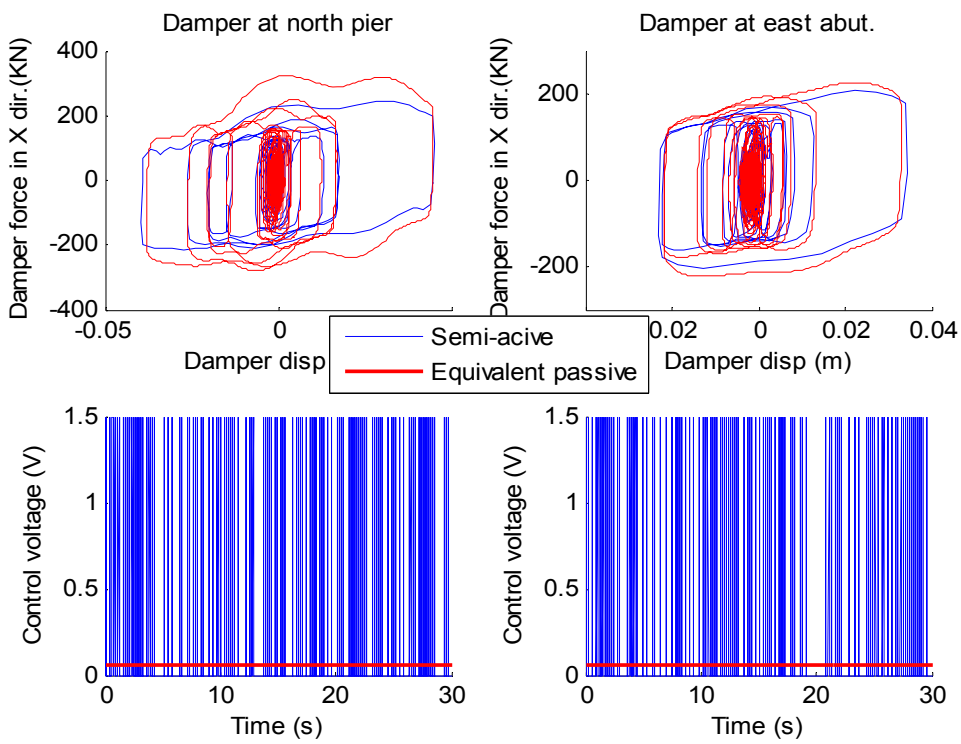


(a) $T_{tgt} = 1s$

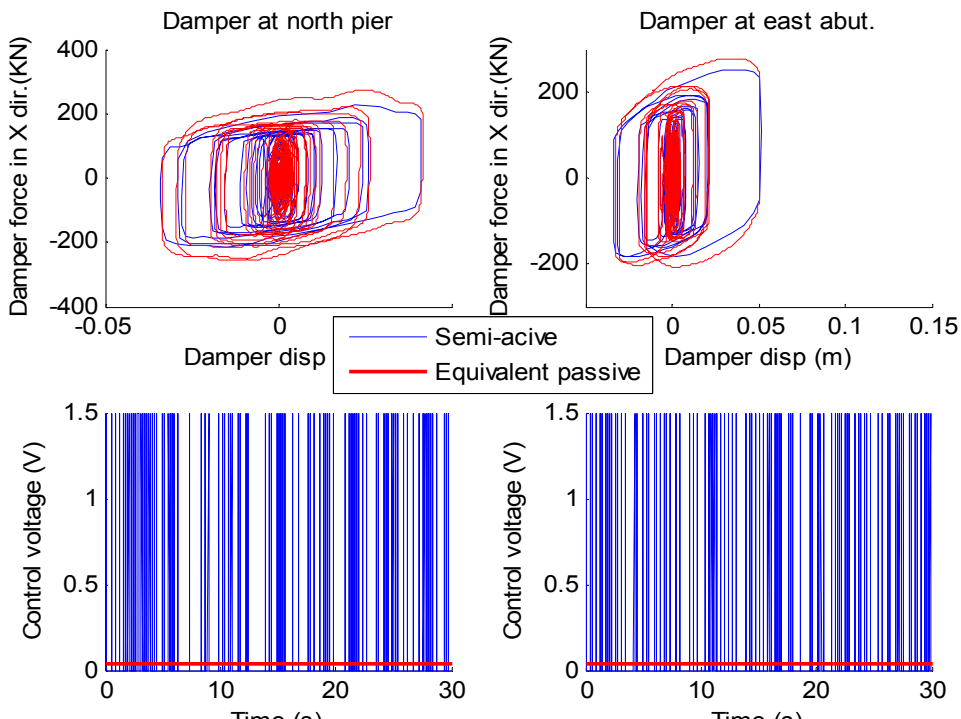


(b) $T_{tgt} = 2s$

Fig. 5.27 Comparison of bearing response by semi-active and its equivalent passive control



(a) $T_{tgt} = 1\text{ s}$



(b) $T_{tgt} = 2\text{ s}$

Fig. 5.28 Comparison of MR damper response by semi-active and its equivalent passive control

5.7 Practical Optimal Passive Control Design of MR dampers

In practice, there are inherent variabilities and uncertainties in the seismic response of highway bridges associated with both earthquake motion characteristics and soil structure interactions between the bridge and the approach embankments. Designing the seismic protective devices with a single earthquake motion would apparently limit the robustness of the design. In order to account for this complexity, ten strong ground motions that have been recorded in California relatively close to the fault of major earthquakes are used for designing the seismic protective devices of Painter Street Bridge in this section. A nonlinear time history analyses of the seismically protected Painter Street Bridge (Fig. 5.8) is performed and the correspondent equivalent optimal passive design of the MR dampers is obtained for each earthquake and base isolation configuration ($T_{tgt} = 1s$ and $T_{tgt} = 2s$) utilizing the method proposed in the previous section. Table 5.8 lists in historic order the ten free field records together with their magnitudes and distance of the accelerograph from the causative fault.

Table 5.8 Earthquake records selected for seismic protective device design

Record Station	Earthquake	Magnitude M_w	Dist. to fault (km)	Peak Accel. (g)	Peak Vel. (m/s)
Pacoima Dam	1971 San Fernando	6.6	8.5	1.17 (1.08)	1.14(0.57)
El Centro Array #5	1979 Imperial Valley	6.4	30.4	0.38 (0.53)	0.99(0.52)
El Centro Array #6	1979 Imperial Valley	6.4	29.8	0.44 (0.34)	1.13(0.68)
El Centro Array #7	1979 Imperial Valley	6.4	29.4	0.46 (0.34)	1.13(0.55)
Parachute Test Site	1987 Superstition Hills	6.6	7.2	0.45(0.38)	1.12(0.44)
Los Gatos	1989 Loma Prieta	7.0	6.1	0.56(0.61)	0.95(0.51)
Cape Mendocino	1992 Petrolia	7.0	3.8	1.50 (1.04)	1.25(0.41)
Rinaldi	1994 Northridge	6.7	9.9	0.89 (0.39)	1.75(0.60)
Sylmar	1994 Northridge	6.7	12.3	0.73 (0.60)	1.22(0.54)
Newhall	1994 Northridge	6.7	20.2	0.59 (0.58)	0.96(0.75)

* Peak acceleration values are for the fault normal component. The values of the fault parallel component are offered in parentheses.

As discussed and demonstrated in section 5.1.2, approach embankments are long deformable bodies that can amplify considerably the free-field earthquake motions and interact strongly with the bridge structure. In this study, a shear-wedge model (Zhang 2002), as illustrated in Fig. 5.29, is adopted to estimate the amplification of ground motion at bridge abutments due to kinematic response of the approach embankments.

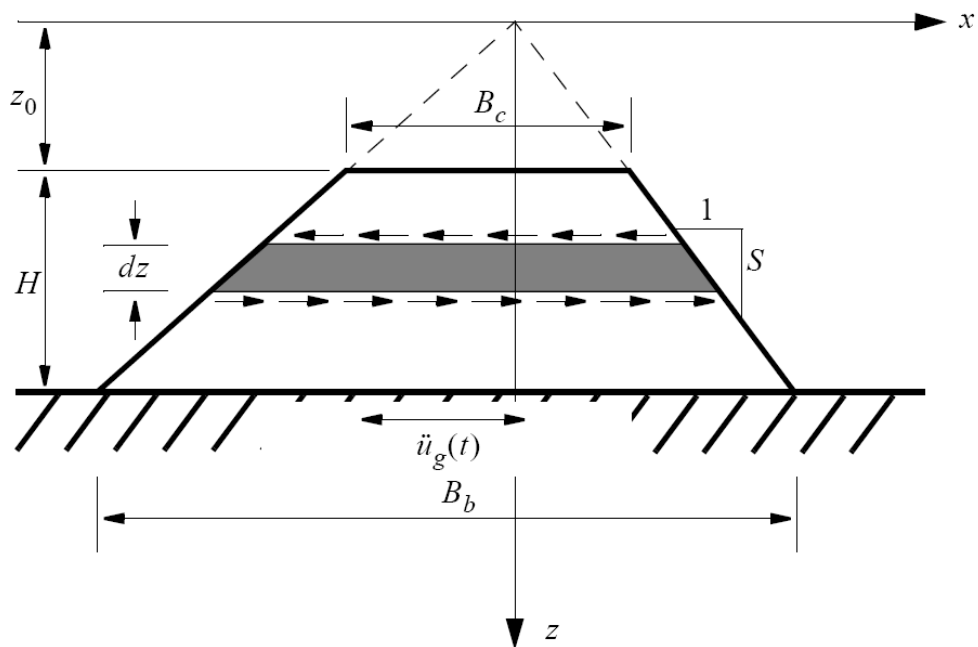


Fig. 5.29 Shear-wedge model of bridge embankments

Based on this shear-wedge model, the amplified input motion to bridge abutments is given by the following equivalent linear approach (Zhang 2002):

$$u^c(t) = \frac{1}{2\pi} \int_{-\infty}^{\infty} I(\omega) u^b(\omega) e^{i\omega t} d\omega \quad (5.26)$$

where $u^c(t)$ is the resultant motion at the crest of the embankment, u^b is the free field ground motion and $I(\omega)$ is the kinematic response function that captures the ground motion amplification which is given by:

$$I(\omega) = 1 + \frac{u_x(z_0)}{u_{g0}} = \frac{c_1 J_0(kz_0) + c_2 Y_0(kz_0)}{u_{g0}} \quad (5.27)$$

where z_0 is the coordinate of embankment crest; u_{g0} is the magnitude of the harmonic input $u_g(t) = u_{g0} e^{i\omega t}$; J_0 and Y_0 are the zero-order Bessel functions of the first and second kind respectively; $k = \omega/V_s$ with V_s is the shear wave velocity of the soil; and c_1 and c_2 are integration constants given by:

$$c_1 = 1 + \frac{u_{g0}}{J_0(k(z_0 + H)) - \frac{J_1(kz_0)}{Y_1(kz_0)} Y_0(k(z_0 + H))}, \quad c_2 = -\frac{J_1(kz_0)}{Y_1(kz_0)} c_1 \quad (5.28)$$

where J_1 and Y_1 are the first-order Bessel functions of the first and second kind respectively, and H is the embankment height.

In calculation of the kinematic response function $I(\omega)$ and the amplified motion at embankment crest $u^c(t)$, the shear wave velocity of soil material V_s is determined by:

$$V_s = \sqrt{G(\gamma)/\rho} \quad (5.29)$$

where $G(\gamma)$ are ρ are the shear modulus and density of the soil material, and γ is the average shear strain over height of the embankment in the scenario of shear-wedge model. It's noted that $G(\gamma)$ is dependent of the average shear strain γ that is directly determined by the maximum crest relative displacement of the embankment $(u^c - u^b)_{\max}$, therefore iterations are needed to compute the amplified motion at embankment crest in Eq. (5.26) to achieve a converged γ value.

The $G - \gamma$ relation needed in the iteration is adopted from the work of Seed and Idriss (1970), Iwasaki et al. (1978), Tatsuoka et al. (1978), Vucetic and Dobry (1991), among others, as shown in Fig. 5.30(a). The darker line represents an averaged curve of these reported curves, and is the

curve used for iteration in this study. When a converged shear strain is obtained, the hysteretic damping coefficient $\eta(\gamma)$ can be determined by the average curve in Fig. 5.30(b) at the same time.

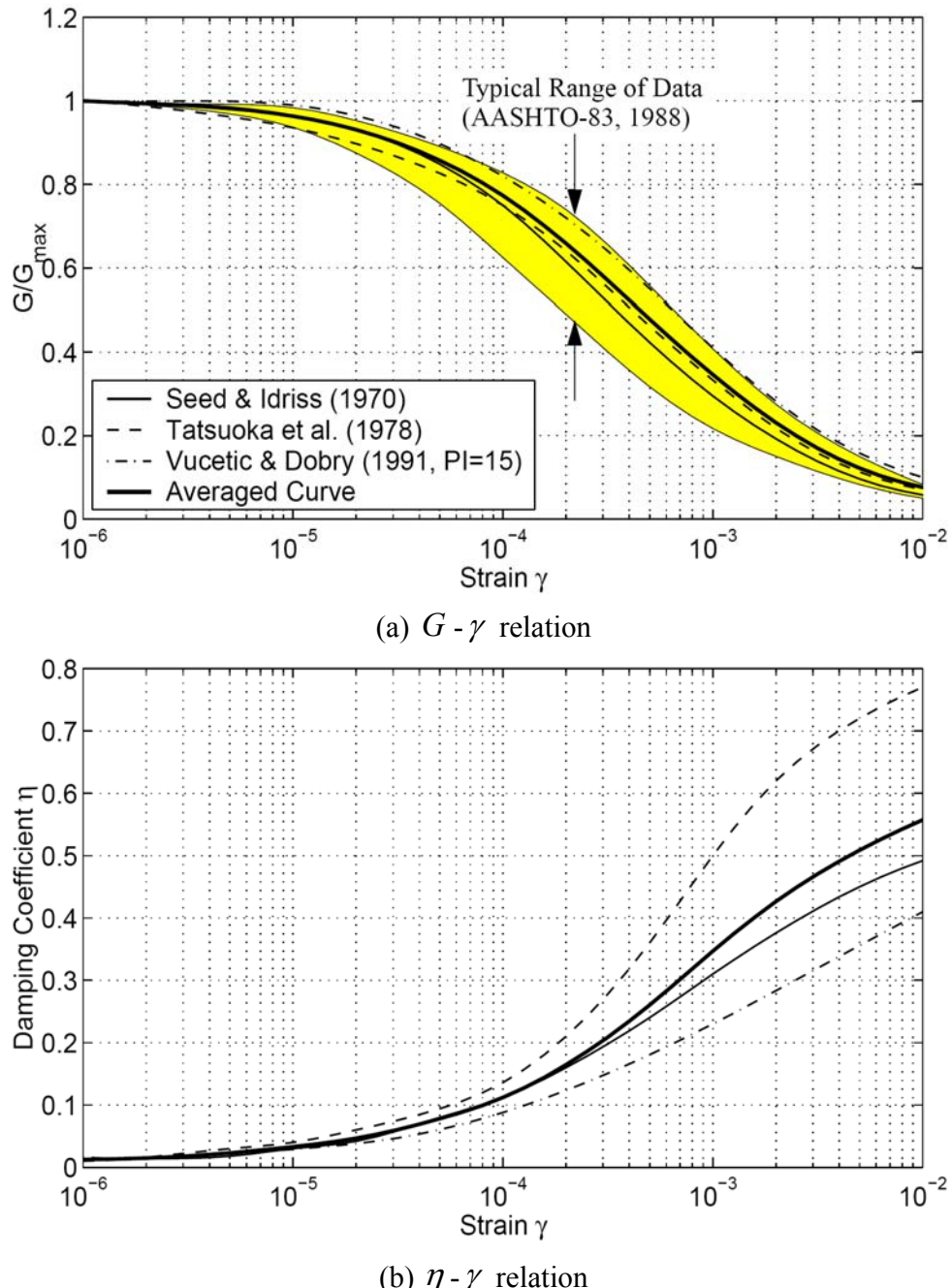


Fig. 5.30 Normalized soil shear modulus and damping coefficient as function of shear strain

Amplified motion at the embankment crest is computed for each free field earthquake motion record in Table 5.8. The converged values for shear modulus, damping coefficient, and average shear strain that result from the shear-wedge analysis are shown in Table 5.9. It's plotted in Fig. 5.31 the free filed ground motion and the amplified motion at embankment crest with Pacoima Dam record for illustration purpose. It's concluded in Zhang's research work (2002) that the kinematic response function along the transverse direction obtained with the shear-wedge approximation can also capture most of the amplification generated due to a longitudinal excitation. So a single kinematic response function is used for both fault-normal (FN) and fault-parallel (FP) motions here. In the simulations, the fault-normal (FN) components of the earthquake records are taken as inputs in X direction and the fault-parallel (FP) components are taken as inputs in Y direction.

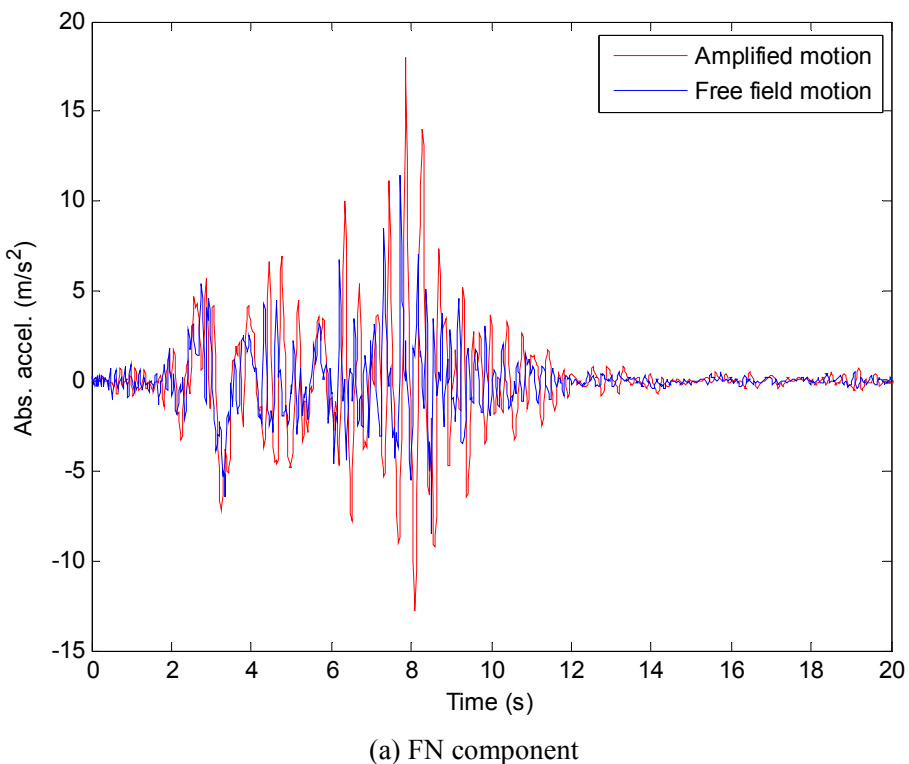
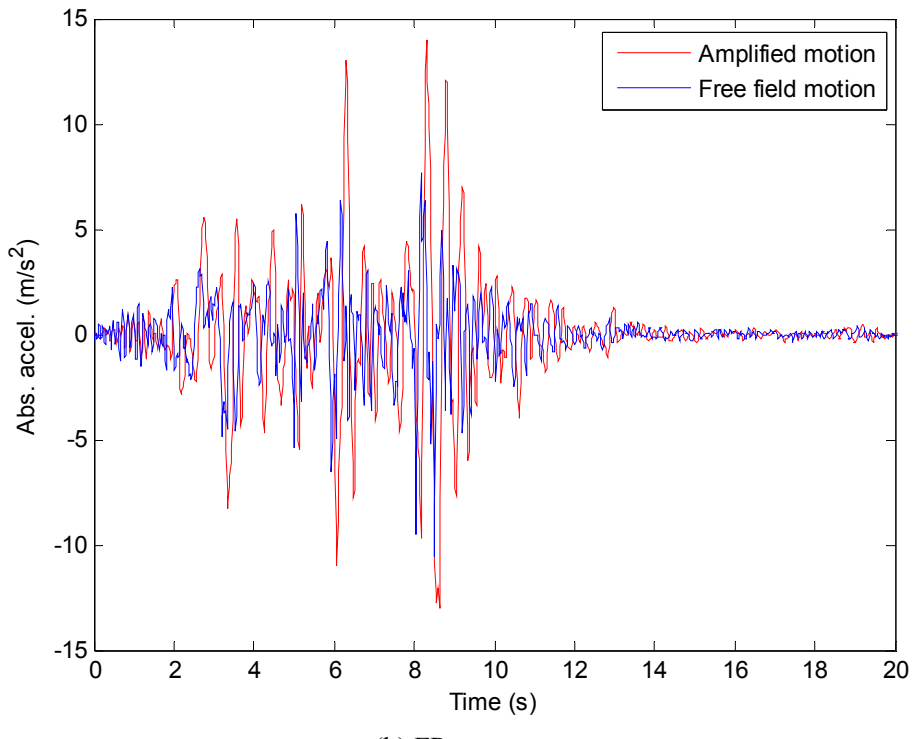


Fig. 5.31 Kinematic response of embankments under Pacoima Dam record



(b) FP component

Fig. 5.31(cont.) Kinematic response of embankments under Pacoima Dam record

The amplified motions from the shear-wedge analysis are used as input motions to the bridge abutments in the simulations for design of seismic protective devices on Painter Street Bridge. On the other hand, input motions at the pile foundations of the center pier columns are assumed to be equal to that of the free-field ground motions due to the fact that the kinematic response factors of pile foundations are close to unity in most cases of excitation.

Besides the kinematic response, soil structure interaction between the approach embankments and bridge structure needs to be considered. In view of the variability in soil strains and frequency content during ground shaking, macroscopic longitudinal and transverse springs and dashpots are used to approximate the presence of embankments. Dynamic stiffness of bridge embankments with a unit width for rigid supporting soil condition is given by:

$$\hat{k}_x(\omega) = G(1+i\eta)B_c L_c k \frac{J_1(kz_0)Y_0[k(z_0+H)] - J_0[k(z_0+H)]Y_1(kz_0)}{Y_0[k(z_0+H)]J_0(kz_0) - J_0[k(z_0+H)]Y_0(kz_0)} \quad (5.30)$$

where G and η are the converged shear modulus and strain of the soil from the kinematic response analysis; B_c is the width of embankment crest; and L_c is the estimation of critical length of the embankment which is computed by:

$$L_c \approx 0.7\sqrt{SB_c H} \quad (5.31)$$

where $S = 1/2$ is the embankment slope of Painter Street Bridge.

Table 5.9 Converged values of the shear modulus, damping coefficient and shear strain under selected strong motion records

Earthquakes	G (MPa)	η	γ (10^{-3})
Pacoima Dam (FN), 1971 San Fernando	7.89	0.51	4.95
Pacoima Dam (FP), 1971 San Fernando	6.48	0.53	6.55
El Centro #5 (FN), 1979 Imperial Valley	11.10	0.47	3.07
El Centro #5 (FP), 1979 Imperial Valley	24.64	0.32	0.81
El Centro #6 (FN), 1979 Imperial Valley	22.30	0.35	0.99
El Centro #6 (FP), 1979 Imperial Valley	23.10	0.34	0.92
El Centro #7 (FN), 1979 Imperial Valley	19.52	0.37	1.26
El Centro #7 (FP), 1979 Imperial Valley	25.46	0.31	0.76
Parachute Test Site (FN), 1987 Superstition Hills	19.04	0.38	1.32
Parachute Test Site (FP), 1987 Superstition Hills	21.11	0.36	1.10
Los Gatos (FN), 1989 Loma Prieta	15.73	0.42	1.82
Los Gatos (FP), 1989 Loma Prieta	17.30	0.40	1.55
Cape Mendocino (FN), 1992 Petrolia	6.26	0.53	6.89
Cape Mendocino (FP), 1992 Petrolia	14.74	0.43	2.01
Rinaldi (FN), 1994 Northridge	5.13	0.55	9.27
Rinaldi (FP), 1994 Northridge	15.28	0.42	1.90
Sylmar (FN), 1994 Northridge	8.21	0.50	4.70
Sylmar (FP), 1994 Northridge	7.18	0.52	5.67
Newhall (N-S), 1994 Northridge	11.43	0.46	2.94
Newhall (E-W), 1994 Northridge	9.83	0.48	3.65

The real and imaginary parts of Eq. (5.30) represent the storage stiffness and loss stiffness of the embankment soil respectively. One can pick up a practical spring and dashpot value by passing a line through the real and imaginary part as illustrated by the darker lines in Fig. 5.32.

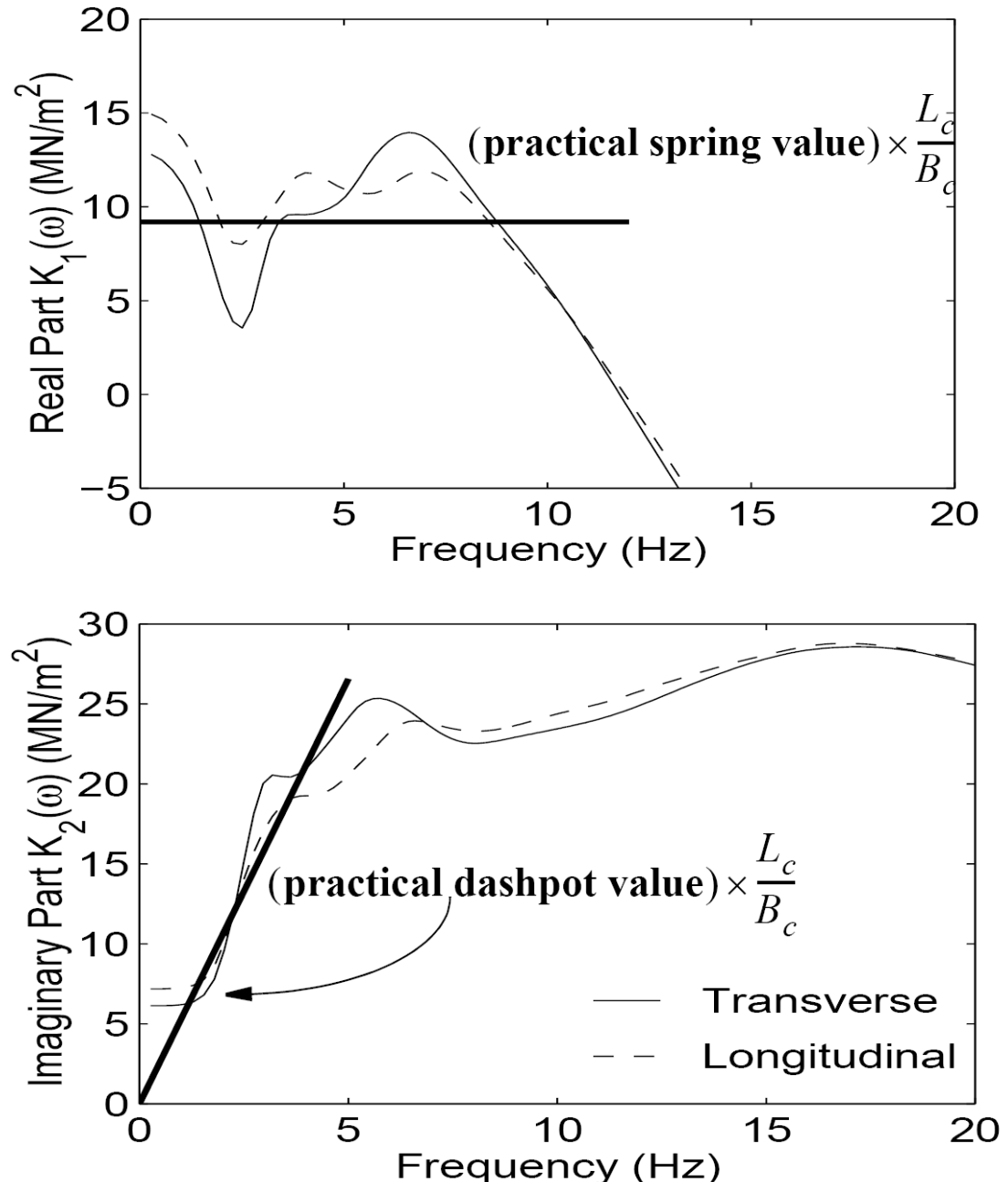


Fig. 5.32 Selection of practical spring and dashpot values of approach embankment

Based on the numerical simulation trials, the spring and dashpot values at east and west abutments only differ slightly from each other due to the different pile group configurations. For simplicity, it is assumed that both abutments adopt the spring and dashpot values of the east abutment. The spring and dashpot values that represent the presence of bridge embankments for simulations under each earthquake record are listed in Table 5.10. The stiffness and dashpot contribution from the pile foundations of embankments which are determined by the method proposed by Zhang (2002) is also shown in Table 5.10.

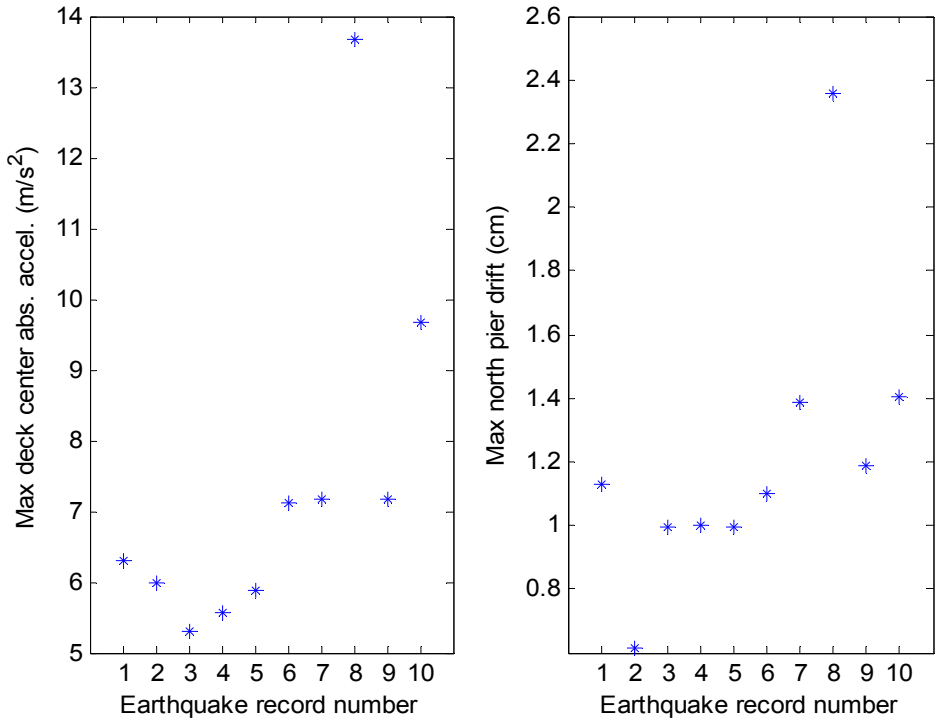
Table 5.10 Spring and dashpot values that approximate the presence of the approach embankments and pile foundations of Painter Street Bridge

	Earthquakes	Embankment + Pile foundations			
		K_x (MN/m)	K_y (MN/m)	C_x (MN•s/m)	C_y (MN•s/m)
1	Pacoima Dam, 1971 San Fernando	120+174	99+150	11+9	9+8
2	El Centro #5, 1979 Imperial Valley	169+224	375+403	12+9	53+11
3	El Centro #6, 1979 Imperial Valley	339+375	352+385	29+11	38+11
4	El Centro #7, 1979 Imperial Valley	297+340	388+413	6+10	59+11
5	Parachute Test Site, 1987 Superstition Hills	290+334	321+360	4+10	16+11
6	Los Gatos, 1989 Loma Prieta	239+290	263+311	12+10	6+10
7	Cape Mendocino, 1992 Petrolia	95+146	224+276	9+8	15+10
8	Rinaldi, 1994 Northridge	78+126	233+284	9+8	14+10
9	Sylmar, 1994 Northridge	125+179	109+162	11+9	10+8
10	Newhall, 1994 Northridge	174+229	150+205	13+9	11+9

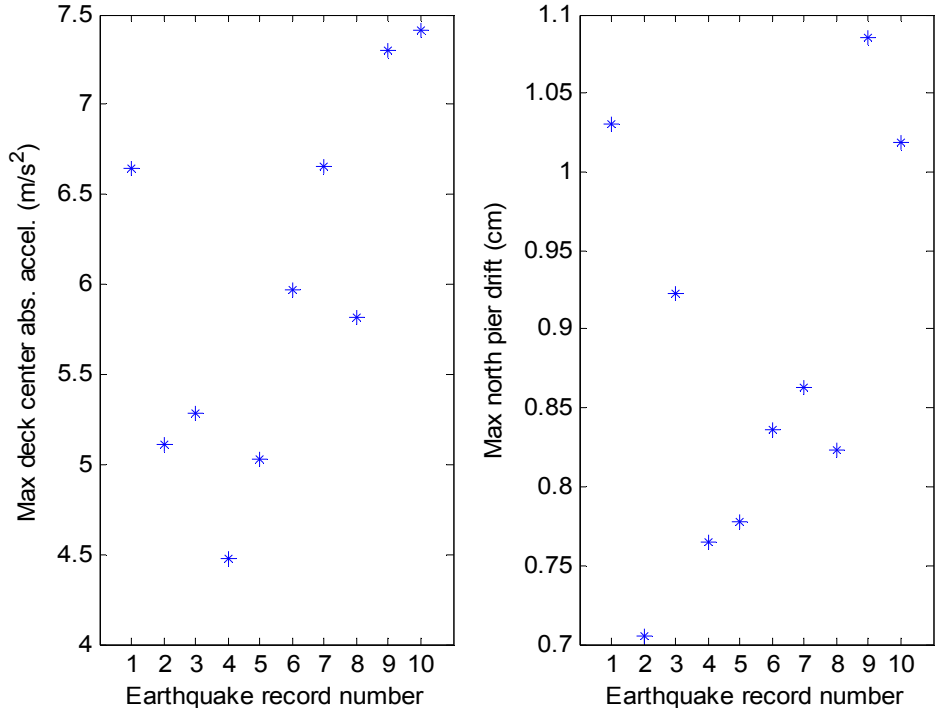
With taking into account the kinematic response of embankments and the soil bridge interaction effects, nonlinear time history analysis of the seismically protected Painter Street Bridge (Fig. 5.8) is performed for each strong ground motion record and the resultant equivalent optimal passive designs of MR dampers are listed in Table 5.11and 5.12, for the two base

isolation configurations ($T_{tgt} = 1s$ and $T_{tgt} = 2s$) respectively. The maximum structural responses, i.e., deck center absolute acceleration and north pier drift, are shown in Fig. 5.33~5.34 for each ground motion record and each base isolation configuration. The horizontal axis of Fig. 5.33~5.34 represents the record number of the ground motions that follow the historic order as listed in Table 5.10, e.g. #1 record is Pacoima Dam record and #10 record is Newhall record.

Table 5.13 and 5.14 contain the average values of ten designs that correspond to ten strong ground motion input cases, for base isolation target period $T_{tgt} = 1s$ and $T_{tgt} = 2s$ respectively. The average design values in Table 5.13 and 5.14 can be taken as the overall optimal passive design of MR dampers with consideration of the uncertainties from different ground motion input scenarios, for base isolation target period $T_{tgt} = 1s$ and $T_{tgt} = 2s$ respectively. If further averaging the design values in Table 5.13 and 5.14, as shown in Table 5.15, the resultant values can be considered as the final optimal passive design of MR dampers on Painter Street Bridge that accounts for uncertainties from both ground motions and base isolation configurations (ranging from $T_{tgt} = 1s$ to $T_{tgt} = 2s$).

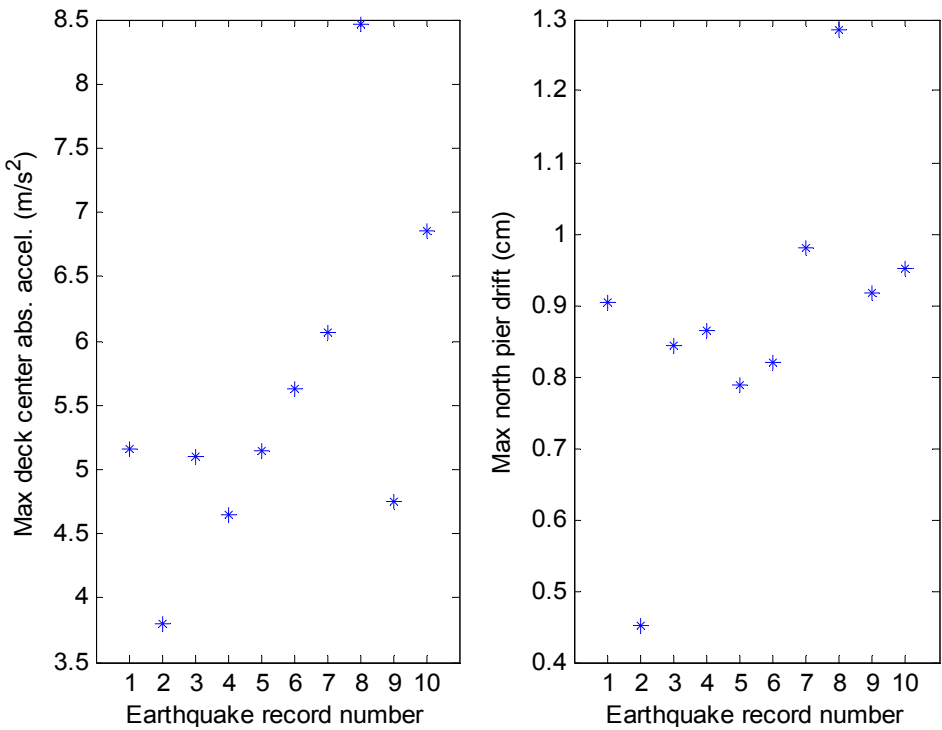


(a) Responses in X direction

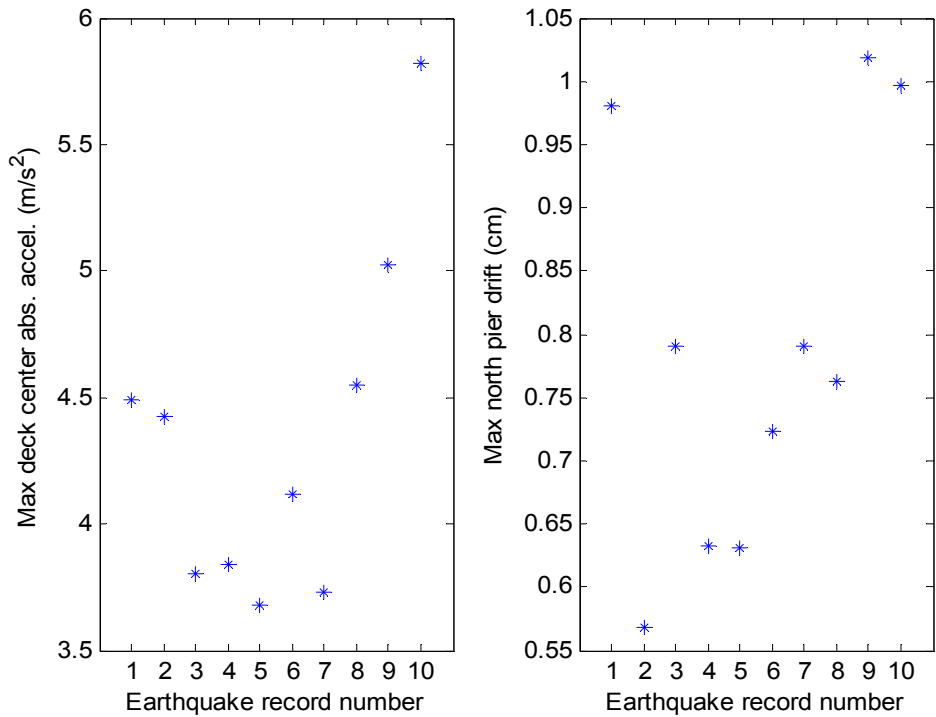


(b) Responses in Y direction

Fig. 5.33 Maximum structural responses under selected earthquake records ($T_{tgt} = 1\text{s}$)



(a) Responses in X direction



(b) Responses in Y direction

Fig. 5.34 Maximum structural responses under selected earthquake records ($T_{tgt} = 2\text{s}$)

Table 5.11 Equivalent optimal passive design of MR dampers for ten ground motions ($T_{tgt} = 1$ s)

MR damper #	1	2	3	4	5	6	7	8
Pacoima Dam, 1971 San Fernando								
$c_{0,ep}$ (KN-s/m)	442.4	1443.7	442.4	1446.0	333.7	1225.6	336.8	1221.8
$c_{1,ep}$ (KN-s/m)	7336.7	21698.5	7336.7	21732.9	5777.5	18570.2	5821.6	18516.3
α_{ep} (KN)	4295.7	10153.3	4295.7	10167.3	3659.8	8877.4	3677.8	8855.4
El Centro #5, 1979 Imperial Valley								
$c_{0,ep}$ (KN-s/m)	204.9	1290.2	205.2	1289.5	193.2	1115.5	195.6	1117.5
$c_{1,ep}$ (KN-s/m)	3928.9	19496.9	3933.9	19487.1	3762.2	16991.4	3796.6	17020.8
α_{ep} (KN)	2905.8	9255.3	2907.8	9251.3	2837.8	8233.4	2851.8	8245.4
El Centro #6, 1979 Imperial Valley								
$c_{0,ep}$ (KN-s/m)	646.2	1743.8	646.2	1743.8	395.9	1527.1	420.6	1517.1
$c_{1,ep}$ (KN-s/m)	10259.1	26003.6	10259.1	26003.6	6669.9	22894.9	7022.9	22752.7
α_{ep} (KN)	5487.6	11909.1	5487.6	11909.1	4023.7	10641.2	4167.7	10583.2
El Centro #7, 1979 Imperial Valley								
$c_{0,ep}$ (KN-s/m)	657.1	1809.4	656.8	1809.8	514.6	1642.3	528.9	1640.9
$c_{1,ep}$ (KN-s/m)	10416.0	26945.1	10411.1	26950.0	8371.3	24547.4	8577.3	24527.7
α_{ep} (KN)	5551.6	12293.1	5549.6	12295.1	4717.7	11315.2	4801.7	11307.2
Parachute Test Site, 1987 Superstition Hills								
$c_{0,ep}$ (KN-s/m)	349.8	1533.2	350.5	1533.6	226.7	1383.5	229.1	1379.0
$c_{1,ep}$ (KN-s/m)	6008.0	22983.2	6017.8	22988.1	4242.8	20835.6	4277.1	20771.8
α_{ep} (KN)	3753.8	10677.2	3757.8	10679.2	3033.8	9801.3	3047.8	9775.3

Table 5.11 (cont.) Equivalent optimal passive design of MR dampers for ten ground motions ($T_{tgt} = 1s$)

MR damper #	1	2	3	4	5	6	7	8
Los Gatos, 1989 Loma Prieta								
$c_{0,ep}$ (KN-s/m)	366.5	1473.7	366.5	1473.0	283.1	1371.5	301.9	1370.8
$c_{1,ep}$ (KN-s/m)	6248.2	22130.0	6248.2	22120.2	5051.8	20663.9	5321.5	20654.1
α_{ep} (KN)	3851.8	10329.3	3851.8	10325.3	3363.8	9731.3	3473.8	9727.3
Cape Mendocino, 1992 Petrolia								
$c_{0,ep}$ (KN-s/m)	510.5	1702.8	510.1	1702.8	375.1	1575.6	367.2	1563.0
$c_{1,ep}$ (KN-s/m)	8312.5	25415.2	8307.6	25415.2	6370.8	23591.2	6258.0	23409.8
α_{ep} (KN)	4693.7	11669.2	4691.7	11669.2	3901.8	10925.2	3855.8	10851.2
Rinaldi, 1994 Northridge								
$c_{0,ep}$ (KN-s/m)	305.4	1461.1	305.0	1461.1	230.8	1234.8	246.9	1231.7
$c_{1,ep}$ (KN-s/m)	5370.5	21948.6	5365.6	21948.6	4301.6	18702.6	4532.1	18658.5
α_{ep} (KN)	3493.8	10255.3	3491.8	10255.3	3057.8	8931.4	3151.8	8913.4
Sylmar, 1994 Northridge								
$c_{0,ep}$ (KN-s/m)	404.1	1234.5	404.1	1234.5	317.3	1302.8	332.0	1303.2
$c_{1,ep}$ (KN-s/m)	6787.6	18697.7	6787.6	18697.7	5542.1	19678.4	5753.0	19683.3
α_{ep} (KN)	4071.7	8929.4	4071.7	8929.4	3563.8	9329.3	3649.8	9331.3
Newhall, 1994 Northridge								
$c_{0,ep}$ (KN-s/m)	363.8	1546.2	363.8	1545.9	268.8	1406.7	271.5	1402.6
$c_{1,ep}$ (KN-s/m)	6209.0	23169.5	6209.0	23164.6	4845.9	21169.0	4885.1	21110.1
α_{ep} (KN)	3835.8	10753.2	3835.8	10751.2	3279.8	9937.3	3295.8	9913.3

Table 5.12 Equivalent optimal passive design of MR dampers for ten ground motions ($T_{tgt} = 2s$)

MR damper #	1	2	3	4	5	6	7	8
Pacoima Dam, 1971 San Fernando								
$c_{0,ep}$ (KN-s/m)	405.2	1430.7	405.2	1430.3	288.9	1192.1	289.6	1186.9
$c_{1,ep}$ (KN-s/m)	6802.3	21512.2	6802.3	21507.3	5135.2	18089.7	5145.0	18016.2
α_{ep} (KN)	4077.7	10077.3	4077.7	10075.3	3397.8	8681.4	3401.8	8651.4
El Centro #5, 1979 Imperial Valley								
$c_{0,ep}$ (KN-s/m)	203.8	854.7	204.2	855.0	187.4	719.3	194.9	718.3
$c_{1,ep}$ (KN-s/m)	3914.2	13250.1	3919.1	13255.0	3678.9	11308.4	3786.8	11293.7
α_{ep} (KN)	2899.8	6707.5	2901.8	6709.5	2803.8	5915.6	2847.8	5909.6
El Centro #6, 1979 Imperial Valley								
$c_{0,ep}$ (KN-s/m)	602.1	1618.0	602.7	1618.0	407.2	1521.2	442.8	1520.2
$c_{1,ep}$ (KN-s/m)	9626.6	24199.2	9636.4	24199.2	6831.7	22811.6	7341.7	22796.9
α_{ep} (KN)	5229.7	11173.2	5233.7	11173.2	4089.7	10607.2	4297.7	10601.2
El Centro #7, 1979 Imperial Valley								
$c_{0,ep}$ (KN-s/m)	602.7	1859.7	602.7	1859.7	568.9	1789.2	583.3	1789.2
$c_{1,ep}$ (KN-s/m)	9636.4	27665.9	9636.4	27665.9	9151.0	26655.8	9356.9	26655.8
α_{ep} (KN)	5233.7	12587.1	5233.7	12587.1	5035.7	12175.1	5119.7	12175.1
Parachute Test Site, 1987 Superstition Hills								
$c_{0,ep}$ (KN-s/m)	281.1	1388.6	281.4	1389.0	239.0	1235.1	249.3	1233.4
$c_{1,ep}$ (KN-s/m)	5022.4	20909.1	5027.3	20914.0	4419.3	18707.5	4566.4	18683.0
α_{ep} (KN)	3351.8	9831.3	3353.8	9833.3	3105.8	8933.4	3165.8	8923.4

Table 5.12 (cont.) Equivalent optimal passive design of MR dampers for ten ground motions
 $(T_{tgt} = 2\text{s})$

MR damper #	1	2	3	4	5	6	7	8
Los Gatos, 1989 Loma Prieta								
$c_{0,ep}$ (KN-s/m)	353.2	1395.8	353.2	1395.1	279.7	1292.9	280.1	1305.6
$c_{1,ep}$ (KN-s/m)	6057.0	21012.1	6057.0	21002.3	5002.8	19536.2	5007.7	19717.6
α_{ep} (KN)	3773.8	9873.3	3773.8	9869.3	3343.8	9271.3	3345.8	9345.3
Cape Mendocino, 1992 Petrolia								
$c_{0,ep}$ (KN-s/m)	430.5	1761.2	429.1	1761.6	402.4	1491.8	413.4	1477.8
$c_{1,ep}$ (KN-s/m)	7165.1	26253.7	7145.5	26258.6	6763.1	22389.9	6920.0	22188.9
α_{ep} (KN)	4225.7	12011.1	4217.7	12013.1	4061.7	10435.3	4125.7	10353.3
Rinaldi, 1994 Northridge								
$c_{0,ep}$ (KN-s/m)	283.1	1377.3	282.8	1377.7	240.4	1177.0	236.0	1176.0
$c_{1,ep}$ (KN-s/m)	5051.8	20747.3	5046.9	20752.2	4438.9	17874.0	4375.2	17859.2
α_{ep} (KN)	3363.8	9765.3	3361.8	9767.3	3113.8	8593.4	3087.8	8587.4
Sylmar, 1994 Northridge								
$c_{0,ep}$ (KN-s/m)	308.4	1207.8	307.7	1207.1	283.5	1093.6	292.7	1097.4
$c_{1,ep}$ (KN-s/m)	5414.7	18315.3	5404.8	18305.4	5056.7	16677.5	5189.1	16731.5
α_{ep} (KN)	3511.8	8773.4	3507.8	8769.4	3365.8	8105.4	3419.8	8127.4
Newhall, 1994 Northridge								
$c_{0,ep}$ (KN-s/m)	366.2	1313.1	365.9	1312.7	260.9	1246.1	274.2	1250.2
$c_{1,ep}$ (KN-s/m)	6243.3	19825.5	6238.4	19820.6	4733.1	18864.4	4924.3	18923.3
α_{ep} (KN)	3849.8	9389.3	3847.8	9387.3	3233.8	8997.4	3311.8	9021.4

Table 5.13 Practical optimal passive design of MR dampers ($T_{tgt} = 1\text{s}$)

MR damper #	1	2	3	4	5	6	7	8
$c_{0,ep}$ (KN-s/m)	425.1	1523.9	425.1	1524.0	313.9	1378.5	323.1	1374.8
$c_{1,ep}$ (KN-s/m)	7087.7	22848.8	7087.7	22850.8	5493.6	20764.5	5624.5	20710.5
α_{ep} (KN)	4194.1	10622.4	4194.1	10623.2	3544.0	9772.3	3597.4	9750.3

Table 5.14 Practical optimal passive design of MR dampers ($T_{tgt} = 2\text{s}$)

MR damper #	1	2	3	4	5	6	7	8
$c_{0,ep}$ (KN-s/m)	383.6	1420.7	383.5	1420.6	315.8	1275.8	325.6	1275.5
$c_{1,ep}$ (KN-s/m)	6493.4	21369.0	6491.4	21368.1	5521.1	19291.5	5661.3	19286.6
α_{ep} (KN)	3951.8	10018.9	3951.0	10018.5	3555.2	9171.6	3612.4	9169.6

Table 5.15 Final optimal passive design parameters of MR dampers for $T_{tgt} = [1 \ 2]\text{s}$

MR damper #	1	2	3	4	5	6	7	8
$c_{0,ep}$ (KN-s/m)	404.4	1472.3	404.3	1472.3	314.9	1327.2	324.3	1325.1
$c_{1,ep}$ (KN-s/m)	6790.5	22108.9	6789.5	22109.4	5507.3	20028.0	5642.9	19998.6
α_{ep} (KN)	4072.9	10320.7	4072.5	10320.9	3549.6	9471.9	3604.9	9459.9

5.8 Concluding Remarks

Highway bridges are susceptible to various levels of damages as observed in past major earthquakes. Seismic protective devices, in either passive or adaptive forms, such as base isolators and MR dampers, can be used to improve the seismic performances.

Utilizing the hybrid simulation in UI_SimCor, time history analysis of a typical highway bridge, Painter Street Overcrossing, is performed through integrating the main structure modeled in OpenSees and the seismic protective devices and control algorithm implemented in Matlab. This methodology allows convenient modeling of complex nonlinear elements and application of structural control algorithm that are not available in common commercial FE softwares.

With classical structural control theory, LQG regulator with Kalman filter, the optimal control force is obtained and leads to the optimal structural response of base isolated Painter Street Bridge equipped with semi-actively controlled MR dampers through clipped optimal control algorithm. The structural response from semi-active control serves as the standard/target to optimally design the passive parameters of MR dampers.

A novel approach to perform optimal passive design of MR dampers is proposed in this study. It's achieved by replacing the time-varying control voltage command of MR damper with an equivalent constant input which is the average over time of the control voltage history given by numerical analysis of the semi-actively controlled structure. The equivalent passive design is able to closely mimic the effects of the adaptive semi-active control and is more reliable and feasible in real world application.

There exists inherent variability and uncertainties in the seismic response of highway bridges due to earthquake motion characteristics and soil-structure-interaction effects. In practice, one can account for this complexity by performing nonlinear time history analysis with a group of ground motion records and appropriately modeling the bridge embankments and foundations to reflect the kinematic and inertial soil-bridge interactions. On this basis, the equivalent passive design procedure proposed by this study can be applied and lead to optimal selection of the design parameters of seismic protective devices on the highway bridge.

6. Conclusions and Future Work

6.1 Conclusions

Buildings and bridges are susceptible to various levels of damages as observed in past major earthquakes. The damages can result from insufficient force or displacement design capacity compared to excessive demands due to seismic shaking. Structural control through seismic protective devices is essential to achieve certain performance goal and realize structural response reduction in terms of eliminating excessive displacement and acceleration.

Seismic protective devices, in either passive or adaptive passive forms, can be used to improve the seismic performances of highway bridges in high seismicity regions. However, careful selection of optimum stiffness and damping properties of these devices is important to fulfill their advantages and achieve multi-performance objectives when subject to earthquakes that have various frequency contents and intensities.

Supplemental energy dissipation in the form of nonlinear viscous dampers is often used to improve the performance of structures. The optimal amount of nonlinear damping is needed to achieve the desired performance of inelastic structures. Through numerical investigation using dimensional analysis, the nonlinear damping required to achieve the optimal performance of inelastic structures is quantified. A dimensionless nonlinear damping ratio is proposed which decisively quantifies the effects of nonlinear damping devices, such as nonlinear viscous dampers, on structural responses (e.g. drift and total acceleration) of inelastic structures subject to pulse-type near-fault ground motions. It is demonstrated that the added nonlinear damping is not always beneficial for inelastic structures, resulting in the increase of their total accelerations under certain ground motions.

A critical structure-to-pulse frequency ratio exists, under which an optimal nonlinear damping needs to balance between the increases of total acceleration and the reductions of the structural drift. The optimal damping for inelastic structures is a function of both nonlinear structural behavior and the ground motion properties, i.e. whether larger nonlinear damping is beneficial depends on the relative frequency between the structure and the input motion. By finding the equivalent SDOF system for a MDOF inelastic structure, the nonlinear damping ratio is generalized to characterize more realistic structures and could be applied for seismic protective device design, such as optimally determining the amount and position of nonlinear viscous dampers in a MDOF inelastic structure.

Alternatively, to achieve the optimal responses using seismic protective devices, one could use active or semi-active control theory to guide the selection of mechanical properties of passive devices, such that the effects of active or semi-active control are duplicated. However, the structural control of nonlinear structures cannot be easily conducted due to the difficulties in modeling of complex structures and in implementing the control algorithms within the typical finite element programs.

An existing hybrid simulation software (UI-SIMCOR) is adopted and modified to perform the dynamic analysis of nonlinear structures equipped with seismic protective devices. This hybrid scheme provides an approach to isolate the nonlinear seismic protective devices to be modeled in a software that can fully simulate its behavior while keeping other parts of a nonlinear structure numerically modeled in general FEM platform. Utilizing the hybrid numerical simulation scheme proposed based on UI_SimCor, the response of a highway bridge can be obtained by integrating various numerical and physical components as well as using different computational platforms. The commonly used seismic protective devices, including

nonlinear viscous dampers, base isolators and MR dampers, are implemented to numerically investigate their validity under this hybrid simulation framework. UI_SimCor is also updated by this study to accommodate more realistic scenarios such as consideration of multiple support excitations.

In particular, this study adopts OpenSees to model the nonlinear main structure while the seismic protective devices and the control algorithms are implemented in Matlab. Through the hybrid simulation scheme proposed, the advantages of these two computational programs are fully utilized, i.e. the practice of modeling complex nonlinear structures in OpenSees and characterizing seismic control devices which cannot be modeled in general FEM softwares in Matlab enables the accurate and realistic seismic response assessment of highway bridges with control devices.

An experimental program is finished to verify the numerical results and structural performance by hybrid numerical simulation scheme. RTHS and shake table tests are performed with a 3-story steel frame structure controlled by a MR damper. It's validated by the experimental study that the numerical hybrid simulation scheme proposed has a high level of accuracy and efficiency, thus this methodology can be utilized for further analysis and design of seismic control devices to optimally select the device parameters.

A 3D global dynamic analysis is employed in this study for a highway bridge, Painter Street Overcrossing, where the nonlinear structure is built in OpenSees including the soil-structure interaction elements while the seismic protective devices and control algorithms are implemented in Matlab. LQG regulator with Kalman filter is adopted to obtain the optimal structural response of base isolated Painter Street Bridge equipped with semi-actively controlled MR dampers through clipped optimal control algorithm. The structural response from semi-

active control serves as the standard/target to optimally design the passive parameters of MR dampers. Hybrid simulation scheme makes the convenient application of structural control algorithm that is not available in common commercial FEM softwares possible.

A novel approach to perform optimal passive design of MR dampers is proposed for highway bridge application. It's achieved by replacing the time-varying control voltage command of MR damper with an equivalent constant input which is the average over time of the control voltage history given by numerical analysis of the semi-actively controlled bridge. The equivalent passive design is able to closely mimic the effects of the adaptive semi-active control and is more reliable and feasible in real world application. A comprehensive implementation strategy and procedure are developed to provide the required stiffness and damping properties (within practical/achievable range) of MR dampers for optimal structural responses of highway bridges.

6.2 Recommendations for Future Work

Through the findings of this research, a number of important areas related to the optimal design of seismic control devices and risk evaluation of highway bridges can be further studied. Recommendations for future research directions are as follows:

- (i) Define different levels of performance index for highway bridge system with components of various importance levels and output requirements to fulfill engineering and statistic need in design of highway bridges under a variety of excitation types, structural configurations and soil properties.
- (ii) Implement other nonlinear control theories on the control and design procedure. This study adopts clipped optimal control based on LQG regulator, which is developed for a linear

based system. In the future application, other nonlinear control theories, such as Sliding Mode Control (SMC) for nonlinear system, can be accommodated in the application of seismic control device design.

(iii) Consider comprehensive uncertainties by applying fragility function to address the probability of failure and meet the performance objective. Further identify the effects of stiffness and damping properties of seismic protective devices by comparing the damage potential for given earthquake intensity (as manifested by the fragility functions).

(iv) Develop a comprehensive design scheme and strategy for passive control devices under PBEE framework. Given certain performance objective of highway bridges, the design scheme will lead to the determination of optimal mechanical properties and locations of the seismic protective devices such that general engineering or social objectives could be achieved.

References

- Agrawal, A.K., Tan, P., Nagarajaiah, S. and Zhang, J. (2009). "Benchmark Structural Control Problem for A Seismically Excited Highway Bridge-Part I: Phase I Problem Definition", *Structural Control and Health Monitoring*, 16(5), 509-529.
- Aiken, I.D., Nims, D.K., and Kelly, J.M. (1992). "Comparative Study of Four Passive Energy Dissipation Systems", *Bulletin of the New Zealand National Society for Earthquake Engineering*, 25(3), 175-192.
- Amin, N. and Mokha, A. S. (1995). "Base Isolation Gets Its Day in Court", *Civil Engineering, ASCE*, 65(2), 44-47.
- Bergman, D.M. and Hanson, R.D. (1993). "Viscoelastic Mechanical Damping Devices Tested at Real Earthquake Displacement", *Earthquake Spectra*, 9(3), 389-418.
- Buckle, I.G., Mayes, R.L. (1990). "Seismic Isolation History: Application and Performance - A World Review", *Earthquake spectra*, (6), 161-201.
- Caicedo, J.M. (2011). "Practical Guidelines for the Natural Excitation Technique and the Eigensystem Realization Algorithm (ERA) for Modal Identification Using Ambient Vibration", *Experimental Techniques*, 35(4), 52-58.
- Caicedo, J.M., Dyke, S.J. and Johnson, E.A. (2004). "Natural Excitation Technique and Eigensystem Realization Algorithm for Phase I of the IASC-ASCE Benchmark Problem: Simulated Data", *Journal of Engineering Mechanics*, 130(1), 49-60.
- Caltrans. (1994). "The Continuing Challenge: the Northridge Earthquake of January 17, 1994", Report to the Director, California Department of Transportation, Sacramento, CA.
- Carlson, J.D. and Spencer, B.F. Jr. (1996a). "Magneto-Rheological Fluid Dampers for Semi-Active Seismic Control", *Proc. of the 3rd Int. Conf. on Motion and Vibr. Control*, Chiba, Japan, (3), 35-40.
- Carlson, J.D. and Spencer, B.F. Jr. (1996b). "Magneto-Rheological Fluid Dampers: Scalability and Design Issues for Application to Dynamic Hazard Mitigation", *Proc. of 2nd Int. Wkshp. on Struc. Control*, Hong Kong, 99-109.
- Carrión, J.E., Spencer, B.F. Jr. and Phillips, B.M. (2009). "Real-Time Hybrid Testing of A Semi-Actively Controlled Structure with An MR Damper", *American Control Conference, 2009*, 5234-5240.

- Castaneda, N., Gao, X. and Dyke, S. (2012). "A Real-Time Hybrid Testing Platform for the Evaluation of Seismic Mitigation in Building Structures", *Structures Congress, 2012*, Chicago, Illinois.
- Chang, K.C., Chang, D.W., Tsai, M.H. and Sung, Y.C. (2000). "Seismic Performance of Highway Bridges", *Earthquake Engineering and Engineering Seismology*, 2(1), 55-77.
- Chang, S.P., Makris, N., Whittaker, A.S. and Thompson, A.C.T. (2002). "Experimental and Analytical Studies on the Performance of Hybrid Isolation System", *Earthquake Engineering and Structural Dynamics*, 31(2), 421-443.
- Chang, K.C., Soong, T.T., Oh, S.T. and Lai, M.L. (1995). "Seismic Behavior of Steel Frame with Added Viscoelastic Dampers", *Journal of Structural Engineering*, ASCE, 121(10), 1418-1426.
- Chen, C. and Ricles, J.M. (2009). "Improving the Inverse Compensation Method for Real-Time Hybrid Simulation through A Dual Compensation Scheme", *Earthquake Engineering & Structural Dynamics*, 38(10), 1237-1255.
- Chopra, A.K. (2001). "Dynamics of Structures: Theory and Applications to Earthquake Engineering", Prentice Hall, Prentice-Hall International, 2001.
- Christenson, R.E., Lin, Y.Z., Emmons, A.T. and Bass, B. (2008). "Large-Scale Experimental Verification of Semi-active Control through Real-Time Hybrid Simulation", *Journal of Structural Engineering*, 134(4), 522-535.
- Cimellaro, G.P., Lavan, O., and Reinhorn, A.M. (2008). "Design of Passive Systems for Control of Inelastic Structures", *Earthquake Engineering & Structural Dynamics*, 38(6), 783-804.
- Constantinou, M.C., Soong T.T. and Dargush, G.F. (1998). "Passive Energy Dissipation System for Structural Design and Retrofit", Multidisciplinary Center for Earthquake Engineering Research Monograph Series, No. 1.
- Constantinou, M.C. and Symans, M.D. (1993). "Experimental Study of Seismic Response of Buildings with Supplemental Fluid Dampers", *Structural Design of Tall and Special Buildings*, 2(2), 93-132.
- Darby, A.P., Blakeborough, A. and Williams, M.S. (1999). "Real-Time Substructure Tests Using Hydraulic Actuator", *Journal of Engineering Mechanics*, 125(10), 1133-1139.
- Datta, T.K. (2003). "A State-of-the-Art Review on Active Control Of Structures", *Journal of Earthquake Technology*, ISET, 40(1), 1-17.
- Diotallevi, P.P., Landi, L. and Dellavalle, A. (2012). "A Methodology for the Direct Assessment of the Damping Ratio of Structures Equipped with Nonlinear Viscous Dampers", *Journal of Earthquake Engineering*, 16(3), 350-373.

- Dyke, S.J., Spencer, B.F. Jr., Sain, M.K. and Calson, J.D. (1996). "Modeling and Control of Magneto-Rheological Dampers for Seismic Response Reduction", *Smart Mat. and Struct.*, (5), 565-575.
- Dyke, S.J., Yi, F. and Calson, J.D. (1999). "Application of Magneto-Rheological Dampers to Seismically Excited Structures", *Proc. of the Intl. Modal Anal. Conf.*, Kissimmee, Florida, February 8-11.
- Eberhard, M.O., Mookerjee, A. and Parrish, M. (2001). "Uncertainties in Performance Estimates for RC Columns", Pacific Earthquake Engineering Research Center, Richmond, CA.
- Federal Emergency Management Agency (FEMA). (2003). "The Disaster Resistant University Guide", Washington, DC.
- Ghobarah, A. and Ali, H.M. (1988). "Seismic Performance of Highway Bridges", *Journal of Engineering Structures*, 10(3), 157-166.
- Giraldo, D., Yoshida, O.S., Dyke, J. and Giacosa, L. (2004). "Control-Oriented System Identification Using ERA", *Structural Control and Health Monitoring*, (11), 311-326.
- Gluck, N., Reinhorn, A.M., Gluck, J. and Levy, R. (1996). "Design of Supplemental Dampers for Control of Structures", *Journal of Structural Engineering*, 122(12), 1394-1399.
- Goldberg, D.E., Korb, B. and Deb, K. (1989). "Messy Genetic Algorithms: Motivation, Analysis and First Results", *Complex Systems*, 5(3), 493-530.
- Han, Q., Du, X.L., Liu, J.B., Li, Z.X., Li, L.Y., and Zhao, J.F. (2009). "Seismic Damage of Highway Bridges during the 2008 Wenchuan Earthquake", *Earthquake Engineering and Engineering Vibration*, 8(2), 263-273.
- Housner, G.W., Bergman, L.A., Caughey, T.K. and Chassiakos, A.G. (1997). "Structural Control: Past, Present, and Future", *Journal of Engineering Mechanics*, 123(9), 897-971.
- Idriss, I.M., Seed, H.B. and Serff, N. (1974). "Seismic Response by Variable Damping Finite Elements", *Journal of Geotechnical Engineering*, 100(GT1), 1-13.
- Ikeda, Y., Sasaki, K., Sakamoto, M. and Kobori, T. (2001). "Active Mass Driver System as the First Application of Active Structural Control", *Earthquake Eng. and Struct. Dyn.*, (30), 1575-1595.
- Inaudi, J.A. and Kelly, J.M. (1993). "Optimum Damping in Linear Isolation Systems", *Earthquake Engineering & Structural Dynamics*, 22(7), 583-598.
- Iwasaki, T., Tatsuoka, F. and Takagi, Y. (1978). "Shear Moduli of Sands under Cyclic Torsional Shear Loading", *Soils and Foundations*, 18(1), 39-56.

- Jacobsen, L.S. (1930). "Steady Forced Vibration as Influenced by Damping", *Transactions, ASME*, 52(1), 169-181.
- Juang, J.N. and Pappa, R.S. (1985). "An Eigensystem Realization Algorithm for Modal Parameter Identification and Model Reduction", *Journal of Guidance, Control and Dynamics*, 8(5), 620-627.
- Kalman, R.E. (1960). "A New Approach to Linear Filtering and Prediction Problems", *Journal of Basic Engineering*, 82(1), 35-45.
- Kawamura, S., Kitazawa, K., Hisano, M. and Nagashima, I. (1988). "Study of A Sliding Type Base Isolation System: System Composition and Element Properties", *Proc. of 9th WCEE*, Tokyo-Kyoto, (5), 735-740.
- Kawashima, K. (2004). "Seismic Isolation of Highway Bridges", *Journal of Japan Association for Earthquake Engineering*, 4(3) (Special Issue), 283-297.
- Kelly, J.M. (1999). "The Role of Damping in Seismic Isolation", *Earthquake Engineering & Structural Dynamics*, 28(1), 3-20.
- Ko, J.M., Ni, Y.Q., Chen, Z.Q. and Spencer, B.F. Jr. (2002). "Implementation of MR Dampers to Dongting Lake Bridge for Cable Vibration Mitigation", *Proc. of the 3rd World Conference on Structural Control*, Como, Italy.
- Kunde, M.C. and Jangid, R.S. (2003). "Seismic Behavior of Isolated Bridges: A State-of-the-Art Review", *Electronic Journal of Structural Engineering*, (3), 140-170.
- Kwon, O.S., Elnashai, A.S. and Spencer, B.F. Jr. (2008). "A Framework for Distributed Analytical and Hybrid Simulations", *Structural Engineering and Mechanics*, 30(3), 331-350.
- Kwon, O.S., Nakata, N., Park, K.S., Elnashai, A. and Spencer, B.F. Jr. (2007). "User Manual and Examples for UI-SimCor V2.6", Dept. of Civil & Environmental Engineering, UIUC, Illinois.
- Madden, G.J., Symans, M.D. and Wongprasert, N. (2002). "Experimental Verification of Seismic Response of Building Frame with Adaptive Sliding Base-Isolation System", *Journal of Structural Engineering*, 128 (8), 1037-1045.
- Mahin, S.A. and Shing, P.B. (1985). "Pseudo-Dynamic Method for Seismic Testing", *Journal of Structural Engineering*, 111(7), 1482-1503.
- Makris, N. and Black, C.J. (2004a). "Dimensional Analysis of Rigid-Plastic and Elastoplastic Structures under Pulse-Type Excitations", *Journal of Engineering Mechanics*, 130(9), 1006-1018.

- Makris, N. and Black, C.J. (2004b). "Dimensional Analysis of Bilinear Oscillators under Pulse-Type Excitations", *Journal of Engineering Mechanics*, 130(9), 1019-1031.
- Makris, N. and Chang, S.P. (1998). "Effect of Viscous, Viscoplastic and Friction Damping on the Response of Seismic Isolated Structures", *Journal of Earthquake Technology*, ISET, 35(4), 113-141.
- Makris, N. and Zhang, J. (2004). "Seismic Response Analysis of A Highway Overcrossing Equipped with Isolation Bearings and Fluid Dampers", *Journal of Structural Engineering*, ASCE, 130(6), 830-845.
- McCallen, D.B. and Romstad, K.M. (1994). "Analysis of A Skewed Short-Span Box-Girder Overpass", *Earthquake Spectra*, 10(4), 729-755.
- Maragakis, E.A. and Jennings, P.C. (1987). "Analytical Models for the Rigid Body Motions of Skew Bridges", *Earthquake Engineering and Structural Dynamics*, 15(8), 923-44.
- Meehan, J.F. (1971). "Damage to Transportation Systems, the San Fernando, California Earthquake of February 9, 1971", USGS Professional Paper 733, U.S. Government Printing Office, Washington, DC, 241-244.
- Ministry of Construction. (1995). Committee for Investigation on the Damage of Highway Bridges Caused by the Hyogo-ken Nanbu Earthquake, Japan. Report on the Damage of Highway Bridges by the Hyogo-ken Nanbu Earthquake.
- Naeim, F. and Kelly, J.M. (1999). "Design of Seismic Isolated Structures: from Theory to Practice", John Wiley, New York, NY.
- Nagarajaiah, S. and Sun, X.H. (2000). "Response of Base-Isolated USC Hospital Building in Northridge Earthquake", *Journal of Structural Engineering*, 126(10), 1177-1186.
- Nakashima, M., Kaminosono, N., Ishida, M. and Ando, K. (1990). "Integration Techniques for Substructure Pseudo Dynamic Test", *Proc. of 4th U.S. National Conf. on Earthquake Engineering*, Palm Springs, CA, 515-524.
- Nagarajaiah, S., Narasimhan, S., Agrawal, A. and Tan, P. (2009). "Benchmark Structural Control Problem for A Seismically Excited Highway Bridge - Part III: Phase II Sample Controller for the Fully Base-Isolated Case", *Structural Control and Health Monitoring*, (16), 549-563.
- Nagarajaiah, S., Narasimhan, S. and Johnson, E. (2008). "Structural Control Benchmark Problem: Phase II - Nonlinear Smart Base-Isolated Building Subjected to Near-Fault Earthquakes", *Structural Control and Health Monitoring*, (15), 653-656.
- Office of Emergency Services. (1995). Vision 2000: Performance-Based Seismic Engineering of Buildings, Prepared by Structural Engineers Association of California, Sacramento, CA.

- Ozdagli, A., Xi, W., Li, B., Dyke, S.J., Wu, B. and Zhang, J. (2013a). "Actual Hammer Test on A 3DOF Structure after Structural Modification", Network for Earthquake Engineering Simulation.
- Ozdagli, A., Xi, W., Li, B., Dyke, S.J., Wu, B., Zhang, J. and Ding, Y. (2013b). "Preliminary Hammer Test on A 3DOF Structure after Structural Modification", Network for Earthquake Engineering Simulation.
- Ohtori, Y., Christenson, R.E., Spencer, B.F. and Dyke, S.J. (2004). "Benchmark Control Problems for Seismically Excited Nonlinear Buildings", *Journal of Engineering Mechanics*, 130(4), 366-385.
- Ou, J.P. (2003). "Structural Vibration Control: Active, Semi-Active and Smart Control Systems", Press of Science, China.
- Panichacarn, V. (2006). "A Structural Health Monitoring Approach Using ERA: Real Numbered Mode Shape Transformation and Basis Mode Screening", ProQuest.
- Porter, K.A. (2003). "An Overview of PEER's Performance-Based Earthquake Engineering Methodology", *Proceedings of the Ninth International Conference on Application of Statistic and Probability in Civil Engineering*, San Francisco, CA.
- Rai, N.K., Reddy, G.R., Ramanujam, S., Venkatraj, V. and Agrawal, P. (2009). "Seismic Response Control Systems for Structures", *Defence Science Journal*, 59(3), 239-251.
- Roberts, J.E. (2005). "Caltrans Structural Control for Bridges in High-Seismic Zones", *Earthquake Engineering and Structural Dynamics*, (34), 449-470.
- Saouma, V. and Sivaselvan M.V. (2008). "Hybrid Simulation: Theory, Implementation and Applications", Taylor & Francis, Inc., London, UK.
- Shing, P.B., Nakashima, M. and Bursi, O.S. (1996). "Application of Pseudo-Dynamic Test Method to Structural Research", *Earthquake Spectra*, 12(1), 29-56.
- Shukla, A.K. and Datta, T.K. (1999). "Optimal Use of Viscoelastic Dampers in Building Frames for Seismic Force", *Journal of Structural Engineering*, 125(4), 401-409.
- Spencer, B.F. Jr. (1996). "Recent Trends in Vibration Control in the USA", *Proc. of 3rd Int. Conf. on Mointion and Vibration Control*, Chiba, Japan, 2, K1-K6.
- Spencer, B.F. Jr., Dyke, S.J., Sain, M.K. and Carlson, J.D. (1997c). "Phenomenological Model for Magneto-Rheological Dampers", *Journal of Engineering Mechanics*, ASCE, 123(3), 230-238.
- Spencer, B.F. Jr. and Nagarajaiah, S. (2003). "State of the Art of Structural Control", *Journal of Structural Engineering*, 29(7), 845-856.

- Soong, T.T. and Dargush, G.F. (1997). "Passive Energy Dissipation Systems in Structural Engineering", Wiley & Sons, New York.
- Soong, T.T. and Spencer, B.F. Jr. (2002). "Supplemental Energy Dissipation: State-of-the-Art and State-of-the-Practice", *Engineering Structures*, 24(3), 243-259.
- Structural Engineers Association of California. (1999). Recommended Lateral Force Requirements and Commentary, Sacramento, CA.
- Symans, M.D., Charney, F.A., Whittaker, A.S., Constantinou, M.C., Kircher, C.A., Johnson, M.W. and McNamara, R.J. (2008). "Energy Dissipation Systems for Seismic Applications: Current Practice and Recent Developments", *Journal of Structural Engineering*, 134(1), 3-21.
- Symans, M.D. and Constantinou, M.C. (1997a). "Experimental Testing and Analytical Modeling of Semi-Active Fluid Dampers for Seismic Protection", *Journal of Intelligent Material Systems and Structures*, 8(8), 644-657.
- Symans, M.D. and Constantinou, M.C. (1997b). "Seismic Testing of A Building Structure with A Semi-Active Fluid Damper Control System", *Earthquake Engineering and Structural Dynamics*, 26 (7), 759-777.
- Symans, M.D. and Constantinou M.C. (1998). "Passive Fluid Viscous Damping Systems for Energy Dissipation", *Journal of Earthquake Technology*, 35(4), 185-206.
- Tang, Y.C. and Zhang, J. (2011). "Response Spectrum-oriented Pulse Identification and Magnitude Scaling of Forward Directivity Pulses in Near-Fault Ground Motions", *Soil Dynamics and Earthquake Engineering*, 31(1), 59-76.
- Tarakji, G. (1992). "Lessons Not Learned from 1989 Loma Prieta Earthquake", *Journal of Professional Issues in Engineering Education and Practice*, 118(2), 132-138.
- Tatsuoka, F., Iwasaki, T. and Takagi, Y. (1978). "Hysteretic Damping of Sands under Cyclic Loading and Its Relation to Shear Modulus", *Soils and Foundations*, 18(2), 25-40.
- United States General Accounting office. (1992). The Nation's Highway Bridges Remain at Risk from Earthquakes, Report to Congressional Requesters.
- Vucetic, M. and Dobry, R. (1991). "Effect of Soil Plasticity on Cyclic Response", *Journal of Geotechnical Engineering*, ASCE, 117(1), 89-107.
- Wanitkorkul, A. and Filiatrault, A. (2008). "Influence of Passive Supplemental Damping Systems on Structural and Nonstructural Seismic Fragilities of a Steel Building", *Engineering Structures*, 30(3), 675-682.

- Wu, B., Ou, J.P. and Soong, T.T. (1997). "Optimal Placement of Energy Dissipation Devices for Three-dimensional Structures", *Engineering Structures*, 19(2), 113-125.
- Zayas, V., Low, S.S. and Main, S.A. (1987). "The FPS Earthquake Resisting System, Experimental Report", Report No. UCB/EERC-87/01, Engineering Research Center, University of California, Berkeley, CA.
- Zhang, J. (2002). "Seismic Response Analysis and Protection of Highway Overcrossings Including Soil-Structure Interaction", *Ph.D. Thesis*, Dept. of Civil and Environmental Engineering, University of California, Berkeley, CA.
- Zhang, J. and Huo, Y.L. (2009). "Evaluating Effectiveness and Optimum Design of Isolation Devices for Highway Bridges Using Fragility Function Method", *Engineering Structures*, 31(8), 1648-1660.
- Zhang, J. and Makris, N. (2001). "Seismic Response Analysis of Highway Overcrossing including Soil-Structure Interaction", Report No. PEER-01/02, Pacific Earthquake Engineering Research Center, University of California, Berkeley.
- Zhang, J. and Makris, N. (2002). "Kinematic Response Functions and Dynamic Stiffnesses of Bridge Embankments", *Earthquake Engineering and Structural Dynamics*, 31(11), 1933-1966.
- Zhang, J. and Makris, N. (2002). "Seismic Response Analysis of Highway Overcrossings including Soil-Structure Interaction", *Earthquake Engineering and Structural Dynamics*, 31(11), 1967-1991.
- Zhang, J. and Tang, Y.C. (2009). "Dimensional Analysis of Structures with Translating and Rocking Foundations under Near-Fault Ground Motions", *Soil Dynamics and Earthquake Engineering*, 29(10), 1330-1346.